Understanding Orchestrated Chemical Reactions in Toluene/*o*-Xylene Monooxygenase from *Pseudomonas Sporium* OX1

by

Woon Ju Song
B.Sc., Ewha Womans University (2003)
M.Sc., Ewha Womans University (2005)

SUBMITTED TO THE DEPARTMENT OF CHEMISTRY IN PARTIAL FULFILLMENT OF THE REQUIREMENTS FOR THE DEGREE OF

DOCTOR OF PHILOSOPHY IN CHEMISTRY

AT THE

MASSCHUSETTS INSTITUTE OF TECHNOLOGY

MAY 2011
[June 2011]

Signature of Author: ______________________

Department of Chemistry
May 4, 2011

Certified by: ______________________

Stephen J. Lippard
Arthur Amos Noyes Professor of Chemistry
Thesis Supervisor

Accepted by: ______________________

Robert W. Field
Haslem and Dewey Professor of Chemistry
Chairman, Departmental Committee on Graduate Studies

This doctoral thesis has been examined by a Committee of the Department of Chemistry as follows:

Daniel G. Nocera
The Henry Dreyfus Professor of Energy and Professor of Chemistry
Committee Chairman

Stephen J. Lippard
Arthur Amos Noyes Professor of Chemistry
Thesis Supervisor

JoAnne Stubbe
Novartis Professor of Chemistry and Professor of Biology

Understanding Orchestrated Chemical Reactions in Toluene/*o*-Xylene Monooxygenase from *Pseudomonas Sporium* OX1

by

Woon Ju Song

Submitted to the Department of Chemistry on May 20, 2011, in partial fulfillment of the requirements for the Degree of Doctor of Philosophy

ABSTRACT

Chapter 1. Geometric and Functional Versatility of Carboxylate-Bridged Nonheme-Diiron Motifs: sMMO and ToMO. Several metalloenzymes utilize a carboxylate-bridged non-heme diiron motif for dioxygen activation. Despite their conserved diiron active site structures and mechanisms of dioxygen activation, they catalyze a wide range of chemical transformations. These observations suggest that diiron-containing enzymes have distinct active sites and secondary/tertiary environments that are tuned for their dedicated biological functions. Detailed studies of two diiron-containing enzymes in the family of bacterial multicomponent monooxygenases (BMMs), soluble methane monooxygenase (sMMO) and toluene/*o*-xylene monooxygenase (ToMO), are described. The functions and structures of the three or four components of sMMO and ToMO are summarized. Distinctly different dioxygen activation chemistry and hydrocarbon specificity is observed for these two enzymes. A comparison of these two enzymes provides insight into the evolution of diiron-containing enzymes as well as their differing chemical mechanisms of catalysis.

Chapter 2. Role of an Active Site Threonine in the Determination of Distinctive Dioxygen Reactivity in Toluene/*o*-Xylene Monooxygenase Hydroxylase. Dioxygen activation of toluene/*o*-xylene monooxygenase hydroxylase (ToMOH) exhibits the

formation of a diiron(III) intermediate having unprecedented spectroscopic properties. To evaluate whether an active site threonine plays a role in the determination of the dioxygen chemistry in ToMOH, a T201S variant was prepared by site-directed mutagenesis. We reported the observation of a novel intermediate in the reaction of reduced ToMOH T201S variant with dioxygen in the presence of its cognate regulatory protein (ToMOD). This species, $T201_{peroxo}$, is the first oxygenated intermediate of any toluene monooxygenase to display an optical band. The optical and Mössbauer spectroscopic properties of the intermediate allowed us to assign it as a peroxodiiron(III) species, similar to H_{peroxo} in soluble methane monooxygenase hydroxylase (sMMOH). This result indicates that mutation of the T201 to serine altered the dioxygen chemistry of ToMOH in part to be more similar to that of sMMOH. Computational studies suggest that the T201 mutation can greatly perturb the energetics of the enzyme, which might be responsible for the distinct dioxygen reactivity of sMMOH and ToMOH. Structures of the oxygenated intermediates of ToMOH are proposed.

Chapter 3. Role of an Active Site Threonine in the Kinetics of Dioxygen Activation in Toluene/*o*-Xylene Monooxygenase Hydroxylase. To elucidate the role of a strictly conserved T201 residue during dioxygen activation of toluene/*o*-xylene monooxygenase hydroxylase (ToMOH), T201S, T201G, T201C, and T201V variants of this enzyme were prepared by site-directed mutagenesis. X-ray crystal structures of all variants were obtained. Steady-state activity, regiospecificity, and single-turnover yields were also determined for the T201 mutants. Dioxygen activation by the reduced T201 variants was monitored by stopped-flow UV-vis and Mössbauer spectroscopy. These studies demonstrated that the same dioxygen activation mechanism is preserved in the T201S, T201C, and T201G variants; however, both formation and decay kinetics of a peroxodiiron(III) intermediate, T201$_{\text{peroxo}}$, were greatly altered, revealing that the T201 residue is critically involved in dioxygen activation. Rate-limiting steps in dioxygen activation of the T201S, T201C, and T201G variants were identified, revealing that T201 plays a major role in proton transfer, which is required to generate the peroxodiiron(III) intermediate. The role of the active site threonine residue in ToMOH is analogous to that of cytochrome P450 monooxygenases, suggesting it as a general threonine-dependent process in Nature to control proton transfer.

Chapter 4. Mechanistic Studies of Reactions of Peroxodiiron(III) Intermediates in the T201 Variants of Toluene/*o*-Xylene Monooxygenase Hydroxylase. Site-directed mutagenesis studies of a strictly conserved T201 residue in the active site of toluene/*o*-xylene monooxygenase hydroxylase (ToMOH) revealed that a single mutation can facilitate kinetic isolation of two distinct peroxodiiron(III) species, designated T201$_{\text{peroxo}}$ and ToMOH$_{\text{peroxo}}$, during dioxygen activation. In Chapter 2 and 3, we characterized both oxygenated intermediates by UV-vis and Mössbauer spectroscopy, proposed structures from DFT and QM/MM computational studies, and elucidated chemical steps involved in dioxygen activation through the kinetic studies of T201$_{\text{peroxo}}$ formation. In Chapter 4, we investigated the kinetics of T201$_{\text{peroxo}}$ decay to explore the reaction mechanism of the oxygenated intermediates following O_2 activation. The decay rates of T201$_{\text{peroxo}}$ were monitored in the absence and presence of external (phenol) or internal (tryptophan residue in I100W variant) substrates under pre-steady-state conditions. Three possible reaction models for the formation and decay of T201$_{\text{peroxo}}$ were evaluated, and the results demonstrate that this species is on the pathway of arene oxidation and appears to be in equilibrium with ToMOH$_{\text{peroxo}}$.

Chapter 5. Tracking a Defined Route of O_2-Migration in a Dioxygen-Activating Diiron Enzyme, Toluene/*o*-Xylene Monooxygenase Hydroxylase. For numerous enzymes reactive toward small gaseous compounds, growing evidence indicates that these substrates diffuse into active site pockets through defined pathways in the protein matrix. Toluene/*o*-xylene monooxygenase hydroxylase (ToMOH) is a dioxygen-activating carboxylate-bridged nonheme-diiron enzyme. Structural analyses of the resting state enzyme suggest two possible pathways for dioxygen to access the α-subunit diiron center, a series of hydrophobic cavities or long solvent-exposed channel. To distinguish which pathway is utilized for dioxygen transfer, the dimensions of the cavities and channel were varied by site-directed mutagenesis and confirmed by X-ray crystallography. The rate of dioxygen access to the active site was monitored by measuring the formation rate of an oxygenated intermediate ($T201_{peroxo}$), a process that is dependent on O_2 concentration. Altering the dimensions of the cavity but not the channel drastically changed the rate of dioxygen activation by the reduced enzyme. These results explicitly reveal that the cavities in the ToMOH α-subunit are not merely artifacts of protein packing/folding but rather programmed routes of dioxygen movement through the protein matrix. This conclusion indicates that conformational changes are required during catalysis to form a dioxygen trajectory and that the temporary opening/closing of the cavities control dioxygen transfer. Given that the cavities are present in all BMMs, the breathing motion presumably controls dioxygen consumption in all BMMs. This study represents the first approach to track kinetically a defined transient pathway by which a small gaseous molecule gains access to a diiron enzyme.

Appendix A. Insights into the Different Dioxygen Activation Pathways of Methane and Toluene Monooxygenase Hydroxylases. The methane and toluene monooxygenase hydroxylases (MMOH and TMOH, respectively) have almost identical active sites, yet the physical and chemical properties of their oxygenated intermediates, designated P*, H_{peroxo}, Q and Q* in MMOH, and $ToMOH_{peroxo}$ in toluene/*o*-xylene monooxygenase hydroxylase (ToMOH), are substantially different. We review and compare the structural differences in the vicinity of the active sites of these enzymes and discuss the differences that give rise to the distinct behavior of dioxygen reactivity in sMMOH and ToMOH. In particular, analysis of multiple crystal structures reveals that T213 of MMOH and analogous T201 of TMOH, located in the immediate vicinity of the active site, have different rotamer configurations. We study the rotation energy profiles of these threonine residues with the use of molecular mechanics (MM) and quantum mechanics/molecular mechanics (QM/MM) computational methods and put forward a hypothesis according to whether T201 and T213 play an important role in the formation of different types of peroxodiiron(III) species in MMOH and ToMOH. The hypothesis is indirectly supported by QM/MM calculations of the peroxodiiron(III) models of ToMOH and the theoretically computed Mössbauer spectra. It also helps explain the formation of two distinct peroxodiiron(III) species in the T201S mutant of ToMOH. Additionally, a role for the regulatory protein (ToMOD), which is essential for oxygenated intermediate formation and the protein functioning in the ToMO system, is advanced.

Appendix B. Multiple Roles of Component Proteins in Bacterial Multicomponent Monooxygenases: Phenol Hydroxylase and Toluene/*o*-Xylene Monooxygenase from *Pseudomonas sp.* OX1. Phenol hydroxylase (PH) and toluene/*o*-xylene monooxygenase

(ToMO) from *Pseudomonas sp.* OX1 require three or four protein components to activate dioxygen for the oxidation of aromatic substrates at a carboxylate-bridged diiron center. In this study, we investigated the influence of the hydroxylases, regulatory proteins, and electron-transfer components of these systems on substrate consumption and product generation. Single-turnover experiments revealed that only complete systems containing all three or four protein components are capable of oxidizing phenol, a major substrate for both enzymes. Under ideal conditions, the hydroxylated product yield was ~50% of the diiron centers for both systems, suggesting that these enzymes operate by half-sites reactivity mechanisms. Single-turnover studies indicated that the PH and ToMO electron-transfer components exert regulatory effects on substrate oxidation processes taking place at the hydroxylase active sites, most likely through allostery. Steady state NADH consumption assays showed that the regulatory proteins facilitate the electron-transfer step in the hydrocarbon oxidation cycle in the absence of phenol. Under these conditions, electron consumption is coupled to H_2O_2 formation in a hydroxylase-dependent manner. Mechanistic implications of these results are discussed.

Thesis Supervisor: Stephen J. Lippard

Title: Arthur Amos Noyes Professor of Chemistry

Dedicated to my family who always believed in me

Acknowledgements

Last five years are one of the most unforgettable and precious time in my life, which allowed me to challenge myself how hard I can try and how much I can enjoy chemistry. I had tough moments but I came all the way here because many people helped me and strengthen me.

Foremost, I would truly like to thank my research advisor, Prof. Steve Lippard, who committed his life to teaching and supporting his students. He never stops learning and enjoying science, which always has motivated me and many others. In addition, he expects all students to meet his high standards. Although I had no backgrounds in biochemistry when I joined his lab and had (and still have) poor writing skill, he has been patient in me and never doubting on my capability. In addition to having his guidance and support on my research, I was fortunate to learn how he can maintain five subgroups and organize the lab in an efficient manner.

It was my great honor to have Prof. Dan Nocera and Prof. JoAnne Stubbe as my thesis committee. They appreciated my chemistry and gave me thorough insights and helpful critiques of my work. In addition to their guidance during oral exams and thesis defense, their lectures are one of the best classes that I have taken. I would also like to thank other inorganic chemistry professors, Prof. Richard Schrock and Christopher Cummins, who balanced my knowledge in inorganic chemistry. I also like to thank Prof. Wonwoo Nam, who was my research advisor of Master Degree at Ewha. He was the teacher who opened my eyes into the world of bioinorganic chemistry. Without his guidance and support, I would not be here.

Experiments that I have performed could have not been achieved without my collaborators. Mössabauer experiments were carried out by Prof. Boi Hanh Huynh and Dr. Sunil G. Naik at Emory University and Prof. Carsten Krebs and Dr. Wei Jiang at the Penn State University. Computational calculation studies were carried out by Prof. Richard Friesner, Dr. Arteum Bochevarov, and Jianing Li at Columbia University. X-ray crystal structures were determined by a former lab mate, Dr. Michael McCormick, and Prof. Matthew Sazinsky, Jeffery Lin, and Grant Gucinski at Pomona College.

Dr. Leslie Murray, Dr. Christy Tinberg, and Dr. Rachel Behan were incredible mentors and supporters who helped me to perform all experiments that I presented in my thesis. They were also the best friends who make my MIT life more than enjoyable. I would also like to thank my class mates, Loi Do, Alex Lichtscheidl, and Maggie Flook, who went through the good and tough times together at MIT. They helped me every step on the way here. Many Lippard lab members were also great resources and friends. I learned many things-how to approach the problems, to analyze/present results, and to be great lab mates-simply by being in the lab with them. I am especially grateful to Dr. Nora Graf, Dr. Wee Han Ang, Dr. Lindsey McQuade, Dr. Zachary J. Tonzetich, Dr. Elisa Tomat, Dr. Michael Pluth, Dr. Daniela Buccella, Dr. Ying Song, Dr. Mi Hee Lim, Eric Victor, and Ali Liang. I would also like to thank my friends here including Jeewoo Lim, Sunkyu Han, Sunghee Son, Jungyun Kim, Yoonjin Lee, Bonjun Koo, Sarah Lee, Doory Kim, Hong Geun Lee, Donghyun Kim, and many others for their supports and friends in Korea (too many to list here!) for their friendship.

Most of all, I'd like to thank my parents, Chang Gyu Song and Young Hee Choi, who gave me all talents that I have, therefore, this thesis is dedicated to them. I also thank my sister, Jiyoon Song, who believes in me more than myself, and my family for their incredible supports.

TABLE OF CONTENTS

Chapter 3. Role of an Active Site Threonine in the Kinetics of Dioxygen Activation in Toluene/*o*-Xylene Monooxygenase Hydroxylase........93

LIST OF TABLES

LIST OF SCHEMES

LIST OF CHARTS

LIST OF FIGURES

LIST OF EQUATIONS

ABBREVIATIONS

$[2Fe\text{-}2S]_{ox}$	oxidized form of [2Fe-2S] ferredoxin
$[2Fe\text{-}2S]_{red}$	reduced form of [2Fe-2S] ferredoxin
2Fe-THR	a dihedral angle of Fe1-Fe2-C_β-O
ACP	acyl-acyl carrier protein
AF	antiferromagnetically coupled
AMOs	alkene monooxygenases, a subclass of BMMs
AR-H	arene substance
AR-OH	phenolic substance
AurF	*p*-aminobenzoate *N*-oxygenase or amine oxygenase
BDE	bond dissociation energy
BMMs	bacterial multicomponent monooxygenases
C2,3O	catechol 2,3-dioxygenase
CD	circular dichroism
CLK-1	an aging-associated enzyme in ubiquinone biosynthesis
CmlA	amino acid beta-hydroxylase
δ	isomer shift, a Mössbauer parameter
Δ9D	Δ^9 desaturase
ΔE_Q	quadrupole splitting, a Mössbauer parameter
$\Delta S^\ddagger$	entropy of activation
D_2O	deuterium oxide
DFT	density functional theory

Dnase	deoxyribonuclease
dNTP	deoxynucleotide triphosphate
DTT	dithiothreitol
E. coli	*Escherichia coli*
EPR	electron paramagnetic resonance or electron spin resonance (ESR)
ET	electron transfer
ESI-MS	electron spray ionization-mass spectrometry
FAD	flavin adenine dinucleotide
FAD_{ox}	oxidized form of flavin adenine dinucleotide, FAD
FAD_{sq}	semireduced or semiquinone form of flavin adenine dinucleotide, FADH
FAD_{hq}	reduced form of flavin adenine dinucleotide, $FADH_2$
hDOHH	human deoxyhypusine hydroxylase
H_{peroxo}	a secondly generated oxygenated diiron(III) species in sMMOH, also named as P
Hr	hemerythrin
IPTG	isopropylthiogalactopyranoside
J	coupling constant
k_2	second-order rate constant
k_{cat}	catalytic constant or turnover number
k_{cat}/K_M	catalytic efficiency
k_{decay}	decay rate constant
k_{form}	formation rate constant
K_M	Michaelis constant, a measure of the substrate concentration required for effective catalysis to occur

k_{obs}	observed rate constant
KIE	kinetic isotope effect
KSIE	kinetic solvent isotope effect
$KSIE_{decay}$	kinetic solvent isotope effect from the decay process
$KSIE_{decay1}$	kinetic solvent isotope effect from the first decay process, k_{decay1}
$KSIE_{decay2}$	kinetic solvent isotope effect from the second decay process, k_{decay2}
LB	Luria-Bertani medium
LMCT	ligand to metal charge transfer
MCD	magnetic circular dichroism
MIOX	*myo*-inositol oxygenase
MM	molecular mechanics
MOPS	3-(N-morpholino)propanesulfonic acid
mU	a unit in specific steady-state activity assay, nmol of formed product per minute
NADH	nicotinamide adenine dinucleotide, reduced form
NADPH	nicotinamide adenine dinucleotide phosphate, reduced form
nd	not determined
NMR	nuclear magnetic resonance
OD_{600}	optical density at 600 nm
P	a secondly generated oxygenated diiron(III) species in sMMOH, also named as H_{peroxo}
P^*	a firstly generated oxygenated diiron(III) species and a precursor to P in sMMOH
P450	cytochrome P450 monooxygenases

PAGE	polyacrylamide gel electrophoresis
PCET	proton coupled electron transfer
PCR	polymerase chain reaction
PDB	protein data bank
PEG	polyethylglycol
PH	phenol hydroxylase
PHs	three-component phenol hydroxylases, a subclass of BMMs
PHH	a hydroxylase component of PH
PMT	photomultiplier
Q	a di(μ-oxo)diiron(IV) intermediate observed in sMMOH
O*	a decomposed product of Q in sMMOH
QM/MM	quantum mechanics/molecular mechanics
Rbr	rubrethryin
RFQ	rapid freeze quench
R-H	hydrocarbon substrate
r.m.s.	root mean square
RMSD	root mean square deviation
RNR-R1	ribonucleotide reductase R1 subunit
RNR-R2	ribonucleotide reductase R2 subunit
R-OH	oxidized hydrocarbon product
SDS	sodium dodecyl sulfate
sMMO	soluble methane monooxygenase
sMMOs	soluble methane monooxygenases, a subclass of BMMS

sMMOB	a regulatory protein component of soluble methane monooxygenase
sMMOD	an inhibitory protein component of soluble methane monooxygenase
sMMOH	a hydroxylase component of soluble methane monooxygenase
sMMOR	a reductase component of soluble methane monooxygenase
S_{total}	total number of spin quantum number
$\mathrm{T201}_{\mathrm{peroxo}}$	a diferric oxygenated intermediate observed in a few T201 variant enzymes of ToMOH
$\mathrm{T201}_{\mathrm{peroxo}}*$	a decomposed product of $\mathrm{T201}_{\mathrm{peroxo}}$ observed in T201C variant enzyme of ToMOH
T4mo	toluene 4-monooxygenase
T4moC	a Rieske protein component of T4mo
T4moD	a regulatory protein component of T4mo
T4moH	a hydroxylase component of T4mo
T4moHD	a complex of toluene 4-monooxygenase hydroxylase (T4moH) and regulatory protein (T4moD)
T4moF	a reductase component of T4mo
TauD	taurine α-ketoglutarate-dependent hydroxylase
TBE	Tris/Borate/EDTA buffer
TMO	4-component toluene monoooxygenase
TMOs	four-component alkene/arene monooxygenase, a subclass of BMMs
TMOH	toluene monooxygenase hydroxylase
ToMO	toluene/*o*-xylene monooxygenase
ToMOC	a Rieske protein component of ToMO
ToMOD	a regulatory protein component of ToMO

ToMOF	a reductase component of ToMO
ToMOH	a hydroxylase component of ToMO
ToMOH$_{ox}$	oxidized state of ToMOH
ToMOH$_{peroxo}$	a diferric oxygenated intermediate observed in the wild-type ToMOH
ToMOH$_{red}$	reduced state of ToMOH
ToMOH$_{red}$D	a complex of ToMOH$_{red}$ and ToMOD
TRIS/HCl	(hydroxymethyl)aminomethane/hydrochloric acid
X	a (μ-oxo)Fe$_2$(III/IV) intermediate in RNR-R2

Chapter 1.

Geometric and Functional Versatility of Carboxylate-Bridged Nonheme-Diiron Motifs: sMMO and ToMO

1.1. EVOLUTION OF DIIRON-CONTAINING ENZYMES: GEOMETRIC VARIABILITY FOR DIVERSE FUNCTIONS.

Several classes of metalloenzymes have independently evolved a surprisingly similar structural motif, a carboxylate-bridged nonheme-diiron center, from a pair of conserved (D/E)$X_{30\text{-}37}EX_2H$ ligand sequences (Figure 1.1).[1-3] Two iron ions are coordinated by two histidine (His) residues, four aspartate/glutamate (Asp/Glu) residues, and a few exogenous ligands such as oxide (O^{2-}), water (H_2O), and/or hydroxide (OH^-). The chemistry occurring at these carboxylate-bridged diiron scaffolds has been structurally, spectroscopically, and theoretically scrutinized in the class of bacterial multicomponent monooxygenases (BMMs), which includes soluble methane monooxygenase hydroxylase (sMMOH)[4-6] and toluene monooxygenase hydroxylase (TMOH).[7] Other well-studied systems include the R2-subunit of ribonucleotide reductase (RNR-R2),[8,9] and soluble acyl-acyl carrier protein (ACP) desaturase including stearoyl-ACP Δ^9 desaturase (Δ^9D).[10,11] A few other diiron enzymes can be also included in the family, such as rubrerythrin (Rbr),[12] hemerythrin,[13] ferritin,[14] *myo*-inositol oxygenase (MIOX),[15] *p*-aminobenzoate *N*-oxygenase (AurF),[16,17] human deoxyhypusine hydroxylase (hDOHH),[18] amino acid beta-hydroxylase (CmlA),[19] and an aging-associated enzyme in the ubiquinone biosynthesis pathway (CLK-1),[20] although these proteins may not feature strictly conserved (D/E)$X_{30\text{-}37}EX_2H$ ligand sets.[a] High homology of the active site structures allows them to perform similarly operative catalytic reactions (Scheme 1.1).

---

[a] Not every diiron enzyme listed here is structurally characterized and therefore presented in Figure 1.1. Sequence analyses and alignments of the listed diiron enzymes, however, demonstrated that they most likely contain analogous carboxylate-bridged non-heme diiron active sites.

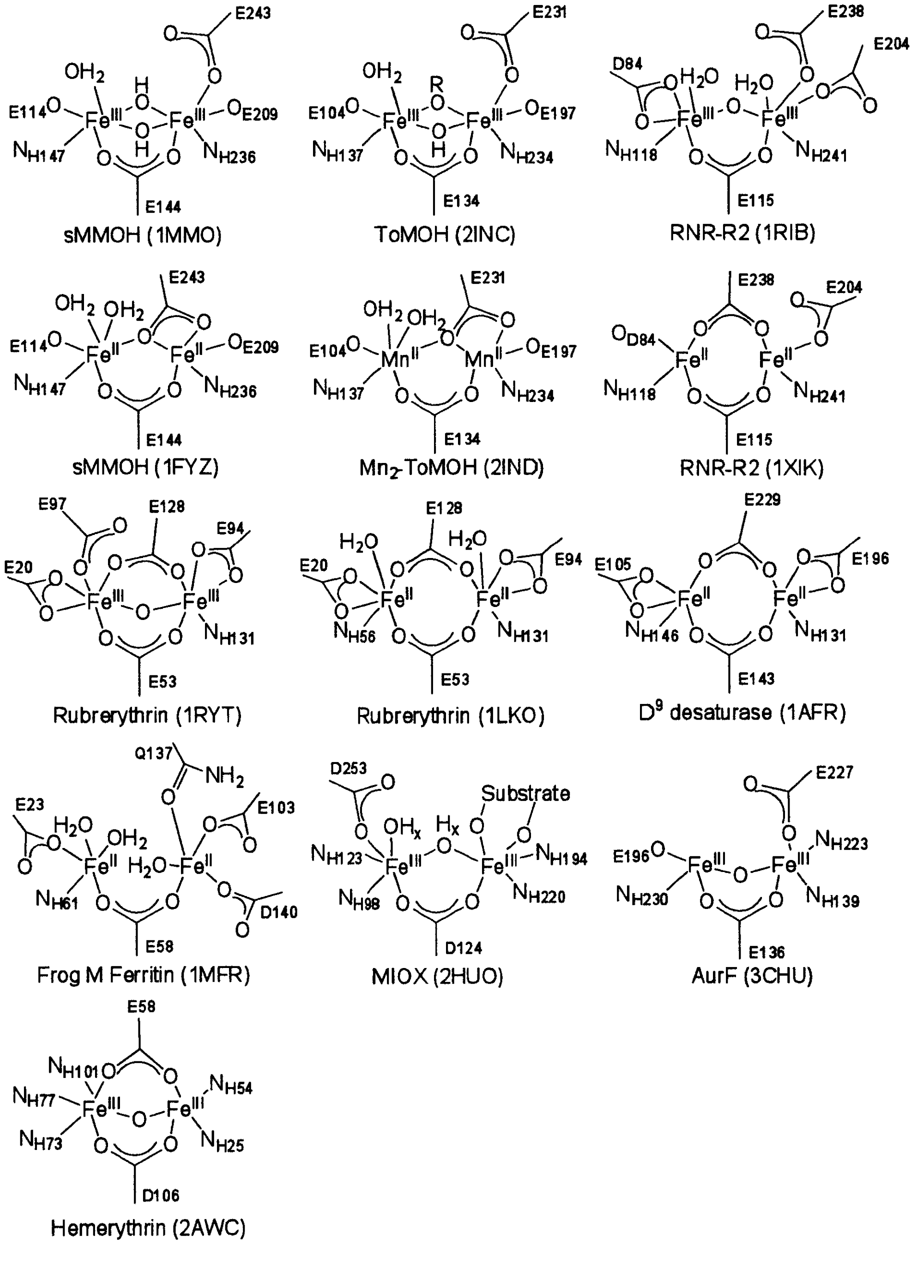

sMMOH (1MMO)

ToMOH (2INC)

RNR-R2 (1RIB)

sMMOH (1FYZ)

Mn_2-ToMOH (2IND)

RNR-R2 (1XIK)

Rubrerythrin (1RYT)

Rubrerythrin (1LKO)

D^9 desaturase (1AFR)

Frog M Ferritin (1MFR)

MIOX (2HUO)

AurF (3CHU)

Hemerythrin (2AWC)

Figure 1.1 Representation of carboxylate-bridged nonheme-diiron active sites in diiron-containing enzymes. PDB codes are represented in parenthesis. Because no structure of reduced ToMOH is reported, the dimanganese-substituted ToMOH structure, which is known to resemble the geometry of the diiron(II) state, is depicted for comparison. A MIOX structure contains a few of water-derived molecules but the protonation states of them are not identified and depicted by OH_x (x = 0-2).

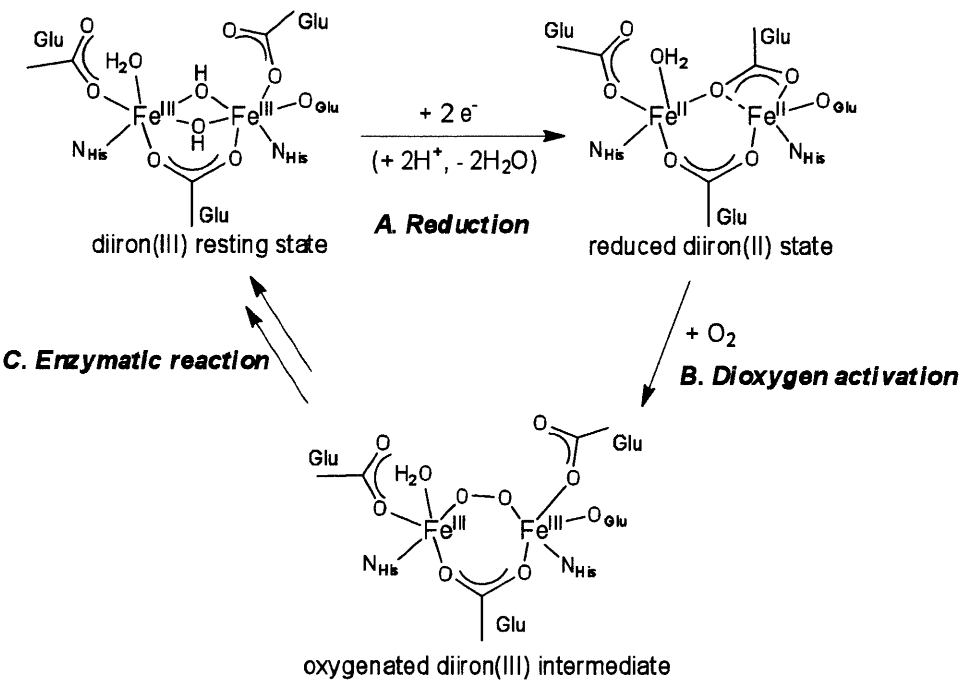

Scheme 1.1 A Classic Catalytic Cycle of Diiron-Containing Enzymes. The geometry of the diiron sites depicted is primarily based on the structures of the BMMs. The protonation states of peroxo and/or glutamate ligands are not identified.

Several diiron-containing enzymes have been purified, commonly as the diiron(III) form. Spectroscopic studies of the diiron(III) resting states of sMMOH,[21] TMOH,[22,23] Δ^9D,[24] MIOX,[15] AurF,[25] CmlA,[19] and CLK-1[20] have revealed that their Mössbauer parameters are similar with δ = ~0.5 mm/s and ΔE_Q = ~0.7 - 1.9 mm/s. The magnitude of the latter parameter depends on the identity of solvent-derived ligands, being lower for μ-hydroxo and higher for μ-oxo species. Two high spin Fe(III) ions of the resting state are usually antiferromagnetically coupled to form a diamagnetic species.

Transfer of two-electrons to the diiron(III) resting states, presumably coupled to proton translocation, generates the diiron(II) states of the enzyme (Scheme 1.1A).[b,26,27] Diiron(II) species typically exhibit Mössbauer parameters of δ = ~1.3 mm/s and ΔE_Q = ~2-3 mm/s, and the two Fe(II) ions are weakly ferromagnetically coupled to display an EPR signal at g ~15-16 in sMMOH,[28] TMOH,[22,23,29] Δ^9D,[24] MIOX,[27,30] AurF,[25] hDOHH,[18] and CLK-1.[20]

The diiron(II) state can activate molecular oxygen via two electron transfers from two iron(II) atoms to the half-occupied antibonding π^* orbitals of dioxygen (Scheme 1.1B).[3] This reaction typically results in the formation of oxygenated diiron(III) species.[c,31] Most of characterized oxygenated diiron(III) intermediates share spectroscopic properties with those of sMMOH, Δ^9D, the wild-type and a few variants of RNR-R2, ferritin, and hDOHH (Table 1.1A). Absorption of the oxygenated diiron(III) intermediates typically display ~600-800 nm (ε = ~1200-3000 $cm^{-1}M^{-1}$), originating from peroxo to iron(III) charge transfer (LMCT) transition. Their Mössbauer parameters are also similar, having δ = ~0.5 mm/s and ΔE_Q = ~1.5 mm/s, and they typically have two antiferromagnetically coupled high spin Fe(III) ions. Resonance Raman spectra of the oxygenated diiron(III) species of the RNR-R2 W48F/D84E variant, Δ^9D, and ferritin display symmetric Fe—O and O—O stretching modes at ~450-500 cm^{-1} and ~850-900 cm^{-1}, respectively, indicating that the chemical identity of these oxygenated diiron(III) species may be cis-μ-1,2 peroxodiiron(III).

---

[b] Upon one electron transfer to the diiron(III) resting state, some diiron enzymes form a mixed-valence Fe_2(II/III) species. This intermediate, however, is typically unstable and catalytically inactive except for that of MIOX.

[c] Formation of a diiron(II/III)-superoxo species has been proposed as a transient species in the reaction of diiron(II) sites with O_2 and the hypothesis was supported by the studies of synthetic diiron-modeling complexes. No such species has been observed in any diiron-containing enzyme, however.

Table 1.1 Spectroscopic Properties of Oxygenated Diiron(III) Intermediates of Diiron-Containing Enzymes.

Enzyme	Absorption, λ_{max} (nm)/ε ($cm^{-1}M^{-1}$)	Mössbauer, $\delta/\Delta E_Q$ (mm/s)	Magnetism, J (cm^{-1})	Resonance Raman (cm^{-1})
A. Classic Peroxodiiron(III) Intermediates				
sMMOH[28,32,33]	600-650/1500	0.66/1.51	AF[a]	nd[b]
Δ^9 desaturase[34]	~700/1100	0.68/1.90 0.64/1.06	AF[a]	898
RNR-R2 *E. Coli*[35]	700/nd[b]	0.66/1.51	nd[b]	nd[b]
RNR-R2 Mouse[36]	700/1500	0.63/1.73	nd[b]	nd[b]
RNR-R2 D84E[37,38]	700/1500	0.63/1.58	$J = 50$	868
RNR-R2 D84E/W48F[38,39]	~700/ nd[b]	nd[b]	AF[a], $J = 50$	458, 499, 870
Frog M or H-type ferritin[39-42]	650/1000	0.62/1.08 or 0.62/1.06	AF[a], $J = 70$ -75	851
hDOHH[18]	630/2800	[c]0.55/1.16 0.58/0.88	AF, $J = 50$-70	457, 476, 811
B. Non-Classic Peroxodiiron(III) Intermediates				
ToMOH [23]	none	0.55/0.67	AF[a]	nd[b]
RNR-R2 W48A/Y122F[43,44]	500/<100	~0.3/~0.8 ~0.3/~1.2	nd[b]	nd[b]
AurF[25]	500/500	0.54/-0.66 0.61/ 0.35	AF[a]	nd[b]

[a]Antiferromagnetically coupled. [b]Not determined. [c]An alternative assignment of two quadruple doublets of $\delta_1 = 0.49$ and $\Delta E_{Q1} = 1.05$, $\delta_2 = 0.63$ and $\Delta E_{Q2} = 0.99$ is possible.

Oxygenated diiron(III) intermediates can directly catalyze chemical transformations or further convert to higher-valent intermediates that participate in catalysis (Scheme 1.1C). Oxygenated intermediates then regenerate the resting diiron(III) state upon the reaction of cognate substrates, followed by structural rearrangements and/or addition of protons or water.

Despite the similarities in active site structures and chemical nature of the dioxygen activation step, diiron-containing enzymes perform diverse chemical reactions (Table 1.2). Most diiron-containing enzymes are involved in two-electron oxidation chemistry. For example, BMMs, hDOHH, CmlA, and CLK-1 oxidize the C—H bonds of their cognate substrates (oxygenase activity). Δ^9D introduces a C=C bond via C—H abstraction (desaturase activity). Ferritin oxidizes Fe_2(II) ions to produce μ–oxo or μ-hydroxo Fe_2(III) biomineral precursors (ferroxidase activity). In contrast, some diiron enzymes are involved in chemistry other than two-electron oxidations. RNR-R2 catalyzes the one-electron oxidation of a specific active site tyrosine residue (Y122) that mediates cysteinyl radical formation in the neighboring RNR-R1 subunit. Additionally, MIOX and AurF carry out the four-electron oxidation of their associated substrates, *myo*-inositol and *p*-aminobenzoate, respectively. A wide range of functions within a ubiquitous structural motif most likely arises from modification of structural and chemical properties of their active sites as well as their global second and third coordination sphere environments.

Table 1.2 A Summary of Diverse Functions of Diiron-Containing Enzymes.

enzyme	substrate	product
sMMOH	CH_4	CH_3OH
TMOH	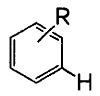	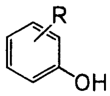
RNR-R2	Y122	Y122-radical
Δ^9D	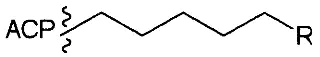	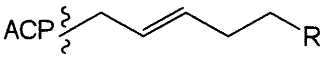
ferritin	$(Fe^{2+})_n$	$(Fe^{3+})_n$
Hr	no catalytic reaction	no catalytic reaction
Rbr	H_2O_2[a]	H_2O[a]
AurF	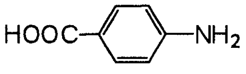	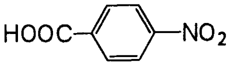
ClmA	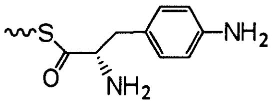	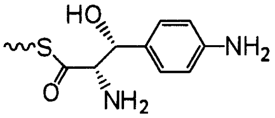
MIOX	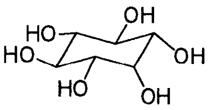	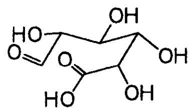
hDOOH	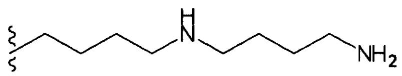	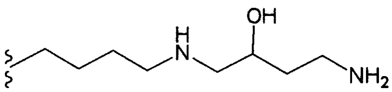
CLK-1	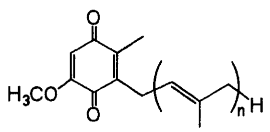	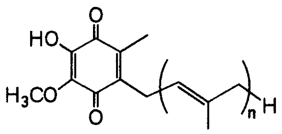

[a] Hydrogen peroxidase oxidase and ferroxidase activity was reported in rubrerythrin, however, the native function of the enzyme is not well understood.

Although the active sites of diiron-containing enzymes bear a strong resemblance, the conformation and/or identity of coordinating ligands are not identical to one another (Figure 1.1). Reduced BMMs, including sMMOH and TMOH, favor six or five coordinating ligands for each iron atom.[45-47] An empty site for O_2 binding, is available at one Fe atom. In contrast, the binding modes of aspartate and glutamate ligands of RNR-R2 are distinct from those of the BMMs and the diiron center of RNR-R2 lacks solvent-derived ligands, such as hydroxide or water, which are observed in BMMs. As a result, the diferrous center of RNR-R2 contains iron atoms that are coordinated by four and five or four and four ligands.[48,49,d] These structural differences, having lower number of bidentate ligands, are possibly responsible for the significantly longer Fe···Fe distance of the diferrous state of RNR-R2 relative to that of sMMOH, 3.9 Å vs 3.1 Å, respectively.[48,50] The diiron(II) states of RNR-R2 are different from those of the BMMs in their magnetic properties as well. The diiron(II) state of RNR-R2 is antiferromagnetically coupled, giving rise to $S_{\mathrm{total}} = 0$, whereas those of the BMMs are weakly ferromagnetically coupled.[51] Fine-tuning of the diiron active site contributes to this differentiation of the physical properties of the diiron enzymes.

Studies of a mutant of RNR-R2 demonstrate that even a slight perturbation at the diiron sites can substantially alter the dioxygen chemistry. Substitution of an aspartate ligand of RNR-R2 by a glutamate (D84E) greatly perturbs the geometry of the diiron center.[51,52] Interestingly, the dioxygen reactivity of the enzyme changed and a stable oxygenated diiron(III) intermediate formed that was not observed with the wild-type

---

[d] The X-ray crystal structure of RNR-R2 and CD/MCD experiments of this protein gave inconsistent results regarding the coordination environment of the diiron(II) state.

protein.[37] This intermediate is spectroscopically similar to an oxygenated intermediate observed in sMMOH (H_{peroxo} or P). This result indicates that the coordination environment of the diiron center is designed to exhibit specific dioxygen reactivity.

In contrast to the BMMs and RNR-R2, Δ^9 desaturase (Δ^9D) contains a symmetric, diiron(II) site in which both iron atoms are five-coordinate. Even though coordinatively unsaturated sites for dioxygen-binding are available, dioxygen reactivity is very slow for this protein.[53] Introduction of a substrate (ACP), however, causes the diiron core to rearrange such that one iron atom is 5-coordinate and the other is 4-coordinate, permitting a favorable electronic structure for both iron atoms to react with dioxygen.[34,54] In addition, a comparison between hemerythrin (Hr) and Δ^9 D suggested that the presence of a solvent-derived bridging ligand, such as oxo or hydroxo, is critical for superexchange between the two irons and it may determine the relative energies of μ-1,2- versus end-on oxygenated diiron(III) states.[55] Structures of some other enzymes reveals that coordinating ligands are more drastically diversified from the enzymes that we have described above (Figure 1.1). One of the Fe ions in ferritin is ligated exclusively to carboxylates instead of having a glutamate/histidine ligand set[56] and a histidine ligand of rubrerythrin is dissociated from the iron atom at the diiron(III) state of the enzyme.[57] Such structural differences are postulated to be the major factor in controlling the function of diiron center.[42]

In addition to the diiron motif, residues adjacent to the active sites can differentiate the diiron chemistry of these enzymes. BMMs and Δ^9 desaturase catalyze two-electron hydrocarbon oxidation and desaturation reactions, respectively, and no additional electrons are required during dioxygen activation. The active sites of BMMs and Δ^9 desaturase mostly consist of hydrophobic residues that cannot participate in redox chemistry. RNR-R2, however, requires one extra electron during its catalytic cycle for tyrosyl radical formation.

The W48 residue of RNR-R2,[e] a residue near the surface, is responsible for the electron efflux and formation of a high-valent, (μ-oxo)diiron(III/IV) intermediate, X. Introduction by site-directed mutagenesis of a redox active tryptophan residue near the active site in a BMM can mimic aspects of the chemistry observed in RNR-R2 at the expense of its native hydrocarbon oxidation activity.[58,59] An internal substrate for RNR-R2, a tyrosine residue (Y122), is also a distinctive feature found only near the diiron site of RNR-R2.[60] Instead of Y122, BMMs such as sMMOH and ToMOH and Δ^9D contain cysteine, glutamine, and leucine residues, respectively (Figure 1.2).[f,61,62]

The size of the active site pocket is variable in diiron-containing enzymes. Given the function of RNR-R2, external hydrocarbon substrate is not required and should be prevented from accessing the diiron active site. Thus, F208 is located above the diiron center, filling the space so that external substrate cannot access to the active site (Figure 1.2). In contrast, both BMM and Δ^9D contain a threonine residue in their active site pockets, maintaining enough empty space above the diiron center so that their natural substrates can enter. BMMs contain hydrophobic cavities and/or a long, hydrophobic channel that are believed to act as the substrate access/product egress pathway.[46,47,63] Δ^9 desaturase catalyzes the length and regiospecific oxidation of long bulky substrates, such as 18:0-ACP; therefore, its hydrophobic channel is a critical feature of catalysis.[53,64]

---

[e] The numbering of RNR-R2 residues is that of the the RNR-R2 from *E. coli* enzyme.

[f] A few of attempts have been made to elucidate the role of the residues in sMMOH and ToMOH, at the same positions as Y122 in RNR-R2, but the results were either inconclusive or indicated that the residues are not essential for catalysis.

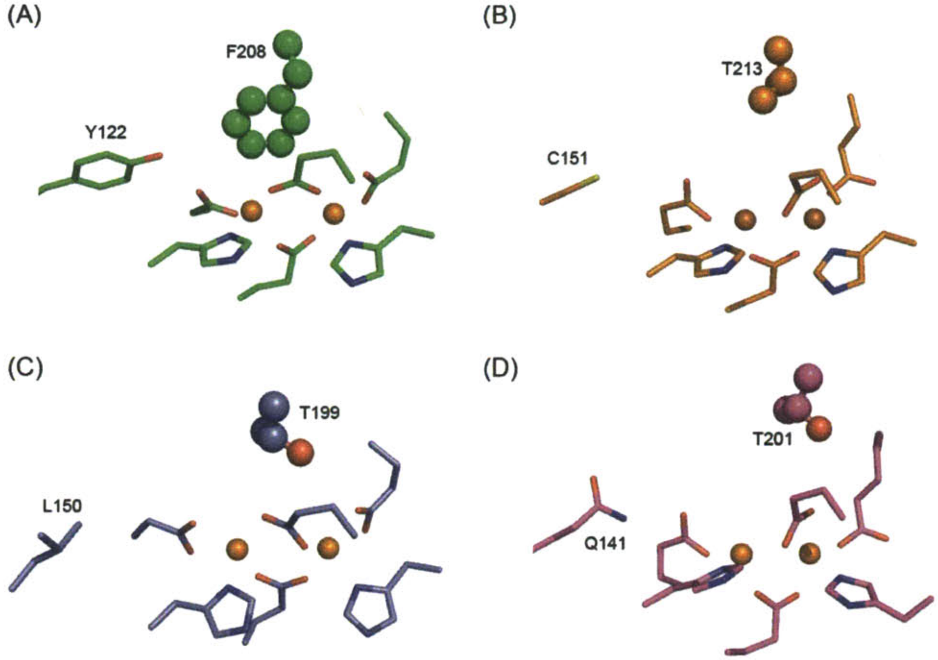

Figure 1.2 Diiron active sites of the reduced diiron sites. (A) RNR-R2 (PDB 1XIK), (B) sMMOH (1FYZ), (C) Δ^9D (PDB 1AFR), and (D) ToMOH (PDB 2IND). Because no structure is reported for reduced ToMOH, dimanganese-substituted ToMOH, which is known to resemble the geometry of the diiron(II) state, is depicted for comparison. The diiron center and coordinating/adjacent residues are represented with orange spheres and sticks, respectively. Oxygen, nitrogen, and sulfur atoms were colored in red, blue, and yellow, respectively. The side chains of the amino acids above the diiron atoms, F208, T213, T199, and T201 residues of RNR-R2, sMMOH, Δ^9D, and ToMOH, respectively, were represented in spheres.

Diiron enzymes also facilitate the formation of different oxygenated intermediates that are suited for specific biochemical reactions. The canonical mechanism of dioxygen chemistry in diiron enzymes involves the production of an oxygenated diiron(III) intermediate from the reaction of diiron(II) and dioxygen, as described above (Scheme 1.1B).

Some diiron enzymes capable of generating peroxodiiron(III) intermediates proceed to form higher-valent oxygenated species. In sMMOH, one or two proton transfer events to the peroxodiiron(III) intermediate facilitate O—O bond cleavage to generate a di(μ-oxo)diiron(IV) species, Q.[65,66] Spectroscopic and structural studies suggest that the two high-spin iron(IV) atoms of Q are antiferromagnetically coupled and that its geometry is that of a diamond-core with a short Fe···Fe distance of 2.46 Å.[67] Kinetic studies of Q, absorbing the strong optical band at ~420 nm, suggest that it is the species responsible for methane oxidation.[28,68,69] The conversion of peroxodiiron(III) to Q is therefore indispensable for the function of sMMOH and might be a consequence of evolution in sMMOH. Therefore, comparison of sMMOH with other diiron enzymes, in particular with other BMMs, can provide the chemical knowledge to understand how diiron enzymes have adapted for their individual functions.[g] In contrast to sMMOH, RNR-R2 engages in reductive O—O bond cleavage, converting its oxygenated diiron(III) species to a diiron(III/IV) intermediate with concomitant formation of a W48-cation radical ($W48^{+\cdot}$).[70] The mixed-valent iron center then readily accepts an additional electron from Y122 to form the catalytic Y122-radical, again supporting the idea that dioxygen chemistry of the diiron centers are optimized for their biological functions.[71]

Recently, a few oxygenated diiron(III) intermediates having atypical spectroscopic properties have been reported for toluene/*o*-xylene monooxygenase (ToMOH),[23] a double mutant of RNR-R2 (W44A/Y122F),[43] and AurF (Table 1.1B).[17,25] Even studies of MIOX demonstrated that the diiron(III) intermediate is not involved in catalysis,[27,30] indicating that nonclassical chemical mechanisms can operate in some diiron enzymes, tuning their

---

[g] This topic is discussed in Chapter 2.

dioxygen chemistry for their individual biological functions.

Substrates themselves can also control dioxygen chemistry in diiron enzymes. A few diiron enzymes, including Δ^9D[34,72] and CmlA,[19] require their cognate hydrocarbon substrates to form oxygenated intermediates. This feature is reminiscent of catalysis by cytochrome P450 monooxygenases (P450) and taurine α-ketoglutarate-dependent hydroxylase (TauD), in which dissociation of an axial water ligand is triggered by introduction of substrate into active site is necessary for dioxygen activation.[73,74] Substrate-triggered catalysis is beneficial for productive coupling of electron/dioxygen consumption to hydrocarbon oxidation. In contrast, several diiron enzymes including the BMMs activate dioxygen in the absence of the substrate, implying that an alternative mechanism(s) may control the consumption of dioxygen in these enzymes.[h]

The carboxylate- and histidine-rich metal binding motif can house metals other than iron to maintain biological functions.[75] RNR-R2 from *Chlamydia trachomatis* lacks the catalytic tyrosine residue in the active site.[76] The tyrosyl residue, however, is replaced presumably by formation of a Mn(IV)/Fe(III) cofactor.[77] In addition, another RNR-R2 class (Class 1b) utilizes a dimanganese cofactor.[78] These recent findings show that the metal-binding repertoire of the carboxylate-bridged motif can be expanded to include new chemistries.

Chemical reactions of the diiron enzymes are also optimized through component protein interactions. Several diiron-containing enzymes require interactions with cognate components for proper function. A half-sites reactivity was demonstrated in RNR-R2, presumably due to component interactions between the subunits.[79] In addition, Δ^9

---

[h] This topic is discussed in Chapter 5.

desaturase exhibits component interactions with a redox partner, a [2Fe2S] ferredoxin, which participates in functions beyond electron transfer.[72,80] The structures and functions of the component enzymes in BMMs are discussed in greater detail in the following section.

1.2. STUDIES OF A CANONICAL BMM ENZYMES, sMMO.

BMMs are a class of metalloenzymes that metabolize unactivated hydrocarbons to provide a carbon and energy source for their host organisms. During BMM catalysis, several chemical reactions occur: inter- and intra-molecular electron transfer, proton transfer, dioxygen activation, and hydrocarbon oxidation.[4,5] Efficient catalysis therefore requires control of supply and consumption of four substrates, protons, electrons, dioxygen, and hydrocarbons, as well as release of two products, water and oxidized hydrocarbons. If these processes are not kinetically and energetically coupled, undesired side reactions can occur, such as formation of hydrogen peroxide, which can eventually deactivate the enzyme. Nature's strategy to orchestrate these multiple reactions in an efficient manner is to allocate the individual chemical steps to multiple components. BMMs contain three or four components, including a reductase, a hydroxylase, a regulatory protein and/or Rieske protein.[81,82] Understanding the structures and functions of the individual BMM components has been one of our major interests.

BMMs are categorized into four subclasses: soluble methane monooxygenases (sMMOs), four-component alkene/arene monooxygenases (TMOs), three-component phenol hydroxylases (PHs), and alkene monooxygenases (AMOs), all of which are believed to have evolved from a common ancestor.[81,82] sMMO is the most extensively investigated BMM. Studies of sMMO from two organisms, *Methylococcus capsulatus* (Bath)[4] and *Methylosinus trichosporium* OB3b,[5] were independently carried out. Both enzymes convert methane to methanol under ambient conditions, even though methane is one of the most difficult hydrocarbons to oxidize because of its strong C—H bond (BDE = 104 kcal/mole) and kinetic stability. To understand their chemical mechanisms, sMMOs have been extensively explored. sMMO contains three components: a reductase (sMMOR), a regulatory protein (sMMOB), and a hydroxylase (sMMOH).[i,83]

1.2.1. The Reductase Component of sMMO, sMMOR.

The reductase component of sMMO, sMMOR, is an iron-sulfur flavoprotein that shuttles electrons from NAD(P)H through its FAD and [2Fe-2S] cofactors to the cognate hydroxylase component. sMMOR (38.5 kDa) has been spectroscopically characterized by UV-vis, Mössbauer, and EPR spectroscopy.[84,85] Its structure, however, has not been fully elucidated. NMR structures of the major domains of sMMOR from *Methylococcus capsulatus* (Bath) have been solved (Figure 1.3A-B).[86,87]

BMM catalysis is initiated by binding of NADH to the reductase. The redox potentials of the $FAD_{ox/sq}$, $FAD_{sq/hq}$, and $[2Fe\text{-}2S]_{ox/red}$ forms of sMMOR are known. These values are not perturbed by introduction of the component proteins to the reductase, presumably because electron transfer within the reductase occurs independent of the other components.[85,88] Kinetic studies of electron transfer from NADH to FAD and FAD to the [2Fe-2S] cluster were performed with sMMOR domain fragments. The two domains of sMMOR presumably interact such that their cofactors are proximally poised for rapid

---

[i] sMMO has been cited as a three-component system. A fourth component (sMMOD, 12 kDa), however, has been reported. The function of sMMOD is not yet understood, but it has been shown to inhibit MMOH activity. This is thought to occur by competitive inhibition, because it binds to sMMOH, presumably at the site of sMMOB interaction, thereby preventing formation of the active sMMOH-sMMOB complex.

electron transfer.[89]

For efficient catalysis, electron transfer from sMMOR to sMMOH should occur at an optimum rate. If electron donation from sMMOR to the hydroxylase were too slow, the overall turnover rate would be low. Conversely, too fast an electron transfer to the sMMOH might quench the reactive intermediates, causing the futile consumption of O_2 and electrons.[88] Kinetic studies of the sequential electron transfer from sMMOR to sMMOH suggest that electron transfer is possibly gated by the local conformational changes associated with isomerization of the ternary complex between sMMOR, sMMOH, and sMMOB.[88,90]

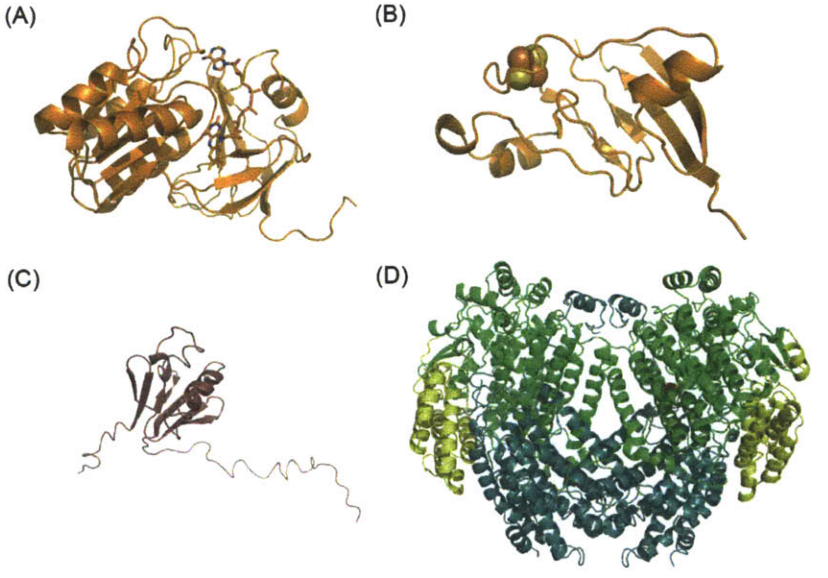

Figure 1.3 X-ray and NMR structures of sMMO components from *Methylococcus capsulatus* (Bath) (A) The FAD-containing domain of sMMOR (PDB 1TVC) (B) The [2Fe-2S]-containing domain of sMMOR (PDB 1JQ4). (C) sMMOB (PDB 1CKV) (D) sMMOH (PDB 1MTY). The FAD cofactor in sMMOR is represented by sticks. Oxygen and nitrogen atoms are colored in red and blue, respectively. The [2Fe-2S] cofactor of sMMOR is depicted by spheres and iron and sulfur atoms are colored in orange and yellow, respectively.

sMMOR functions as more than a simple electron donor to the hydroxylase, however. Both sMMOR and sMMOB modulate the redox potential values of sMMOH such that two consecutive electron transfers to one diiron active site become more favorable than one electron transfer to each diiron site.[91,92] Because the diiron(II) but not the mixed-valent diiron(II/III) form of the sMMOH enzyme is the chemically relevant species in catalysis, regulation of electron distribution by sMMOR is critical for catalysis. sMMOR also facilitates the production of single-turnover yields near ~100%, possibly through component interactions with sMMOH-sMMOB complex.[26,92] Furthermore, sMMOR can alter product distribution of sMMOH for nitrobenzene oxidation.[21]

1.2.2. The Regulatory Protein of sMMO, sMMOB

The sMMO regulatory or auxiliary protein, sMMOB (15.5 kDa), does not contain metals, organic cofactors, or prosthetic groups (Figure 1.3C). The multiple functions of sMMOB during catalysis have been extensively explored. sMMOB increases rates of steady-state product formation,[93] modulates the redox potential of the diiron sites of sMMOH,[91,94] alters product distribution of various hydrocarbon oxidation,[95] and adjusts the diiron coordination environments.[96,97] Mutagenesis studies of sMMOB demonstrated that it may control the rates of dioxygen activation and substrate entry to the diiron centers.[98-100] Interactions of sMMOB with sMMOH or with the sMMOH-sMMOR complex have been observed in biochemical studies. In contrast, sMMOB is believed not to interact with sMMOR in the absence of sMMOH.[88,90] Although the structure of the sMMOH-sMMOB complex is not yet available, saturation-recovery EPR experiments demonstrated that the distance between the diiron sites in sMMOH and the surface of sMMOB is ~15 ± 4 Å.[101] The distance constraint suggests that a canyon region located above the diiron active sites at the hydroxylase dimer interface is a strong candidate for the binding site of sMMOB. X-ray crystal structures of hydroxylase-regulatory protein complexes of other BMMs support this proposal.[47,102]

1.2.3. The Hydroxylase Component of sMMO, sMMOH.

sMMOH is a 251 kDa, dimeric protein of having an $\alpha_2\beta_2\gamma_2$ configuration (Figure 1.3D). Each α-subunit contains a diiron active site, where dioxygen activation and hydrocarbon oxidation occur. The diiron active sites are housed in a four α-helix bundle. Except for a threonine, an asparagine, and the diiron ligands, the active sites are surrounded by hydrophobic residues, possibly to protect the reactive oxidant generated during the catalytic cycle from adventitious quenching reactions.[j]

Two electron transfer to oxidized sMMOH forms a diiron(II) state (Scheme 1.1 and Figure 1.1). The crystal structure of chemically reduced sMMOH revealed that the two bridging hydroxide ligands dissociate upon reduction, presumably via protonation and release of a water molecule(s).[50,103] Reduction of the diiron site also triggers a conformational change of a coordinating glutamate ligand (E243 in sMMOH), which provides a coordination site for O_2 binding. Further structural changes occur in the adjacent glutamine residue (N214 in sMMOH), which presumably interacts with sMMOB.

Reduced sMMOH activates dioxygen only in the presence of sMMOB. sMMOB binding to sMMOH triggers a conformational change in sMMOH that greatly favors its reaction with dioxygen. The rate of dioxygen activation is accelerated ~1000 fold in the presence of the regulatory protein,[104] although the mechanism by which this acceleration

---

[j] The roles of the adjacent threonine residue are discussed in Chapter 2 and 3.

occurs is not understood. The crystal structure of sMMOH pressurized with xenon gas, a surrogate for dioxygen, suggested that dioxygen travels through several hydrophobic cavities to occur diiron sites.[63]

During dioxygen activation at the diiron centers of sMMOH, a Michaelis complex between reduced sMMOH and dioxygen[68,104] or a transient mixed-valent superoxo complex are probably generated, although neither of these species has been observed directly. The first observed oxygenated intermediate is a diiron(III) species termed H_{peroxo} or P.[32,65] Further kinetic studies of dioxygen activation provided evidence for the existence of a precursor to H_{peroxo} or P, P*.[28,66] As discussed above, H_{peroxo} or P readily converts to a diiron(IV) species, Q, which is thought to be the reactive oxidant for converting methane to methanol. Reaction of Q with hydrocarbon (RH) occurs via H-atom abstraction followed by rebound of the resulting methyl radical with the bridging iron ligand to form alcohol product (ROH).[105] The diiron sites return to the resting state of the enzyme, di(μ-OH)Fe_2(III), presumably upon the acquisition of two water molecules. Recent reports demonstrated that H_{peroxo} or P are also kinetically competent for the oxidation of electron-rich hydrocarbon substrates,[106,107] although the reactions are probably not be physiologically relevant.

1.3. EXTENDED BMMs STUDIES: Toluene/o-Xylene Monooxygenase (ToMO) and Toluene 4-Monooxygenase (T4mo).

Genetic and structural characterization of other BMMs revealed many similarities to of sMMO,[46,108] suggesting that the roles of each component and their chemical mechanisms might also be similar. Despite analogous structures, BMMs display divergent substrate specificities. To understand how this class of enzymes has evolved to achieve different types of chemical transformations, we extended our work on sMMO to other BMMs. Two BMMs were isolated from *Pseudomonas sporium* OX1, the four component toluene/*o*-xylene monooxygenase (ToMO) and the three component phenol hydroxylase (PH).[109] *Pseudomonas sporium* OX1 utilizes aromatic hydrocarbons such as phenol, toluene, and *o*-xylene as their sole carbon and energy sources.[109] ToMO is the first enzyme in the catabolism of arenes, producing substituted phenols (Scheme 1.2).[110] PH and catechol 2, 3-dioxygenase (C2,3O) then consecutively oxidize the alcohols, producing catechol and 2-hydroxymuconic semialdehyde derivatives, respectively. These metabolites are then further broken down into citric acid cycle intermediates. The regiospecificity and relative kinetic parameters of these metabolic enzymes are optimized for the utilization of substrates.[111,112] In addition, another four component toluene 4-monooxygenase from *Pseudomonas mendocina* KR1 (T4mo) has been extensively investigated.[22] In contrast to sMMO, all components of ToMO, PH, and T4mo can be can be prepared by recombinant expression in *Escherichia coli*,[22,111,113] which facilitated systematic studies to explore the chemical mechanisms of BMMs during catalysis.

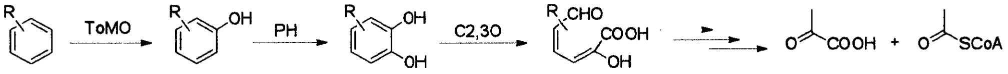

Scheme 1.2 Proposed Catabolic Routes for Arene Susbtrates by *Pseudomonas sporium* OX1.

In this section, the functions and structures of the four ToMO components, the reductase (ToMOF), the Rieske protein (ToMOC), the regulatory protein (ToMOD), and the hydroxylase (ToMOH), as well the analogous proteins from the T4mo system (T4moF, T4moC, T4moD, and T4moH, respectively), are discussed.

1.3.1. The Reductase Components of ToMO (ToMOF) and T4mo (T4moF).

The reductase components of ToMO (ToMOF, ~38 kDa) and T4mo (T4moF) presumably play an analogous role to sMMOR of sMMO.[85,93] ToMOF initiates electron transfer from NAD(P)H to ToMOH via its FAD and [2Fe-2S] domains.[113] Unlike sMMO, however, the electrons are transferred from ToMOF to a mediator Rieske protein (ToMOC) instead of directly to the hydroxylase (ToMOH). Therefore, direct component interaction between ToMOF and ToMOH may not occur during catalysis.

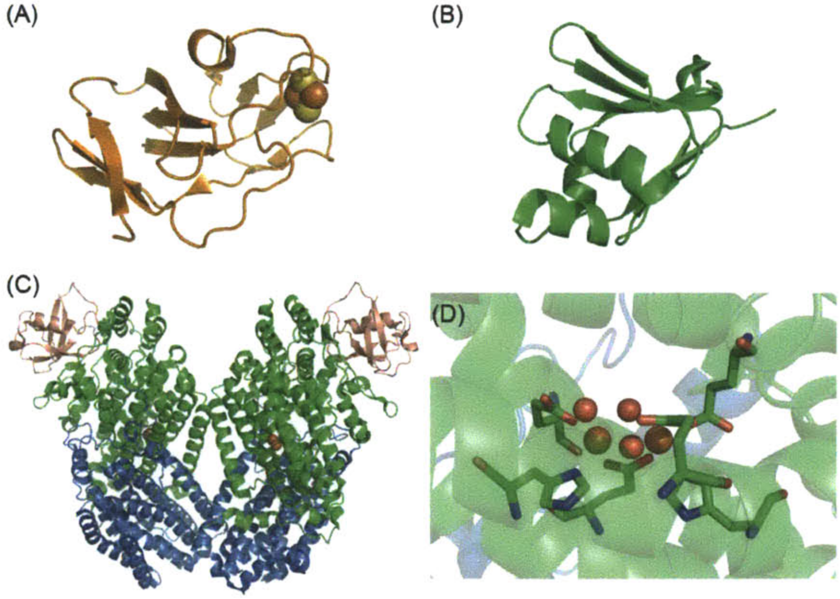

Figure 1.4 X-ray and NMR structures of the ToMO or T4mo components (A) The Rieske component of T4mo, T4moC (PDB 1SJG) (B) The regulatory protein of T4mo, T4moD (PDB 2BF2) (C) The hydroxylase component of ToMO, ToMOH (PDB 2INC) (D) The diiron active site of ToMOH. The iron and sulfur atoms of the [2Fe-2S] cofactor of T4moC are represented by orange and yellow spheres, respectively. The α, β, γ subunits of ToMOH in (C) are colored in green, blue, and pink, respectively. Iron atoms and water

molecules of ToMOH in (D) are shown by orange and red spheres, respectively. Carbon, nitrogen, and oxygen atoms comprising of diiron-coordinating ligands are depicted by green, blue, and red sticks, respectively.

1.3.2. The Rieske Proteins of ToMO (ToMOC) and T4mo (T4moC).

A Rieske protein (ToMOC, ~12 kDa) is present only in four component BMMs.[113] It contains a Rieske [2Fe-2S] cluster, comprising two cysteine and two histidine residues as iron-coordinating ligands (Figure 1.4A). The ligand configuration is different from a typical [2Fe-2S] having four cysteine ligands, which increases the redox potential for the $Fe^{3+/2+}$ couple relative to those of typical [2Fe-2S] clusters.[114] Hydrogen bonding residues that reside near the cofactor as well as the shape and electrostatics of the protein surface result in its ability to be a highly specialized electron mediator protein between its cognate reductase and hydroxylase proteins. An NMR structure of T4moC[114] revealed that its [2Fe-2S] cluster is exposed to the surface of the enzyme, possibly allowing for only a short gap between the hydroxylase and Rieske protein for facile electron transfer. Interactions between T4moC and the T4moD were observed in biochemical studies,[115] implying that the ternary complex T4moC-T4moH-T4moD might form in vivo, as similarly suggested for sMMO.[90] The necessity of the fourth, Rieske component in the ToMO and T4mo systems relative to other BMMs is not yet understood.[k]

1.3.3. The Regulatory Proteins of ToMO (ToMOD) and T4mo (T4moD).

The regulatory proteins of ToMO (ToMOD, ~12 kDa) and T4mo (T4moD) are presumed to play a parallel role to that of sMMOB, as described above (Figure 1.4B).

---

[k] Further studies have been performed to reveal the role(s) of a Rieske protein of ToMO and the results were described in Appendix B.

Interactions between the regulatory protein and the hydroxylase in the ToMO and T4mo systems increase steady-state activity for arene oxidation,[22,113] perturb the diiron coordination environments of the hydroxylases,[29,116] and possibly enable dioxygen activation in the hydroxylase components.[58] Studies of fluorophore-conjugated T4moD suggested that the regulatory protein interacts with the hydroxylase (T4moH) and the Rieske protein (T4moC), but not with the reductase (T4moF).[117,l]

1.3.4. The Hydroxylase Components of ToMO (ToMOH) and T4mo (T4moH).

The hydroxylase of ToMO (ToMOH) is $\alpha_2\beta_2\gamma_2$ heterodimer of ~206 kDa (Figure 1.4C). Sequence and structural alignments of ToMOH with sMMOH demonstrated that its α- and β- subunits are relatively similar whereas its γ-subunits are quite dissimilar.[46] Long-range conformational or compression effects from the γ-subunit to the active site might therefore be different for ToMO. The diiron active site structure of ToMOH is identical to that of sMMOH, except for the binding mode of one histidine residue (H234).[m] The hydrogen-bonding network near the diiron centers of ToMOH, T4moH, and the hydroxylase component of phenol hydroxylase (PHH) are strictly conserved with those of sMMOH, suggesting a conserved proton translocation pathway.[47,102] A canyon region is also conserved at the dimer interface in ToMOH, T4moH, and PHH, suggesting that the binding site of the regulatory protein on the hydroxylase is conserved in all BMMs. In addition, hydrophobic cavities, proposed to be methane or dioxygen transfer pathways in

---

[l] Further studies have been performed to reveal the role(s) of a regulatory protein of ToMO and the results are included in Appendix B.

[m] Previously, it was postulated that the binding-mode of this histidine might be responsible for the distinct dioxygen chemistry of sMMOH and ToMOH. Further structural and spectroscopic studies of other BMMs, PHH, however, suggested that this hypothesis is irrelevant.

sMMOH,[63] are also found in ToMOH, T4moH, and PHH, implying that dioxygen might migrate from bulk solvent to the active sites via a conserved mechanism.

A major structural difference between sMMOH, ToMOH, and T4moH is the presence of a channel that leads from the active site to the protein exterior only in two latter enzymes. This channel mostly consists of hydrophobic residues and is ~6-10 Å in width and ~35 Å in length. Because sMMOH and ToMOH/T4moH display different substrate specificities, in that ToMOH/T4moH requires bulky, aromatic hydrocarbons whereas sMMO oxidizes small substrates, this channel is probably a route of arene substrate ingress and/or product egress. Studies of the function of this channel are inconclusive, however, because an analogous pathway is absent in PHH, which also hydroxylates bulky arene substrates.[n]

Another significant difference between sMMOH and ToMOH is their single-turnover yields. Although single turnover yields of ~100% per diiron center are observed for sMMOH in the presence of component proteins, those of ToMOH are only ~50%.[92,118] Single turnover studies monitoring dioxygen activation in ToMOH suggested that this enzyme operates by a half-sites reactivity mechanism.[58] It is likely that both of the diiron sites in ToMOH do not undergo a productive catalytic cycle simultaneously. Instead, the process might be controlled by long-range negative cooperativity. The reason why sMMOH and ToMOH display such differences in protein allostery is unknown but may be relevant to differing component interactions between the hydroxylase and the regulatory and/or the Rieske proteins.[115,o] Half-sites reactivity is also displayed by RNR-R2[79] and Δ^9D,[34] suggesting that it might be a commonly operative mechanism in dimeric diiron enzymes.

---

[n] Inconsistencies between the ToMOH/T4moH and PHH structures are discussed in Chapter 5.

[o] Single-turnover yields reported in the various BMMs are not consistent. ToMO and PH exhibit half-sites reactivity whereas sMMO show ~100% single-turnover yields.

1.4. THE DISTINCTIVE DIOXYGEN CHEMISTRY OF sMMOH AND ToMOH.

The dioxygen activation chemistry of ToMOH was expected to be very similar to that of sMMOH due to the high structural homology of their active sites. The oxygenated intermediate of ToMO ($\mathrm{ToMOH_{peroxo}}$) exhibits Mössbauer parameters of 0.54 and 0.67 mm/s for the isomer shift and quadrupole splitting, respectively.[23] The values, however, differ significantly from those of oxygenated intermediates observed in sMMOH. Furthermore, $\mathrm{ToMOH_{peroxo}}$ displays no optical feature in the visible region of the spectrum. Together, these observations suggest that the geometry of $\mathrm{ToMOH_{peroxo}}$ is distinct from the oxygenated diiron(III) intermediates observed in sMMOH, RNR-R2, and Δ^9D described above (Table 1.2). In addition, the diiron(IV) intermediate observed for sMMOH was not detected for ToMOH, indicating that the reactivity profile of dioxygen chemistry is different. Although the structure and the formation mechanism of $\mathrm{ToMOH_{peroxo}}$ remain unidentified, the accelerated decay rate of $\mathrm{ToMOH_{peroxo}}$ in the presence of phenol substrate demonstrated that this species is kinetically competent for arene oxidation.[23]

The strikingly different dioxygen chemistry of the nearly geometrically identical diiron centers of ToMOH and sMMOH imply that subtle but critical changes near the active sites may diversify their dioxygen chemistry. Given that sMMOH and ToMOH catalyze different hydrocarbon oxidation reactions, their discrete dioxygen chemistry is possibly a consequence of evolution in BMMs.

1.5. ORGANIZATION & SCOPE OF THESIS.

The major goals of this thesis are (1) to understand how the ToMO system performs arene oxidation, especially by comparison to sMMO system and (2) to elucidate chemical mechanisms, which might apply to all BMMs, from the studies of ToMO (Scheme 1.3). To tune its reactivity, ToMO may have adopted several strategies described above.

The chemical mechanism by what ToMOH generates a unique oxygenated intermediate from the ubiquitous diiron(II) motif and its structure are discussed in Chapter 2. Attention is drawn to the second coordination spheres of the diiron active sites. A structural comparison of ToMOH with sMMOH was carried out, suggesting that, although both enzymes contain a threonine residue near the active site (T201 in ToMOH and T213 in sMMOH), these amino acids differ in their rotameric state between the two enzymes. We therefore tested whether this seemingly minor conformational change of the active site threonine is a significant factor in controlling dioxygen chemistry. Computational calculations of dioxygen activation in ToMOH were also carried out in collaboration with the Friesner Lab at Columbia University (Appendix A).

In Chapter 3, the role of the active site threonine residue during dioxygen activation is probed. Previous studies of sMMOH and other diiron-containing enzymes suggested that the active site threonine might play an important role in catalysis, similar to that of a conserved threonine in the cytochrome P450 monooxygenases. In this chapter, we investigated the chemical steps involved in dioxygen activation and the role of the active site threonine residue during dioxygen activation of T201 variants of ToMOH.

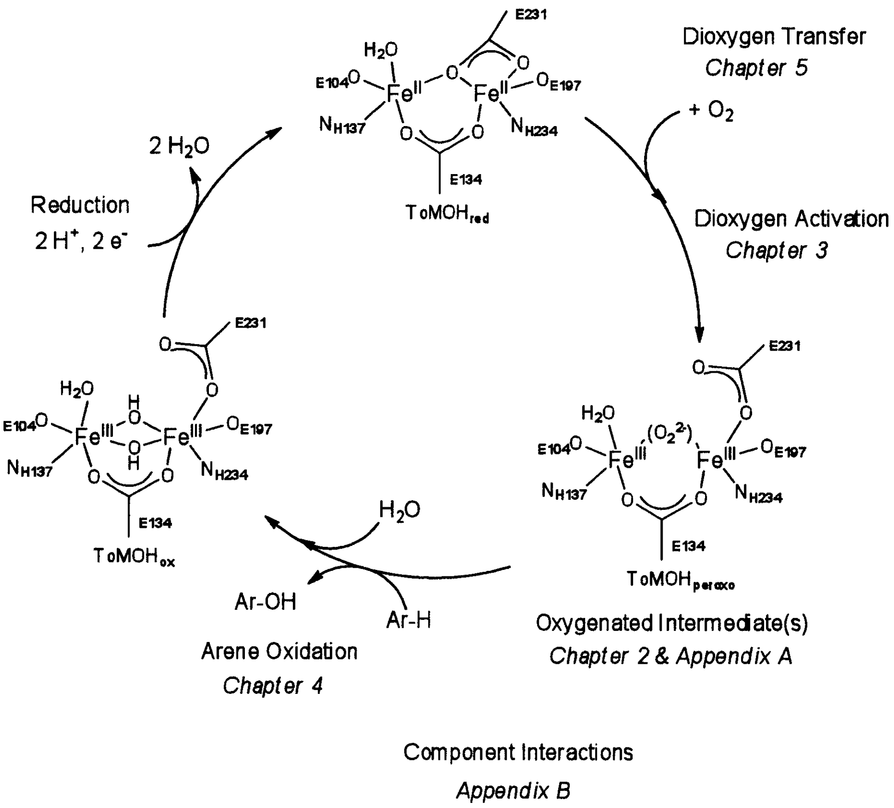

Scheme 1.3 Outline of the Thesis Represented in the Proposed Catalytic Cycle of ToMOH. Aromatic substrate and product are represented as Ar-H and Ar-OH, respectively. The protonation states of peroxo and glutamate ligands are not identified.

In Chapter 4, mechanistic kinetic studies were described to investigate the reaction pathways of oxygenated intermediates and their arene-oxidizing activity in the T201 variants of ToMOH. Both external and internal arene substrates were utilized for the kinetic studies in order to evaluate three possible reaction mechanisms.

In Chapter 5, structural and kinetic studies of dioxygen activation of the T201S variants were carried to explore the dioxygen transfer pathway to the active site of ToMOH. In contrast to a large number of dioxygen-activating metalloenzymes, which require cognate substrates for dioxygen activation, including the diiron enzymes discussed above, BMMs form oxygenated intermediates in the absence of hydrocarbons. Given that uncoupling of electron transfer/dioxygen activation with hydrocarbon oxidation in BMMs can lead to unproductive catalysis, we propose that ToMOH and possibly all BMMs might operate with a strategy to regulate dioxygen consumption for efficient catalysis. To understand how consumption of dioxygen is controlled in BMMs, the dioxygen transfer pathway in ToMOH was investigated. In contrast to previous indirect crystallographic studies of the O_2 ingress pathways conducted with the resting state enzyme, the rates of dioxygen migration to the active site were measured directly by kinetic studies of ToMO variants, which probe the dynamics of conformational changes and component interactions during catalysis. In addition, component interactions of ToMO were investigated in parallel to the PH system by monitoring the rate and quantities of substrate consumption and product formation under various conditions (Appendix B).

REFERENCES

1. Feig, A. L.; Lippard, S. J. (1994) *Chem. Rev. 94*, 759-805.
2. Kurtz, D. M. J. (1997) *J. Biol. Inorg. Chem. 2*, 159-167.
3. Solomon, E. I.; Brunold, T. C.; Davis, M. I.; Kemsley, J. N.; Lee, S.-K.; Lehnert, N.; Neese, F.; Skulan, A. J.; Yang, Y.-S.; Zhou, J. (2000) *Chem. Rev. 100*, 235-349.
4. Merkx, M.; Kopp, D. A.; Sazinsky, M. H.; Blazyk, J. L.; Müller, J.; Lippard, S. J. (2001) *Angew. Chem. Int. Ed. 40*, 2782-2807.
5. Wallar, B. J.; Lipscomb, J. D. (1996) *Chem. Rev. 96*, 2625-2657.
6. Tinberg, C. E.; Lippard, S. J. (2011) *Acc. Chem. Res. 44*, 280-288.
7. Sazinsky, M. H.; Lippard, S. J. (2006) *Acc. Chem. Res. 39*, 558-566.
8. Stubbe, J.; Nocera, D. G.; Yee, C. S.; Chang, M. C. Y. (2003) *Chem. Rev. 103*, 2167-2202.
9. Stubbe, J.; van der Donk, W. A. (1998) *Chem. Rev. 98*, 705-762.
10. Fox, B. G.; Lyle, K. S.; Rogge, C. E. (2004) *Acc. Chem. Res. 37*, 421-429.
11. Shanklin, J.; Guy, J. E.; Mishra, G.; Lindqvist, Y. (2009) *J. Biol. Chem. 284*, 18559-18563.
12. deMaré, F.; Kurtz, D. M. J.; Nordlund, P. (1996) *Nat. Struct. Biol. 3*, 539-546.
13. Stenkamp, R. E. (1994) *Chem. Rev. 94*, 715-726.
14. Harrison, P. M.; Arosio, P. (1996) *Biochim. Biophys. Acta. 1275*, 161-203.
15. Xing, G.; Hoffart, L. M.; Diao, Y.; Sandeep Prabhu, K.; Arner, R. J.; Reddy, C. C.; Krebs, C.; Bollinger, J. M., Jr. (2006) *Biochemistry 45*, 5393-5401.
16. Choi, Y. S.; Zhang, H.; Brunzelle, J. S.; Nair, S. K.; Zhao, H. (2008) *Proc. Natl. Acad. Sci. U.S.A. 105*, 6858-6863.
17. Li, N.; Korboukh, V. K.; Krebs, C.; Bollinger, J. M., Jr. (2010) *Proc. Natl. Acad. Sci. U.S.A. 107*, 15722-15727.
18. Vu, V. V.; Emerson, J. P.; Martinho, M.; Kim, Y. S.; Münck, E.; Park, M. H.; Que, L., Jr. (2009) *Proc. Natl. Acad. Sci. U.S.A. 106*, 14814-14819.
19. Makris, T. M.; Chakrabarti, M.; Münck, E.; Lipscomb, J. D. (2010) *Proc. Natl. Acad. Sci. U.S.A. 107*, 15391-15396.
20. Behan, K. R.; Lippard, S. J. (2010) *Biochemistry 49*, 9679-9681.
21. Liu, K. E.; Valentine, A. M.; Wang, D.; Huynh, B. H.; Edmondson, D. E.; Salifoglou, A.; Lippard, S. J. (1995) *J. Am. Chem. Soc. 117*, 10174-10185.
22. Pikus, J. D.; Studts, J. M.; Achim, C.; Kauffmann, K. E.; Münck, E.; Steffan, R. J.; McClay, K.; Fox, B. G. (1996) *Biochemistry 35*, 9106-9119.

23. Murray, L. J.; Naik, S. G.; Ortillo, D. O.; García-Serres, R.; Lee, J. K.; Huynh, B. H.; Lippard, S. J. (2007) *J. Am. Chem. Soc. 129*, 14500-14510.
24. Broadwater, J. A.; Achim, C.; Münck, E.; Fox, B. G. (1999) *Biochemistry 38*, 12197-12204.
25. Korboukh, V. K.; Li, N.; Barr, E. W.; Bollinger, J. M., Jr.; Krebs, C. (2009) *J. Am. Chem. Soc. 131*, 13608–13609.
26. Fox, B. G.; Froland, W. A.; Dege, J. E.; Lipscomb, J. D. (1989) *J. Biol. Chem. 254*, 10023-10033.
27. Xing, G.; Barr, E. W.; Diao, Y.; Hoffart, L. M.; Prabhu, K. S.; Arner, R. J.; Reddy, C. C.; Krebs, C.; Bollinger, J. M., Jr. (2006) *Biochemistry 45*, 5402-5412.
28. Lee, S.-K.; Nesheim, J. C.; Lipscomb, J. D. (1993) *J. Biol. Chem. 268*, 21569-21577.
29. Schwartz, J. K.; Wei, P.-p.; Mitchell, K. H.; Fox, B. G.; Solomon, E. I. (2008) *J. Am. Chem. Soc. 130*, 7098-7109.
30. Xing, G.; Diao, Y.; Hoffart, L. M.; Barr, E. W.; Prabhu, K. S.; Arner, R. J.; Reddy, C. C.; Krebs, C.; Bollinger, J. M., Jr. (2006) *Proc. Natl. Acad. Sci. U.S.A. 103*, 6130-6135.
31. Shan, X.; Que, L., Jr. (2005) *Proc. Natl. Acad. Sci. U.S.A. 102*, 5340-5345.
32. Liu, K. E.; Wang, D.; Huynh, B. H.; Edmondson, D. E.; Salifoglou, A.; Lippard, S. J. (1994) *J. Am. Chem. Soc. 116*, 7465-7466.
33. Liu, K. E.; Valentine, A. M.; Qiu, D.; Edmondson, D. E.; Appelman, E. H.; Spiro, T. G.; Lippard, S. J. (1995) *J. Am. Chem. Soc. 117*, 4997-4998.
34. Broadwater, J. A.; Ai, J.; Loehr, T. M.; Sanders-Loehr, J.; Fox, B. G. (1998) *Biochemistry 37*, 14664-14671.
35. Tong; Chen, S.; Lloyd, S. G.; Edmondson, D. E.; Huynh, B. H.; Stubbe, J. (1996) *J. Am. Chem. Soc. 118*, 2107-2108.
36. Yun, D.; García-Serres, R.; Chicalese, B. M.; An, Y. H.; Huynh, B. H.; Bollinger, J. M., Jr. (2007) *Biochemistry 46*, 1925-1932.
37. Bollinger, J. M., Jr.; Krebs, C.; Vicol, A.; Chen, S.; Ley, B. A.; Edmondson, D. E.; Huynh, B. H. (1998) *J. Am. Chem. Soc. 120*, 1094-1095.
38. Moënne-Loccoz, P.; Baldwin, J.; Ley, B. A.; Loehr, T. M.; Bollinger, J. M., Jr. (1998) *Biochemistry 37*, 14659-14663.
39. Krebs, C.; Bollinger, J. M., Jr.; Theil, E. C.; Huynh, B. H. (2002) *J. Biol. Inorg. Chem. 7*, 863-869.
40. Pereira, A. S.; Small, W.; Krebs, C.; Tavares, P.; Edmondson, D. E.; Theil, E. C.; Huynh, B. H. (1998) *Biochemistry 37*, 9871-9876.

41. Moënne-Loccoz, P.; Krebs, C.; Herlihy, K.; Edmondson, D. E.; Theil, E. C.; Huynh, B. H.; Loehr, T. M. (1999) *Biochemistry 38*, 5290-5295.
42. Hwang, J.; Krebs, C.; Huynh, B. H.; Edmondson, D. E.; Theil, E. C.; Penner-Hahn, J. E. (2000) *Science 287*, 122-125.
43. Saleh, L.; Krebs, C.; Ley, B. A.; Naik, S.; Huynh, B. H.; Bollinger, J. M., Jr. (2004) *Biochemistry 43*, 5953-5964.
44. Skulan, A. J.; Brunold, T. C.; Baldwin, J.; Saleh, L.; Bollinger, J. M., Jr.; Solomon, E. I. (2004) *J. Am. Chem. Soc. 126*, 8842-8855.
45. Rosenzweig, A. C.; Frederick, C. A.; Lippard, S. J.; Nordlund, P. (1993) *Nature 366*, 537-543.
46. Sazinsky, M. H.; Bard, J.; Di Donato, A.; Lippard, S. J. (2004) *J. Biol. Chem. 279*, 30600-30610.
47. Bailey, L. J.; McCoy, J. G.; Phillips, J., George N.; Fox, B. G. (2008) *Proc. Natl. Acad. Sci. U.S.A. 105*, 19194-19198.
48. Logan, D. T.; Su, X.-D.; Åberg, A.; Regnström, K.; Hajdu, J.; Eklund, H.; Nordlund, P. (1996) *Structure 15*, 1053-1064.
49. Pulver, S. C.; Tong, W. H.; Bollinger, J. M., Jr.; Stubbe, J.; Solomon, E. I. (1995) *J. Am. Chem. Soc. 117*, 12664-12678.
50. Rosenzweig, A. C.; Pär, N.; Takahara, P. M.; Frederick, C. A.; Lippard, S. J. (1995) *Chem. Biol. 2*, 409-418.
51. Wei, P.-p.; Skulan, A. J.; Mitic, N.; Yang, Y.-S.; Saleh, L.; Bollinger, J. M., Jr.; Solomon, E. I. (2004) *J. Am. Chem. Soc. 126*, 3777-3788.
52. Voegtli, W. C.; Khidekel, N.; Baldwin, J.; Ley, B. A.; Bollinger, J. M., Jr.; Rosenzweig, A. C. (2000) *J. Am. Chem. Soc. 122*, 3255-3261.
53. Cahoon, E. B.; Lindqvist, Y.; Schneider, G.; Shanklin, J. J. (1997) *Proc. Natl. Acad. Sci. U.S.A. 94*, 4872-4877.
54. Yang, Y.-S.; Broadwater, J. A.; Pulver, S. C.; Fox, B. G.; Solomon, E. I. (1999) *J. Am. Chem. Soc. 121*, 2770-2783.
55. Wei, P.-p.; Skulan, A. J.; Wade, H.; DeGrado, W. F.; Solomon, E. I. (2005) *J. Am. Chem. Soc. 127*, 16098-16106.
56. Ha, Y.; Shi, D.; Small, G. W.; Theil, E. C.; Allewell, N. M. (1999) *J. Biol. Inorg. Chem. 4*, 243-256.
57. Smoukov, S. K.; Davydov, R. M.; Doan, P. E.; Sturgeon, B.; Kung, I. Y.; Hoffman, B. M.; Kurtz, D. M. J. (2003) *Biochemistry 42*, 6201-6208.
58. Murray, L. J.; García-Serres, R.; Naik, S.; Huynh, B. H.; Lippard, S. J. (2006) *J. Am. Chem. Soc. 128*, 7458-7459.

59. Murray, L. J.; García-Serres, R.; McCormick, M. S.; Davydov, R.; Naik, S. G.; Kim, S.-H.; Hoffman, B. M.; Huynh, B. H.; Lippard, S. J. (2007) *Biochemistry 46*, 14795-14809.

60. Nordlund, P.; Eklund, H. (1993) *J. Mol. Biol. 232*, 123-164.

61. Smith, T. J.; Slade, S. E.; Burton, N. P.; Murrell, J. C.; Dalton, H. (2002) *Appl. Environ. Microbiol. 68*, 5265-5273.

62. Pikus, J. D.; Studts, J. M.; McClay, K.; Steffan, R. J.; Fox, B. G. (1997) *Biochemistry 36*, 9283-9289.

63. Whittington, D. A.; Rosenzweig, A. C.; Frederick, C. A.; Lippard, S. J. (2001) *Biochemistry 40*, 3476-3482.

64. Lindqvist, Y.; Huang, W.; Schneider, G.; Shanklin, J. (1996) *The EMBO Journal 15*, 4081-4092.

65. Lee, S.-K.; Fox, B. G.; Froland, W. A.; Lipscomb, J. D.; Münck, E. (1993) *J. Am. Chem. Soc. 115*, 6450-6451.

66. Tinberg, C. E.; Lippard, S. J. (2009) *Biochemistry 48*, 12145-12158.

67. Shu, L.; Nesheim, J. C.; Kauffmann, K.; Münck, E.; Lipscomb, J. D.; Que, L., Jr. (1997) *Science 275*, 515-518.

68. Valentine, A. M.; Stahl, S. S.; Lippard, S. J. (1999) *J. Am. Chem. Soc. 121*, 3876-3887.

69. Ambundo, E. A.; Friesner, R. A.; Lippard, S. J. (2002) *J. Am. Chem. Soc. 124*, 8770-8771.

70. Bollinger, J. M., Jr.; Tong, W. H.; Ravi, N.; Huynh, B. H.; Edmondson, D. E.; Stubbe, J. (1994) *J. Am. Chem. Soc. 116*, 8024-8032.

71. Bollinger, J. M., Jr.; Edmondson, D. E.; Huynh, B. H.; Filley, J.; Norton, J. R.; Stubbe, J. (1991) *Science 253*, 292-298.

72. Lyle, K. S.; Haas, J. A.; Fox, B. G. (2003) *Biochemistry 42*, 5857-5866.

73. Meunier, B.; de Visser, S. P.; Shaik, S. (2004) *Chem. Rev. 104*, 3947-3980.

74. Costas, M.; Mehn, M. P.; Jensen, M. P.; Que, L., Jr. (2004) *Chem. Rev. 104*, 939-986.

75. Dismukes, G. C. (1996) *Chem. Rev. 96*, 2909-2926.

76. Högbom, M.; Stenmark, P.; Voevodskaya, N.; McClarty, G.; Gr□slund, A.; Nordlund, P. (2004) *Science 305*, 245-248.

77. Jiang, W.; Yun, D.; Saleh, L.; Barr, E. W.; Xing, G.; Hoffart, L. M.; Maslak, M.-A.; Krebs, C.; Bollinger, J. M., Jr. (2007) *Science 316*, 1188-1191.

78. Cotruvo, J. A. J.; Stubbe, J. (2011) *Biochemistry 50*, 1672-1681.

79. Sjöberg, B.-M.; Karlsson, M.; Jörnvall, H. (1987) *J. Biol. Chem. 262*, 9736-9743.

80. Reipa, V.; Shanklin, J.; Vilker, V. (2004) *Chem. Commun.* 2406-2407.

81. Leahy, J. G.; Batchelor, P. J.; Morcomb, S. M. (2003) *FEMS Microbiol. Rev. 27*, 449-479.

82. Notomista, E.; Lahm, A.; Di Donato, A.; Tramontano, A. (2003) *J. Mol. Evol. 56*, 435-445.

83. Merkx, M.; Lippard, S. J. (2002) *J. Biol. Chem. 277*, 5858-5865.

84. Fox, B. G.; Hendrich, M. P.; Surerus, K. K.; Andersson, K. K.; Froland, W. A.; Lipscomb, J. D.; Münck, E. (1993) *J. Am. Chem. Soc. 115*, 3688-3701.

85. Kopp, D. A.; Gassner, G. T.; Blazyk, J. L.; Lippard, S. J. (2001) *Biochemistry 40*, 14932-14941.

86. Müller, J.; Lugovskoy, A. A.; Wagner, G.; Lippard, S. J. (2002) *Biochemistry 41*, 42-51.

87. Chatwood, L. L.; Müller, J.; Gross, J. D.; Wagner, G.; Lippard, S. J. (2004) *Biochemistry 43*, 11983-11991.

88. Gassner, G. T.; Lippard, S. J. (1999) *Biochemistry 38*, 12768-12785.

89. Blazyk, J. L.; Lippard, S. J. (2002) *Biochemistry 41*, 15780-15794.

90. Blazyk, J. L.; Gassner, G. T.; Lippard, S. J. (2005) *J. Am. Chem. Soc. 127*, 17364-17376.

91. Liu, K. E.; Lippard, S. J. (1991) *J. Biol. Chem. 266*, 12836-12839.

92. Liu, Y.; Nesheim, J. C.; Paulsen, K. E.; Stankovich, M. T.; Lipscomb, J. D. (1997) *Biochemistry 36*, 5223-5233.

93. Fox, B. G.; Liu, Y.; Dege, J. E.; Lipscomb, J. D. (1991) *J. Biol. Chem. 266*, 540-550.

94. Paulsen, K. E.; Liu, Y.; Fox, B. G.; Lipscomb, J. D.; Münck, E.; Stankovich, M. T. (1994) *Biochemistry 33*, 713-722.

95. Froland, W. A.; Ansersson, K. K.; Lee, S.-K.; Liu, Y.; Lipscomb, J. D. (1992) *J. Biol. Chem. 267*, 17588-17597.

96. DeWitt, J. G.; Rosenzweig, A. C.; Salifoglou, A.; Hedman, B.; Lippard, S. J.; Hodgson, K. O. (1995) *Inorg. Chem. 34*, 2505-2515.

97. Pulver, S. C.; Froland, W. A.; Lipscomb, J. D.; Solomon, E. I. (1997) *J. Am. Chem. Soc. 119*, 387-395.

98. Brazeau, B. J.; Wallar, B. J.; Lipscomb, J. D. (2001) *J. Am. Chem. Soc. 123*, 10421-10422.

99. Waller, B. J.; Lipscomb, J. D. (2001) *Biochemistry 40*, 2220-2233.

100. Brazeau, B. J.; Lipscomb, J. D. (2003) *Biochemistry 42*, 5618-5631.

101. MacArthur, R.; Sazinsky, M. H.; Kühne, H.; Whittington, D. A.; Lippard, S. J.; Brudvig, G. W. (2002) *J. Am. Chem. Soc. 124*, 13392-13393.

102. Sazinsky, M. H.; Dunten, P. W.; McCormick, M. S.; Di Donato, A.; Lippard, S. J. (2006) *Biochemistry 45*, 15392-15404.

103. Whittington, D. A.; Lippard, S. J. (2001) *J. Am. Chem. Soc. 123*, 827-838.

104. Liu, Y.; Nesheim, J. C.; Lee, S.-K.; Lipscomb, J. D. (1995) *J. Biol. Chem. 270*, 24662-24665.

105. Baik, M.-H.; Gherman, B. F.; Friesner, R. A.; Lippard, S. J. (2002) *J. Am. Chem. Soc. 124*, 14608-14615.

106. Beauvais, L. G.; Lippard, S. J. (2005) *J. Am. Chem. Soc. 127*, 7370-7378.

107. Tinberg, C. E.; Lippard, S. J. (2010) *Biochemistry 49*, 7902-7912.

108. Coufal, D. E.; Blazyk, J. L.; Whittington, D. A.; Wu, W. W.; Rosenzweig, A. C.; Lippard, S. J. (2000) *Eur. J. Biochem. 267*, 2174-2185.

109. Baggi, G.; Barbieri, P.; Galli, E.; Tollari, S. (1987) *Appl. Environ. Microbiol. 53*, 2129-2132.

110. Arenghi, F. L. G.; Berlanda, D.; Galli, E.; Sello, G.; Barbieri, P. (2001) *Appl. Environ. Microbiol. 67*, 3304-3308.

111. Cafaro, V.; Izzo, V.; Scognamiglio, R.; Notomista, E.; Capasso, P.; Casbarra, A.; Pucci, P.; Di Donato, A. (2004) *Appl. Environ. Microbiol. 70*, 2211-2219.

112. Cafaro, V.; Notomista, E.; Capasso, P.; Di Donato, A. (2005) *Appl. Environ. Microbiol. 71*, 4736-4743.

113. Cafaro, V.; Scognamiglio, R.; Viggiani, A.; Izzo, V.; Passaro, I.; Notomista, E.; Dal Piaz, F.; Amoresano, A.; Casbarra, A.; Pucci, P.; Di Donato, A. (2002) *Eur. J. Biochem. 269*, 5689-5699.

114. Elsen, N. L.; Moe, L. A.; McMartin, L. A.; Fox, B. G. (2007) *Biochemistry 46*, 976-986.

115. Mitchell, K. H.; Studts, J. M.; Fox, B. G. (2002) *Biochemistry 41*, 3176-3188.

116. Rudd, D. J.; Sazinsky, M. H.; Merkx, M.; Lippard, S. J.; Hedman, B.; Hodgson, K. O. (2004) *Inorg. Chem. 43*, 4579-4589.

117. Moe, L. A.; McMartin, L. A.; Fox, B. G. (2006) *Biochemistry 45*, 5478-5485.

118. Tinberg, C. E.; Song, W. J.; Izzo, V.; Lippard, S. J. (2011) *Biochemistry 50*, 1788-1798.

Chapter 2.

Role of an Active Site Threonine Residue in the Determination of Distinctive Dioxygen Reactivity in Toluene/*o*-Xylene Monooxygenase Hydroxylase

* Reproduced in part with permission from three following publications,

1. Woon Ju Song, Rachel K. Behan, Sunil G. Naik, Boi Hanh Huynh, Stephen J. Lippard "Characterization of a Peroxodiiron(III) Intermediate in the T201S Variant of Toluene/*o*-Xylene Monooxygenase Hydroxylase from *Pseudomonas sp.* OX1" *J. Am. Chem. Soc.* **2009**, *131*, 6074-6075

2. Arteum D. Bochevarov, Jianing Li, Woon Ju Song, Richard A. Friesner, Stephen J. Lippard "Insights into the Different Dioxygen Activation Pathways of Methane and Toluene Monooxygenase Hydroxylases" *J. Am. Chem. Soc.* **2011**, *133*, 7384-7397

3. Woon Ju Song and Stephen J. Lippard "Mechanistic Studies of Reactions of Peroxodiiron(III) Intermediates in T201 Variants of Toluene/*o*-Xylene Monooxygenase Hydroxylase" *Biochemistry,* **2011**, *Accepted*

2.1. INTRODUCTION

Carboxylate-bridged diiron centers are common active site motifs found in various metalloenzymes, such as soluble methane monooxygenase hydroxylase (sMMOH), ribonucleotide reductase R2-subunit (RNR-R2), Δ^9 desaturase (Δ^9D), and ferritin.[1-3] Although diiron enzymes can perform a wide range of dioxygen-dependent chemical transformations, their active sites and chemical mechanism of dioxygen activation are strikingly similar. Diiron(II) enzymes can activate dioxygen and form peroxodiiron(III) intermediates by two electron transfers from two Fe(II) ions to dioxygen. Oxygenated diiron(III) intermediates in diiron enzymes typically display spectroscopic properties, such as optical bands at ~600-800 nm (ε = ~1500-2500 cm^{-1}) and Mössbauer parameters of δ = ~0.6 mm/s and ΔE_Q = ~1.5 mm/s.[4-9] The similar chemical features of the oxygenated diiron(III) intermediates indicate that diiron protein scaffolds are operative in a similar fashion during dioxygen activation and that the process is energetically favorable.

In addition to sMMOH, another enzyme in the family of bacterial multicomponent monooxygenases (BMMs), toluene/*o*-xylene monooxygenase hydroxylase (ToMOH), has been recently explored. A transient diiron(III) intermediate of ToMOH, tentatively assigned as a peroxodiiron(III) species ($ToMOH_{peroxo}$), was identified from the reaction of reduced ToMOH and dioxygen by time-dependent Mössbauer spectroscopy.[10] The reaction of $ToMOH_{peroxo}$ with phenol demonstrated that this intermediate is kinetically competent for arene oxidation. Although ToMOH is similar to sMMOH both in sequence[11] and active site structure,[12] the spectroscopic properties of $ToMOH_{peroxo}$ were unexpectedly different from those of the oxygenated intermediates generated in sMMOH. Whereas the oxygenated diiron(III) intermediate in sMMOH (P or H_{peroxo}) displays the typical optical and Mössbauer spectra described above, $ToMOH_{peroxo}$ has no optical bands in the visible region and features distinct Mössbauer parameters of δ = 0.54 mm/s and ΔE_Q = 0.67 mm/s.[10] In addition, no other high-valent intermediate, like the diiron(IV) species (Q) in sMMOH that is responsible for methane oxidation, was observed in ToMOH. These results suggest that ToMOH$_{\mathrm{peroxo}}$ exhibits a geometry distinct from those of other peroxodiiron(III) intermediates characterized in carboxylate-bridged diiron proteins and that unidentified chemical machinery controls the dioxygen chemistry with the diiron motif, causing ToMOH to be distinct from previously characterized diiron-containing enzymes.

Because the diiron-coordinating ligands of sMMOH and ToMOH are identical, we drew our attention to the secondary active site environments. Both sMMOH and ToMOH contain an active site pocket that is primarily hydrophobic, with the exception of one threonine and one asparagine residue (T213/N214 in sMMOH and T201/N202 in ToMOH).[12,13] The active site threonine residue has been proposed to play a critical role in proton transfer to the diiron centers, analogous to a conserved threonine in the active site of cytochrome P450 monooxygenases.[13-15] Recently, a structure of other BMMs, toluene 4-monooxygenase hydroxylase (T4moH), demonstrated that its active site threonine residue can form a hydrogen bond to the diiron center via a newly positioned water molecule,[16] supporting the possibility that this residue may be essential for enzymatic function. Experiments to elucidate the role of this residue have not been carried out, however.

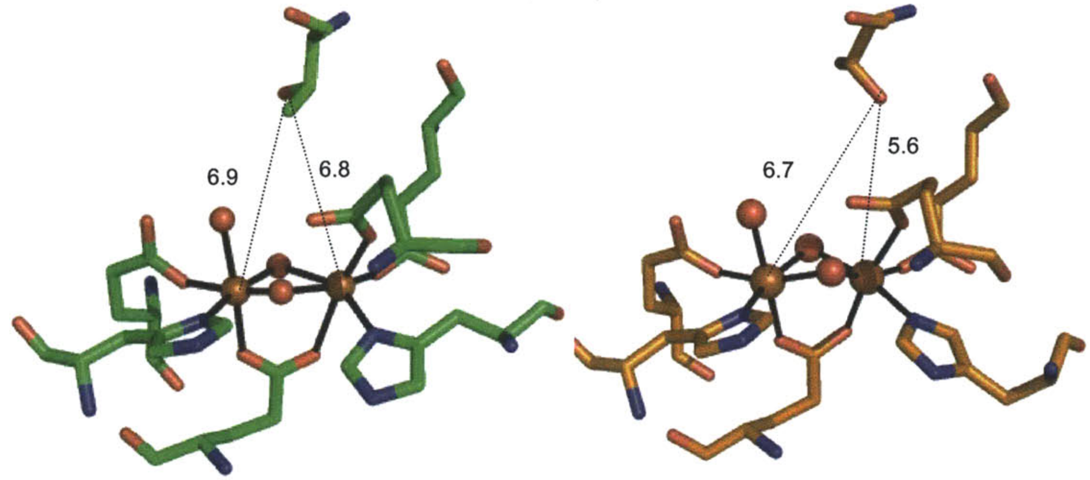

Figure 2.1 Active site threonine residues near the diiron centers of sMMOH and ToMOH. (Left) sMMOH (PDB 1MTY), (Right) ToMOH (2INC). Diiron atoms and water molecules are represented as orange and red spheres, respectively. Carbon, nitrogen, and oxygen atoms of sMMOH are displayed as green, blue, and red sticks, respectively. Carbon, nitrogen, and oxygen atoms of ToMOH are shown as orange, blue, and red sticks, respectively. The distances between diiron atoms and the oxygen atom of the hydroxyl group at T213 in sMMOH or at T201 in ToMOH are depicted by dotted lines.

Further structural comparisons between the active site threonine residue of sMMOH, T213, and that of ToMOH, T201, demonstrated that its conformation is noticeably different in the two proteins (Figure 2.1). The hydroxyl group of ToMOH T201 points toward the diiron sites whereas that of sMMOH T213 points away from the diiron centers. Consequently, the distance and angle of the threonine hydroxyl group with respect to the diiron atoms are different in sMMOH and ToMOH. Based on this observation, we proposed a hypothesis that this slight structural difference in the vicinity of the active sites may be responsible for generating different oxygenated intermediates in sMMOH and ToMOH. To evaluate the proposal, ToMOH T201 was substituted with serine because this conservative mutation probably exerts the least structural perturbation on the enzyme while possibly changing the sterically-imposed rotational strain of the hydroxyl group. To evaluate our hypothesis, the dioxygen chemistry was explored in the T201S variant.

2.2. MATERIALS AND METHODS

General Considerations. Plasmids containing the genes for the toluene/*o*-xylene monooxygenase components, pET22b(+)/touBEA, pET22b(+)/touF, pET22b(+)/touC, and pET22b(+)/touD, were supplied by Professor Alberto Di Donato. Heterologous expression and preparation of three ToMO component proteins, ToMOH, Rieske protein (ToMOC), and regulatory protein (ToMOD) were carried out as described previously.[17]

Previous preparative procedures for the ToMO reductase protein (ToMOF) require its recovery from inclusion bodies, which demand an additional refolding step. We therefore developed a method for obtaining soluble recombinant ToMOF. The vector, pET22b(+)/touF was transformed into *E. coli* BL21(DE3) competent cells on LB/agar plates (300 μg/L ampicillin) by standard procedures. A starter culture was grown in 300 mL of LB media at 37 °C overnight. Two different media components were used for protein expression and each produced similar yields of protein, 1mg per 1L growth media. One contained 25 g LB plus an additional 17.5 g NaCl and the other used 10 g bactotryptone, 5 g yeast extract, 5 g NaCl, and 3 g glucose per 1 L of distilled water. Before the cell inoculation, 100 mg/L ampicillin was added to the media. At an OD_{600} of ~0.7-0.8, the temperature was lowered to 25 °C and protein expression was initiated by adding 0.1 mM IPTG at 25 °C. After 10 h, the cells were pelleted by centrifugation at 7000 rpm for 7 min, frozen in liquid nitrogen, and stored at – 80 °C for further use. This cell paste (~35 g) was thawed in 100 mL of cracking solution comprising 25 mM MOPS pH 7.3 buffer containing 10 % glycerol, 4 mM 1,4-dithiothreitol (DTT), 0.05 g $MgCl_2$ and 40 unit DNase. The cells were then sonicated on ice using 2.5 sec output and 15 sec pauses for 12 min. The soluble cell extract was separated from insoluble material by ultra-centrifugation for 1.5 h at 35,000 rpm, decanted, then filtered through 0.2-μm membranes. This extract was loaded immediately on to a Q-Sepharose column (26 × 300 mm) equilibrated with 25 mM MOPS buffer at pH 7.3 with 4 mM 1,4-dithiothreitol at a flow rate of 2 $\mathrm{mL{\cdot}min^{-1}}$. After the column had been washed and equilibrated with the purification buffer, ToMOF was eluted with a 1.35 L linear gradient from 0 to 350 mM NaCl at a flow rate of 1.5 $\mathrm{mL{\cdot}min^{-1}}$. Fractions containing ToMOF, which eluted around 140 mM NaCl, were pooled on the basis of SDS/PAGE analysis and the ratio of A_{280}/A_{454}, as published previously.[17] The ToMOF solution was concentrated using Millipore centrifugal devices (M.W. 3000) and loaded on to a Superdex 75 column (26 × 950 mm) equilibrated with 25 mM MOPS buffer at pH 6.8 containing 10 % glycerol, 4 mM DTT, and 250 mM NaCl. ToMOF was eluted with a 500 mL linear flow rate of 0.65 $\mathrm{mL{\cdot}min^{-1}}$, and the ToMOF-containing fractions were identified by the same procedure as the first purification step. The pure protein was drop-frozen in liquid nitrogen and stored at −80 °C. ToMOF prepared by this new preparation method showed identical features to refolded protein from inclusion bodies in an SDS-TRIS/HCl gradient gel, ESI-MS, iron and FAD analyses, and activity, as published previously.[17]

Site Directed Mutagenesis of T201S ToMOH. Conversion of T201 into T201S was performed by site-directed mutagenesis as described previously,[18] using the parent pET22b(+)/touBEA plasmid with the following designed primers: 5'-C GAA ACA GGC TTC <u>AGC</u> AAT ATG CAG TTT C-3' and 5'-G AAA CTG CAT ATT <u>GCT</u> GAA GCC TGT TTC G-3'. The primers were obtained from Invitrogen. For polymerase chain reaction (PCR), DNA Polymerase pfU Turbo, dNTPs, and reaction buffer were purchased from Stratagene and an MJ Research MiniCycler was used for PCR. PCR products were digested with DpnI for 3 h at 37 °C. The expected (8227 bp) PCR product was visualized on a 1 % agarose gel, excised, extracted into TBE buffer, and transformed into XL-1 Blue Supercompetent cells as recommended by the manufacturer (Stratagene). Cells were grown on LB/agar plates containing ampicillin (100 μg/mL) at 37 °C overnight. Colonies were picked and grown in 5 mL LB cultures (LB media, 300 μg ampicillin/mL) at 37 °C overnight. A Qiagen Mini-Prep kit was used to isolate the plasmids from each colony. The sequence of each plasmid was confirmed using five different primers (T7 promoter, T7 terminator, and three custom-ordered from Invitrogen) at the MIT BioPolymers Lab. The T201S variant of ToMOH was expressed in *E. coli* and purified using the same procedure as the wild-type enzyme.[10,17] An iron content was performed, using the ferrozine colorimetric assay.[19] Methods for determining specific activity and Michaelis-Menten kinetics for the substrate phenol,[10,17] measurements of the regiospecificity of toluene and *o*-xylene oxidation,[20] and single-turnover assays[21] were also described previously.

Stopped-Flow UV-Vis Experiments of the Reaction of Reduced T201S ToMOH and ToMOD with Dioxygen. An optical band corresponding to an oxygenated intermediate of ToMOH T201S was monitored by using a HiTech DX2 stopped-flow spectrophotometer. Drive syringes and flow lines of this instrument were made anaerobic by passage of at least 10 mL of anaerobic solution of 4 mM sodium dithionite in 25 mM MOPS, pH 7 buffer. Excess dithionite was removed by flushing the syringes with anaerobic buffer. T201S ToMOH was reduced anaerobically by reacting the protein with excess sodium dithionite in the presence of an equimolar amount of methyl viologen for 30 min. Reduced protein (~200-300 μM) was then dialyzed against 1 L of 25 mM MOPS, pH 7.0 buffer for ~3 hr, anaerobically. Following dialysis, 3 equiv[a] of regulatory protein (ToMOD) relative to the hydroxylase was added. The solution (ToMOH$_{red}$D) was transferred to a tonometer and loaded into the anaerobic stopped flow instrument. This solution was mixed against an equal volume of O_2-saturated 25 mM MOPS, pH 7.0 buffer. The temperature was thermostatted at 4 °C with a circulating water bath and checked with thermocoupler connected to the reaction cell. Data were collected using either a PMT (photomultiplier) for halogen lamp illumination or a diode array detector for a xenon arc lamp. The time-dependent absorbance data were analyzed by the software package, *Kinetic Studio* (TgK Scientific) and Origin 6.1 (OriginLab Corporation). A two-exponential function derived from the ToMOH$_{red}$→ T201$_{peroxo}$→ ToMOH$_{ox}$ model gave the best fit (eq 2.1). For simplicity, ToMOH$_{red}$, T201$_{peroxo}$, and ToMOH$_{ox}$ and rate constants for the conversion are abbreviated as A, B, and C and k_1 and k_2, respectively.

$$\text{Abs}= \varepsilon_c*[A]_0+(\varepsilon_A-\varepsilon_C)*[A]_0*\exp(-k_1*x)+(\varepsilon_B-\varepsilon_C)*[A]_0*k_1/(k_2-k_1)*(\exp(-k_1*x)-\exp(-k_2*x))$$

(eq 2.1)

Rapid Freeze-Quench and Mössbauer Sample Preparation. To obtain ^{57}Fe enriched T201S ToMOH samples, we prepared cell-growth media containing 10 g of tryptone, 10 g of NaCl, and 2 g of casamino acids per 1.5 L of distilled water in a 2-L baffled flask. After cooling the autoclaved media, 5 g/L glucose and 0.25 g/L $MgSO_4$ were added. A starter culture was grown overnight at 37 °C and used to inoculate the larger cultures, which were supplemented with 0.1 mg/L ampicillin. At an OD_{600} of 0.7-0.8, the temperature was lowered to 25 °C and protein expression was induced by adding IPTG to a final

---

[a] In ToMO system, maximal coupling is achieved when ToMOD is present at ≥ 2 equiv of ToMOH. To assure that the component interacts are fully achieved during these experiments, we used 3 equiv of ToMOD.

concentration of 25 μM. $^{57}FeCl_3$ was prepared by dissolving ^{57}Fe powder (Cambridge Isotope, 95.6% enriched) in ~2 mL of concentrated hydrochloric acid. Each culture was supplemented with a final concentration of 25 μM $^{57}FeCl_3$ at 0 and 2.5 h after initiating the induction. After 5 h, the cells were pelleted by centrifugation at 7000 rpm for 7 min, frozen in liquid nitrogen, and stored in a –80 °C freezer until use. The purification procedures were identical to those for wild type protein.[17]

For Mössbauer experiments, 500-900 μM of ^{57}Fe-enriched T201S $ToMOH_{red}$ was mixed with 3 equiv of ToMOD in 25 mM MOPS, pH 7.0. This solution was transferred to a 1 mL RFQ syringe, anaerobically. A 4-syringe ram freeze quench apparatus from Update Instruments (Madison, WI) was used in all freeze quench experiments. The reaction was cooled to 4 °C using an ice water bath. As in the stopped-flow experiments, T201S $ToMOH_{red}$ with regulatory protein was added in a 1:1 ratio with O_2-saturated buffer. The reaction was aged in an appropriate length delay line, depending on the reaction time (45 ms or 200 ms), and then quenched by spraying into a cold isopentane bath at -140 °C. The RFQ experiments were performed in collaboration with Dr. Rachel K. Behan (Lippard Lab, MIT). Detailed experimental conditions for the RFQ and Mössbauer experiments are the same as previously reported.[22] For the reduced and oxidized samples, the protein solution was transferred into a Mössbauer cup and rapidly frozen in liquid N_2. To prepare oxygenated samples at ~100 s after reaction initiation with dioxygen, a solution of T201S $ToMOH_{red}$ and ToMOD was manually mixed with an equal volume of O_2-saturated buffer at 4 °C for 100 s and the reactions were quenched by rapidly spraying the solution into liquid nitrogen. The following Mössbauer experiments were carried out by Dr. Sunil G. Naik and Prof. Boi Hanh Huynh (Emory University, Atlanta, GA).

2.3. RESULTS AND DISCUSSION

Arene-Oxidizing Reactivity of T201S ToMOH. The steady-state activity for conversion of phenol to catechol by T201S ToMOH was measured to be 2400 ± 300 mU/mg (mU = nmol/min), compared to that of wild-type enzyme, 1200 ± 200 mU/mg, respectively. A Michaelis-Menten kinetic analysis revealed k_{cat} and $k_{\text{cat}}/K_{\text{M}}$ values for T201S of 0.08 ± 0.03 s^{-1} and 0.02 $\mu\text{M}^{-1}\text{s}^{-1}$, respectively, which are not greatly different from those of the wild-type enzyme, 0.049 ± 0.003 s^{-1} and 0.011 ± 0.003 $\mu\text{M}^{-1}\text{s}^{-1}$. The T201S variant also produced the same single-turnover yield as did the wild-type enzyme for phenol oxidation, ~50% of the diiron sites. The regiospecificity of T201S for phenol and toluene hydroxylation was not changed, producing catechol and *o*:*m*:*p*-cresol at a 3:2:5 ratio, respectively. The regiospecificity of T201S for *o*-xylene hydroxylation was slightly perturbed. The ratio of the two products 2,3-dimethylphenol to 3,4-dimethylphenol was changed from 2:8 to 4:6.[23] The conserved arene-oxidizing activity of T201S variant relative to the wild-type enzyme suggests that T201S ToMOH is a functionally conserved mutant to the wild-type.

Single-Mixing Stopped-Flow Studies of Dioxygen Activation in the T201S Variant of ToMOH and ToMOD. Pre-steady-state dioxygen activation at the reduced diiron(II) center of T201S ToMOH was investigated by stopped-flow spectrophotometry and time-dependent Mössbauer spectroscopy, as similarly performed with the wild-type enzyme. Although an oxygenated intermediate generated in the wild-type enzyme, $\text{ToMOH}_{\text{peroxo}}$, exhibited no optical feature in the visible region, surprisingly, we observed a new transient intermediate ($\text{T201}_{\text{peroxo}}$) with a broad absorption band at λ_{max} = ~650 nm ($\Delta\lambda_{\text{max}}$ = ~675 nm) (Figure 2.2). This feature provides the first optical spectroscopic evidence for an oxygenated intermediate in any toluene monooxygenase. A typical kinetic trace of the growth and decay of the transient intermediate is provided together with the fit. The absorbance at 675 nm maximizes at ~40 ms after dioxygen is mixed at 4.0 ± 0.1 °C. Fitting the time-dependent absorption spectra to a $\text{ToMOH}_{\text{red}} \rightarrow \text{T201}_{\text{peroxo}} \rightarrow$ diiron(III) product analytical model yielded $k_{\text{form}} = 85 \pm 11\ \text{s}^{-1}$ and $k_{\text{decay}} = 2.9 \pm 0.2\ \text{s}^{-1}$. The intermediate is only observed in the presence of the regulatory protein (ToMOD), which is consistent with previous reports of oxygenated intermediates in BMMs, such as H_{peroxo} or Q of sMMOH,[24] and $\text{ToMOH}_{\text{peroxo}}$ in wild type.[10]

(A)

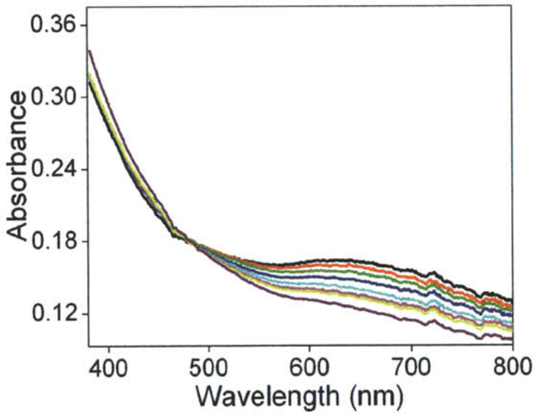

(B)

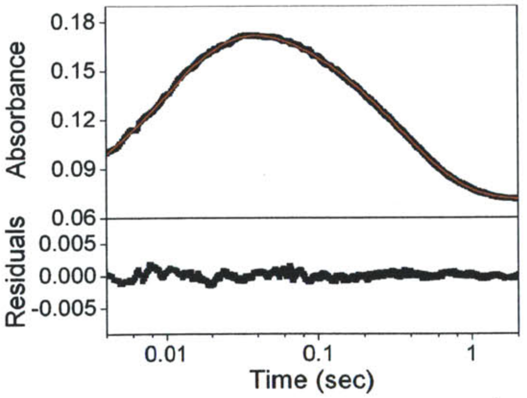

(C)

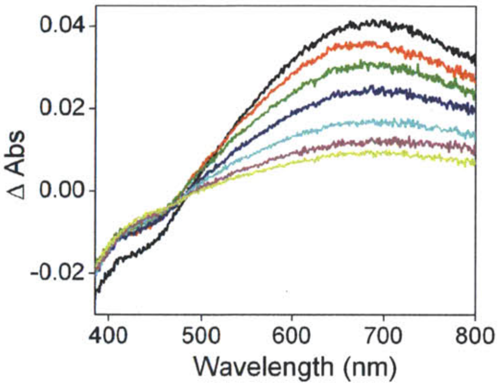

Figure 2.2 UV-vis spectra of the reaction of reduced ToMOH T201S with dioxygen-saturated buffer in the presence of ToMOD. [ToMOH] = ~120 μM, [ToMOD] = 360 μM in 25 mM MOPS, pH 7.0 at 4.0 ± 0.1 °C. (A) Spectrum detected in diode array mode. (B) Time-dependent absorption trace monitored at 675 nm showing the residuals (bottom) of the raw absorption UV-vis spectrum (black, top) from data fitting (red, top). (C) The time-dependent spectral change obtained by subtraction of the initial spectrum. Spectra collected at 35, 45, 75, 95, 105, 165, and 235 ms after reaction initiation were subtracted from the spectrum collected at 260 ms.

Single-Mixing Mössbauer Studies of Dioxygen Activation in T201S ToMOH and ToMOD. To investigate further the spectroscopic properties of this intermediate, we performed Mössbauer studies with ^{57}Fe-enriched T201S ToMOH. We present the Mössbauer spectra of reduced diiron(II) in the presence of ToMOD (Figure 2.3A), oxidized diiron(III) in the presence of ToMOD (Figure 2.3E), rapid freeze-quenched samples at 45 ms (Figure 2.3B), at 200 ms (Figure 2.3C), and at ~100 s (Figure 2.3D) after reaction initiation with dioxygen. The spectra corresponding to the diiron(II) and the diiron(III) product of T201S ToMOH were fit to two quadrupole doublets having $\delta = 1.32$ mm/s and $\Delta E_Q = 2.32$ and $\delta = 1.32$ mm/s and 3.16 mm/s and one quadrupole doublets having $\delta = 0.50$ mm/s and $\Delta E_Q = 0.82$, respectively. Within experimental error, these parameters are indistinguishable from those of wild type ToMOH. When T201S ToMOH$_{red}$ was allowed to react with dioxygen (Figure 2.3B-C), we observed that only 50% of the diiron(II) sites proceed through the catalytic cycle, whereas the rest slowly oxidizes to the diiron(III) product without forming the intermediate, suggesting a half-sites reactivity as reported for wild type ToMOH, RNR-R2, and Δ^9D.[8,10,25] Upon reaction of T201S ToMOH$_{red}$ with dioxygen in the presence of ToMOD, two distinctive transient intermediates accumulate (Figure 2.3B-C). One of the intermediates displays Mössbauer parameters very similar to those of the diiron(III) intermediate of wild type ToMOH (ToMOH$_{peroxo}$), with δ = 0.55 mm/s and ΔE_Q = 0.70 mm/s. ToMOH$_{peroxo}$ accounts for approximately 40% of total iron at 45 ms, 45% of total iron at 200 ms, and decays fully by ~100 s (Figure 2.3D), displaying a kinetic behavior that is similar to that of ToMOH$_{peroxo}$ in the wild type enzyme. As for the wild type, ToMOH$_{peroxo}$ generated in T201S variant of the enzyme also has no optical band in the visible range.

The other intermediate, which corresponds kinetically to the optical changes observed by stopped-flow optical spectroscopy, displays Mössbauer parameters identical to those of H$_{peroxo}$ in sMMOH, with δ = 0.67 mm/s and ΔE_Q = 1.51 mm/s, implying that structure of T201$_{peroxo}$ is similar to the structure of H$_{peroxo}$ in sMMOH, but different from that of ToMOH$_{peroxo}$. This intermediate accounts for ~10% and ~5% of total iron in the Mössbauer spectra of the sample collected at 45 ms and 200 ms, respectively (Figure 2.2B-C), which allows us to estimate the molar extinction coefficient of T201$_{peroxo}$ to be ε_{675} = ~1500 cm^{-1} M^{-1}. This value is within the range of those reported for peroxo-to-iron charge transfer bands in several diiron(III) peroxo enzyme intermediates described above, as well as synthetic model complexes.[26,27] Given these spectroscopic similarities, we assign this species as a peroxodiiron(III) intermediate (T201$_{peroxo}$) presumably having a *cis*-μ-1,2[28,29] or

μ-η^2,η^2 geometry,[28,29] as proposed previously.

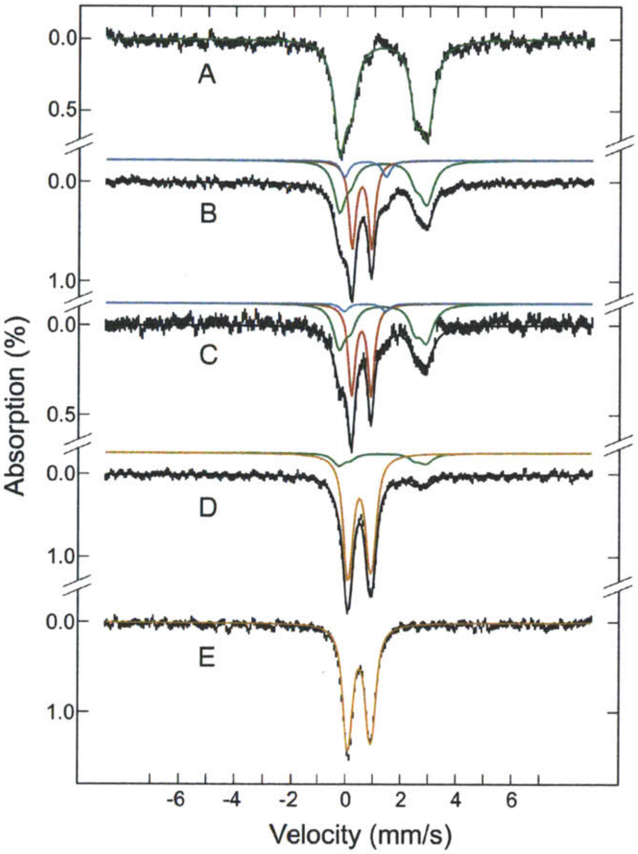

Figure 2.3 Mössbauer spectra of freeze-quenched samples from reaction of T201S ToMOH$_{red}$D with O$_2$. The spectra (vertical bars) were collected at 4.2 K in a 50-mT field parallel to the γ-beam. The three spectra correspond to (A) the diiron(II) starting material, (B) 45 ms after mixing with O$_2$, (C) 200 ms after mixing with O$_2$, (D) ~100 s after mixing with O$_2$, and (E) the oxidized diiron(III) sample. The green, red, cyan and orange lines are simulated spectra of the unreacted diiron(II) protein, ToMOH$_{peroxo}$, T201$_{peroxo}$, and diiron(III) product or the resting diiron(III) state, respectively. The solid line overlaid with the experimental spectrum in B is the composite spectrum.

Although accurate formation and decay rates of ToMOH$_{peroxo}$ were not measured in the T201S variant, time-dependent Mössbauer spectra demonstrated that accumulated concentrations of ToMOH$_{peroxo}$ in the T201S variant are comparable to those of the wild-type enzyme, suggesting that kinetics of ToMOH$_{peroxo}$ in the T201S enzyme are presumably comparable to those of the wild-type, k_{form} = ~26 s^{-1} and k_{decay} = 0.045 s^{-1}.[10] The kinetic parameters of the two discrete diiron(III) intermediates, ToMOH$_{peroxo}$ and T201$_{peroxo}$, reveal that T201$_{peroxo}$, which has formation and decay rate constants of 85 s^{-1} and 2.9 s^{-1}, respectively, is probably not a precursor of ToMOH$_{peroxo}$. These data suggest that T201S mutation caused a bifurcation in the pathway of dioxygen activation of the enzyme (Scheme 2.1). T201$_{peroxo}$ is therefore observed not because the reaction of ToMOH and dioxygen is kinetically perturbed but possibly because the energetics of the reaction between ToMOH$_{red}$ and dioxygen are partially altered by the single mutation at the T201 residue. Given that T201$_{peroxo}$ resembles the spectroscopic properties of H$_{peroxo}$ in sMMOH, the perturbation probably relates to the difference in the dioxygen chemistry between sMMOH and ToMOH.

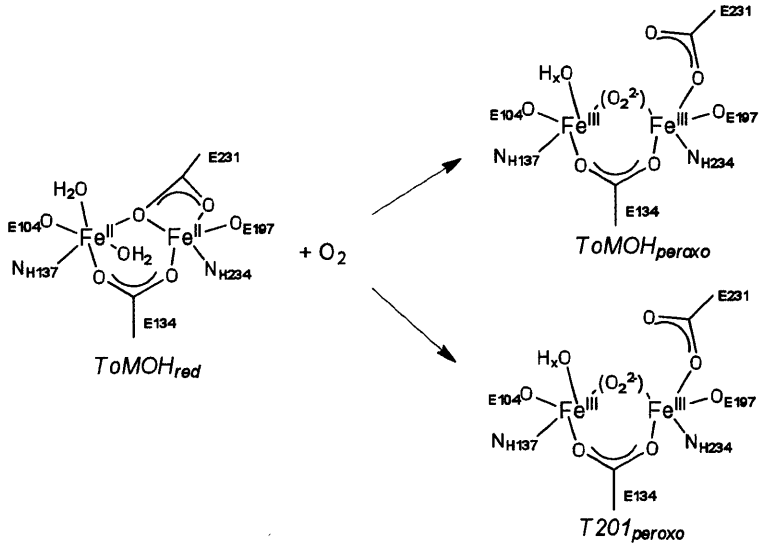

Scheme 2.1 Proposed Bifurcated Dioxygen Activation Pathways in the T201S Variant of ToMOH. The geometries of the peroxo-units of ToMOH$_{peroxo}$ and T201$_{peroxo}$ are not specified. Iron-coordinating water molecules are represented as OH$_X$ due to a possibility of deprotonation.

Computational Studies of ToMOH.[b] Computational calculation studies were carried out to evaluate whether the single mutation at T201 residue can perturb the energetics of diiron active site greatly enough to form a novel intermediate in T201S variant and to ask whether the slight difference at the active site threonine residue is relevant to the differential dioxygen reactivity of sMMOH and ToMOH enzymes.[30] First, a series of single-point energies for different dihedral angles defined by 2Fe-THR (Fe_1-Fe_2-C_β-O), were calculated by molecular mechanics (MM) (Figure 2.4A). The dihedral angle is determined to be positive when the hydroxyl group points toward the diiron center whereas 2Fe-THR exhibits a negative value for the opposite conformation of the threonine residue. Energy was plotted as a function of the dihedral angle 2Fe-THR. The calculation results for sMMOH and ToMOH are consistent with their crystal structures in that 2Fe-THR angle displays rotational energy minima of -102.9° and 139.2° for sMMOH and ToMOH, respectively (Figure 2.4B). Interestingly, the T201S mutation of ToMOH produced dramatic changes in the rotation energy curve. While the absolute minimum at the positive 2Fe-THR angle was preserved, the energies for the negative angles are drastically reduced. Given that the T201S mutation partially converts the enzyme into a sMMOH-like one in terms of dioxygen activity, the changes in the relative rotational energetics at T201 by T201S mutation suggest that the threonine residue may be closely related to the formation of specific oxygenated intermediates. If then, we can speculate that $ToMOH_{peroxo}$ possibly favors a positive 2Fe-THR angle, in which the hydroxyl group of T201 can form H-bonding interactions. $T201_{peroxo}$ of ToMOH and H_{peroxo} of sMMOH, in contrast, may

---

[b] This work is primarily carried out in Prof. Richard Friesner's lab at Columbia University. A full description of the results is included in Appendix A.

display a negative 2Fe-THR angle and may not require a direct interaction with the threonine residue.

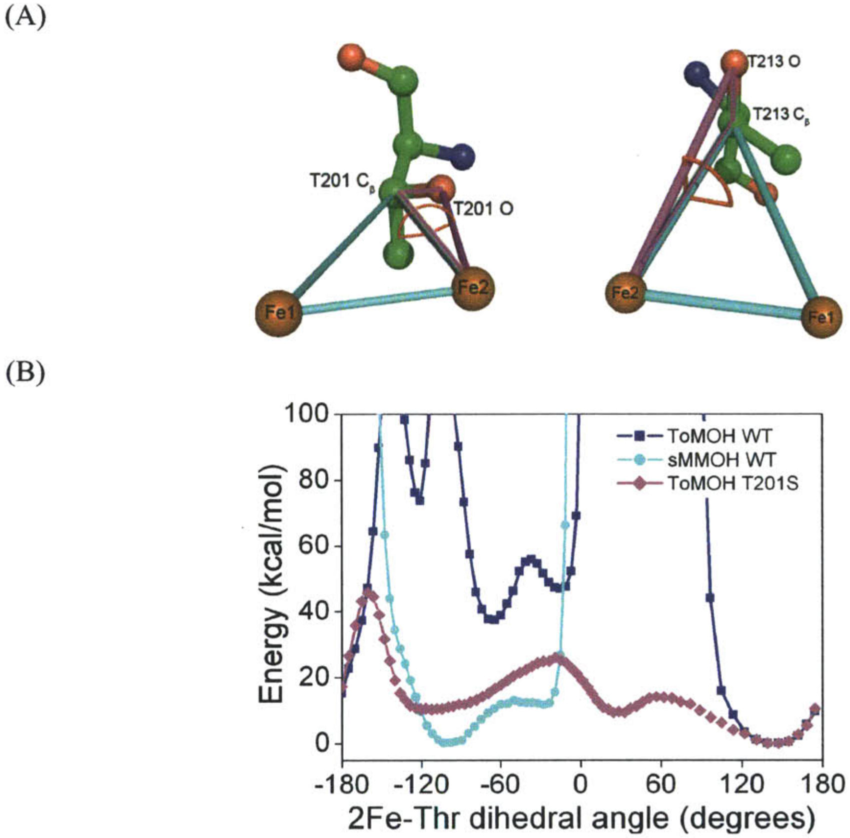

Figure 2.4 Rotational energies of the active site threonine residues of sMMOH, ToMOH, and the ToMOH T201S variant. (A) 2Fe-THR dihedral angles in ToMOH (left, 2INC) and sMMOH (right, 1MMO). The dihedral angle is depicted by red compass. Two planes comprising of the dihedral angle are represented as cyan and pink lines, each of which is consisted of Fe1, Fe2, and C_β at T201 or T213 and Fe2, C_β, and O at T201 or T213 residues, respectively. The angle measured clockwise from a plane (in cyan) to the other (in pink) is defined as a positive angle and vise versa. The 2Fe-THR dihedral angles in ToMOH (2INC) and in sMMOH (1MMO) are 161.8° and -90.1°, respectively. (B) Relative rotational energies of active threonine residues in the ToMOH wild-type, sMMOH, and T201S variant of ToMOH.

The relative energies of possible oxygenated intermediates were optimized by

QM/MM. ToMOH favors the formation of *cis*-μ-1,2-peroxodiiron(III) or μ-1,1-peroxodiiron(III) geometries, but not μ-η^2,η^2 structure. The results are distinct from those of sMMOH, where a μ-η^2,η^2 peroxodiiron(III) structure was preferred for the geometry of H_{peroxo},[28,29] For ToMO, conversion of the peroxodiiron(III) to a Q-type diiron(IV) intermediate was an energetically uphill process by ~4.7 kcal/mol.[c] The formation of a Q-like high valent species may not be energetically favorable in ToMOH if the peroxodiiron(III) but not Q is stabilized by the hydrogen-bonding interactions with the active site threonine residue.

Perturbation in the Dioxygen Chemistry of ToMOH Induced by the T201S Mutation. Although the T201S mutant is a functionally conserved enzyme for arene oxidation, dioxygen chemistry distinct from wild-type ToMOH is observed. Based on experimental and theoretical studies, the formation of the novel oxygenated intermediate $T201_{peroxo}$ is presumably influenced by the alteration of hydrogen-bonding effects from the T201S residue. Given that the net effect of the T201S mutation is the removal of a methyl group, it is possible that the side chain may be indirectly involved in the formation of the hydrogen bonding with the peroxo-unit of $ToMOH_{peroxo}$. The structure of wild-type ToMOH demonstrated that the methyl group at T201 is located adjacent to F196 (Figure 2.5). Therefore, the methyl group at T201 possibly enforces particular degrees of rotational conformation through a hydrophobic interaction with F196, thereby restricting the position of the T201 hydroxyl group with respect to the diiron sites. The T201S mutant, however, has no such steric limitation and presumably displays a higher degree of rotational freedom,

---

[c] The relative energy reported here was calculated for unprotonated peroxo diiron(III) species. Further computational studies of a more promising structure of $ToMOH_{peroxo}$, hydroperoxo diiron(III), are in progress.

allowing it to form a sMMOH-like orientation. In this manner, hydrogen-bonding from the hydroxyl group to ToMOH$_{peroxo}$ can be significantly weaker than for the wild-type enzyme, leading to the formation of a H$_{peroxo}$-like intermediate, T201$_{peroxo}$. In contrast, sMMOH contains a glycine residue (G208) near T213, which cannot exhibit hydrophobic interactions. This might be the one of the reasons why the hydroxyl group at T213 of sMMOH features an alternative conformation from that of ToMOH. These observations imply that the geometry of the intermediate formed might be substantially determined by the second-shell of the diiron sites.

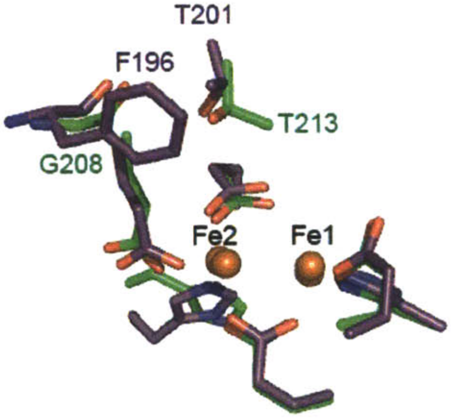

Figure 2.5 Overlaid structures of ToMOH (2INC) and sMMOH (1MTY). Fe atoms are represented by orange spheres. Iron-coordinating ligands and adjacent residues in ToMOH and sMMOH are represented by purple and green sticks, respectively. Oxygen and nitrogen atoms were colored in red and blue, respectively. Solvent derived coordinating ligands, water and hydroxide molecules, were omitted for clarity.

Previous studies of a conserved mutation at a iron-coordinating residue of RNR-R2 (D84E) also demonstrated that a single mutation can perturb the kinetics and/or energetics of dioxygen activation.[6,31] As a result of the mutation, an oxygenated diiron(III) intermediate was kinetically isolated, which was hardly detectable in wild-type RNR-R2.[32] Spectroscopic properties of the diiron(III) intermediate resembles those of H$_{peroxo}$ of sMMOH. Site-mutagenesis studies of both ToMOH and RNR-R2, therefore, suggest that dioxygen chemistry can be easily perturbed even by a single conserved mutation at the coordinating or the secondary environments of the diiron center.

Proposed Geometries of Oxygenated Intermediates of ToMOH. The distinct spectroscopic properties of $ToMOH_{peroxo}$ relative to those of previously characterized peroxodiiron(III) species suggest that the geometry of $ToMOH_{peroxo}$ displays neither a *cis*-μ-1,2- nor a μ-η^2,η^2- configuration. $ToMOH_{peroxo}$ does not feature an optical band in the visible region, indicating that peroxo ligand to metal charge transfer (LMCT), typically observed at ~600-800 nm (ε = 1500 - 2500 $cm^{-1}M^{-1}$), is significantly diminished and/or shifted. Based on analogous dicopper chemistry and Mössbauer parameter calculations, we propose that $ToMOH_{peroxo}$ contains a protonated peroxo-unit, possibly having a μ-1,1-hydroperoxo-diiron(III) geometry (Scheme 2.2).

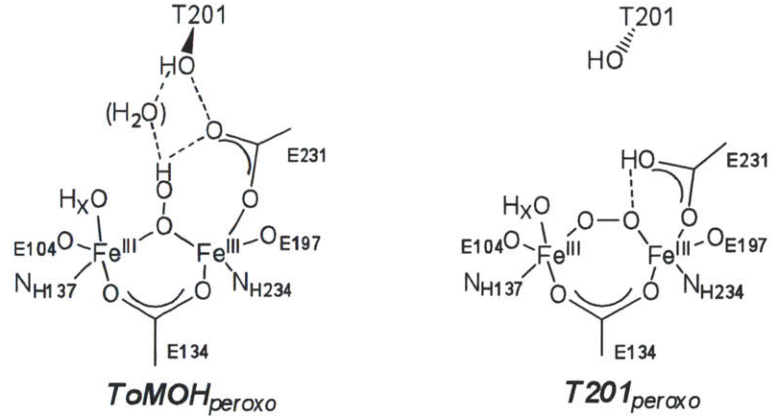

Scheme 2.2 Proposed Structures of $ToMOH_{peroxo}$ and $T201_{peroxo}$. Iron-coordinating water molecules are represented as OH_X due to the possibility of deprotonation (x= 1 or 2).

Previously, spectroscopic and computational studies of dicopper complexes have demonstrated unprotonated end-on versus μ-1,1-hydroperoxo dicopper(II) species.[33,34] The results suggest that protonation of the peroxo unit significantly stabilize the π^* orbital from the O_2^{2-} ligand, shifting the LMCT transition by ~5000 cm^{-1} to higher energy. In addition, the studies suggested that protonation possibly increase the electronegativity of the peroxide unit, substantially reducing the degree of charge donation to the metal, which could weaken the band.

If the protonation event occurs to the peroxodiiron(III) center in the similar fashion, the characteristic LMCT band at 600 – 800 nm might not be observed. Furthermore, the anionic charge of the coordinating glutamate ligands of diiron enzymes may decrease the charge on Fe(III) and further reduce the total peroxide-to-iron charge transfer.[35] These results suggest that a μ-1,1 hydroperoxo diiron(III) species may exhibit no optical band in the visible region and is a plausible model for $\text{ToMOH}_{\text{peroxo}}$. In addition to the T201S variant of ToMOH, studies of a RNR-R2 variant (W48A/Y122F) exhibited a novel diiron(III) intermediate having very weak electronic transitions at ~500 nm (ε < ~100 M^{-1} cm^{-1}).[36d] The diiron(III) intermediate (P') is generated from a *cis*-μ-1,2-peroxodiiron(III) species, possibly by the addition of water or a proton to the diiron center;[37] again, protonation of the peroxo unit may substantially alter the LMCT band.

Calculations of Mössbauer parameters support our proposed structure for $\text{ToMOH}_{\text{peroxo}}$. The results indicate that μ-1,1 hydroperoxo diiron(III), but not the deprotonated μ-1,1, *cis*-μ-1,2, or singly-protonated *cis*-μ-1,2 peroxo geometries, can best reproduce the experimentally measured Mössbauer parameters of $\text{ToMOH}_{\text{peroxo}}$.[30] More

---

[d] The Mössbauer spectrum of this intermediate were fit to two quadrupole doublets having δ = ~0.3 and ΔE_Q = ~0.8 and δ = ~0.3 and ΔE_Q = ~1.2, the former of which is similar to those of $\text{ToMOH}_{\text{peroxo}}$.

importantly, the proposed structure of $\text{ToMOH}_{\text{peroxo}}$, μ-1,1 hydroperoxodiiron(III), can form strong hydrogen bonds with T201, which is suggested to be an important factor for generating a distinctive oxygenated intermediate in ToMOH.

Relation between Structure and Reactivity of $\text{ToMOH}_{\text{peroxo}}$. ToMOH specializes in arene oxidation and therefore presumably contains an oxygenated intermediate that is optimized for arene oxidation. To perform aromatic hydroxylation, two-electron transfer from a substrate to this electrophilic oxidant is more favorable than one-electron oxidation or C—H homolysis of the substrate, owing to the high redox potentials and large C—H bond dissociation energies of arenes.[38] A Hammett plot for the oxidation of *para*-substituted phenols in ToMOH exhibits a negative slope, representing the electrophilic character of $\text{ToMOH}_{\text{peroxo}}$.[10] Because protonation of the peroxo-diiron(III) can lead to the enhanced electrophilicity and thus arene-oxidizing reactivity, formation of a μ-1,1-hydroperoxo-diiron(III)-like species in ToMOH may be a consequence of evolution to have enhanced substrate specificity of BMMs.

A proposed mechanism of arene oxidation by $\text{ToMOH}_{\text{peroxo}}$ is represented in Scheme 2.3. Electrophilic attack of the hydroperoxo unit of $\text{ToMOH}_{\text{peroxo}}$ on the arene ring initiates the oxidation, followed by formation of an arene-oxide species that is weakly bound to the diiron center. Addition of water and rearrangement of the transient state can provide the arene product and return the resting state diiron site.

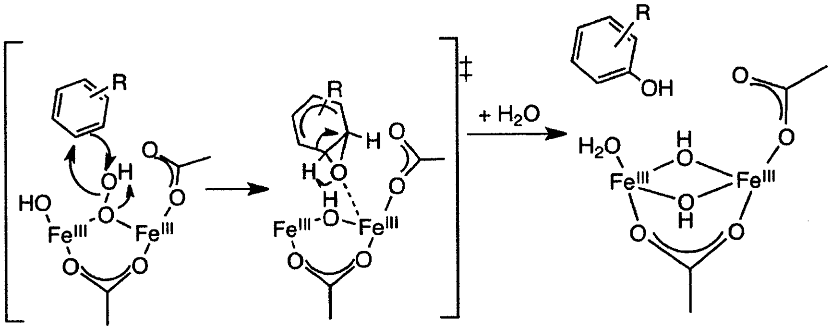

Scheme 2.3 Proposed Chemical Mechanism of Arene Oxidation by $ToMOH_{peroxo}$.

2.4 CONCLUDING REMARKS

We report the first observation of an oxygenated intermediate having an optical band in ToMOH, generated by a single, conservative mutation of the T201 residue. The reaction of the T201S variant of ToMOH with dioxygen generates both $T201_{peroxo}$ and $ToMOH_{peroxo}$, the former being similar to H_{peroxo}. Time-resolved optical and rapid freeze-quench Mössbauer experiments strongly support the assignment of $T201_{peroxo}$ as a peroxodiiron(III) species. Although further studies are required to define the mechanism of dioxygen activation and the role of T201, our results raise the interesting possibility that single amino acid in the vicinity of the active site perturbs the thermodynamics of dioxygen activation at a carboxylate-bridged non-heme diiron enzyme. Further QM/MM and DFT calculation studies suggest that the specific rotamer of the active site threonine of ToMOH and sMMOH is related to their distinct dioxygen reactivity. The structure of $ToMOH_{peroxo}$ is proposed as a μ-1,1 hydroperoxo diiron(III) species based on the absence of an optical band in the visible region and its unique Mössbauer parameters. The proposed structure of $ToMOH_{peroxo}$ is further supported by the hypothesis that the hydrogen bonding interaction between T201 and the active site hydroperoxo may drive the formation of the discrete intermediate, which can exhibit optimized reactivity for arene oxidation.

ACKNOWLEDGEMENTS

I thank Dr. Sunil G. Naik and Prof. Boi Hanh Huynh (Emory University, Atlanta, GA) for their significant contributions to the Mössbauer studies. I thank Dr. Rachel K. Behan (Lippard Lab, MIT) for rapid freeze-quench experiment and helpful discussion. I also thank Prof. J. Stubbe (MIT) for use of her freeze-quench apparatus and Dr. L. J. Murray (MIT) for helpful comments on the manuscript. I also thank Dr. Arteum D. Bochevarov, Jianing Li, and Prof. Richard A. Friesner (Columbia University, New York, NY) for the computational studies.

REFERENCE

1. Wallar, B. J.; Lipscomb, J. D. (1996) *Chem. Rev. 96*, 2625-2657.
2. Solomon, E. I.; Brunold, T. C.; Davis, M. I.; Kemsley, J. N.; Lee, S.-K.; Lehnert, N.; Neese, F.; Skulan, A. J.; Yang, Y.-S.; Zhou, J. (2000) *Chem. Rev. 100*, 235-349.
3. Merkx, M.; Kopp, D. A.; Sazinsky, M. H.; Blazyk, J. L.; Müller, J.; Lippard, S. J. (2001) *Angew. Chem. Int. Ed. 40*, 2782-2807.
4. Lee, S.-K.; Nesheim, J. C.; Lipscomb, J. D. (1993) *J. Biol. Chem. 268*, 21569-21577.
5. Liu, K. E.; Wang, D.; Huynh, B. H.; Edmondson, D. E.; Salifoglou, A.; Lippard, S. J. (1994) *J. Am. Chem. Soc. 116*, 7465-7466.
6. Bollinger, J. M., Jr.; Krebs, C.; Vicol, A.; Chen, S.; Ley, B. A.; Edmondson, D. E.; Huynh, B. H. (1998) *J. Am. Chem. Soc. 120*, 1094-1095.
7. Baldwin, J.; Krebs, C.; Saleh, L.; Stelling, M.; Huynh, B. H.; Bollinger, J. M., Jr.; Riggs-Gelasco, P. J. (2003) *Biochemistry 42*, 13269-13279.
8. Broadwater, J. A.; Ai, J.; Loehr, T. M.; Sanders-Loehr, J.; Fox, B. G. (1998) *Biochemistry 37*, 14664-14671.
9. Pereira, A. S.; Small, W.; Krebs, C.; Tavares, P.; Edmondson, D. E.; Theil, E. C.; Huynh, B. H. (1998) *Biochemistry 37*, 9871-9876.
10. Murray, L. J.; Naik, S. G.; Ortillo, D. O.; García-Serres, R.; Lee, J. K.; Huynh, B. H.; Lippard, S. J. (2007) *J. Am. Chem. Soc. 129*, 14500-14510.
11. Coufal, D. E.; Blazyk, J. L.; Whittington, D. A.; Wu, W. W.; Rosenzweig, A. C.; Lippard, S. J. (2000) *Eur. J. Biochem. 267*, 2174-2185.
12. Sazinsky, M. H.; Bard, J.; Di Donato, A.; Lippard, S. J. (2004) *J. Biol. Chem. 279*, 30600-30610.
13. Rosenzweig, A. C.; Frederick, C. A.; Lippard, S. J.; Nordlund, P. (1993) *Nature 366*, 537-543.
14. Lee, S.-K.; Lipscomb, J. D. (1999) *Biochemistry 38*, 4423-4432.
15. Lovell, T.; Li, J.; Noodleman, L. (2001) *Inorg. Chem. 40*, 5267-5278.
16. Bailey, L. J.; McCoy, J. G.; Phillips, J., George N.; Fox, B. G. (2008) *Proc. Natl. Acad. Sci. U.S.A. 105*, 19194-19198.
17. Cafaro, V.; Scognamiglio, R.; Viggiani, A.; Izzo, V.; Passaro, I.; Notomista, E.; Dal Piaz, F.; Amoresano, A.; Casbarra, A.; Pucci, P.; Di Donato, A. (2002) *Eur. J. Biochem. 269*, 5689-5699.
18. Murray, L. J.; García-Serres, R.; Naik, S.; Huynh, B. H.; Lippard, S. J. (2006) *J. Am. Chem. Soc. 128*, 7458-7459.

19. Gibbs, C. R. (1976) *Anal. Chem. 48*, 1197-1201.
20. Mitchell, K. H.; Studts, J. M.; Fox, B. G. (2002) *Biochemistry 41*, 3176-3188.
21. Tinberg, C. E.; Song, W. J.; Izzo, V.; Lippard, S. J. (2011) *Biochemistry 50*, 1788-1798.
22. Ravi, N.; Bollinger, J. M., Jr.; Huynh, B. H.; Stubbe, J.; Edmondson, D. E. (1994) *J. Am. Chem. Soc. 116*, 8007-8014.
23. Cafaro, V.; Notomista, E.; Capasso, P.; Di Donato, A. (2005) *Appl. Environ. Microbiol. 71*, 4736-4743.
24. Liu, Y.; Nesheim, J. C.; Lee, S.-K.; Lipscomb, J. D. (1995) *J. Biol. Chem. 270*, 24662-24665.
25. Sjöberg, B.-M.; Karlsson, M.; Jörnvall, H. (1987) *J. Biol. Chem. 262*, 9736-9743.
26. Kim, K.; Lippard, S. J. (1996) *J. Am. Chem. Soc. 118*, 4914-4915.
27. Yamashita, M.; Furutachi, H.; Tosha, T.; Fujinami, S.; Saito, W.; Maeda, Y.; Takahashi, K.; Tanaka, K.; Kitagawa, T.; Suzuki, M. (2007) *J. Am. Chem. Soc. 129*, 2-3.
28. Gherman, B. F.; Baik, M.-H.; Lippard, S. J.; Friesner, R. A. (2004) *J. Am. Chem. Soc. 126*, 2978-2990.
29. Rinaldo, D.; Philipp, D. M.; Lippard, S. J.; Friesner, R. A. (2007) *J. Am. Chem. Soc. 129*, 3135-3147.
30. Bochevarov, A. D.; Li, J.; Song, W. J.; Lippard, S. J.; Friesner, R. A. (2011) *J. Am. Chem. Soc. 133*, 7384-7397.
31. Wei, P.-p.; Skulan, A. J.; Mitic, N.; Yang, Y.-S.; Saleh, L.; Bollinger, J. M., Jr.; Solomon , E. I. (2004) *J. Am. Chem. Soc. 126*, 3777-3788.
32. Tong; Chen, S.; Lloyd, S. G.; Edmondson, D. E.; Huynh, B. H.; Stubbe, J. (1996) *J. Am. Chem. Soc. 118*, 2107-2108.
33. Karlin, K. D.; Cruse, R. W.; Gultneh, Y. (1987) *J. Chem. Soc., Chem. Commun.* 599-600.
34. Root, D. E.; Mahroof-Tahir, M.; Karlin, K. D.; Solomon , E. I. (1998) *Inorg. Chem. 37*, 4838-4848.
35. Skulan, A. J.; Brunold, T. C.; Baldwin, J.; Saleh, L.; Bollinger, J. M., Jr.; Solomon , E. I. (2004) *J. Am. Chem. Soc. 126*, 8842-8855.
36. Saleh, L.; Krebs, C.; Ley, B. A.; Naik, S.; Huynh, B. H.; Bollinger, J. M., Jr. (2004) *Biochemistry 43*, 5953-5964.
37. Jensen, K. P.; Bell, C. B.; Clay, M. D.; Solomon , E. I. (2009) *J. Am. Chem. Soc. 131*, 12155-12171.
38. Meunier, B.; de Visser, S. P.; Shaik, S. (2004) *Chem. Rev. 104*, 3947-3980.

Chapter 3.

Role of an Active Site Threonine in the Kinetics of Dioxygen Activation in Toluene/*o*-Xylene Monooxygenase Hydroxylase

* Reproduced in part with permission from the following publication,

Woon Ju Song, Michael S. McCormick, Rachel K. Behan, Matthew H. Sazinsky, Wei Jiang, Jeffery Lin, Carsten Krebs, Stephen J. Lippard "Active Site Threonine Facilitates Proton Transfer during Dioxygen Activation at the Diiron Center of Toluene/*o*-Xylene Monooxygenase Hydroxylase" *J. Am. Chem. Soc.* **2010**, *132,* 13582-13585.

3.1. INTRODUCTION

The role of a strictly conserved threonine residue at the active sites of bacterial multicomponent monooxygenase (BMM) hydroxylases has been discussed for more than a decade.[1-5] In particular, it has been conjectured that the threonine might participate in a hydrogen-bonding network leading from the protein surface to a metal-bound, active dioxygen moiety, facilitating proton transfer required to generate and stabilize oxygenated intermediates. Such speculation for the function of the threonine residue is based in part on analogy to studies of cytochrome P450 monooxygenases (P450), where a similarly positioned threonine in the active site heme pocket facilitates proton transfer to the distal oxygen atom. This event leads to the formation of an oxoiron(IV) porphyrin π-cation radical.[6-9] Replacing the threonine residue with alanine uncouples this process, liberating hydrogen peroxide. Unlike P450, however, few studies of diiron monooxygenases have been conducted in sufficient detail to determine whether the threonine residue does play a role during O_2 activation and, if so, whether it operates in a manner similar to that of P450.

Toluene/*o*-xylene monooxygenase hydroxylase (ToMOH) is a carboxylate-bridged nonheme-diiron enzyme in the BMM family.[10,11] A threonine residue (T201) is located adjacent to the diiron active sites, where dioxygen and hydrocarbons bind. Previous structural studies of ToMOH and toluene 4-monooxygenase hydroxylase (T4moH) revealed the hydroxyl group of T201 to be a part of a hydrogen-bonding network within the active site, involving a glutamate ligand (E231), a coordinated water molecule, and, in complex with the regulatory protein (T4moHD), an ordered water molecule in the cavity.[12,13] Elucidation of a role of the active site threonine in BMMs has been impeded for multiple reasons, however. In particular with ToMOH enzyme, an oxygenated intermediate that is generated upon reaction of the reduced enzyme with O_2, $ToMOH_{peroxo}$, does not absorb in the visible region,[14] hampering the accurate kinetic studies to probe the role the active site threonine residue during O_2 activation. Recent studies of a functionally conservative ToMOH variant (T201S), however, demonstrated that two oxygenated species, $ToMOH_{peroxo}$ and $T201_{peroxo}$, were generated upon the reaction of the reduced hydroxylase and regulatory protein ($ToMOH_{red}D$) with O_2. The latter intermediate exhibits an optical band at ~600 - 800 nm ($\varepsilon_{675\ nm} \approx 1500\ cm^{-1}M^{-1}$) and Mössbauer parameters of $\delta = 0.67$ mm/s and $\Delta E_Q = 1.51$ mm/s.[15] Given the spectroscopic properties of $T201_{peroxo}$, we assign this species as a peroxodiiron(III) intermediate.

Although $T201_{peroxo}$ is not observed in the wild-type enzyme, the oxygenated intermediate can reflect the chemical mechanism of dioxygen activation in ToMOH. Here we report the results of T201 variants of the ToMOH enzyme, T201S, T201C, T201G, and T201V, prepared by site-directed mutagenesis, to elucidate a role of the active site threonine during O_2 activation. We report the X-ray crystal structures, steady-state activity, regiospecificity for toluene and *o*-xylene oxidation, single-turnover yields, and pre-steady state kinetics of dioxygen activation in the T201 variants.

3.2. MATERIALS AND METHODS

General Considerations. Plasmids containing the genes for the toluene/*o*-xylene monooxygenase components were supplied by the laboratory of Professor Alberto Di Donato, Naples, Italy. Heterologous expression and purification of four ToMO component proteins, the hydroxylase (ToMOH), Rieske (ToMOC), reductase (ToMOF), and regulatory (ToMOD) proteins, were carried out as described.[15,16] Conversion of T201 to T201C, T201G, and T201V was performed by site-directed mutagenesis as described previously,[15,17] using a parent pET22b(+)/touBEA plasmid with the following designed primers: 5′-C GAA ACA GGC TTC GGT AAT ATG CAG TTT C-3′ and 5′-G AAA CTG CAT ATT ACC GAA GCC TGT TTC G-3′ for T201G; 5′-C GAA ACA GGC TTC GTT AAT ATG CAG TTT CTC G-3′ and 5′-C GAG AAA CTG CAT ATT AAC GAA GCC TGT TTC G-3′ for T201V; and 5′-CA TTC GAA ACA GGC TTC TGC AAT ATG CAG TTT CTC-3′ and 5′-GAG AAA CTG CAT ATT GCA GAA GCC TGT TTC GAA TG-3′ for T201C. The primers were obtained either from Invitrogen or Integrated DNA Technologies. The sequence of each plasmid was confirmed using five different primers (T7 promoter, T7 terminator, and three custom-ordered from Invitrogen) at the MIT BioPolymers Lab. T201 variants of ToMOH (T201S, T201C, T201G, and T201V) were expressed in E. *coli* and purified using the same procedure as the wild-type protein.[16] Detailed procedures for determinations of iron contents,[18] specific activity[14] and single-turnover yield with phenol,[19] and the regiospecificity of toluene and *o*-xylene oxidation[20] were described previously.

Crystallization, Data collection, Structure Determination, and Refinement. X-ray crystallographic studies of T201X ToMOH were carried out by Dr. Michael S. McCormick (Lippard Lab, MIT), Jeffery Lin (Pomona College, Claremont, CA), and Prof. Matthew H. Sazinsky (Pomona College, Claremont, CA). The crystallization conditions for ToMOH T201X enzymes followed previously published procedures.[12] X-ray diffraction data were collected at the SSRL on beam line 11-1 or 12-2. Phasing of ToMOH T201X data was accomplished by using EPMR and the 1.85 Å native ToMOH coordinates (PDB code 2INC) as described previously.[12] Crystallographic coordinates have been deposited in the

RCSB databank, with accession codes 3N1X, 3N1Y, 3N1Z, and 3N20, for T201C, T201G, T201S, and T201V, respectively.

Mössbauer Sample Preparation. ^{57}Fe-enriched T201G ToMOH samples were prepared as described previously.[15] T201G ToMOH was reduced anaerobically by reacting the protein with excess sodium dithionite in the presence of an equimolar amount of methyl viologen for 30 min. Then, the reduced protein (~600 μM in 25 mM MOPS, pH 7.0 buffer) was dialyzed against 1 L of 25 mM MOPS, pH 7.0 buffer for ~3 hr, anaerobically to remove the reacted/unreacted reducing agents. Following dialysis, 3 equiv of regulatory protein with respect to hydroxylase was added to the reduced ToMOH T201G enzyme. The protein solution was transferred into a Mössbauer cup and rapidly frozen in liquid N_2. To prepare oxygenated samples of the T201G variant, a solution of reduced ToMOH T201G and 3 equiv of ToMOD with respect to hydroxylase was manually mixed with an equal volume of O_2-saturated buffer at 4 °C for 15 s and the reaction was quenched by rapidly spraying the solution into liquid nitrogen. The freeze-quench experiments were performed in collaboration with Dr. Rachel K. Behan (Lippard Lab, MIT). Mössbauer experiments were carried out by Dr. Wei Jiang and Prof. Carsten Krebs (The Penn State University, University Park, PA).

Kinetic Studies of Oxygenated Intermediates of ToMOH T201X Variants (X = S, C, G, V) by Optical Spectroscopy. The optical band of the oxygenated intermediate of the ToMOH T201 variants was monitored by using a HiTech DX2 stopped-flow spectrophotometer, as described previously.[15] T201X ToMOH (~200-300 μM in 25 mM MOPS, pH 7.0) was reduced anaerobically by reacting the protein with excess sodium dithionite in the presence of an equimolar amount of methyl viologen for 30 min. The reduced protein was dialyzed against 1 L of 25 mM MOPS, pH 7.0 buffer for ~3 hr, anaerobically, at room temperature. Following dialysis, 3 equiv of the regulatory protein relative to the hydroxylase was added to the reduced T201X ToMOH sample. The solution was transferred to a tonometer and loaded into the anaerobic stopped flow instrument. This solution was mixed against an equal volume of O_2-saturated 25 mM MOPS, pH 7.0 buffer. The temperature was thermostatted using a circulating water bath. Data were collected using either a PMT (photomultiplier tube) for halogen lamp illumination or a diode array detector for a xenon arc lamp illumination. For experiments in which the O_2 concentration was varied, dioxygen-saturated buffer ($[O_2]$ = ~1.22 mM at 25 °C)[21] was mixed with nitrogen-saturated buffer in an appropriate ratio to dilute the concentration of dioxygen. For experiments in which the pH condition was varied, buffers of varying pH (6.5 - 8.0) were prepared with 25 mM MOPS buffer by adjusting the pH using NaOH or HCl. For kinetic solvent isotope effect (KSIE) measurements, deuterium oxide (99.9%) was purchased from Cambridge Isotope Laboratories or Icon Isotopes and used to prepare 25 mM MOPS buffer, pL 7.0. The pL value was adjusted by adding an appropriate amount of NaOD or DCl (Aldrich) to the solution. Upon varying the reaction conditions, including temperature and pH, no distinguishable differences in the optical feature of $T201_{peroxo}$ were observed. The time-dependent absorbance data were analyzed by the software packages Kinetic Studio (TgK Scientific) and Origin 6.1 (OriginLab Corporation). For reaction of the T201C variant, the best fit was obtained with a three-exponential analytic function, corresponding to $ToMOH_{red} \rightarrow T201_{peroxo} \rightarrow T201^*_{peroxo} \rightarrow ToMOH_{ox}$, where $T201^*_{peroxo}$ and $ToMOH_{ox}$ are the sequential decay products of $T201_{peroxo}$ (eq 3.1). For simplicity, each component, $ToMOH_{red}$, $T201_{peroxo}$, $T201^*_{peroxo}$, and $ToMOH_{ox}$, and their conversion rate constants are represented as A, B, C, and D, and as k_1, k_2, and k_3, respectively.

$$\mathrm{Abs} = [A]_0 *(\varepsilon_D +((\varepsilon_A - \varepsilon_D)*\exp(-k_1*x))+((\varepsilon_B - \varepsilon_D)*k_1*1/(k_2-k_1)*(\exp(-k_1*x)-\exp(-k_2*x)))+((\varepsilon_c-\varepsilon_D)* k_1*k_2*1/(k_2- k_1)*(1/(k_3- \mathrm{k1})*(\exp(-k_1*x)-\exp(-k_3*x))-1/(k_3- k_2)*(\exp(-k_2*x)-\exp(-k_3*x))))) \quad \text{(eq 3.1)}$$

The initial enzyme concentration is defined by $[A]_o$. For dioxygen activation analyses of the T201S and T201G variants, a two-exponential function derived from the model $\mathrm{ToMOH_{red}} \rightarrow \mathrm{T201_{peroxo}} \rightarrow \mathrm{ToMOH_{ox}}$ gave the best fit (eq 3.2). For simplicity, $\mathrm{ToMOH_{red}}$, $\mathrm{T201_{peroxo}}$, and $\mathrm{ToMOH_{ox}}$ and rate constants for the conversion are abbreviated as A, B, and C and k_1 and k_2, respectively.

$$\mathrm{Abs}= \varepsilon_c*[A]_0+(\varepsilon_A-\varepsilon_C)*[A]_0*\exp(-k_1*x)+(\varepsilon_B-\varepsilon_C)*[A]_0*k_1/(k_2-k_1)*(\exp(-k_1*x)-\exp(-k_2*x)) \quad \text{(eq 3.2)}$$

3.3. RESULTS and DISCUSSION

Structural Determination of T201X ToMOH Variants (X = S, C, G, V). X-ray crystal structure determinations of all four T201 variants revealed the absence of any global structural differences or dramatic shift in the geometry of the T201 backbone or side-chain atoms (Table 3.1). The overlaid structures of the wild-type and T201 variants indicate that the diiron(III) cofactors and coordinating ligands are well aligned (Figure 3.1-3.2). The orientation of the hydroxyl group of T201S is identical to that of the wild-type enzyme, suggesting that the T201S variant retains the capacity to form hydrogen-bonding interactions in the active site similar to those in the native protein. In contrast, the hydrophobic side chains of T201G, T201C, and T201V do not participate in hydrogen bonding. One notable feature is rotation about the C_α-C_β bond in both the T201C and

T201V variants, where thiol and methyl groups, respectively, point in the same direction as the methyl group of the wild-type enzyme toward the hydrophobic cavity.

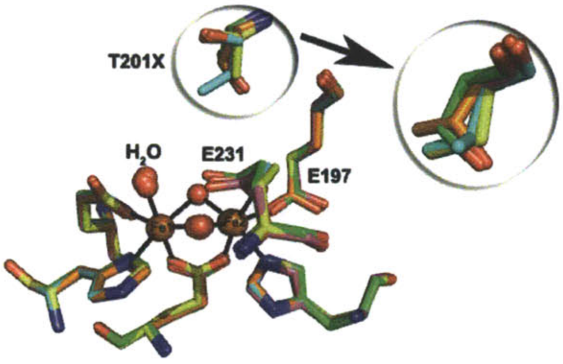

Figure 3.1 Overlaid X-ray crystal structures of ToMOH wild-type (PDB 2INC, orange) and T201X variants: T201S (green), T201G (pink), T201C (yellow), and T201V (cyan). Iron atoms and water/hydroxide ligands are represented as orange and red spheres, respectively. Ligands and T201X residues are depicted as sticks. Nitrogen and oxygen atoms are colored in blue and red, respectively. T201X residues are rotated counter-clockwise and expanded for clarity.

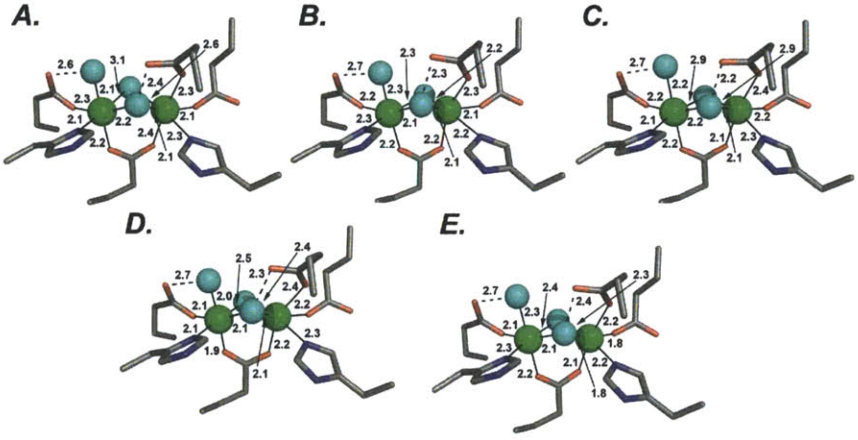

Figure 3.2 Active site coordination and geometry of ToMOH wild-type and T201X variants. (A) ToMOH T201G, (B) T201S, (C) T201V, (D) T201C, (E) wild type (PDB Code 2INC). Iron atoms are displayed as green spheres and solvent and oxygen ligands derived from PEG are shown as cyan spheres. Amino acid side chains are exhibited as sticks in grey (carbon), blue (nitrogen), and red (oxygen). Interatomic distances are represented in angstroms.

Table 3.1 X-ray Data Collection, Phase Determination, and Refinement Statistics of T201X Variants (X = S, G, C, V).

	T201S	T201G	T201C	T201V
Data Collection				
Beamline	SSRL 11-1	SSRL 11-1	SSRL 12-2	SSRL 11-1
Wavelength (Å)	0.979	0.979	0.979	0.979
Space Group	$P3_121$	$P3_121$	$P3_121$	$P3_121$
Unit cell dimensions (Å)	182.8 x 182.8 x 68.9	183.0 x 183.0 x 68.7	183.249 x 183.249 x 68.128	182.9 x 182.9 x 68.6
Resolution range (Å)	50.0 - 2.90	50.0 - 2.10	50-2.4	50.0 - 1.90
Total Reflections	223666	1151797	1539056	1801358
Unique Reflections	29616	74572	48523	98258
Completeness (%)[a]	100 (99.9)	96.7 (92.9)	99.2 (96.8)	95.5 (84.6)
$I/\sigma(I)$[a]	22.7 (7.7)	30.8 (3.8)	11.3 (4.2)	36.8 (2.9)
R_{sym} (%)[a,b]	10.4 (31.2)	10.3 (56.0)	9.3 (48.3)	9.8 (66.0)
Refinement				
R_{cryst} (%)[c]	18.4	22.3	18.4	20.6
R_{free} (%)[d]	22.5	23.5	24.3	21.8
Average B-value ($Å^2$)	19.6	35.6	55.5	33.9
r.m.s deviation bond length (Å)	0.008	0.007	0.031	0.006

r.m.s deviation bond angles (°)	1.54	1.36	2.39	1.36
No. Protein Atoms	7337	7335	7370	7338
No. Non-Protein Atoms	159	248	164	699
Fe Atoms	2	2	2	2
Water Molecules	101	196	152	597
PEG-400 Fragments	2	2	1	4
Glycerol Molecules	3	2	0	4
RMSD to Wild-Type ToMOH	0.170	0.136	0.178	0.114
PDB Code	3N1Z	3N1Y	3N1X	3N20

[a] Values in parentheses are for the highest resolution shell. [b] $R_{sym} = \Sigma_i\Sigma_{hkl}|I_i(hkl) - \langle I(hkl)\rangle| / \Sigma_{hkl}\langle I(hkl)\rangle$, where $I_i(hkl)$ is the *i*th measured diffraction intensity and $\langle I(hkl)\rangle$ is the mean intensity for the Miller index (*hkl*). [c] $R_{cryst} = \Sigma_{hkl}||F_o(hkl)| - |F_c(hkl)|| / \Sigma_{hkl}|F_o(hkl)|$. [d] $R_{free} = R_{cryst}$ for a test set of reflections (5% in each case).

Reactivity of Arene Oxidation in T201X ToMOH Variants. The steady-state activity of the T201 variants was measured using phenol as a substrate (Table 3.2). The maximum product formation rates, given by the specific activity, are comparable for all T201 variants, ranging from ~0.3 to 2.2 times the wild-type activity. Michaelis-Menten kinetics of the T201 variants were also determined (Table 3.2 and Figure 3.3). The catalytic rate constants (k_{cat}) for all T201 variants are similar to those of the wild type, indicating that substitution of the T201 side chain does not significantly perturb the maximum efficiency for aromatic hydroxylation. In contrast, substrate specificity, as revealed by $k_{\text{cat}}/K_{\text{M}}$, is diminished by about 2 orders of magnitude for the T201G, T201C, and T201V variants relative to those of the wild-type and T201S variant. This result suggests that T201S is a functionally conserved variant, as described previously,[15] and that the lack of a hydroxyl group at the T201 position perturbs at least one step during catalysis. A similar effect was observed for T4moH[5] and for P450[6-9] when the analogous threonine residues were replaced with alanine. In addition, single turnover yields of T201G, T201C, and T201V were significantly reduced from those of the wild-type and the T201S variant (Table 3.2), implicating a critical role of having a hydroxyl group at the T201 position.

The regiospecificity for phenol oxidation in the T201 variants does not change, as all variants produced catechol exclusively. For toluene oxidation, however, the T201C, T201V, and T201G variants exhibit significant changes in product distribution (Table 3.3). These results indicate that the T201 substitutions reshape the substrate-binding pocket, altering the orientation of substrate in the active site. The T201 variants also gave different product distributions for *o*-xylene oxidation. The ratio of the two products, 2,3-dimethylphenol and 3,4-dimethylphenol, reflects the steric environment at the T201 sites, with the bulkier side chains conveying a higher ratio of 3,4-dimethylphenol vs 2,3- dimethylphenol. This finding suggests that the side chain of the T201 residue may guide and orient hydrocarbon substrates as they enter the diiron active site. It is plausible that the side chain of the T201 residue also interacts with dioxygen, a co-substrate, during catalysis.

Table 3.2 Steady-State Activity and Single-Turnover Yields of T201X Variants of ToMOH for Phenol Oxidation (X = S, C, G, V).

	wild-type	T201S	T201G	T201C	T201V
Specific activity (mU/mg)	1100 ± 100	2400 ± 300	1900 ± 200	1600 ± 200	390 ± 20
k_{cat} (s^{-1})	0.04 ± 0.01	0.08 ± 0.04	0.08 ± 0.02	0.09 ± 0.02	0.016 ± 0.009
k_{cat}/K_M	0.02 ± 0.01	0.017 ± 0.009	$(2.0 \pm 0.9) \times 10^{-4}$	$(2,8 \pm 0.8) \times 10^{-4}$	$(1.3 \pm 0.9) \times 10^{-4}$
Single-turnover yields per diiron sites (%)	56 ± 7	59 ± 6	33 ± 8	26 ± 1	27 ± 9

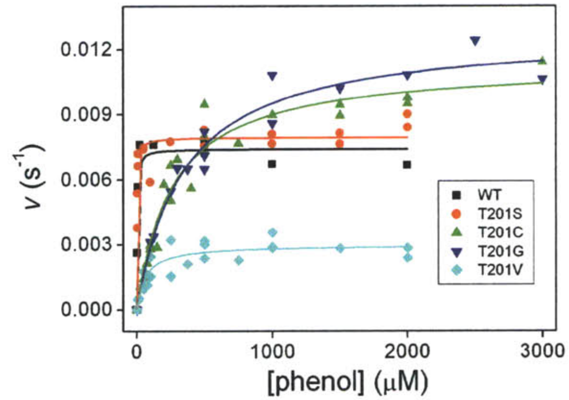

Figure 3.3 Michaelis-Menten kinetic profiles of ToMOH wild-type and T201X variants for phenol oxidation.

Table 3.3 Product Distribution of ToMOH T201X Variants in Toluene and *o*-Xylene Oxidation (X = S, C, G, V).

toluene oxidation					
	wild-type	T201S	T201C	T201G	T201V
o-cresol (%)	30 ± 2	31 ± 1	32 ± 1	59 ± 1	18 ± 1
m-cresol (%)	21 ± 1	16 ± 0	27 ± 1	13 ± 1	32 ± 1
p-cresol (%)	47 ± 1	51 ± 1	36 ± 1	25 ± 1	37 ± 1
benzyl alcohol (%)	2 ± 1	2 ± 1	4 ± 1	3 ± 1	12 ± 1
o-xylene oxidation					
2,3-dimethyl phenol (%)	19	36	32	64	15
3,4-dimethyl phenol (%)	81	64	68	36	85
2-methyl benzyl alcohol (%)	nd[a]	nd[a]	nd[a]	nd[a]	nd[a]

[a] Not detected.

Single-Mixing Stopped-Flow UV-Vis and Mössbauer Studies of Dioxygen Activation in the T201X Variants of ToMOH and ToMOD. A premixed solution of T201 variants of reduced ToMOH and ToMOD ($\mathrm{ToMOH_{red}D}$) was treated with O_2-saturated buffer and monitored by freeze-quench Mössbauer and stopped-flow UV-vis spectroscopy. Two of the variants, T201G and T201C, also exhibit broad, transient optical features that absorb maximally at $\Delta\lambda$ = ~675 nm (Figure 3.4), which are identical to those observed for the T201S variant.

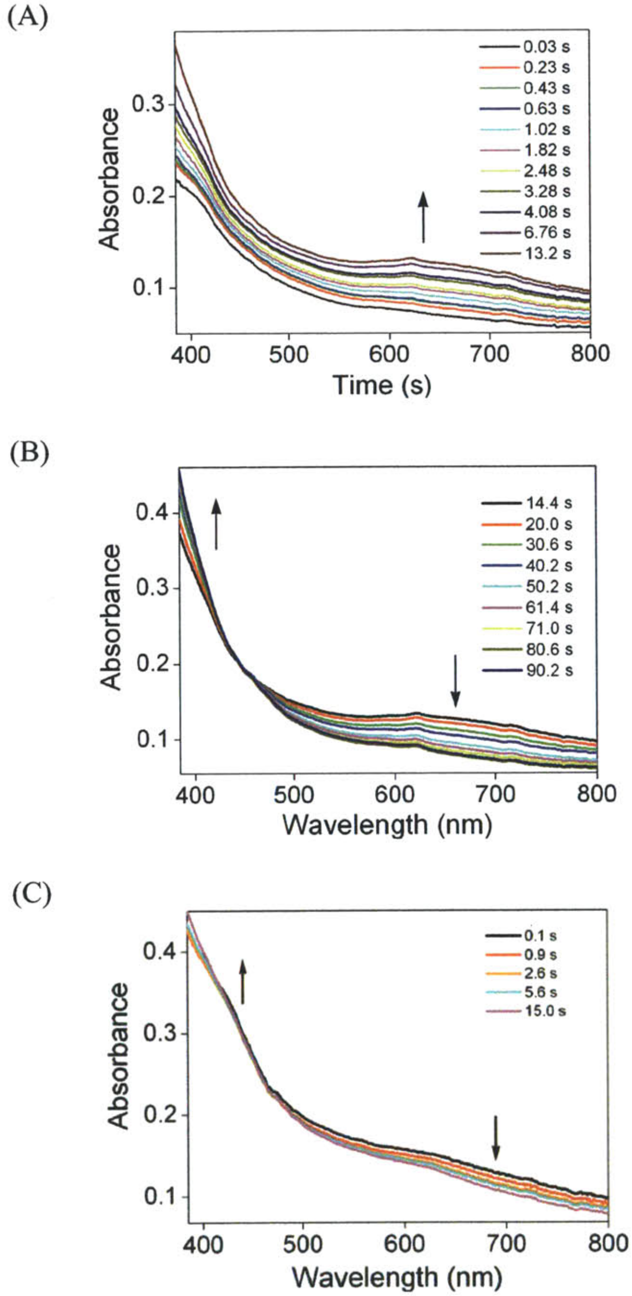

Figure 3.4 Absorption changes in the reaction of T201X ToMOH$_{red}$ and ToMOD with dioxygen-saturated buffer (X = C, G). [ToMOH$_{red}$ T201X] = ~150 μM, [ToMOD] = 450 μM in 25 mM MOPS, pH 7.0 at 4.0 ± 0.1 °C. (A) Time-dependent formation of ToMOH. (B) Time-dependent decay of T201$_{peroxo}$ in ToMOH T201G (C) Time-dependent decay of T201$_{peroxo}$ in ToMOH T201C at various reaction times.

The Mössbauer spectrum of a sample of T201G ToMOH$_{red}$ and ToMOD, which was allowed to react for 15 s with O_2, the time of maximum accumulation of the 675 nm feature observed by stopped-flow UV-vis spectrophotometry, reveals the presence of a quadrupole doublet with parameters nearly identical to those reported for T201$_{peroxo}$ in T201S ToMOH. This feature accounts for ~10% of the total iron absorbance (Figure 3.5).[1] Based on single-mixing stopped-flow and Mössbauer studies of dioxygen activation in the T201C and T201G variants, we conclude that the optical changes at ~675 nm observed in the T201 variants (T201S/C/G) originate from formation and decay of an identical species, T201$_{peroxo}$. The Mössbauer spectrum of T201G variant also exhibited ToMOH$_{peroxo}$, which accounts for ~10% of total iron. Formation of the two oxygenated intermediates suggests that the mechanism of dioxygen activation is conserved in T201S, T201C, and T201G variants.[15] No optical bands, however, appeared in the UV-vis region upon the addition of O_2 to the T201V variant of ToMOH$_{red}$D.

---

[1] The spectrum also reveals the presence of other diiron(III) species that amount to 35 ± 7% of the total intensity of the spectrum and the identity of the species is not understood.

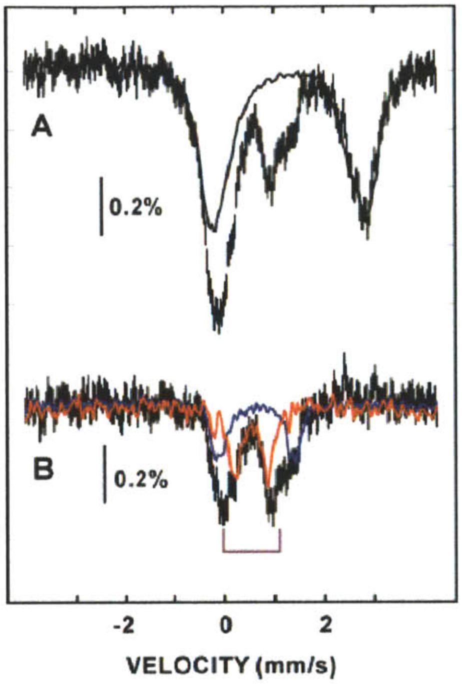

Figure 3.5 4.2-K/53-mT Mössbauer spectra of dioxygen activation in T201G variant of ToMOH. (A) Spectrum of an anaerobic solution of T201G $ToMOH_{red}D$ ($[^{57}Fe]/[ToMOH]$ = 3.9 ± 0.1, 600 μM of ToMOH and 1.8 mM ToMOD), which was mixed at 4°C with an equal volume of an O_2-saturated buffer solution for ca. 15 s before manual freezing of the sample (vertical bars). The spectrum of an anaerobic control sample is overlaid as a solid line and is scaled to account for 63% of the total intensity of the spectrum of the 15-s sample. (B) Removal of the features of the anaerobic complex results in the "reference spectrum" of the diiron(III/III) complexes in T201G reduced ToMOH and ToMOD after a 15 s reaction time (vertical bars). Comparison of this spectrum to experimental reference spectra of $T201_{peroxo}$ (blue line) and $ToMOH_{peroxo}$ (red line), which were prepared by removal of the respective three other quadrupole doublets from the difference spectrum described in the left panel, reveals that ~10% of each species is present in the 15 s sample of the T201G reduced ToMOH and ToMOD complex. In addition, there is additional broad absorption observed (purple bracket), which emanates from a quadrupole doublet with parameters [$\delta \approx 0.5$ mm/s and $\Delta E_Q \approx 1.1$ mm/s] typical of high-spin Fe(III) and is assigned to one or more additional diiron(III/III) complexes.

Kinetic Studies of $T201_{peroxo}$ in the T201X Variants of ToMOH. To further characterize the O_2 activation reactions in the T201 variants of ToMOH and to understand which chemical step in this process may be perturbed by the T201 substitution, premixed solutions of T201X $ToMOH_{red}D$ were reacted with O_2-saturated buffer under various reaction conditions and monitored by stopped-flow UV-vis spectroscopy. The kinetics of $T201_{peroxo}$ formation and decay in the three T201 variants (T201S/C/G) were investigated by monitoring the time-dependence of the absorption at 675 nm. The formation and decay rates of $T201_{peroxo}$ in T201C variant were best fit to three consecutive, irreversible processes: $ToMOH_{red} \rightarrow T201_{peroxo} \rightarrow T201^{*}_{peroxo} \rightarrow ToMOH_{ox}$, where $T201^{*}_{peroxo}$ and $ToMOH_{ox}$ are two sequential decay products of $T201_{peroxo}$ (Figure 3.6A). For T201G, the traces were fit to a model describing two consecutive, irreversible reactions, as noted previously for the T201S variant: $ToMOH_{red} \rightarrow T201_{peroxo} \rightarrow ToMOH_{ox}$ (Figure 3.6B).[15] Results of these kinetic studies are summarized in Table 3.4. The formation rate constant of $T201_{peroxo}$ in T201C is nearly identical to that of the T201S variant. The formation rate constant in the T201G variant, however, is ~700 times lower than that in the T201S variant. The similarity in formation rates of $T201_{peroxo}$ in T201S and T201C variants implies that the thiol group of T201C may function like a hydroxyl group, at least during formation of $T201_{peroxo}$. In contrast, the lack of a functional group in the T201G variant dramatically reduces the rate of $T201_{peroxo}$ formation. This striking difference indicates that the rate-determining step for $T201_{peroxo}$ formation is greatly perturbed by the identity of the amino acid at position T201 and that this residue is critically involved in controlling the kinetics of dioxygen activation.

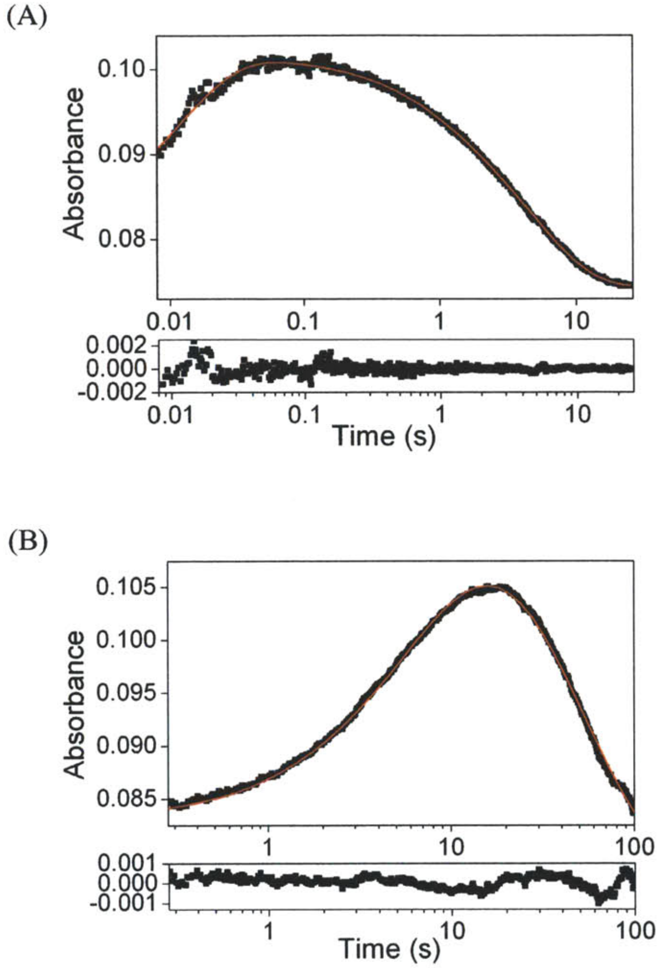

Figure 3.6 Representative time-resolved stopped-flow absorption changes at 675 nm in the reaction of reduced T201X ToMOH and ToMOD (~150 μM and 450 μM, respectively) with O_2-saturated buffer at 4 °C. (A) X= T201C. (B) X = T201G variant. The formation and decay traces of $T201_{peroxo}$ (black dots) were fit as described in the experimental section (red solid line). The best fit in T201C enzyme gave the following parameters: $\varepsilon_{ToMOHred} = 527 \pm 4$ $cm^{-1}M^{-1}$, $\varepsilon_{T201peroxo} = 663.1 \pm 0.3$ $cm^{-1}M^{-1}$, $\varepsilon_{T201peroxo}{}^{*} = 609 \pm 3$ $cm^{-1}M^{-1}$, $\varepsilon_{ToMOHox} = 486.3 \pm 0.5$ $cm^{-1}M^{-1}$, $k_1 = 82 \pm 2$ s^{-1}, $k_2 = 1.2 \pm 0.1$ s^{-1}, and $k_3 = 0.204 \pm 0.004$ s^{-1} when the initial concentration of the enzyme, $[ToMOH_{red}]_0$, set to 0.00015 M, was assumed to be equal to the concentration of $T201_{peroxo}$ generated in the reaction ($R^2 = 0.998$). The best fit in T201G variant gave the following parameters: $\varepsilon_{ToMOHred} = 593.0 \pm 0.4$ $cm^{-1}M^{-1}$, $\varepsilon_{T201peroxo} = 826 \pm 2$ $cm^{-1}M^{-1}$, $\varepsilon_{ToMOHox} = 558 \pm 3$ $cm^{-1}M^{-1}$, $k_1 = 0.128 \pm 0.002$ s^{-1}, and $k_2 = 0.0209 \pm 0.0007$ s^{-1} when $[ToMOH_{red}]_0$, was set to 0.00014 M ($R^2 = 0.996$). The estimated value for $\varepsilon_{T201peroxo}$ in the kinetic analysis is lower than we have previously determined from the combination of the UV-vis and Mössbauer spectra (~1500 $cm^{-1}M^{-1}$), possibly because of the bifurcated process that not all of $ToMOH_{red}$ is converted to $T201_{peroxo}$ species.

Table 3.4 Formation and Decay Rate Constants of T201$_{\mathrm{peroxo}}$ in the Reaction of Reduced T201X ToMOH and ToMOD with Dioxygen. [a]

	k_{form} (s^{-1})	k_{decay} (s^{-1})
T201S	130 ± 7[b]	2.9 ± 0.2
T201C	93 ± 3	1.9 ± 0.2 0.23 ± 0.03
T201G	0.11 ± 0.01	0.035 ± 0.003
T201V	nd[c]	nd[c]

[a]Reactions were observed by stopped-flow optical spectrophotometry in 25 mM MOPS pH 7.0 buffer at 4 °C. [b]This value differs slightly from the previously reported value of 85 ± 11 s^{-1}. This difference is thought to be due to variance within different batches of purified protein. [c]Not determined.

This result also suggests why no T201$_{\mathrm{peroxo}}$ was observed for the T201V variant. The lack of a hydrogen-bonding residue in the T201 position retards a key chemical step involved in formation of T201$_{\mathrm{peroxo}}$, presumably proton transfer. At present we cannot rule out the possibility that T201$_{\mathrm{peroxo}}$ is not generated in the T201V enzymes due to changes in the thermodynamic stability of the oxygenated species. For T201G, formation of T201$_{\mathrm{peroxo}}$ was observed because a solvent-derived proton can be situated in the active site and serve as a hydrogen-bonding residue, although this interaction is probably not as strong as hydroxyl group at T201 site. Presumably, there is room for such in the active site of T201G variant but not in the T201V variant of ToMOH.

Kinetic Studies of T201$_{\mathrm{peroxo}}$ in the T201S Variant of ToMOH under Various Reaction Conditions. To elucidate the mechanism of T201$_{\mathrm{peroxo}}$ formation and the role of the T201 residue in this process, kinetic studies were performed at variable temperature, variable O_2 and H^+ concentrations, and with D_2O as solvent. When the dioxygen concentration was varied in its reaction with T201S variant of ToMOH$_{\mathrm{red}}$D, the formation rate constants (k_{form}) were linearly proportional to [O_2], yielding a second-order rate constant of $k_2 = 0.22 \pm 0.01$ $s^{-1}\mu M^{-1}$ (Figure 3.7A, black squares). The results demonstrate that T201$_{\mathrm{peroxo}}$ is generated in an irreversible process and that formation of T201$_{peroxo}$ is kinetically limited by the bimolecular reaction between ToMOH$_{red}$ and O$_2$. From these data, k_{form} of T201$_{peroxo}$ in the T201S enzyme can be represented as $k[O_2]$ ($k_{form} \approx k[O_2]$). To our knowledge, this behavior reveals the first example where dioxygen has been determined to be rate-limiting in a pre-steady-state reaction of any BMM hydroxylase.

(A)

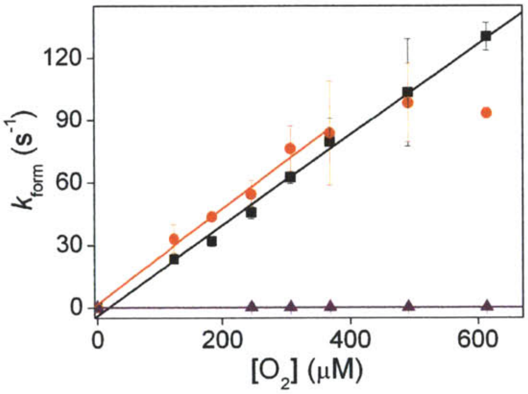

(B)

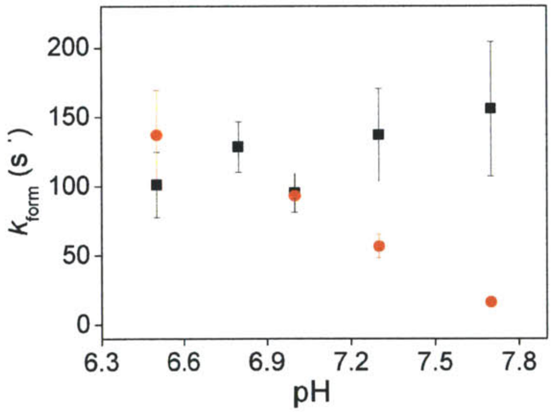

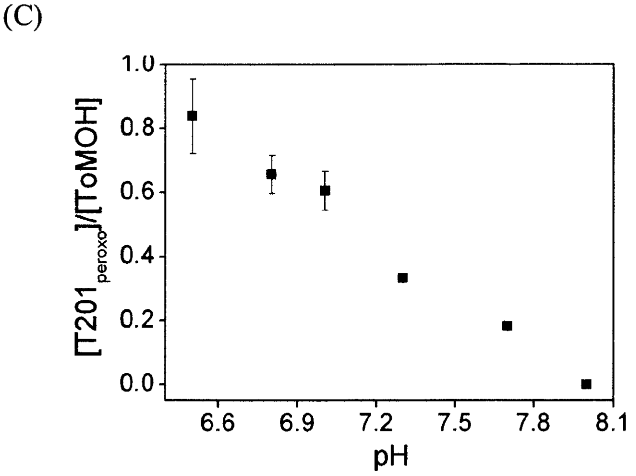

Figure 3.7 Formation rates and the concentrations of T201$_{peroxo}$ in T201 variants of ToMOH. (A) Formation rates of T201$_{peroxo}$ measured in the reactions of T201S (black squares), T201C (red circles), and T201G (purple triangles) with varying O_2 concentrations. (B) Formation rates of T201$_{peroxo}$ in T201S (black squares) and T201C (red circles) under various pH values. (C) The ratio of T201$_{peroxo}$ to total protein concentration formed in the reaction of T201S with O_2 under various pH values.

This interpretation is strongly supported by the negative value of $\Delta S^{\ddagger}$, -71 ± 2 J mol^{-1}K^{-1} (Figure 3.8A). We therefore conclude that chemical steps during O_2 activation, such as structural rearrangements in the active site, component interactions, and water/proton translocation, occur much more rapidly than the associative reaction with dioxygen.

The rate constants for T201$_{peroxo}$ formation at various pH values (Figure 3.7B, black squares) and in D_2O were also measured. From pH 6.5 to 7.7, the formation rate constant does not change significantly. When the buffer was prepared with deuterium oxide (pL 7.0 at 5 °C), the kinetic solvent isotope effect (KSIE) was 0.92 ± 0.11, consistent with our hypothesis that proton translocation is not kinetically involved in this process.

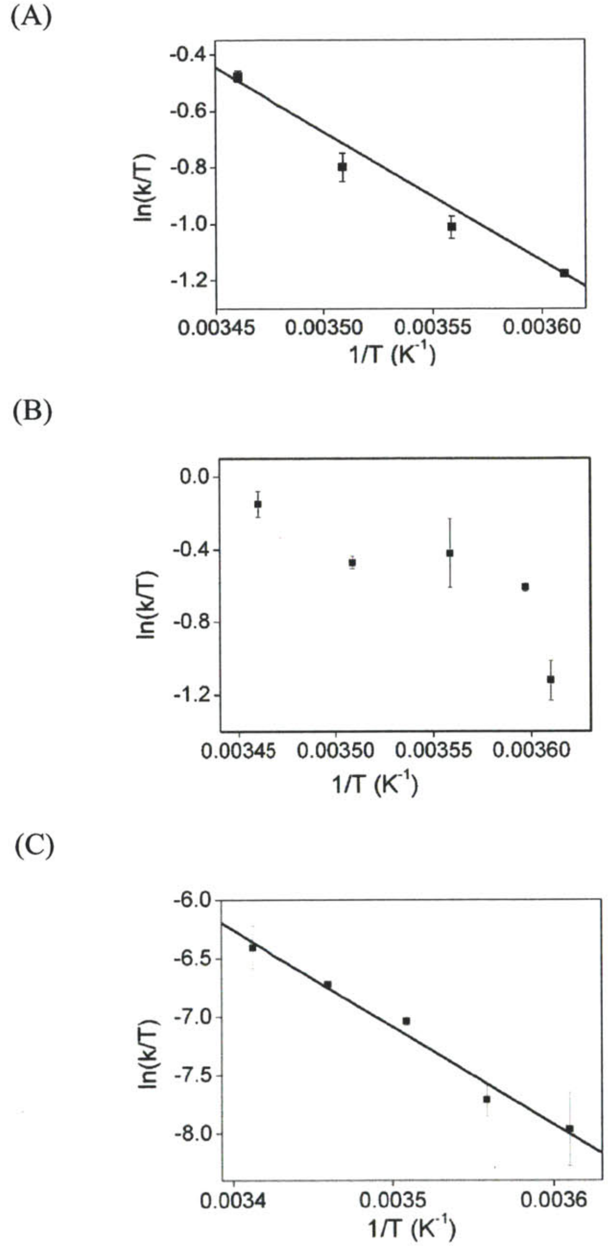

Figure 3.8 Eyring plots of the formation rates of T201$_{peroxo}$ in T201 variants. (A) T201S (B) T201C (C) T201G Time-resolved stopped-flow absorption spectra at 675 nm monitoring the reaction of reduced T201X ToMOH and ToMOD (~150 μM and 450 μM, respectively) with O_2 saturated buffer. Data were collected between 4 and 20 °C. Data for the T201S and T201G variants were linearly fit to measure activation parameters, $\Delta H^{\ddagger}$ = 37.7 kJ mol^{-1} and $\Delta S^{\ddagger}$ = -71.2 J mol^{-1}K^{-1} for T201S and $\Delta H^{\ddagger}$ = 68.4 kJ mol^{-1} and $\Delta S^{\ddagger}$ = -35.7 J mol^{-1}K^{-1} for T201G variant.

Proton transfer is, however, indispensable to the formation of $\text{T201}_{\text{peroxo}}$. By fitting the time-resolved optical spectra to the model $\text{ToMOH}_{\text{red}} \rightarrow \text{T201}_{\text{peroxo}} \rightarrow \text{ToMOH}_{\text{ox}}$ using the measured molar absorptivity of $\text{T201}_{\text{peroxo}}$ from the UV-vis and Mössbauer data, we can estimate the concentration of $\text{T201}_{\text{peroxo}}$ generated from the reaction of $\text{ToMOH}_{\text{red}}$ with dioxygen.[2] The fraction of $\text{T201}_{\text{peroxo}}$ formed compared to total protein then can be calculated (Figure 3.7C). When the ratio was measured under various pH conditions, more $\text{T201}_{\text{peroxo}}$ was generated at higher proton concentrations, indicating that proton transfer is coupled to dioxygen consumption, although it is not observed kinetically.

Kinetic Studies of $\text{T201}_{\text{peroxo}}$ in the T201C Variant of ToMOH under Various Reaction Conditions. For the T201C variant, the $\text{T201}_{\text{peroxo}}$ formation rate constants vary linearly with $[O_2]$ over the range of ~150 - 400 μM. At higher O_2 concentrations, however, a plateau is reached (Figure 3.7, red circles). The partial O_2-dependence of $\text{T201}_{\text{peroxo}}$ formation indicates that the rate is not simply limited by dioxygen diffusion to the active site ($k_{\text{form}} \neq k[O_2]$). Reactions not involved in the rate-determining step for the T201S variant are slowed solely due to the T201S → T201C mutation. $\text{T201}_{\text{peroxo}}$ formation rate constants for the T201C enzyme display nonlinear Eyring behavior over a temperature range of 4 - 16 °C (Figure 3.8B). This nonlinearity could arise from a temperature-dependent combination of multiple processes rather than a simple associative reaction between the hydroxylase and O_2. The formation rate constant depends on pH, indicating that higher proton concentrations accelerate the formation of $\text{T201}_{\text{peroxo}}$ (Figure 3.7B, red circles). These results reveal that the rate-determining step of $\text{T201}_{\text{peroxo}}$ formation in the T201C variant

---

[2] The estimated concentration of $\text{T201}_{\text{peroxo}}$ is not the same as the accumulated amount of the intermediate because the latter value is determined by the combination of both formation and decay rate constants as well as the population of $\text{ToMOH}_{\text{red}}$ converted to $\text{T201}_{\text{peroxo}}$, whereas the former value is irrespective of the rate constants.

changes from that in the T201S variant, possibly reflecting a combination of O_2 association and proton-transfer events.

Kinetic Studies of T201$_{\text{peroxo}}$ in the T201G Variant of ToMOH under Various Reaction Conditions. The T201G mutation evoked an even more substantial effect on the T201$_{\text{peroxo}}$ formation kinetics. The rate constants displayed no dependence on O_2 concentration over a range of ~150 – 612 μM (Figure 3.7A, purple triangles). The $\Delta S^{\ddagger}$ value of -35 ± 3 J mol^{-1} K^{-1} for T201$_{\text{peroxo}}$ formation is significantly less negative than for the T201S mutant (Figure 3.8C). These data indicate that formation of T201$_{\text{peroxo}}$ in T201G variant is controlled by a different chemical step than occurs in the T201S enzyme (see above). The KSIE value for the formation process in T201G ToMOH is 5.7 ± 0.7, indicating that generation of T201$_{\text{peroxo}}$ is limited by a requisite proton translocation step ($k_{\text{form}} \approx k[\text{H}^+]$). The large KSIE value observed for the T201G enzyme implies that more than one proton translocation is involved in the rate-determining step of T201$_{\text{peroxo}}$ formation.[22] These studies demonstrate that chemical steps representing T201$_{\text{peroxo}}$ formation are altered by substitution of T201 in ToMOH.

Comparison of the Rate-Determining Step of Dioxygen Activation in the T201 Variants of ToMOH. We can assume that an associative reaction between dioxygen and the diiron center probably occurs at the same rate ($k[O_2]$) for all T201 variants, given that T201 mutants retain the overall structure and arene-oxidizing reactivities. For T201S, this step is rate-limiting because proton transfer is rapid ($k_{\text{form}} \approx k[O_2]$). For T201C and T201G, proton transfer is the slow step and is followed by more rapid O_2 binding. Removal of the hydroxyl group at the T201 position disturbs the formation rates of T201$_{\text{peroxo}}$ by retarding proton transfer ($k_{\text{form}} \approx k[\text{H}^+]$). These data support the long-standing hypothesis that the hydroxyl group at residue T201 plays a major role in the facilitation of proton transfer during O_2 activation in ToMOH and most likely all BMMs hydroxylases. On the basis of the pre-steady-state kinetics of T201$_{peroxo}$ in the T201 variants, we propose a chemical mechanism for dioxygen activation (Scheme 3.1).

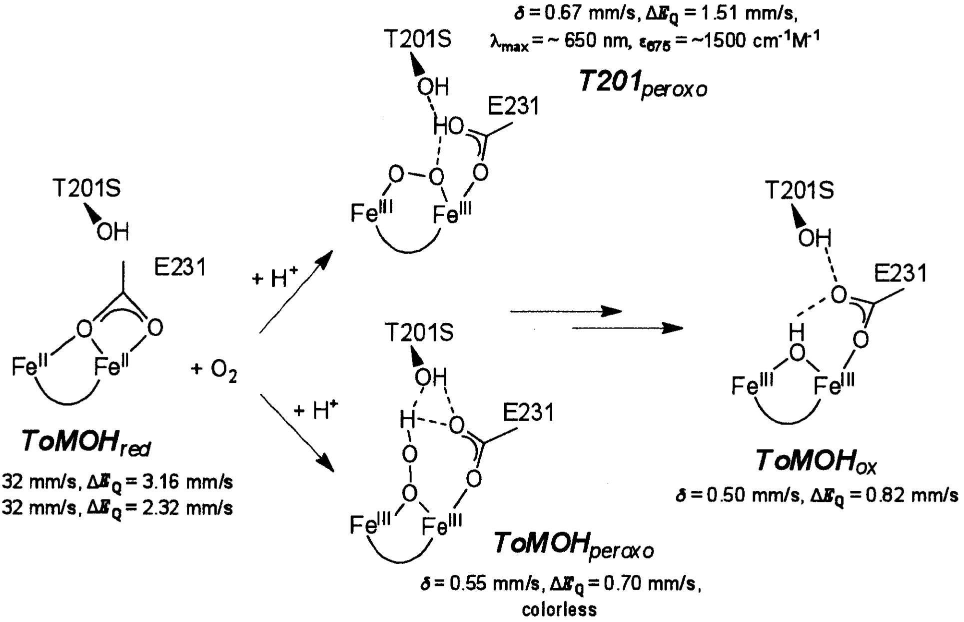

Scheme 3.1 Proposed Mechanism of Dioxygen Activation in the T201 Variants of ToMOH. Possible hydrogen bonds between T201, E231, and oxygenated intermediates are represented as dotted lines. A water molecule might be positioned between the side chains of residues T201 and E231.

Consumption of dioxygen is coupled to proton transfer into the active site, followed by formation of T201$_{peroxo}$. Protonation of the peroxo unit of T201$_{peroxo}$, however, is unlikely because it would quench the peroxo-to-iron charge transfer optical band.[23] Instead, we postulate that the proton is transferred to the adjacent and shifting glutamate residue (E231), a process was recently demonstrated in a synthetic diiron model complex.[24] Consequently, proton-assisted dissociation of the E231 bridging oxygen atom may accompany O_2 binding and activation at the diiron center. Further kinetic studies of diiron modeling complexes support the assignment of E231 as the protonation site, where reorganization of a shifting carboxylate is determined to be a rate-determining step during dioxygen activation.[25] This hypothesis is also supported by the fact that both BMMs and Δ^9D contain an active site threonine residue and both display a similar carboxylate shift.[26] Therefore, this interplay could be a global feature of diiron-containing enzymes featuring an analogous active site threonine residue.

The protonation at E231 could then form a hydrogen bond to an adjacent oxygen atom of T201$_{\mathrm{peroxo}}$, possibly a μ-1,2-peroxodiiron(III) unit[27-29] In contrast, proton transfer directly to the peroxo moiety could lead to the formation of ToMOH$_{\mathrm{peroxo}}$, which exhibits no optical bands. A μ-1,1-hydroperoxodiiron(III) geometry has been proposed as the structure of ToMOH$_{\mathrm{peroxo}}$ on the basis of QM/MM, DFT, and Mössbauer computational studies.[30] Given that the proposed structure of ToMOH$_{\mathrm{peroxo}}$ requires a proton during dioxygen activation, we suggest that the proposed role of T201 is operative in the native enzyme during dioxygen activation.

The decay rate of T201$_{\mathrm{peroxo}}$ is also significantly altered for the T201 variants (Table 3.4). The decay rates decrease in the same order as the formation rates. Because the primary decay pathway of ToMOH$_{\mathrm{peroxo}}$ in the absence of hydrocarbon substrates is protonation of the peroxo unit and subsequent release of hydrogen peroxide,[14] the decay rates for the T201 variants may be also related to their abilities to facilitate proton transfer. The reactivity and decay mechanism of T201$_{\mathrm{peroxo}}$ is discussed in the following chapter (Chapter 4).

In addition to the process of dioxygen activation, proton transfer also occurs in ToMOH during the reduction of the resting state of the enzyme, presumably via proton coupled electron transfer (PCET).[31] Given that proton translocation during dioxygen activation is facilitated by the active site threonine residue in association with a shifting glutamate (E231), the PCET process at diiron centers might be also regulated by the interplay of the residues. Structures of T201A variant of T4moH supported the hypothesis on the role of T201 residue. Whereas reduction of the diiron sites of the wild-type enzyme triggers a conformational change of E231 from monodentate to bidentate ligand, T201A variant of T4moH revealed no such redox-dependent coordination change at E231,[5] suggesting that the hydroxyl group at T201 is essential for the orchestrated motion of the active sites both in reduction and dioxygen activation steps.

Proposed Proton Translocation Pathway of ToMOH and a Common Role of an Active Site Threonine Residue during Dioxygen Activation. The role of the active site threonine residue evaluated here and the extended hydrogen bonding network near the diiron center suggest that the proton transfer pathway of ToMOH and T4moH is reminiscent to that of P450 (Figure 3.9). Although the active site structures and substrate specificity of ToMOH/T4moH and P450 are very different, the strikingly similar role of their active site threonine residues indicates that a shared mechanism may apply to various metalloenzymes.

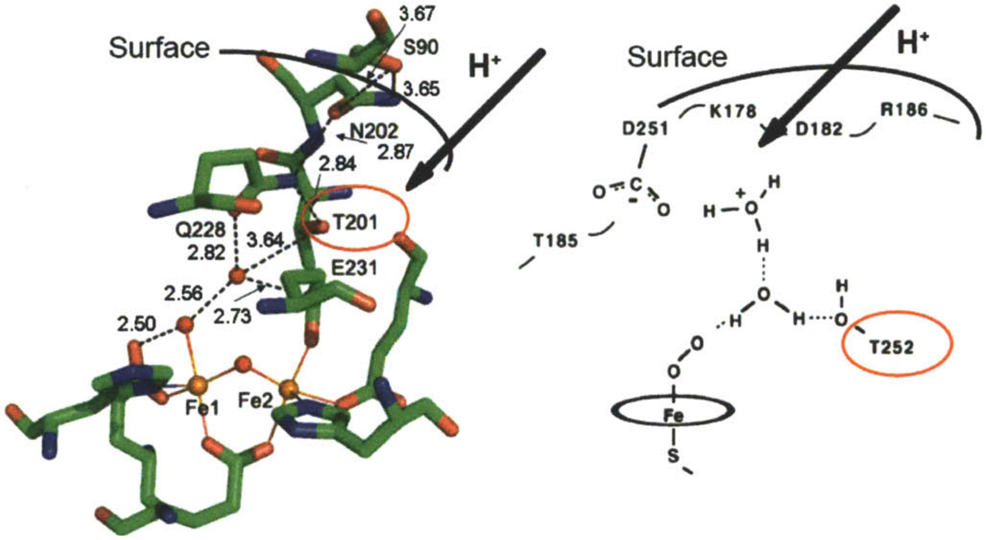

Figure 3.9 Proposed proton translocation pathway of T4moHD (PDB 3DHI) (left) and the analogous hydrogen-bonding network of P450 (PDB 1DZ4, ref 22) (right). Carbon, nitrogen, and oxygen atoms in the T4moHD structure are represented by green, blue, and red sticks. Diiron atoms and coordinated water/hydroxide molecules are depicted by orange and red spheres. Active site threonine residues are highlighted with red circles. The proposed hydrogen bonding networks adjacent to T201 in TMOH and T252 in P450 are displayed with dotted lines. Proton access from bulk solvent to the active sites is represented by black arrows.

3.4. CONCLUDING REMARKS

Steady-state activity, single-turnover yields, and pre-steady-state kinetic studies of several T201 variants of ToMOH support the long-standing but previously untested hypothesis that the threonine hydroxyl group in the active site plays a major role in catalysis. Kinetic studies of $\mathrm{T201_{peroxo}}$ in the T201 variants conducted under pre-steady-state conditions explicitly demonstrate that the threonine residue controls the formation and decay rates of $\mathrm{T201_{peroxo}}$ by facilitating proton translocation during dioxygen activation. The role of T201 in ToMOH that we have uncovered here is analogous to that of threonine near the active site of P450, supporting that Nature uses active site threonine residues to control proton transfer reactions.

ACKNOWLEDGEMENTS

I thank Dr. Michael S. McCormick (Lippard Lab, MIT), Jeffery Lin (Pomona College, Claremont, CA), and Prof. Matthew H. Sazinsky (Pomona College, Claremont, CA) for the X-ray crystallographic studies. I also thank Dr. Rachel K. Behan (Lippard Lab, MIT) for freeze-quench experiment and helpful discussion. I also thank Dr. Wei Jiang and Prof. Carsten Krebs (The Penn State University, University Park, PA) for their significant contributions to the Mössbauer studies.

REFERENCE

1. Rosenzweig, A. C.; Brandstetter, H.; Whittington, D. A.; Nordlund, P.; Lippard, S. J.; Frederick, C. A. (1997) *Proteins 29*, 141-152.
2. Lee, S.-K.; Lipscomb, J. D. (1999) *Biochemistry 38*, 4423-4432.
3. Pikus, J. D.; Mitchell, K. H.; Studts, J. M.; McClay, K.; Steffan, R. J.; Fox, B. G. (2000) *Biochemistry 39*, 791-799.
4. Lovell, T.; Li, J.; Noodleman, L. (2001) *Inorg. Chem. 40*, 5267-5278.
5. Elsen, N. L.; Bailey, L. J.; Hauser, A. D.; Fox, B. G. (2009) *Biochemistry 48*, 3838-3846.
6. Imai, M.; Shimada, H.; Watanabe, Y.; Matsushima-Hibiya, Y.; Makino, R.; Koga, H.; Horiuchi, T.; Ishimura, Y. (1989) *Proc. Natl. Acad. Sci. U.S.A. 86*, 7823-7827.
7. Martinis, S. A.; Atkins, W. M.; Stayton, P. S.; Sligar, S. G. (1989) *J. Am. Chem. Soc. 111*, 9252-9253.
8. Yeom, H.; Sligar, S. G.; Li, H.; Poulos, T. L.; Fulco, A. J. (1995) *Biochemistry 34*, 14733-14740.
9. Altarsha, M.; Benighaus, T.; Kumar, D.; Thiel, W. (2009) *J. Am. Chem. Soc. 131*, 4755-4763.
10. Sazinsky, M. H.; Lippard, S. J. (2006) *Acc. Chem. Res. 39*, 558-566.
11. Murray, L. J.; Lippard, S. J. (2007) *Acc. Chem. Res. 40*, 466-474.
12. Sazinsky, M. H.; Bard, J.; Di Donato, A.; Lippard, S. J. (2004) *J. Biol. Chem. 279*, 30600-30610.
13. Bailey, L. J.; McCoy, J. G.; Phillips, J., George N.; Fox, B. G. (2008) *Proc. Natl. Acad. Sci. U.S.A. 105*, 19194-19198.
14. Murray, L. J.; Naik, S. G.; Ortillo, D. O.; García-Serres, R.; Lee, J. K.; Huynh, B. H.; Lippard, S. J. (2007) *J. Am. Chem. Soc. 129*, 14500-14510.
15. Song, W. J. (2011) Understanding Orchestrated Chemical Reactions in Toluene/*o*-Xylene Monooxygenase from *Pseudomonas Sporium* OX1, Ph.D. Thesis (Massachusetts Institute of Technology, Cambridge, MA).
16. Cafaro, V.; Scognamiglio, R.; Viggiani, A.; Izzo, V.; Passaro, I.; Notomista, E.; Dal Piaz, F.; Amoresano, A.; Casbarra, A.; Pucci, P.; Di Donato, A. (2002) *Eur. J. Biochem. 269*, 5689-5699.
17. Murray, L. J.; García-Serres, R.; Naik, S.; Huynh, B. H.; Lippard, S. J. (2006) *J. Am. Chem. Soc. 128*, 7458-7459.
18. Gibbs, C. R. (1976) *Anal. Chem. 48*, 1197-1201.
19. Tinberg, C. E.; Song, W. J.; Izzo, V.; Lippard, S. J. (2011) *Biochemistry 50*, 1788-1798.
20. Mitchell, K. H.; Studts, J. M.; Fox, B. G. (2002) *Biochemistry 41*, 3176-3188.
21. Wilhelm, E.; Battino, R.; Wilcock, R. J. (1977) *Chem. Rev. 77*, 219-262.
22. Vidakovic, M.; Sligar, S. G.; Li, H.; Poulos, T. L. (1998) *Biochemistry 37*, 9211-9219.
23. Jensen, K. P.; Bell, C. B.; Clay, M. D.; Solomon, E. I. (2009) *J. Am. Chem. Soc. 131*, 12155-12171.
24. Do, L. H.; Hayashi, T.; Moënne-Loccoz, P.; Lippard, S. J. (2010) *J. Am. Chem. Soc. 132*, 1273-1275.

25. LeCloux, D. D.; Barrios, A. M.; Mizoguchi, T. J.; Lippard, S. J. (1998) *J. Am. Chem. Soc. 120*, 9001-9014.
26. Moche, M.; Shanklin, J.; Ghoshal, A.; Lindqvist, Y. (2003) *J. Biol. Chem. 278*, 25072-25080.
27. Kim, K.; Lippard, S. J. (1996) *J. Am. Chem. Soc. 118*, 4914-4915.
28. Moënne-Loccoz, P.; Baldwin, J.; Ley, B. A.; Loehr, T. M.; Bollinger, J. M., Jr. (1998) *Biochemistry 37*, 14659-14663.
29. Skulan, A. J.; Brunold, T. C.; Baldwin, J.; Saleh, L.; Bollinger, J. M., Jr.; Solomon, E. I. (2004) *J. Am. Chem. Soc. 126*, 8842-8855.
30. Bochevarov, A. D.; Li, J.; Song, W. J.; Lippard, S. J.; Friesner, R. A. (2011) *J. Am. Chem. Soc. 133*, ASAP.
31. Rosenzweig, A. C.; Pär, N.; Takahara, P. M.; Frederick, C. A.; Lippard, S. J. (1995) *Chem. Biol. 2*, 409-418.

Chapter 4.

Mechanistic Studies of Reactions of Peroxodiiron(III) Intermediates in T201 Variants of Toluene/*o*-Xylene Monooxygenase Hydroxylase

Reproduced in part with permission from following publication,

Woon Ju Song and Stephen J. Lippard "Mechanistic Studies of Reactions of Peroxodiiron(III) Intermediates in T201 Variants of Toluene/*o*-Xylene Monooxygenase Hydroxylase" *Biochemistry,* **2011**, *Accepted*

4.1. INTRODUCTION

Bacterial multicomponent monooxygenases (BMMs) are capable of activating dioxygen and catalyzing selective organic substrate oxidation.[1,2] The BMMs contain carboxylate-bridged non-heme diiron centers, now a common motif in metalloenzymes[3] including ribonucleotide reductases,[4] desaturases,[5] *myo*-inositol oxygenase,[6] human deoxyhypusine hydroxylase,[7] amine oxygenase,[8] and a recently characterized enzyme on the ubiquinone biosynthesis pathway.[9] Studies of BMMs have mainly focused on soluble methane monooxygenase hydroxylase (sMMOH), revealing two peroxodiiron(III) (P* and P or H_{peroxo}) and a diiron(IV) species (Q) that are generated during dioxygen activation in the presence of a regulatory protein (MMOB).[10-12] Recently, we have been investigating the toluene/*o*-xylene monooxygenase hydroxylase (ToMOH) component of toluene/*o*-xylene monooxygenase (ToMO), which evolved from an ancestor similar to that of sMMO.[13,14] Because the two hydroxylases share very similar diiron active site structures,[15] it seemed plausible that their dioxygen activation mechanisms might proceed through analogous peroxodiiron(III)- and Q-type intermediates. Pre-steady-state studies of dioxygen activation by reduced ToMOH in the presence of its cognate regulatory protein ToMOD (hereafter $ToMOH_{red}D$), however, revealed that this enzyme system generates a previously unprecedented diiron(III) intermediate, $ToMOH_{peroxo}$ (Chart 4.1A).[16] Moreover, no evidence for formation of a Q-like species has yet been identified in ToMOH reactions. These results imply that ToMOH has a different O_2 activation profile from that of sMMOH, oxidizing its substrates via different intermediates.

Chart 4.1 Dioxygen Chemistry in (A) Wild-Type ToMOH and (B) the T201S Variant of ToMOH at 4 °C, pH 7.

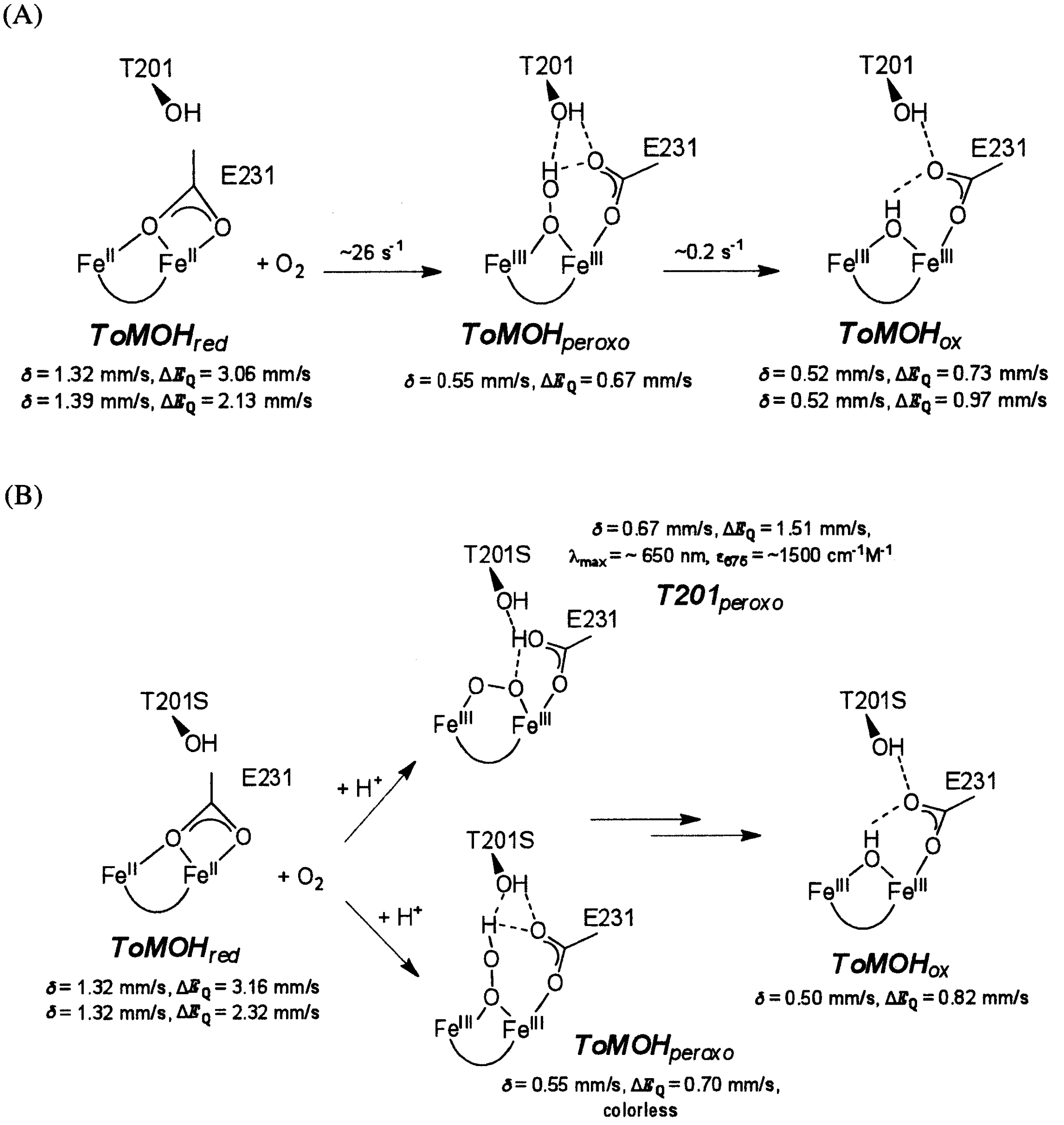

Pre-steady-state studies of dioxygen activation in ToMOH are hampered by the absence of an optical band in the ToMOH$_{\text{peroxo}}$ intermediate. By perturbing the active site structure through the generation of Ser, Cys, and Gly variants of ToMOH T201, however, a residue strictly conserved and located close to the diiron centers in all BMMs, we discovered a novel intermediate, $T201_{peroxo}$. This species forms in addition to $ToMOH_{peroxo}$ in these variants.[17] $T201_{peroxo}$ exhibits UV-vis and Mössbauer spectra similar to those of H_{peroxo} in sMMOH (Chart 1B) and its optical feature allowed us to obtain kinetic parameters of its formation by stopped-flow spectroscopy in the T201 variants under a variety of reaction conditions. DFT and QM/MM calculations revealed how the conformation of the side chain at T201 site perturbs the energetics of two oxygenated species $ToMOH_{peroxo}$ and $T201_{peroxo.}$[18] Our studies further suggested that proton transfer to either the peroxo unit or an adjacent shifting carboxylate ligand (E231) during dioxygen activation can determine the geometry of oxygenated diiron(III) intermediates as either $ToMOH_{peroxo}$ or $T201_{peroxo}$, respectively (Chart 4.1B).[17]

Although accurate stopped-flow kinetic parameters for the formation and decay of $ToMOH_{peroxo}$ could not be measured in the T201S variant, time-dependent Mössbauer spectra obtained from rapid-freeze-quench investigations of its reaction with O_2 in the presence of ToMOD revealed values comparable to those previously obtained with the wild-type enzyme.[17] The data suggested that $T201_{peroxo}$ and $ToMOH_{peroxo}$ are generated by separate pathways, with $T201_{peroxo}$ forming more rapidly than $ToMOH_{peroxo}$, their respective rate constants being $k_{form} = 85 \pm 11\ s^{-1}$ vs. ~ $26\ s^{-1}$ at 4 °C, pH 7.0. Moreover, the decay rate constant of $T201_{peroxo}$ at this temperature ($2.9\ s^{-1}$) is much less than k_{form} of $ToMOH_{peroxo}$ (~ $26\ s^{-1}$), further consistent with $T201_{peroxo}$ and $ToMOH_{peroxo}$ forming by separate pathways during dioxygen activation.

To further probe the properties of $T201_{peroxo}$ and $ToMOH_{peroxo}$ in T201 variants of ToMOH, we explored in the present study three plausible scenarios: (i) that $T201_{peroxo}$ and

$ToMOH_{peroxo}$ are formed and react consecutively; (ii) that $T201_{peroxo}$ and $ToMOH_{peroxo}$ form and react independently; (iii) that $T201_{peroxo}$ and $ToMOH_{peroxo}$ are in equilibrium, with one dominating subsequent reactivity. From the kinetics of the reaction of $T201_{peroxo}$ with arene substrates, following by monitoring changes in its optical spectrum, we were able to evaluate these three working models for formation and decay of $T201_{peroxo}$ and $ToMOH_{peroxo}$ and to identify the arene-oxidizing intermediate(s). In addition to the kinetic studies of $T201_{peroxo}$, the amount of the oxidized phenol or I100W was quantitated in the three T201 variants to further explore the role of T201 during catalysis.

4.2. MATERIALS AND METHODS

General Considerations. Plasmids containing the genes for expressing toluene/*o*-xylene monooxygenase components were supplied by the laboratory of Professor Alberto Di Donato, Naples, Italy. All ToMO components and ToMOH T201X mutants (X= S, C, G) were prepared as described previously.[17,19] I100W/T201X double mutants (X= S, C, G, V) were obtained by using the pET22b(+)/touBEA T201X vector with I100W primers (5′-CAA CTT CAC TTC GGA GCG TGG GCA CTT GAA GAA TAC G-3′ and 5′-C GTA TTC TTC AAG TGC CCA CGC TCC GAA GTG AAG TTG-3′). DNA sequences were confirmed by the MIT-BioPolymers Laboratory. Vectors were transformed into *E. coli* strain BL21(DE3) cells for protein expression. Cell growth and protein purification procedures were as same as for the wild type enzyme. Extinction coefficients at 280 nm of the ToMOH variants were calculated based on the sequence.[20] An iron content was determined, using ferrozine colorimetric assay.[21]

Kinetic Studies of Oxygenated Intermediates in T201X or T201X/I100W (X= S, C, G, V). UV-vis spectra of $T201_{peroxo}$[17] and I100W-radical species[22] were monitored as described previously. Optical bands originating from T201$_{peroxo}$ and the I100W-radical were monitored by using a HiTech DX2 stopped-flow spectrophotometer. The drive syringes and flow lines of this instrument were made anaerobic by passage of at least 10 mL of anaerobic solution of 4 mM sodium dithionite in 25 mM MOPS, pH 7 buffer. The excess dithionite was removed by flushing the syringes with anaerobic buffer. T201X or T201X/I100W ToMOH proteins (~100-200 μM in 25 mM MOPS, pH 7.0) were reduced anaerobically by reacting the protein with excess sodium dithionite in the presence of an equimolar amount of methyl viologen for 10 min. The reduced protein (ToMOH$_{red}$) was dialyzed against 1 L of 25 mM MOPS, pH 7.0 buffer for ~ 3 hr, anaerobically. Following dialysis, 3 equiv of regulatory protein (ToMOD) to the hydroxylase was added to the reduced ToMOH. The solution (ToMOH$_{red}$D) was transferred to a tonometer and loaded into the anaerobic stopped flow instrument. This solution was rapidly mixed against an equal volume of O_2-saturated 25 mM MOPS, pH 7.0 buffer. The temperature was thermostatted at 4 °C using a circulating water bath. Time-dependent optical changes at wavelengths corresponding to the formation and decay of T201$_{peroxo}$ (675 nm) and to those of the I100W-radical species (500 nm) were collected using a PMT (photomultiplier tube) following halogen lamp illumination or a diode-array with a xenon arc lamp. Data were analyzed by the software packages Kinetic Studio (TgK Scientific) and Origin 6.1 (OriginLab Corporation) as described previously.[17] For the T201S and T201G ToMOH variants, an analytical function derived from a model ToMOH$_{red}$→ T201$_{peroxo}$→ ToMOH$_{ox}$ was applied to obtain formation and decay rate constants for T201$_{peroxo}$ (eq 4.1). For simplicity, ToMOH$_{red}$, T201$_{peroxo}$, and ToMOH$_{ox}$ and rate constants for the conversion are abbreviated as A, B, and C and k_1 and k_2, respectively.

$$\text{Abs}= \varepsilon_c*[\text{A}]_0+(\varepsilon_A-\varepsilon_C)*[\text{A}]_0*\exp(-k_1*\text{x})+(\varepsilon_B-\varepsilon_C)*[\text{A}]_0*k_1/(k_2-k_1)*(\exp(-k_1*\text{x})-\exp(-k_2*\text{x}))$$

(eq 4.1)

For the T201C variant, an analytical function corresponding to the model ToMOH$_{red}$→ T201$_{peroxo}$→ T201$_{peroxo}$*→ ToMOH$_{ox}$ was derived to measure the formation and two consecutive decay rate constants of T201$_{peroxo}$, where T201$_{peroxo}$ and ToMOH$_{ox}$ are sequential decay products of T201$_{peroxo}$ (eq 4.2). For simplicity, each component, ToMOH$_{red}$, T201$_{peroxo}$, T201$^{*}_{peroxo}$, and ToMOH$_{ox}$, and their conversion rate constants are represented as A, B, C, and D, and as k_1, k_2, and k_3, respectively.

$$\text{Abs} = [\text{A}]_0 *(\varepsilon_D +((\varepsilon_A - \varepsilon_D)*\exp(-k_1*\text{x}))+((\varepsilon_B - \varepsilon_D)*k_1*1/(k_2-k_1)*(\exp(-k_1*\text{x})-\exp(-k_2*\text{x})))+((\varepsilon_c-\varepsilon_D)* k_1*k_2*1/(k_2- k_1)*(1/(k_3- \text{k1})*(\exp(-k_1*\text{x})-\exp(-k_3*\text{x}))-1/(k_3- k_2)*(\exp(-k_2*\text{x})-\exp(-k_3*\text{x})))))$$

(eq 4.2)

In the T201X/I100W variants, the formation and decay of the T201$_{peroxo}$ and I100W-radical species were fit to analytical functions derived for ToMOH$_{red}$→ T201$_{peroxo}$→ ToMOH$_{ox}$ and I100W-radical precursor→ I100W-radical→ oxidized product of I100W models, respectively (eq 4.1), as described previously.[17,22]

Kinetics of an Oxygenated Intermediate in the Reactions with Arene Substrates. The arene substrate phenol was dissolved in dioxygen-saturated buffer and the solution was rapidly mixed with ToMOH$_{red}$D in a single-mixing stopped flow spectrophotometer at 4 °C. Time-dependent optical changes arising from the formation and decay of T201$_{peroxo}$ were then analyzed, as described previously.[17]

For a kinetic isotope effect (KIE) measurement, phenol (hereafter phenol-h_5) and phenol-2,3,4,5,6-d_5 (hereafter phenol-d_5) (98 atom % D) purchased from Sigma-Aldrich were used without further purification. For kinetic solvent isotope effect (KSIE) measurements, deuterium oxide (99.9 atom % D) purchased from Cambridge Isotope Laboratories or Icon Isotopes was used to prepare 25 mM MOPS buffer, pL 7.0. The pL value was adjusted by adding an appropriate amount of NaOD and DCl solutions (Aldrich). Dioxygen activation of $\text{ToMOH}_{\text{red}}\text{D}$ was monitored at 5 °C, which was thermostatted using a circulating water bath.

4.3. RESULTS and DISCUSSION

Decay Rates of $T201_{peroxo}$ in the Presence of Aromatic Substrates. To determine whether $\text{T201}_{\text{peroxo}}$ is kinetically competent to hydroxylate aromatic substrates, its formation and decay rates were monitored in the presence of phenol. Phenol was selected as substrate because the natural substrates, toluene and *o*-xylene, are less soluble in water. In addition, ToMO displays a high steady state activity with phenol.[16] To observe its effects on the decay rate of $\text{T201}_{\text{peroxo}}$, phenol was dissolved in dioxygen-saturated buffer and rapidly mixed with the same volume of a solution containing reduced T201X ToMOH and ToMOD ($\text{ToMOH}_{\text{red}}\text{D}$). Changes in absorbance at 675 nm, corresponding to formation and decay of $\text{T201}_{\text{peroxo}}$, were monitored using stopped-flow optical spectroscopy (Figure 4.1). The rate constants were then obtained by the fit to an analytical function derived from a model involving two or three consecutive, irreversible steps.

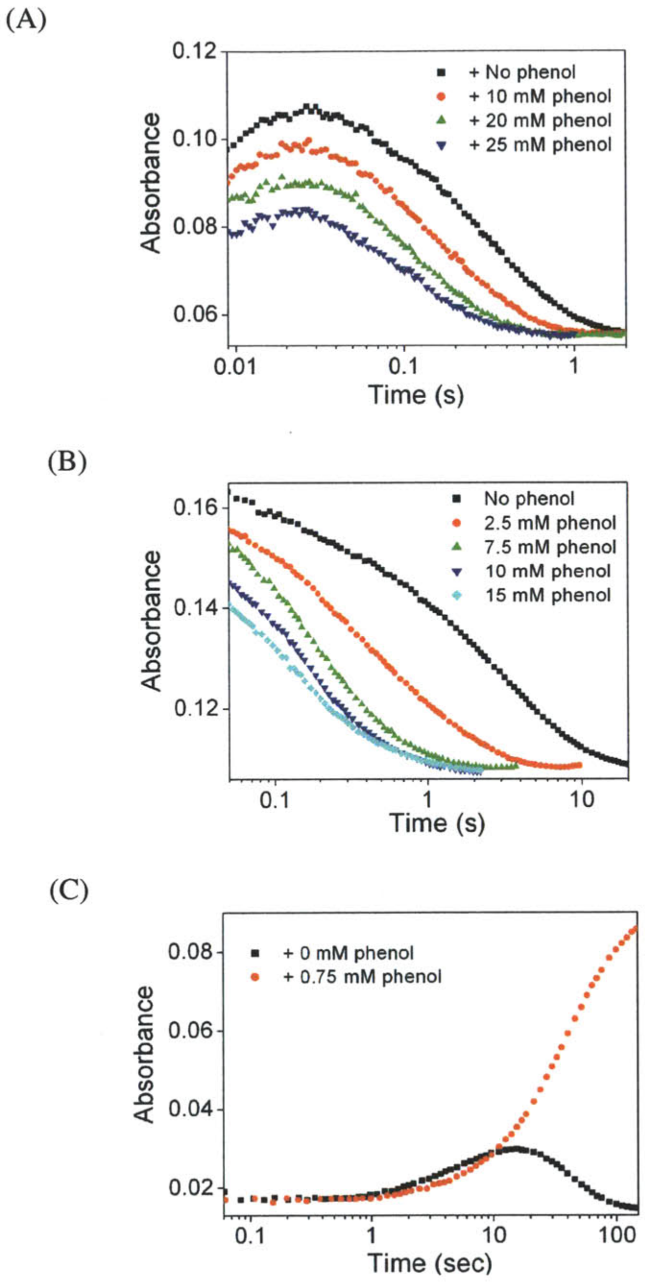

Figure 4.1 Trace of $T201_{peroxo}$ at 675 nm in the absence and presence of phenol in T201 variants of ToMOH at 4 °C. (A) T201S (B) T201C (C) T201G.

In the reaction of phenol and dioxygen with the T201S variant of $ToMOH_{red}D$, the formation rate of $T201_{peroxo}$ was within error unaltered over a 0 - 25 mM range of phenol concentrations (Figure 4.2A). This result indicates that the substrate does not affect the mechanism/rate of dioxygen activation to form T201$_{\mathrm{peroxo}}$.[a] The presence of phenol, however, accelerated the decay of T201$_{\mathrm{peroxo}}$, thereby diminishing the accumulation of this intermediate (Figure 4.1A). Because the decay rate of T201$_{\mathrm{peroxo}}$ in the presence of phenol is much faster than the rate of catechol production measured under steady-state conditions,[17] it is apparent that T201$_{\mathrm{peroxo}}$ is kinetically competent for, and probably on the pathway to, phenol oxidation. A plot of k_{decay} versus phenol concentration yielded a linear relationship, from which we could derive a second-order decay rate constant of 0.18 ± 0.02 $\mathrm{s^{-1}mM^{-1}}$ (Figure 4.2A).

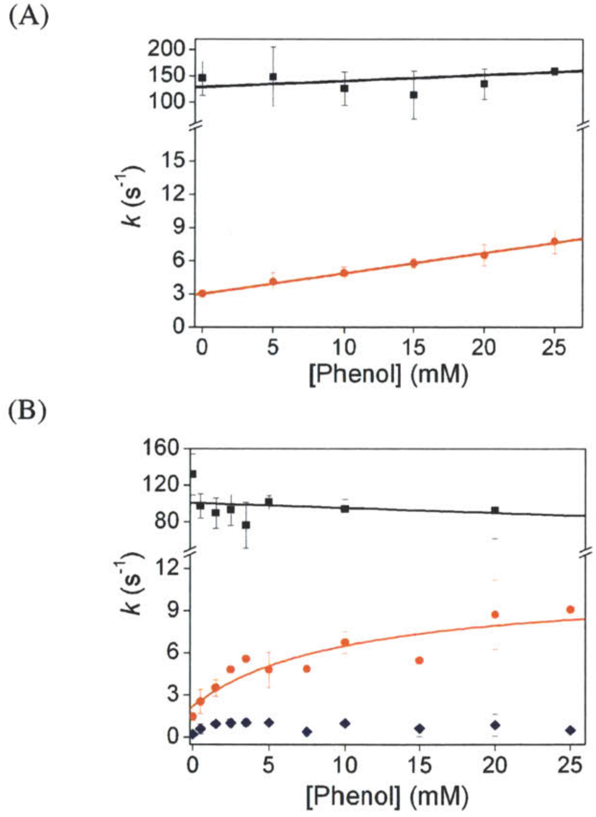

---

[a] The data also implicate that dioxygen and phenol substrates are possibly transferred to the diiron active sites via different pathways. Dioxygen/hydrocarbon transfer pathways are discussed in Chapter 5.

Figure 4.2 Plots of T201$_{\text{peroxo}}$ formation and decay rate constants versus phenol concentrations in the reaction of T201X ToMOH$_{\text{red}}$D with phenol in dioxygen-saturated buffer at 4 °C. (A) T201S (B) T201C Formation and decay rates are represented with black squares and red circles, respectively. For T201C variant, second decay rate constants are shown as navy diamonds. Formation and decay rate constants are plotted with either a linear or a saturation function. Fitting results for the formation and decay rates are represented as black and red lines, respectively.

T201$_{\text{peroxo}}$ is also observed during dioxygen activation of the T201C and T201G variants of ToMOH. T201$_{\text{peroxo}}$ reacts in a similar manner with phenol in the T201C and T201G ToMOH variants. In the absence of arene substrate, T201$_{\text{peroxo}}$ in T201C variant decays by two consecutive process, T201$_{\text{peroxo}} \rightarrow$ T201$_{\text{peroxo}}{}^{*} \rightarrow$ ToMOH$_{\text{ox}}$. Two decay rate constants, k_{decay1} and k_{decay2}, corresponding to the conversion of T201$_{\text{peroxo}}$ to T201$_{\text{peroxo}}{}^{*}$ and of T201$_{\text{peroxo}}{}^{*}$ to ToMOH$_{\text{ox}}$, were obtained. The change in the absorbance of T201$_{\text{peroxo}}$ at 675 nm in T201C variant was recorded in the absence and presence of arene substrate (Figure 4.1B). As described above for the T201S variant, formation rate of T201$_{\text{peroxo}}$ was within error independent of phenol concentration (Figure 4.2B). Less T201$_{\text{peroxo}}$ accumulated when the concentration of phenol was increased due to acceleration of its decay rate. A plot of the first derived decay rate constant (k_{decay1}) versus phenol concentration displayed saturation behavior (Figure 4.2B) and was fit (eq 4.3) to the processes depicted in Scheme 4.1, resulting in k_{sat} and K_{d} of 9 ± 2 s^{-1} and 10 ± 8 mM, respectively. The second rate of the following decay process (k_{decay2}) was slightly perturbed by the presence of phenol, but with no clear dependence on its concentration, suggesting that T201$_{\text{peroxo}}{}^{*}$ may not react directly with substrate.

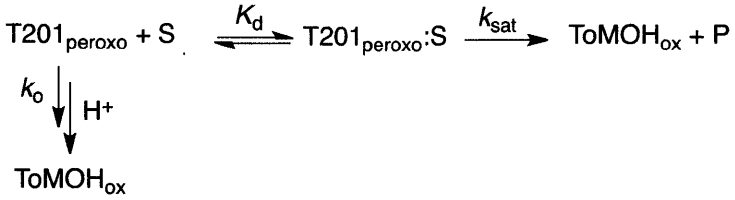

Scheme 4.1 A Model for the Reaction of T201$_{\text{peroxo}}$ and Substrate (Phenol). S and P represent substrate and product, respectively. K_d and k_o values indicate dissociation or apparent Michaelis constant describing the intermediate–substrate complex (T201$_{\text{peroxo}}$:S), and decay rate constant of T201$_{\text{peroxo}}$ in the absence of substrate, respectively.

$$k_{obs} = k_o + \frac{k_{sat}\,[\mathrm{S}]}{K_d + [\mathrm{S}]} \tag{4.3}$$

To study further the arene-oxidizing mechanism of T201$_{\text{peroxo}}$, phenol-d_5 was used in the reaction of T201C ToMOH$_{\text{red}}$D with dioxygen. Arene oxidation typically involves a hybridization change from sp^2 to sp^3 at a phenol carbon atom and, accordingly, an inverse kinetic isotope effect, KIE < 1, was observed.[23] In this manner, the decay rates of T201$_{\text{peroxo}}$ arising from the use of phenol-h_5 versus phenol-d_5 and the resulting KIE can signal kinetic coupling to reaction with phenol. An inverse KIE of 0.82 ± 0.05, listed in Table 4.1, was derived, indicating that the decay of T201$_{\text{peroxo}}$ is kinetically linked to the arene oxidation. T201$_{\text{peroxo}}$ presumably attacks the arene ring in an electrophilic manner to generate an arene-oxide species.[16] No KIE was observed for the following decay rate (k_{decay2}) from T201$_{\text{peroxo}}$*→ ToMOH$_{\text{ox}}$. As suggested above, T201$_{\text{peroxo}}$* is probably not involved in arene oxidation.

Table 4.1 Consecutive Decay Rate Constants for T201$_{\text{peroxo}}$ in the Reaction of T201C ToMOH$_{\text{red}}$D with Phenol in Dioxygen-Saturated Buffer at 4 °C.

	phenol-h_5	phenol-d_5	KIE
k_{decay1} (s^{-1})	7.2 ± 0.3	8.7 ± 0.3	0.82 ± 0.05
k_{decay2} (s^{-1})	2.2 ± 0.2	2.1 ± 0.2	1.1 ± 0.1

Reaction of T201G ToMOH$_{red}$D with a solution of phenol in dioxygen-saturated buffer also led to the formation of T201$_{peroxo}$ (Figure 4.1C). The kinetic behavior of this reaction could not be monitored, however, because the oxidized product, catechol, binds to the diiron core, forming a Fe(III)-catecholate species with characteristic strong, interfering optical bands between 600-1020 nm[24] that mask the optical feature of T201$_{peroxo}$. Binding of catechol to the resting state enzyme after single turnover was also observed for the wild-type and T201S and T201C variants of ToMOH, but the decay rates of T201$_{peroxo}$ for the T201S and T201C variants were much faster than the formation rates of Fe(III)-catecholate species so that optical changes at 675 nm, corresponding to the decay of T201$_{peroxo}$ were not obscured as they were for the T201G variant (data not shown).

Kinetic Solvent Isotope Effect in the Decay of T201$_{peroxo}$ in the Absence and Presence of Arene Substrates. A kinetic solvent isotope effect (KSIE) can be measured when deuterium oxide (D_2O) is used instead of H_2O as the solvent.[25] A proposed chemical mechanism for T201$_{peroxo}$ decay in the absence of arene substrate is protonation of the hydroperoxo unit and subsequent release of hydrogen peroxide.[16,17] If T201$_{peroxo}$ requires a proton(s) in the decomposition pathway and the proton translocation step is coupled to decay of T201$_{peroxo}$, a KSIE > 1 will be observed. The KSIE derived from the decay rates of T201$_{peroxo}$ in the presence of arene substrate, however, can be altered depending on whether or not the reaction is linked to arene oxidation, because a typical KIE for aromatic hydroxylation (KIE < 1) differs from that for proton translocation, as described above. We therefore derived KSIE values from the decay rates of T201$_{peroxo}$ in the absence and presence of phenol to distinguish the kinetically prevailing chemical step in T201$_{peroxo}$ decay and to provide an additional assessment of our previous conclusion that the more enhanced decay of T201$_{peroxo}$ upon addition of phenol is an indication of its kinetic competence.

To measure the KSIE for the decay of T201$_{peroxo}$, the reaction of T201C ToMOH$_{red}$D with dioxygen was monitored in H_2O or D_2O buffer at 5 °C. Two consecutive decay rates of T201$_{peroxo}$ were observed in D_2O buffer, as previously seen in H_2O buffer. The k_{decay1} and k_{decay2} values measured in the two buffers returned KSIE$_{decay1}$ = 3.4 ± 0.3 and KSIE$_{decay2}$ = 6.5 ± 0.1 (Table 4.2). These large KSIE values for the decay process can imply multiple protons in a decay pathway,[26] which presumably, for T201$_{peroxo}$, involve protonation of the peroxo moiety and release of H_2O_2. KSIE$_{decay}$ values > 1 were also observed for the T201S and T201G variants, 1.40 ± 0.11 and 10.6 ± 1.6, respectively (data not shown).[b,27,28] KSIE$_{decay}$ values obtained from the decay rates of T201$_{peroxo}$ increase in the order T201S < T201C < T201G, possibly because of their increasingly poor ability to facilitate proton transfer during the decomposition of T201$_{peroxo}$.

Table 4.2 Consecutive Decay Rate Constants and KSIE Values for T201$_{peroxo}$ in the Reaction of T201C ToMOH$_{red}$D with Dioxygen in H_2O or D_2O Buffer at 5 °C.

	H_2O	D_2O	KSIE
k_{decay1} (s^{-1})	1.9 ± 0.1	0.557 ± 0.007	3.4 ± 0.3
k_{decay2} (s^{-1})	0.241 ± 0.004	0.0382 ± 0.0001	6.5 ± 0.1

---

[b] The origin of unusually large isotope effect from the T201$_{peroxo}$ decay rate for T201G variant is not identified. The large isotope effect may arise when the reaction is associated with multiple isotope-dependent steps, which results in the cumulative isotope effects, or when a hydrogen-tunneling process occurs. Neither scenario can be ruled out at present. Further data analysis suggested that hydrogen tunneling is a plausible event, given that the estimated kinetic parameters for the T201$_{peroxo}$ decay are KSIE = 10.6 ± 1.6, ΔΔH = 1.68 ± 0.17 kcal/mol, and an Arrhenius preexponential factor ratio of A^H : A^D = 0.55 ± 0.06, which are in the typical ranges for hydrogen tunneling process, KSIE (H_2O/D_2O) > 7, ΔΔH > 1.3 kcal/mol, and an Arrhenius preexponential factor ratio of A^H : A^D < 1. Another typical feature for the tunneling process, a curvature in the Arrhenius plot, however, was not observed presumably because the experiments were carried out in narrow temperature ranges of 4 – 20 °C.

Different $\text{KSIE}_{\text{decay}}$ results were obtained when experiments were conducted in the presence of phenol. KSIE studies in the presence of phenol were conducted only with T201C but not the T201S and T201G variants. Although the $\text{KSIE}_{\text{decay}}$ in T201S is > 1, it is not large enough to permit an accurate value to be obtained in the presence of phenol. For the T201G variant, formation of the optical bands of Fe(III)-catecholate, as described previously, made it impossible to measure the $\text{KSIE}_{\text{decay}}$. A solution of T201C $\text{ToMOH}_{\text{red}}\text{D}$ in either H_2O or D_2O buffer was therefore mixed with dioxygen-saturated buffer containing 10 mM phenol. Decay rates of $\text{T201}_{\text{peroxo}}$ in each buffer were measured, yielding $\text{KSIE}_{\text{decay}}$ values of 1.15 ± 0.06 and 2.1 ± 0.2 for two successive steps, respectively (Table 4.3). The dramatically reduced KSIE value for the first decay step compared to that determined in the absence of phenol, 3.4 ± 0.3 □ 1.15 ± 0.06, indicates that decay of $\text{T201}_{\text{peroxo}}$ is no longer entirely dependent on solvent protons but primarily involves an interaction of the peroxodiiron(III) intermediate with phenol.[c] Therefore, the significant decrease in KSIE values due to introduction of the arene substrate supports the conclusion that $\text{T201}_{\text{peroxo}}$ is kinetically competent to hydroxylate phenol.

Table 4.3 Consecutive Decay Rate Constants and KSIE Values for $\text{T201}_{\text{peroxo}}$ in the Reaction of T201C $\text{ToMOH}_{\text{red}}\text{D}$ with Dioxygen and 10 mM Phenol in H_2O or D_2O Buffer at 5 °C.

	H_2O	D_2O	KSIE
k_{decay1} (s^{-1})	7.2 ± 0.3	6.26 ± 0.07	1.15 ± 0.06
k_{decay2} (s^{-1})	2.2 ± 0.2	1.02 ± 0.03	2.1 ± 0.2

---

[c] Given that $\text{KSIE}_{\text{decay}}$ is still >1, the decay of $\text{T201}_{\text{peroxo}}$ may not be fully coupled to the phenol oxidation even in the presence of ~10 mM phenol. The results of steady-state activity of the T201C variant may account for the less change in $\text{KSIE}_{\text{decay}}$, where much higher K_M value of T201C variant than the wild-type or T201S variant was measured, presumably indicating that substrate affinity for the enzyme is decreased due to the T201C mutation.

The $KSIE_{decay}$ result for the second decay process (k_{decay2}) is also considerably perturbed by addition of phenol. Because $T201_{peroxo}$* probably does not react with phenol, as discussed above, the presence of phenol might trigger as yet unidentified reactions, for example, proton-assisted conformational changes that contribute to the decay of $T201_{peroxo}$*.

Studies of T201X/I100W Variants (X = S, C, G, V). As reported previously, I100 is located near the diiron active site where it helps to form a hydrophobic pocket.[15] When I100 residue was mutated to I100W, the indole ring of the installed tryptophan approached the iron atoms, with Fe···C distances ranging from 6.0 to 11.9 Å.[22] Addition of dioxygen to the reduced form of I100W ToMOH and ToMOD demonstrated that the variant activates O_2 at a rate similar to that observed for the wild type enzyme. The decay rate of $ToMOH_{peroxo}$ was accelerated, however, because the tryptophan residue serves as a substrate closely positioned near the active site, reacting with $ToMOH_{peroxo}$ to form diiron(III,IV) and I100W-radical species.[22] The generation of the I100W-radical from $ToMOH_{peroxo}$ was nearly quantitative, and time-dependent RFQ/Mössbauer, EPR, and UV-vis spectroscopic studies revealed that the $ToMOH_{peroxo}$ decay rate corresponds to the formation rate of the I100W-radical species.

Based on these findings, T201X/I100W double mutants were prepared to examine the effect of the tryptophan residue on the decay rate of $T201_{peroxo}$ as well as the formation rate of the anticipated I100W-radical. I100W/T201X variants of ToMOH (X= S, C, G, V), prepared as described previously, contained ~4 iron atoms/protein. When reduced T201S/I100W ToMOH and ToMOD were mixed with dioxygen-saturated buffer in the stopped-flow spectrophotometer at 4 °C, changes in the optical spectra at 675 nm and 500 nm originating from $T201_{peroxo}$ and I100W radical species, respectively, were observed

(Figure 4.3). From the data we computed formation and decay rates of $T201_{peroxo}$ and the I100W-radical species by fitting the optical changes to a function representing two consecutive, irreversible processes (Table 4.4 and Figure 4.4).

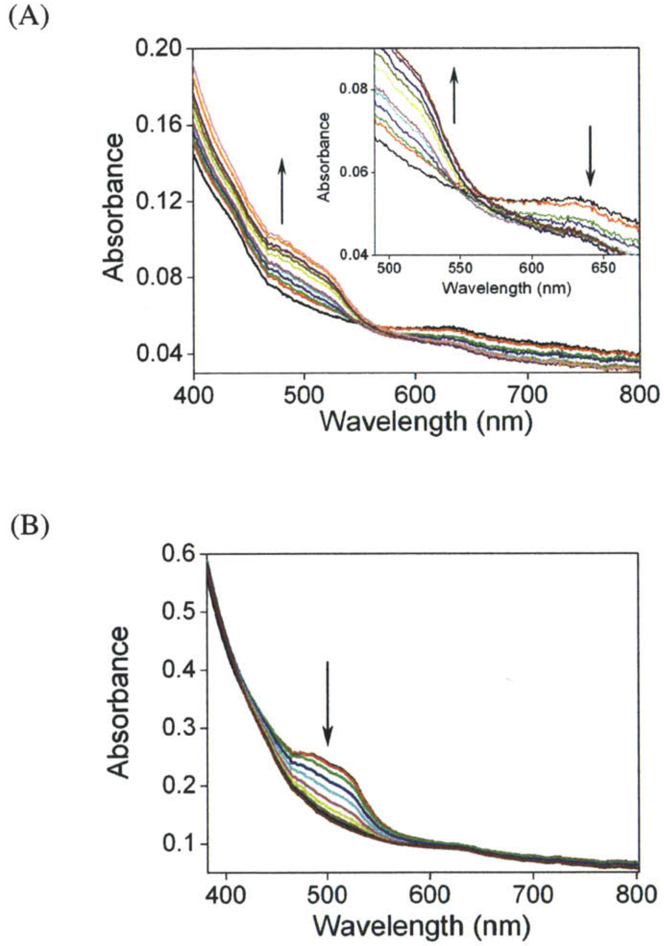

Figure 4.3 Time-dependent optical spectral changes during the reaction of T201S/I100W $ToMOH_{red}D$ with dioxygen at 4 °C. (A) Formation of the tryptophan radical species in T201S/I100W. UV-vis spectra were measured after mixing the enzyme with dioxygen for 60-960 ms (Inset) Enlarged optical changes at 480 - 680 nm. (B) Decay of I100W-radical species in T201S/I100W observed for 1-21 s after the reaction with dioxygen.

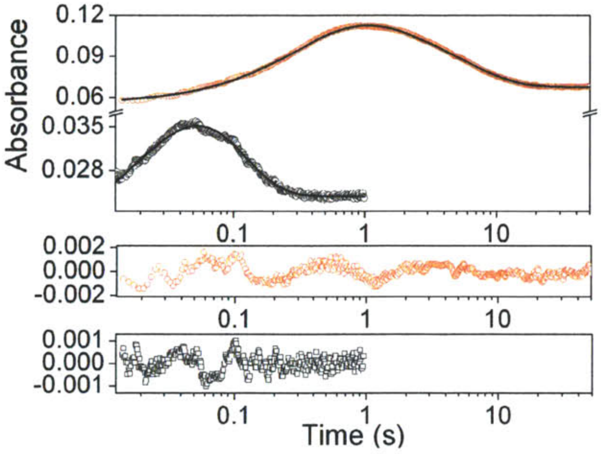

Figure 4.4 Time-dependent optical changes in the reaction of T201S/I100W ToMOH$_{red}$D with dioxygen at 675 nm (black squares) and 500 nm (red circles) at 4 °C. The traces were fit to a function representing two consecutive, irreversible processes. Fitting results are represented as black lines in spectra and with residuals shown below.

Table 4.4 Formation and Decay Rate Constants for T201$_{peroxo}$ and W-Radical Intermediates Generated During Dioxygen Activation of I100, T201S, and T201S/I100W ToMOH$_{red}$D at 4 °C.

	I100W	T201S	T201S/I100W
T201$_{peroxo}$	nd[a]	$k_{form} = 88 \pm 7$ s^{-1} $k_{decay} = 3.1 \pm 0.3$ s^{-1}	$k_{form} = 55 \pm 14$ s^{-1} $k_{decay} = 14.9 \pm 0.4$ s^{-1}
I100W-radical	[b]$k_{form} = 0.804 \pm 0.001$ s^{-1} [b]$k_{decay} = 0.054 \pm 0.002$ s^{-1}	nd[a]	$k_{form} = 2.88 \pm 0.12$ s^{-1} $k_{decay} = 0.19 \pm 0.01$ s^{-1}

[a]Not determined. [b]Taken from ref. 21.

Both the formation and decay rate constants of T201$_{peroxo}$ and I100W-radical species in T201S/I100W were greatly perturbed compared to their values in T201S or I100W single variants.[d] An accelerated decay rate of T201$_{peroxo}$ in T201S/I100W, compared to that in the

---

[d] Dramatic changes due to the I100W mutation in the formation rate constant of T201$_{peroxo}$ is discussed in Chapter 5.

T201S variant, implies that T201$_{peroxo}$ is on the reaction pathway of I100W oxidation, as discussed above for phenol oxidation. Three mechanisms were proposed to account for these data, as portrayed in Scheme 4.2.

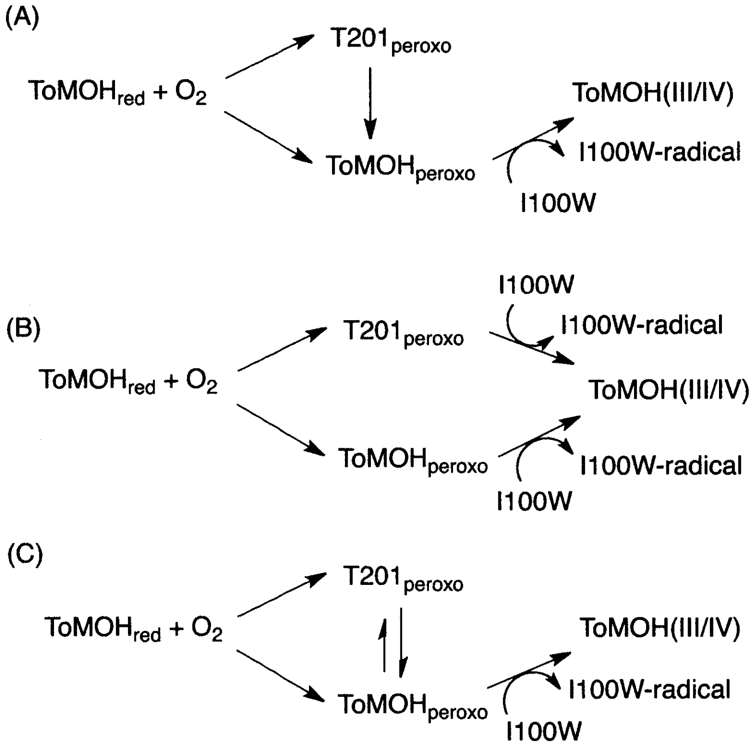

Scheme 4.2 Reaction Models for the Formation and Decay of T201$_{peroxo}$during Dioxygen Activation of T201X/I100W ToMOH.[a] [a]ToMOH$_{red}$ and ToMOH(III/IV) represent diiron(II/II) and diiron(III/IV) redox states, respectively.

The increased T201$_{peroxo}$ decay rate rules out mechanism A in Scheme 4.2, whereby T201$_{peroxo}$ irreversibly decomposes to ToMOH$_{peroxo}$. If mechanism A were operative, only the decay rate of ToMOH$_{peroxo}$, but not that of T201$_{peroxo}$, would be accelerated by introduction of the arene substrate, tryptophan.

Both formation and decay of the I100W radical species are simultaneously well fit by a single exponential function (Table 4.4 and Figure 4.4), which indicates that there is only one kinetically observable precursor, therefore, either T201$_{\text{peroxo}}$ or ToMOH$_{\text{peroxo}}$, but not both. These data therefore exclude mechanism B in Scheme 4.2. The decay rate constant for T201$_{\text{peroxo}}$, 14.9 ± 0.4 s^{-1}, however, is much larger than the formation rate constant of the I100W radical species, 2.8 ± 0.1 s^{-1}, indicating that T201$_{\text{peroxo}}$ does not directly convert to the I100W radical species. No clear isosbestic point was monitored (Figure 4.3A, inset), again supporting that an additional species, presumably ToMOH$_{\text{peroxo}}$, exists along the decay reaction pathway.

A third possible mechanism that we considered is one in which T201$_{\text{peroxo}}$ and ToMOH$_{\text{peroxo}}$ are in equilibrium with one another (Mechanism C, Scheme 4.2). This possibility is supported by the observed kinetic properties of the T201$_{\text{peroxo}}$ and I100W-radical intermediates in the T201S, I100W, and T201S/I100W variants. The chemical equilibrium presumably conveys kinetic competence to T201$_{\text{peroxo}}$ in arene oxidation, although this intermediate does not *directly* react with the substrate. Depletion of ToMOH$_{\text{peroxo}}$ by reaction with I100W converts T201$_{\text{peroxo}}$ to ToMOH$_{\text{peroxo}}$ to maintain the equilibrium.

A possible mechanism for the interconversion of ToMOH$_{\text{peroxo}}$ and T201$_{\text{peroxo}}$ is suggested in Scheme 4.3. A hydrogen-bonded proton on the hydroperoxo unit of ToMOH$_{\text{peroxo}}$ or on an oxygen atom of the adjacent glutamate (E231) in T201$_{\text{peroxo}}$ can easily shift between the two positions, as illustrated in the Scheme. Such proton translocation can trigger reorganization of peroxo unit, altering the geometry of oxygenated diiron(III) species. The relative energetics of the two geometries, 1,1-peroxodiiron(III) and 1,2-peroxodiiron(III), computed QM/MM methods, suggested the energy difference between

$\text{ToMOH}_{\text{peroxo}}$ and $\text{T201}_{\text{peroxo}}$ to be relatively small, and the occurrence of both intermediate species is therefore energetically plausible.

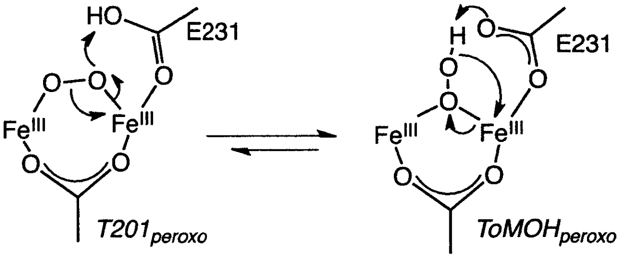

Scheme 4.3 A Proposed Mechanism for the Interconversion of $\text{T201}_{\text{peroxo}}$ and $\text{ToMOH}_{\text{peroxo}}$.

Introduction of I100W has a similar effect on the kinetic properties of $\text{T201}_{\text{peroxo}}$ in the other T201 variants. For T201C/I100W, formation and decay of $\text{T201}_{\text{peroxo}}$ and the I100W radical species were monitored during the reaction of T201C/I100W $\text{ToMOH}_{\text{red}}\text{D}$ with O_2, as described for the T201S/I100W variant. Formation and decay of $\text{T201}_{\text{peroxo}}$ and the I100W-radical species in T201C/I100W monitored at 675 nm and 500 nm, respectively and time-dependent traces were fit to a consecutive two exponential function without inclusion of $\text{T201}_{\text{peroxo}}*$ in the decomposition pathway of $\text{T201}_{\text{peroxo}}$ to ToMOH_{ox} (Table 4.5 and Figure 4.5). Given that a consecutive three-exponential function was required to fit the trace of $\text{T201}_{\text{peroxo}}$ in the T201C single variant, the rapid decay of $\text{T201}_{\text{peroxo}}$ in the reaction with I100W residue does not proceed through $\text{T201}_{\text{peroxo}}*$. Acceleration of the decay rate of $\text{T201}_{\text{peroxo}}$ in T201C/I100W relative to the value in the T201C variant (k_{decay1}) again supports a mechanism in which $\text{T201}_{\text{peroxo}}$ is on the pathway of aromatic hydroxylation through equilibrium with $\text{ToMOH}_{\text{peroxo}}$ (Scheme 4.2C).

Both formation and decay rates of the I100W radical species in T201C/I100W are accelerated by comparison to those of I100W and T201S/I100W variants (Table 4.5).

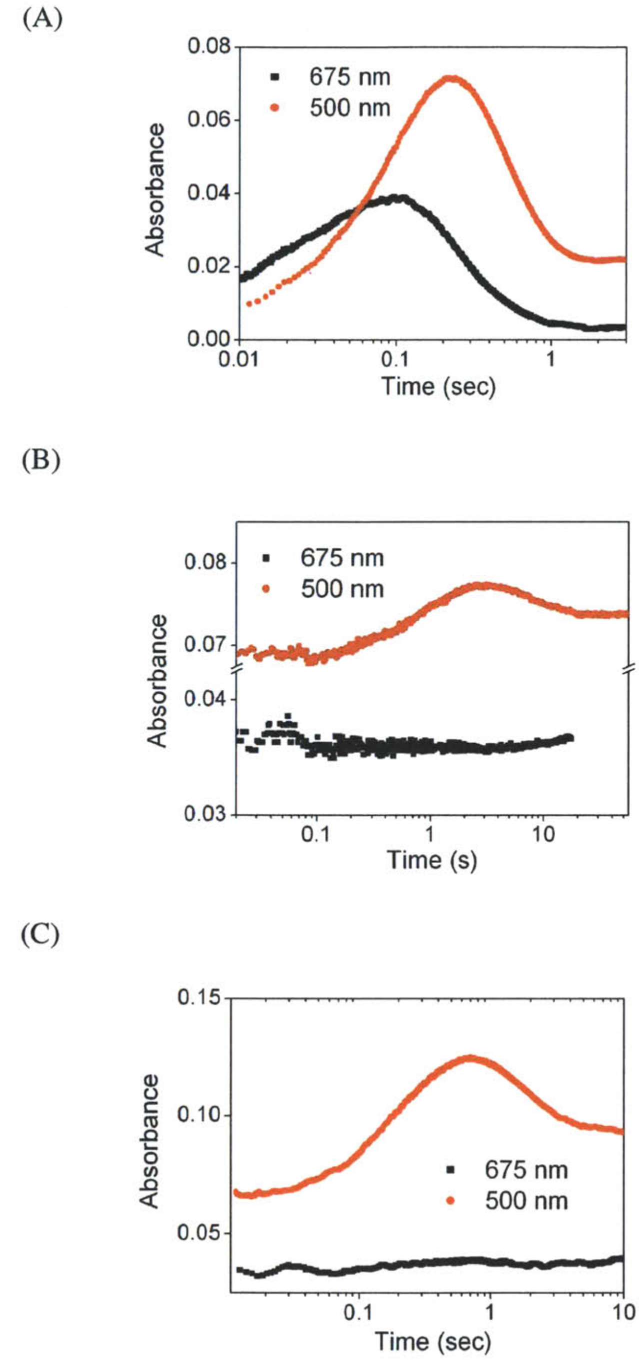

Figure 4.5 Time-dependent optical changes in the reaction of T201X/I00W ToMOH$_{red}$D with dioxygen at 675 nm (black squares) and 500 nm (red circles) at 4 °C. (A) T201C/I100W (B) T201G/I100W (C) T201V/I100W

Table 4.5 Formation and Decay Rate Constants of T201$_{\text{peroxo}}$ and the Tryptophan Radical Species Formed in the Reaction of T201X/I100W ToMOH$_{\text{red}}$D with Dioxygen at 4 °C (X = S, G, C, V).

	T201$_{\text{peroxo}}$		W-radical	
	k_{form}	k_{decay}	k_{form}	k_{decay}
I100W	[a]n.d.	[a]n.d.	0.804 ± 0.001	0.054 ± 0.002
T201S/I100W	55 ± 14	14.9 ± 0.4	2.88 ± 0.12	0.19 ± 0.01
T201C/I100W	18 ± 2	4.2 ± 0.6	5.8 ± 1.1	4.6 ± 0.7
T201G/I100W	[a]nd	[a]nd	0.96 ± 0.16	0.14 ± 0.02
T201V/I100W	[a]nd	[a]nd	3.7 ± 0.5	0.8 ± 0.2

[a]Not determined.

These kinetic characteristics of the I100W radical species in T201C/I100W can be perturbed if the local environment near the active sites is significantly altered. Previous studies with the I100W variant of ToMOH revealed that the formation and decay rates of I100W-radical species are pH-dependent.[22] The rates are accelerated at high pH values, suggesting that deprotonation at tryptophan residue during formation and decay of I100W-radical species is preceded by a fast oxidation. Therefore, the acceleration of the formation and decay rates of I100W-radical species in T201C/I100W relative to rates in the I100W or T201S/I100W variants possibly reflects local pH changes near the active site, induced by the T201C mutation. Because T201C is presumably a poorer residue than T201 or T201S for facilitating H_3O^+ transport to the diiron center,[17] the T201C variant may experience an increase in local pH at the active site.

The T201G/I100W variant also generated the I100W-radical species during dioxygen activation (Figure 4.5 and Table 4.5). No T201$_{\text{peroxo}}$ species could be observed, however, probably because it reacts rapidly with I100W and does not accumulate to a detectable level.

Finally, dioxygen activation by the T201V/I100W variant was investigated (Table 4.5 and Figure 4.5). As expected from the T201V single variant study,[17] T201$_{\text{peroxo}}$ was not detected in T201V/I100W. Possibly proton translocation, required for T201$_{\text{peroxo}}$ generation, is too slow; alternatively, formation of I100W-radical is too rapid to allow the intermediate to build up. Another possibility is that the T201V variant energetically disfavors formation of T201$_{\text{peroxo}}$.[17,18] Reaction of T201V/I100W ToMOH$_{\text{red}}$D with dioxygen also generated the I100W-radical species, possibly because the spectroscopically silent species, ToMOH$_{\text{peroxo}}$, formed and reacted with the tryptophan residue. The kinetic properties of the I100W-radical species in T201V/I100W are slightly different from those of I100W but rather similar to those of T201C/I100W, indicating that the local pH at the active site might similarly be perturbed owing to the presence of the hydrophobic valine side chain.

Finally, dioxygen activation by the T201V/I100W variant was investigated (Table 4.5 and Figure 4.5). As expected from the T201V single variant study,[17] T201$_{\text{peroxo}}$ was not detected in T201V/I100W. Possibly proton translocation, required for T201$_{\text{peroxo}}$ generation, is too slow; alternatively, formation of I100W-radical is too rapid to allow the intermediate to build up. Another possibility is that the T201V variant energetically disfavors formation of T201$_{\text{peroxo}}$.[17,18] Reaction of T201V/I100W ToMOH$_{\text{red}}$D with dioxygen also generated the I100W-radical species, possibly because the spectroscopically silent species, ToMOH$_{\text{peroxo}}$, formed and reacted with the tryptophan residue. The kinetic properties of the I100W-radical species in T201V/I100W are slightly different from those of I100W but rather similar to those of T201C/I100W, indicating that the local pH at the active site might similarly be perturbed owing to the presence of the hydrophobic valine side chain.

Quantification of I100W Radical Species in T201X/I100W Variants. The wild-type ToMOH displays half-sites reactivity, in which only one of the two diiron centers in the dimeric hydroxylase undergoes productive reactivity during single-turnover experiments. The other site can be reduced to the diiron(II) state but does not simultaneously form $\text{ToMOH}_{\text{peroxo}}$ upon introduction of O_2.[16] Half-sites reactivity is also consistently observed in reactions with phenol, whereby 50% catechol per diiron sites form during single turnover experiments.[17,29] In T201S, ~50% phenol oxidation was similarly measured during single-turnover, indicating that the serine variant retains half-sites reactivity.[17] This property seems to be conserved in other T201 variants. Reactions of T201G $\text{ToMOH}_{\text{red}}$D with dioxygen generated oxygenated intermediates at approximately half of the diiron centers. If half-sites reactivity is operative in all the T201G/C/V variants, approximately half of the enzyme present in solution would be able to oxidize phenol in single turnover experiments, but the yields were consistently lower than that value. This result contrasts with our findings for the wild-type and T201S variant. These findings indicate that decay of peroxodiiron(III) species is not tightly coupled to oxidation of hydrocarbon substrate when a hydroxyl group is lacking at position 201, presumably leading to release of hydrogen peroxide, rather than catechol, as an uncoupling product.[e]

Single-turnover yields from the reaction of the internal I100W substrate were also determined for T201X/I100W double variants. The extinction coefficient of the I100W radical species is $\varepsilon_{500\,\text{nm}} = \sim 1500\ \text{cm}^{-1}\text{M}^{-1}$, based on Mössbauer and stopped-flow UV-vis data.[22] Using this value, we were able to quantitate the amount of I100W-radical species generated in reactions of reduced T201X/I100W ToMOH and ToMOD with dioxygen. The

---

[e] We attempted to quantitate the concentration of H_2O_2 in this reaction, but previously reported catalase activity of ToMO led to the inaccurate measurement of H_2O_2 produced during single-turnover.

I100W radical species produced was measured by taking into account of the individual formation and decay rate constants corresponding to the time-dependent spectral changes at 500 nm, as described previously (Table 4.6).

Table 4.6 Quantification of I100W-Radical Species Generated in T201X/I100W ToMOH (X = S, C, G, V).

	I100W	T201S/I100W	T201C/I100W	T201G/I100W	T201V/I100W
Coupling (%)[a]	55 ± 1%	49 ± 1%	36 ± 2%	38 ± 1%	31 ± 2%

[a]per diiron centers

In I100W and T201S/I100W variants, ~50% of the I100W-radical species formed per diiron sites which is consistent with half-sites reactivity and ~50% of single turnover yields during phenol oxidation.[17] By contrast, ~30% of I100W-radical species per diiron sites were generated in the T201C/G/V variants, even though ~50% of the diiron sites presumably reacted with dioxygen. The uncoupling chemistry in T201C/G/V variants is consistent with the single-turnover yields of these species during phenol oxidation. In addition, the results agree with the steady state kinetics showing ~70-150 fold lower k_{cat}/K_M values for the T201C/G/V variants compared to the wild type and T201S enzymes. These results further support the notion that the hydroxyl group at position 201 site is necessary for efficient hydrocarbon oxidation.[17,30]

Comparisons of Oxygenated Intermediates and Their Reactivities in ToMOH and sMMOH. Reaction of sMMOH with dioxygen consecutively generates three oxygenated intermediates, P*, P or H_{peroxo}, and Q, and the latter two species are capable of oxidizing hydrocarbon substrates.[27-29] H_{peroxo} and Q react with substrates through different mechanisms, with H_{peroxo} preferring more electron-rich substrates, such as propylene, ethyl vinyl ether, and diethyl ether, and operating by a two-electron transfer process. In contrast, Q favors one-electron transfer chemistry for methane oxidation.[31] The promiscuous reactivity of sMMOH, therefore, can be attributed, at least in part, to the divergent reactions catalyzed by the two distinctive intermediates.

In contrast, ToMOH has evolved specifically to perform aromatic hydroxylation. A wide and long hydrophobic channel, ~6-10 Å by ~30-35 Å, is present only in toluene monooxygenases, where it most likely serves as the pathway for arene substrate access/product egress.[15,32] This structural feature may explain how ToMOH developed specificity for aromatic substrates. Oxidation of the arene can occur via two-electron transfer from substrates to an electrophilic oxidant, such as H_{peroxo} in sMMOH, the analogous species proposed for amine oxygenase,[33,34] and a hydroperoxoiron(III) intermediate in cytochrome P450 monooxygenase.[35] The $ToMOH_{peroxo}$ intermediate in ToMOH therefore most likely shares the electronic and geometric structures of hydroperoxoiron(III) or peroxodiiron(III) species rather than those of Q in sMMOH.

A mechanism for the oxidation of arenes by $ToMOH_{peroxo}$ is proposed in Scheme 4.4. As previously reported,[16] a Hammett plot for the oxidation of *para*-substituted phenols in ToMOH has a negative slope, consistent with the electrophilic character of $ToMOH_{peroxo}$. Electrophilic attack of the hydroperoxo unit in $ToMOH_{peroxo}$ on the arene ring can initiate the oxidation, followed by formation of an arene-oxide species, weakly bound to the diiron center. Addition of water and rearrangement can provide the arene product and return the resting state diiron site. A similar reaction with an arene substrate might be possible for $T201_{peroxo}$, although not kinetically feasible due to fast conversion to $ToMOH_{peroxo}$. Without such conversion, $T201_{peroxo}$ might participate in futile side reactions, becoming protonated with subsequent O–O bond cleavage and formation of a Q-type product with undesired reactivity.

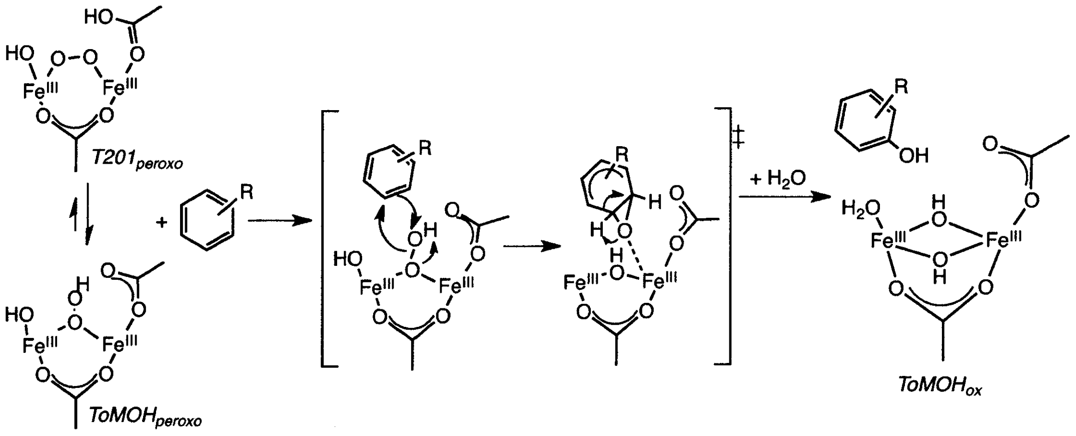

Scheme 4.4 Proposed Mechanism of Aromatic Hydroxylation by ToMOH$_{\text{peroxo}}$ and T201$_{\text{peroxo}}$ in T201 Variants of ToMOH.

4.4 CONCLUDING REMARKS

The present kinetic studies of T201$_{\text{peroxo}}$ in the absence and presence of external (phenol) or internal (tryptophan, as I100W) substrates clearly demonstrate that T201$_{\text{peroxo}}$ is kinetically on the reaction pathway of arene oxidation. Kinetic solvent isotope effects in the reaction of T201$_{\text{peroxo}}$ with phenol confirm this kinetic competence. Three reaction models were considered to account for the measured kinetics of T201$_{\text{peroxo}}$ and I100W-radical species formation and substrate reactivity. The only one that accounts for all of the experimental results requires that T201$_{\text{peroxo}}$ be in the equilibrium with ToMOH$_{\text{peroxo}}$. Acceleration in the decay rate of T201$_{\text{peroxo}}$ in the presence of arene substrates is therefore ascribed to the rapid conversion of T201$_{\text{peroxo}}$ to ToMOH$_{\text{peroxo}}$, the latter being the reactive species in arene oxidation.

REFERENCE

1. Merkx, M.; Kopp, D. A.; Sazinsky, M. H.; Blazyk, J. L.; Müller, J.; Lippard, S. J. (2001) *Angew. Chem. Int. Ed. 40*, 2782-2807.
2. Wallar, B. J.; Lipscomb, J. D. (1996) *Chem. Rev. 96*, 2625-2657.
3. Solomon, E. I.; Brunold, T. C.; Davis, M. I.; Kemsley, J. N.; Lee, S.-K.; Lehnert, N.; Neese, F.; Skulan, A. J.; Yang, Y.-S.; Zhou, J. (2000) *Chem. Rev. 100*, 235-349.
4. Nordlund, P.; Eklund, H. (1993) *J. Mol. Biol. 232*, 123-164.
5. Fox, B. G.; Shanklin, J.; Somerville, C.; Münck, E. (1993) *Proc. Natl. Acad. Sci. U.S.A. 90*, 2486-2490.
6. Xing, G.; Hoffart, L. M.; Diao, Y.; Sandeep Prabhu, K.; Arner, R. J.; Reddy, C. C.; Krebs, C.; Bollinger, J. M., Jr. (2006) *Biochemistry 45*, 5393-5401.
7. Vu, V. V.; Emerson, J. P.; Martinho, M.; Kim, Y. S.; Münck, E.; Park, M. H.; Que, L., Jr. (2009) *Proc. Natl. Acad. Sci. U.S.A. 106*, 14814-14819.
8. Choi, Y. S.; Zhang, H.; Brunzelle, J. S.; Nair, S. K.; Zhao, H. (2008) *Proc. Natl. Acad. Sci. U.S.A. 105*, 6858-6863.
9. Behan, K. R.; Lippard, S. J. (2010) *Biochemistry 49*, 9679-9681.
10. Lee, S.-K.; Fox, B. G.; Froland, W. A.; Lipscomb, J. D.; Münck, E. (1993) *J. Am. Chem. Soc. 115*, 6450-6451.
11. Liu, K. E.; Valentine, A. M.; Qiu, D.; Edmondson, D. E.; Appelman, E. H.; Spiro, T. G.; Lippard, S. J. (1995) *J. Am. Chem. Soc. 117*, 4997-4998.
12. Tinberg, C. E.; Lippard, S. J. (2009) *Biochemistry 48*, 12145-12158.
13. Notomista, E.; Lahm, A.; Di Donato, A.; Tramontano, A. (2003) *J. Mol. Evol. 56*, 435-445.
14. Leahy, J. G.; Batchelor, P. J.; Morcomb, S. M. (2003) *FEMS Microbiol. Rev. 27*, 449-479.
15. Sazinsky, M. H.; Bard, J.; Di Donato, A.; Lippard, S. J. (2004) *J. Biol. Chem. 279*, 30600-30610.
16. Murray, L. J.; Naik, S. G.; Ortillo, D. O.; García-Serres, R.; Lee, J. K.; Huynh, B. H.; Lippard, S. J. (2007) *J. Am. Chem. Soc. 129*, 14500-14510.
17. Song, W. J. (2011) Understanding Orchestrated Chemical Reactions in Toluene/*o*-Xylene Monooxygenase from *Pseudomonas Sporium* OX1, Ph.D. Thesis (Massachusetts Institute of Technology, Cambridge, MA).
18. Bochevarov, A. D.; Li, J.; Song, W. J.; Lippard, S. J.; Friesner, R. A. (2011) *J. Am. Chem. Soc. 133*, 7384-7397.
19. Cafaro, V.; Scognamiglio, R.; Viggiani, A.; Izzo, V.; Passaro, I.; Notomista, E.; Dal Piaz, F.; Amoresano, A.; Casbarra, A.; Pucci, P.; Di Donato, A. (2002) *Eur. J. Biochem. 269*, 5689-5699.
20. Gill, S. C.; von Hippel, P. H. (1989) *Analytical Biochemistry 182*, 319-326.
21. Gibbs, C. R. (1976) *Anal. Chem. 48*, 1197-1201.
22. Murray, L. J.; García-Serres, R.; McCormick, M. S.; Davydov, R.; Naik, S. G.; Kim, S.-H.; Hoffman, B. M.; Huynh, B. H.; Lippard, S. J. (2007) *Biochemistry 46*, 14795-14809.
23. Mitchell, K. H.; Rogge, C. E.; Gierahn, T.; Fox, B. G. (2003) *Proc. Natl. Acad. Sci. U.S.A. 100*, 3784-3789.

24. Cox, D. D.; Que, L., Jr. (1988) *J. Am. Chem. Soc. 110*, 8085-8092.
25. Quinn, D. M.; Sutton, L. D., *Theoretical Basis and Mechanistic Utility of Solvent Isotope Effects, in Enzyme Mechanism from Isotope Effects* CRC Press: Boca Raton, FL., 1991.
26. Vidakovic, M.; Sligar, S. G.; Li, H.; Poulos, T. L. (1998) *Biochemistry 37*, 9211-9219.
27. Kwart, H. (1982) *Acc. Chem. Res. 15*, 401-408.
28. Bahnson, B. J.; Klinman, J. P. (1995) *Methods Enzymol. 249*, 373-397.
29. Tinberg, C. E.; Song, W. J.; Izzo, V.; Lippard, S. J. (2011) *Biochemistry 50*, 1788-1798.
30. Elsen, N. L.; Bailey, L. J.; Hauser, A. D.; Fox, B. G. (2009) *Biochemistry 48*, 3838-3846.
31. Baik, M.-H.; Gherman, B. F.; Friesner, R. A.; Lippard, S. J. (2002) *J. Am. Chem. Soc. 124*, 14608-14615.
32. Bailey, L. J.; McCoy, J. G.; Phillips, G. N. Jr.; Fox, B. G. (2008) *Proc. Natl. Acad. Sci. U.S.A. 105*, 19194-19198.
33. Korboukh, V. K.; Li, N.; Barr, E. W.; Bollinger, J. M., Jr.; Krebs, C. (2009) *J. Am. Chem. Soc. 131*, 13608-13609.
34. Li, N.; Korboukh, V. K.; Krebs, C.; Bollinger, J. M., Jr. (2010) *Proc. Natl. Acad. Sci. U.S.A. 107*, 15722-15727.
35. Meunier, B.; de Visser, S. P.; Shaik, S. (2004) *Chem. Rev. 104*, 3947-3980.

Chapter 5

Tracking a Defined Route for O_2-Migration in a Dioxygen-Activating Diiron Enzyme, Toluene/*o*-Xylene Monooxygenase Hydroxylase

*Reproduced in part with from a following manuscript,

Woon Ju Song, Grant Gucinski, Matthew H. Sazinsky, and Stephen J. Lippard "Tracking a Defined Route for O_2-Migration Pathway in a Dioxygen-Activating Enzyme" **2011**, *submitted*

5.1. INTRODUCTION

A large number of metalloenzymes utilize dioxygen as a substrate. Understanding the process by which O_2 gains access to the active sites in these proteins has been a great challenge. Common substrates in biological systems, such as protons and electrons, require specific environments to facilitate translocation.[1-4] By contrast, gaseous substrates like dioxygen may quickly diffuse through a protein matrix without direct assistance of specific local residues. Several enzymes that utilize gas molecules, such as O_2,[5,6] H_2,[6,7] or CO_2,[8] as substrates have been investigated to understand how these small substances traverse the protein to reach their active sites. Most studies depended primarily on X-ray crystallography combined with Xe pressurization experiments to determine hydrophobic voids within the protein architecture that can be utilized to delineate substrate passage. The strong electron density and similar van der Waals diameter of xenon (4.3 Å) compare to that of O_2 (3.0-4.3 Å) renders it a useful surrogate for visualizing possible dioxygen routes within proteins by X-ray crystal structure analysis.[5,7] Because small gaseous molecules bind in a non-selective manner to the hydrophobic cavities in a protein, however, further evidence is required to elucidate the actual O_2 transfer pathway.

Bacterial multicomponent monooxygenases (BMMs) utilize dioxygen, protons, and electrons as co-substrates for hydrocarbon oxidation. Dioxygen activation, inter- and intra-protein electron transfer, proton translocation, and C–H oxidation occur through orchestrated motions of three or four components, a hydroxylase, regulatory protein, reductase, and/or Rieske protein),[9,10] such that the kinetics of substrate consumption and product formation are finely tuned. BMMs have been extensively investigated over the past two decades.[11,12] Complexity from multiple and concurrent reactions involving several component proteins, however, has impeded the elucidation of important chemical steps during catalysis, including dioxygen migration to the active site.

The first X-ray structure of a BMM, soluble methane monooxygenase hydroxylase (sMMOH),[13] revealed the diiron active center to lie adjacent to a hydrophobic pocket, buried ~ 12 Å beneath the protein surface. As a first step in approximating the dioxygen transfer pathway in sMMOH, a structure using crystals pressurized with xenon gas was obtained.[14] The Xe atoms localize in a few isolated hydrophobic sites in the α-subunits of the enzyme, hereafter referred to as cavities. Similar results were obtained for another BMM, phenol hydroxylase hydroxylase (PHH), suggesting that the conserved cavities possibly function as a universal dioxygen transfer pathway.[15] This working model, derived only from resting state enzyme structures, neglects dynamic and flexible protein motions that might occur during catalysis. Moreover, the discovery of an extended channel through the a-subunits in toluene/*o*-xylene monooxygenase hydroxylase (ToMOH) provided an alternative architecture of potential relevance for dioxygen transfer.[16] This finding raised the question, for the BMM family, how does dioxygen access the active sites and is there a conserved pathway?

To address this question, a method other than structural characterization is required. Measuring substrate specificity (k_{cat}/K_M) for dioxygen in different protein variants is not a feasible approach because it necessitates the critical assumption that the kinetics of dioxygen access will be reflected in a rate-limiting step(s) during steady-state catalysis. Structural modeling and molecular dynamics simulations may not be applicable to BMMs because significant structural changes are expected to occur via component interactions during catalysis. Instead we employed in this work a different method to interrogate the dioxygen transfer pathway in ToMOH. We directly measured the dependence of the rate of oxygenation of the diiron center in the enzyme on the concentration of dioxygen under pre-steady-state conditions and compared the results for several variants in which the volume occupied by the side chain of different amino acids along putative O_2 pathways was altered by site-directed mutagenesis. This approach was possible because an oxygenated intermediate ($T201_{peroxo}$) in a T201S variant of ToMOH, previously monitored during dioxygen activation by reduced ToMOH in the presence of its cognate regulatory protein, ToMOD, forms at rates that are linearly dependent on the concentration of dioxygen.[17] This result indicated that dioxygen access to the diiron site is rate-limiting step in $T201_{peroxo}$ formation under pre-steady state conditions. Thus the $T201_{peroxo}$ formation rate can reveal the rate of dioxygen migration/binding to the diiron active site, which has never been explored in any diiron-containing enzyme. Because T201S is a functionally conserved variant with respect to the wild-type enzyme in steady-state activity, single-turnover yields, and regiospecificity,[17] the results of this study are physiologically relevant to the dioxygen transfer pathway in the native enzyme. Although sMMOH is the more thoroughly investigated BMM, there are two experimental limitations to application of the same methodology for this enzyme. First, the dioxygen access or binding step has never been directly observed. Upon the reaction of reduced sMMOH with dioxygen in the presence of its regulatory protein, the first oxygenated species to appear does so at rates much slower than the decay rate of the reduced diiron centers, indicating that O_2 consumption is coupled with, or preceded by, slower step(s), possibly structural reorganization or formation of uncharacterized intervening species.[18,19] In addition, a recombinant expression system to produce sMMOH variants in sufficient quantities for mutagenesis studies has never been achieved. Toluene monooxygenases including ToMOH can be expressed in *E. coli,* however, thus facilitating site-directed mutagenesis studies.[20,21]

Based on the X-ray structures of ToMOH and an analogous protein, toluene 4-monooxygenase hydroxylase (T4moH),[22] nine residues from among those identified as plausible candidates for the dioxygen transfer pathway were selected for mutagenesis. Variations of amino acid side chains alter the dimensions of the individual pathways as a result of their different molecular volumes. The variants were designed primarily based on size rather than hydrophobicity because steric bulk and the attendant alterations in the volume of the pathways are most critical for controlling O_2 access.[23]

In the experiments described here, a T201S mutation was therefore introduced to provide a sensor, in the form of an optical transition at 675 nm,[17] to detect dioxygen arrival at the diiron sites via formation of the $T201_{peroxo}$ intermediate. Double or triple variants were prepared and crystallographically characterized to evaluate whether or not the additional mutation would modify the dimensions of various hydrophobic sites along a putative pathway chosen for interrogation. Finally, $T201_{peroxo}$ formation rates were individually measured from the reaction of the reduced ToMOH variants and dioxygen in the presence of ToMOD to evaluate whether the steric alterations along the potential O_2-transport pathways would result in significant increases or decreases in the dioxygen transfer rates.

5.2. MATERIALS AND METHODS

General Considerations. Heterologous expression and purification of the four ToMO component proteins were carried out as described previously.[17,20] For site-directed mutagenesis, a pET22b(+)/touBEA T201S plasmid was used as the template as described previously.[17] Primers used to generate the mutations are listed in Table 5.1 and were obtained from Integrated DNA Technologies. Detailed procedures for the expression and purification of the mutants,[17] iron assays,[20] and specific activity assays[24] were described previously. These results are summarized in Table 5.2. Extinction coefficients at 280 nm of the ToMOH variants were calculated based on the sequence.[25]

Crystallization, Data collection, Structure Determination, and Refinement. X-ray crystallographic studies of T201 variants of ToMOH were carried out by Grant Gucinski and Prof. Matthew H. Sazinsky (Pomona College, Claremont, CA). Seven ToMOH T201X variants, T201S/I100W, T201S/I100A, T201S/F205W, T201S/L272E, T201S/I276E, T201S/V271A, and T201S/W167E were crystallized by using previously published procedures.[16] X-ray diffraction data were collected at the NE-CAT beam line 24IDE or at SSRL beam line 12-2 and processed using either HKL2000 or iMosflm. Phasing of ToMOH data was accomplished by using MolRep and the 1.85 Å native ToMOH coordinates (PDB 2INC) as described previously.[26] Refinements and building were carried out by Refmac5 and Coot, respectively (Table 5.3).

Characterization of an Oxygenated Intermediate in ToMOH Variants by Optical Spectroscopy. Optical bands characteristic of the oxygenated intermediate in T201S variants of ToMOH, $T201_{peroxo}$, were monitored by using a HiTech DX2 stopped-flow spectrophotometer. The procedures to measure formation and decay rate constants of $T201_{peroxo}$ were described previously.[17] Second-order formation rate constants were obtained by plotting the pseudo-first order formation rate constants versus the dioxygen concentrations used in the reactions and fit to a liner function to measure the slope (Figure 5.4).

Table 5.1 The primers used for the preparation of ToMOH variants.

Variants	Primers
I100W	5'-CAA CTT CAC TTC GGA GCG TGG GCA CTT GAA GAA TAC G-3'
	5'-C GTA TTC TTC AAG TGC CCA CGC TCC GAA GTG AAG TTG-3'
I100A	5'-CAC TTC GGA GCG GCT GCA CTT GAA GAA TAC-3'
	5'-GTA TTC TTC AAG TGC AGC CGC TCC GAA GTG-3'
W167E	5'-CAT ACT AAC GAA GAA GCC GCA ATC GCG GCA CGG-3'
	5'-CCG TGC CGC GAT TGC GGC TTC TTC GTT AGT ATG-3'
F176A	5'-GCT GCA CGG TCT TTC GCT GAC GAC ATG ATG-3'
	5'-CAT CAT GTC GTC AGC GAA AGA CCG TGC AGC-3'
F176W	5'-GCA CGG TCT TTC TGG GAC GAC ATG ATG ATG -3'
	5'-CAT CAT CAT GTC GTC CCA GAA AGA CCG TGC -3'
F205A	5'-C AGC AAT ATG CAG GCT CTC GGT TTG GCC G-3'
	5'-C GGC CAA ACC GAG AGC CTG CAT ATT GCT G-3'
F205W	5'-GGC TTC AGC AAT ATG CAG TGG CTC GG T TTG GCC GCT GAC-3'
	5'- GTC AGC GGC CAA ACC GAG CCA CTG CAT ATT GCT GAA GCC-3'
L208W	5'-CAG TTT CTC GGT TGG GCC GCT GAC GCT G-3'
	5'-C AGC GTC AGC GGC CCA ACC GAG AAA CTG-3'
L208W/D211W	5'-G TTT CTC GGT TGG GCC GCT TGG GCT GCT G-3'
	5'-C AGC AGC CCA AGC GGC CCA ACC GAG AAA C-3'
V271A	5'-G AAG CTT TTC TCG GCT CTC ACC GGC CC-3'
	5'-GG GCC GGT GAG AGC CGA GAA AAG CTT C-3'
L272A	5'-G CTT TTC TCG GTA GCT ACC GGC CCC ATC-3'
	5'-GAT GGG GCC GGT AGC TAC CGA GAA AAG C-3'
L272E	5'-G CTT TTC TCG GTA GAA ACC GGC CCC ATC-3'
	5'-GAT GGG GCC GGT TTC TAC CGA GAA AAG C-3'
I276E	5'-GTA CTC ACC GGC CCC GAA ATG GAT TAT TAC AC-3'
	5'-GT GTA ATA ATC CAT TTC GGG GCC GGT GAG TAC-3'

5.3. RESULTS AND DISCUSSION

Structural Analysis of ToMOH and Design of Mutants. An X-ray crystal structure of ToMOH revealed three potential access routes leading from the protein exterior to the diiron active sites as putative dioxygen transfer pathways. They are a (i) series of adjacent cavities, (ii) a pore, and (iii) a channel (Figure 5.1A). Similar features occur in the structure of T4moH.[22]

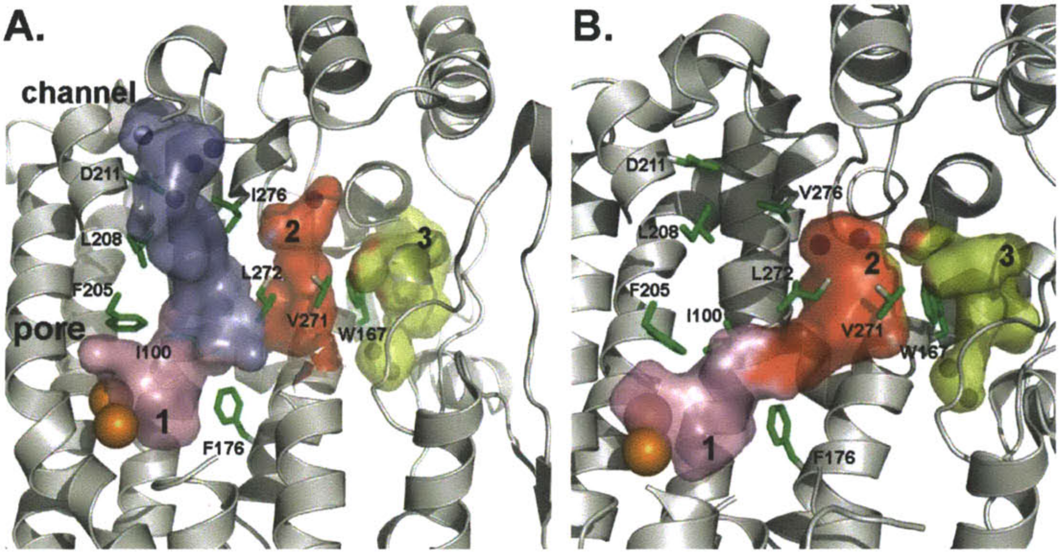

Figure 5.1 Cartoon representations of the cavities and channel in structures. (A) ToMOH (2INC) (B) T4moH-T4moD complex (3I5J). Residues I100, W167, F176, F205, L208, D211, V271, L272, and I276 are depicted as green sticks. Water occupying cavities and channel are represented as blue spheres. The diiron center is denoted by orange spheres.

Route i comprises three adjacent hydrophobic cavities 1, 2, and 3, numbered according to their increasing distance from the diiron active site. They are conserved in all structurally characterized BMMs. In previous X-ray studies conducted with crystals of BMM hydroxylases exposed to Xe under pressure, this inert gas was readily observed in the cavities.[14,15] This finding suggested that the cavities might serve as access routes for O_2 and/or small hydrophobic molecules such as CH_4 to the active site.

The pore, route ii, is the smallest and shortest pathway from bulk solvent to the active sites. It is conserved in some BMMs, with a size and shape that varies depending on the enzyme. Structural studies of PHH and T4moH in complex with their respective regulatory proteins revealed that the latter bind to the hydroxylase where the pore region exits the protein surface.[22,27] Because of this interaction, the pore is no longer exposed to solvent and therefore less likely to provide a route for dioxygen transfer; the regulatory proteins are required for dioxygen activation. Moreover, reduction of the diiron sites triggers conformational changes near the pore region, which would also make the pore unavailable for O_2 transport even in the absence of regulatory protein binding.[28] Based on these observations, we excluded the possibility that the pore is involved in dioxygen transfer.

Route iii, a long hydrophobic channel found only in toluene monooxygenases including ToMOH and T4moH, has a width and length of 6-10 Å and 30-35 Å, respectively, more than sufficient to accommodate dioxygen passage.[16,22] The channel is connected to the diiron active site, overlapping with cavities 1 and 2 at the entryway (Figure 5.1A). It is therefore a plausible path for dioxygen as well as arene substrate transport, for which it was originally proposed. Extensive structural changes occur in the channel upon binding of the regulatory protein (T4moD) to T4moH (Figure 5.1B), however, altering the conformations of amino acid side chains and effectively closing it off from the protein exterior.[22] The structures of the T4mmoH and T4moH/D suggest that the channel will transiently open and close during catalysis. Given that the rate of dioxygen transport must be fast enough to access even a transiently accessible pathway, we considered both the cavities and the channel as candidates for O_2 access to the diiron center.

To evaluate the dioxygen transfer pathway in ToMOH, we selectively mutated six residues that form the cavities, I100, W167, F176, F205, V271, and L272, and three that line the channel, L208, D211, and I276 (Figure 5.1A). Each residue was altered to adjust the channel dimensions in its vicinity. As described above, T201 was also mutated to T201S in order to provide a convenient optical signal, arising from $T201_{peroxo}$ formation, by which to monitor the dioxygen transfer rate constants under pre-steady state conditions.

Fe Content and Specific Steady-State Activity. To assure that the mutations did not perturb the global folding, component interactions, or active site structure of the enzyme system, the iron content and steady-state activity for phenol oxidation were measured. The variants were prepared and characterized as previously described.[17] All 13 variants contained 3-4 iron atoms per protein dimer, similar to the content of the wild-type enzyme (Table 5.2). Specific steady-state activities for phenol oxidation, measured as described previously,[24] are listed in Table 5.2. Results for the T201S/F176A, T201S/V271A, T201S/L272A, and T201S/I276E variants are comparable to those of the wild type enzyme and T201S variant. The activities of T201S/I100A, T201S/W167E, T201S/F205A, and T201S/L272E were reduced but only by ~3-10 fold relative to that of the wild-type enzyme.

Table 5.2 Fe contents and specific steady state activities of ToMOH variants.

Mutants	Fe Contents ([Fe]/[ToMOH])	Specific steady state activity (mU/mg)
Wild-type	3.7 ± 0.6	1200 ± 200
T201S	4.15 ± 0.04	2400 ± 300
T201S/I100A	4.14 ± 0.06	470 ± 130
T201S/I100W	3.43 ± 0.03	nd[b]
T201S/W167E	5.97 ± 0.29[a]	720 ± 50
T201S/F176A	2.72 ± 0.10	1290 ± 80
T201S/F176W	3.19 ± 0.14	nd[b]
T201S/F205A	2.76 ± 0.08	230 ± 50
T201S/F205W	4.72 ± 0.13	nd[b]
T201S/L208W	4.74 ± 0.09	nd[b]
T201S/L208W/D211W	4.10 ± 0.06	nd[b]
T201S/V271A	3.22 ± 0.07	1140 ± 100
T201S/L272A	4.78 ± 0.02	940 ± 140
T201S/L272E	6.8 ± 0.1[a]	310 ± 40
T201S/I276E	5.9 ± 0.1[a]	1400 ± 490

[a] A few variants displayed more than four iron atoms per protein, possibly due to the binding of adventitious Fe ion. In such case, protein was reduced and dialyzed anaerobically for ~3-4 hrs to remove the futile Fe ions. The protein samples after the additional procedure reduced the iron contents up to ~4 Fe ions per protein. [b] Not detected.

These results suggest that some chemical step(s) during steady-state catalysis are slightly perturbed, but that all are still active enzymes. For the substitution of a few residues, specifically I100, F176, or F205 with tryptophan, phenol oxidation activity was lost, probably because the newly supplied tryptophan residue serves as an internal substrate without perturbing dioxygen activation at the diiron center, as previously observed.[29]

Formation of the one-electron oxidized product, a tryptophan-radical species, was monitored at 500 nm under pre-steady state conditions (data not shown), indicating that these variants are still able to activate dioxygen. The T201S/L208W and T201S/L208W/D211W variants were also unable to oxidize phenol. Oxidation of the indole rings in L208W and D211W, however, might be difficult because they are located much farther from the diiron center, and no absorption at 500 nm was observed. The inability of the T201S/L208W and T201S/L208W/D211W variants to function as phenol oxidation catalysts suggests that these mutations perturb the enzyme structure and are therefore not suitable for the current study. Accordingly, they were not further pursued.

Structural and Kinetic Studies of ToMOH Variants. Structural alterations arising from each of the amino acid substitutions were evaluated by X-ray crystallography. Seven variants were prepared and structurally characterized, namely, T201S/I100W, T201S/F205W, T201S/I100A, T201S/L272E, T201S/V271A, T201S/W167E, and T201S/I276E (Figure 5.2 and Table 5.3). None caused misfolding or global structural changes in the protein, only local alterations near the modified side chain. Rates of dioxygen transfer to the diiron active sites were measured by the following procedure. Reduced ToMOH variants in complex with ToMOD (ToMOH$_{\mathrm{red}}$D) (~60-150 μM in 25 mM MOPS, pH 7.0) were allowed to react with O_2-saturated buffer in the stopped-flow spectrophotometer at 4 °C. Time-dependent absorption changes arising from the formation and decay of T201$_{\mathrm{peroxo}}$ were monitored at 675 nm. The traces were very well fit to a function derived from two consecutive irreversible processes, reduced ToMOH $\rightarrow$ T201$_{\mathrm{peroxo}}$ $\rightarrow$ oxidized ToMOH, from which formation rate constants (k_{form}) could be derived.

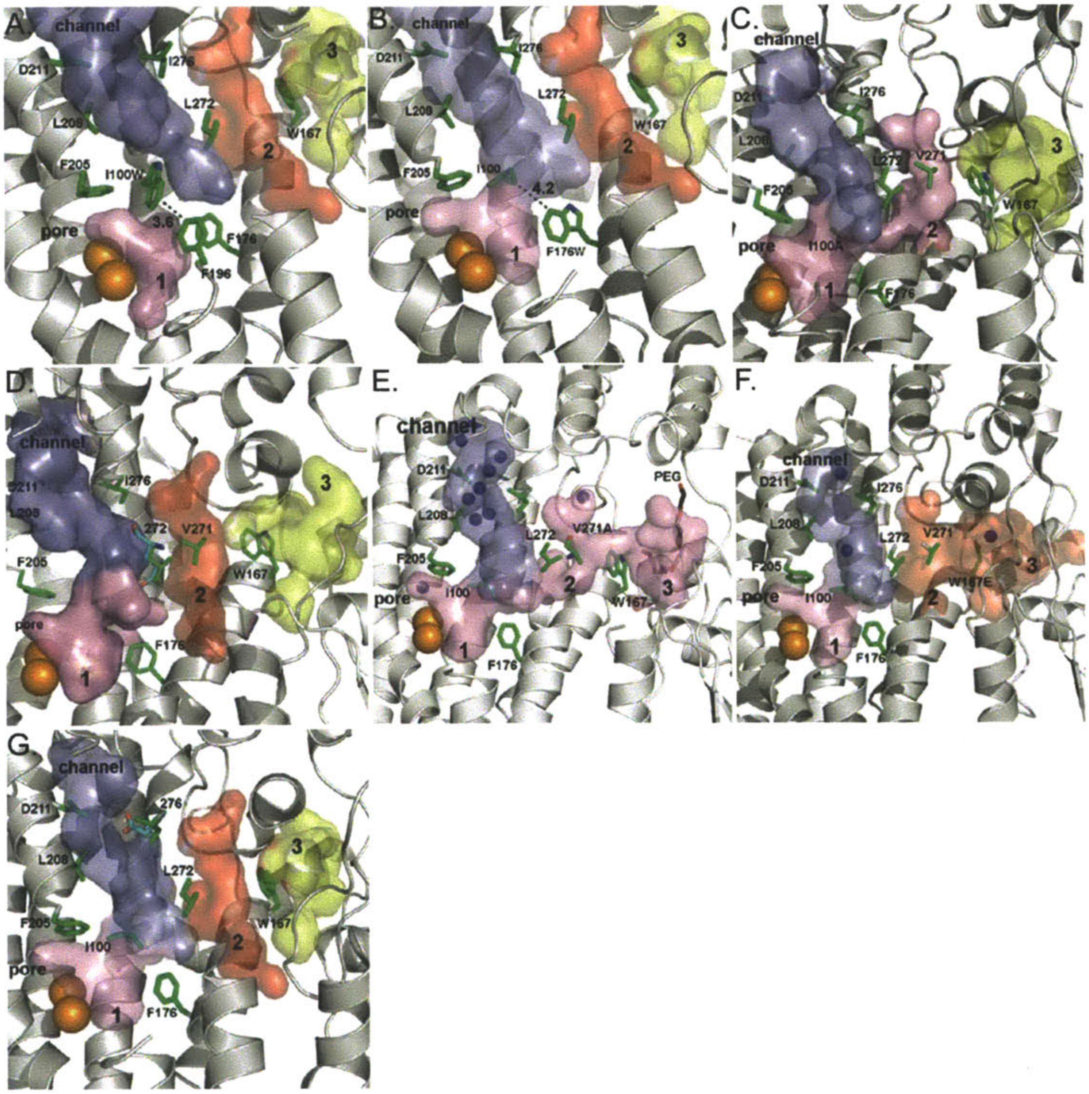

Figure 5.2 Structural comparisons of ToMOH variants. Structures were represented in the same manner as Figure 5.1 (A) T201S/I100W (B) T201S/F176W (C) T201S/I100A (D) T201S/L272E (E) T201S/V271A (F) T201S/W167E (G) T201S/I276E. In Figure 5.2D and Figure 5.2G, side chains of L272 and I276 residues in the wild type were overlaid to the variants and represented in cyan sticks for comparison.

Table 5.3 X-ray data collection and refinement statistics of ToMOH variants.

	T201S/I100A	T201S/I100W	T201S/W167E	T201S/F176W	T201S/V271A	T201S/L272E	T201S/I276E
Data Collection							
Beamline	NE-CAT 24 ID-E	NE-CAT 24 ID-E	NE-CAT 24 ID-E	NE-CAT 24 ID-E	SSRL 12-2	NE-CAT 24 ID-E	NE-CAT 24 ID-E
Wavelength (Å)	0.979	0.979	0.979	0.979	1.034	0.979	0.979
Space Group	$P3_121$	$P3_121$	$P3_121$	$P3_121$	$P3_121$	$P3_121$	$P3_121$
Unit cell dimensions (Å)	182.6 x 182.6 x 67.0	182.8 x 182.8 x 67.7	182.6 x 182.6 x 68.3	183.1 x 183.1 x 68.0	183.4 x 183.4 x 68.3	182.4 x 182.4 x 67.5	183.0 x 183.0 x 68.0
Resolution range (Å)	30.0 - 2.75	50.0 – 3.00	50.0 – 2.80	50.0 – 2.65	50.0 – 2.2	50.0 – 2.80	50.0 – 2.50
Total Reflections	195303	149031	199829	230251	598335	244050	293744
Unique Reflections	27980	24140	29390	36462	66756	30252	43135
Completeness (%)[a]	93.7 (95.3)	96.6 (97.4)	96.6 (97.9)	99.7 (100)	99.7 (100)	99.6 (100)	99.7 (99.8)
$I/\sigma(I)$[a]	21.8 (4.0)	30.1 (9.0)	26.2 (4.6)	33.1 (7.4)	16.4 (6.9)	25.3 (7.2)	26.9 (5.2)
R_{sym} (%)[a,b]	10.2 (42.1)	10.3 (26)	10.1 (42.3)	9.2 (36.6)	10.0 (31.7)	13.9 (40.8)	9.9 (39.3)
Refinement							
R_{cryst} (%)[c]	19.0	18.0	19.5	17.8	15.6	16.4	18.4

R_{free} (%)[d]	25.1	24.1	26.0	23.5	20.0	22.7	23.4
Average B-value ($Å^2$)	64.1	53.0	52.3	45.9	24.2	27.6	42.8
r.m.s deviation bond length (Å)	0.008	0.016	0.015	0.019	0.024	0.016	0.021
r.m.s deviation bond angles (°)	1.11	1.65	1.66	1.81	1.81	1.61	1.83
No. Protein Atoms	7331	7340	7329	7368	7355	7348	7335
No. Non-Protein Atoms	53	57	51	169	586	239	298
Fe Atoms	2	2	2	2	2	2	2
Water Molecules	46	55	49	152	566	212	296
PEG-400 Fragments	1	0	0	0	2	2	0
RMSD to Wild-Type ToMOH	0.20	0.19	0.23	0.16	0.17	0.16	0.15

[a] Values in parentheses are for the highest resolution shell. [b] $R_{sym} = \Sigma_i \Sigma_{hkl} |I_i(hkl) - \langle I(hkl) \rangle| / \Sigma_{hkl} \langle I(hkl) \rangle$, where $I_i(hkl)$ is the ith measured diffraction intensity and $\langle I(hkl) \rangle$ is the mean intensity for the Miller index (hkl). [c] $R_{cryst} = \Sigma_{hkl} ||F_o(hkl)| - |F_c(hkl)|| / \Sigma_{hkl} |F_o(hkl)|$. [d] $R_{free} = R_{cryst}$ for a test set of reflections (5% in each case).

In the T201S single variant, k_{form} is linearly dependent on O_2 concentration, yielding the second-order formation rate constant (k_2) of 0.22 ± 0.01 $\mu M^{-1}s^{-1}$, as reported previously (Figure 5.4A).[17] This value is significantly lower than that expected for a purely diffusion-controlled encounter ($\sim 10^9$ $M^{-1}s^{-1}$), implying that O_2 migration through the protein slows down access to the active site diiron center and is probably coupled to structural fluctuations because the cavities along path i are not fully connected in the X-ray structures.

Tracking O_2 entrance to Cavity 1. The I100 residue is located at the entry position to cavity 1 (Figure 5.1). Based on the sequence and structural alignments, I100 in ToMOH was previously proposed to be the analog of L110 in sMMOH, gating access to the active site.[30] Two different conformations at L110 occur in two crystal forms of sMMOH, suggesting that L110 may shift its position to control the opening of cavity 1 during catalysis. Analogously, different conformations at I100 occur upon binding of the regulatory protein in the T4moHD structure (Figure 5.3A), with the binding of the regulatory protein causing the side chain to swing out, opening access to the diiron center.

Conversion of residue I100 to tryptophan in the T201S/I100W variant partially occludes active site entry from cavity 1, the indole ring stacking on F196 at a nearly van der Waals distance of 3.6 Å (Figure 5.2A). The closest C···C distance of I100 to F196 in the wild-type enzyme is 5.9 Å. The dioxygen transfer rate should therefore be greatly reduced if I100 were on the O_2 transfer pathway. Pre-steady state studies of the reaction of a T201S/I100W ToMOH$_{\text{red}}$D pre-formed complex with O_2 revealed that k_{form} is linearly dependent on the O_2 concentration, but has a rate constant ~3-fold lower than that of the T201S variant (Table 5.4 and Figure 5.4B).

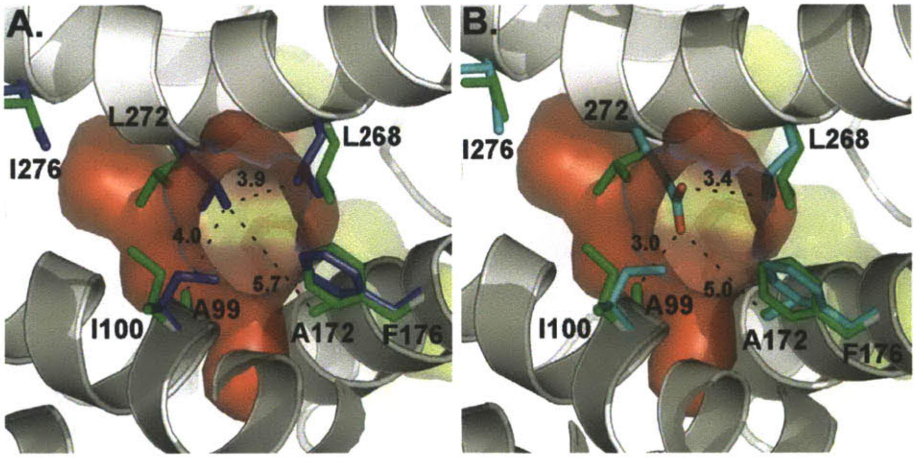

Figure 5.3 Structural comparisons of ToMOH and T4moHD. (A) Superposition of residues gating access between cavities 1 and 2 in T4moH-T4moD (green sticks) and ToMOH (blue sticks) structures. Cavity 2 of the T4moH-T4moD structure was shown as red surfaces. Distances between L272 and L268, A172, and A99 in the T4mo structure were 6.7 Å, 8.0 Å, and 4.5 Å, respectively. (B) Superposition of the T4moH-T4moD complex and ToMOH T201S/L272E (cyan sticks).

Table 5.4 $T201_{peroxo}$ Formation Rates in ToMOH Variants. Second-order formation rate constants were obtained from at least three independently prepared batches of the protein samples. Representative plots of $T201_{peroxo}$ formation rate constants versus dioxygen concentrations were shown in Figure 5.4.

Mutant	Second-order formation rate constant, k_2 ($s^{-1}\mu M^{-1}$)	Relative second-order formation rate constant
T201S	0.22 ± 0.01	-
T201S/I100W	0.06 ± 0.01	0.29 ± 0.05
T201S/L272E	0.12 ± 0.02	0.57 ± 0.10
T201S/I276E	0.29 ± 0.08	1.38 ± 0.39
T201S/V271A	0.48 ± 0.06	2.29 ± 0.31
T201S/W167E	0.92 ± 0.10	3.37 ± 0.55

The data indicate the I100W mutation retards dioxygen transfer, consistent with cavity 1 being the dioxygen transfer pathway. The decay rate of the $T201_{peroxo}$ intermediate in the T201S/I100W variant was accelerated relative to the value in the T201S variant because the indole ring at I100W can serve as an internal substrate for T201$_{peroxo}$, as described previously.[17]

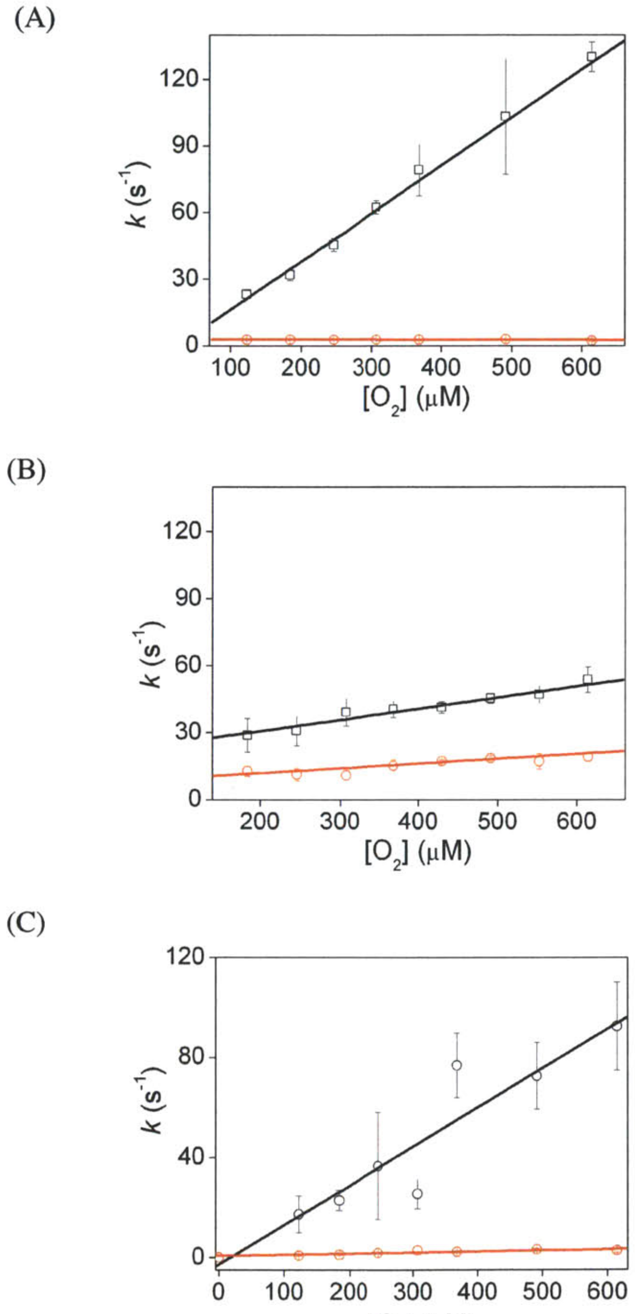

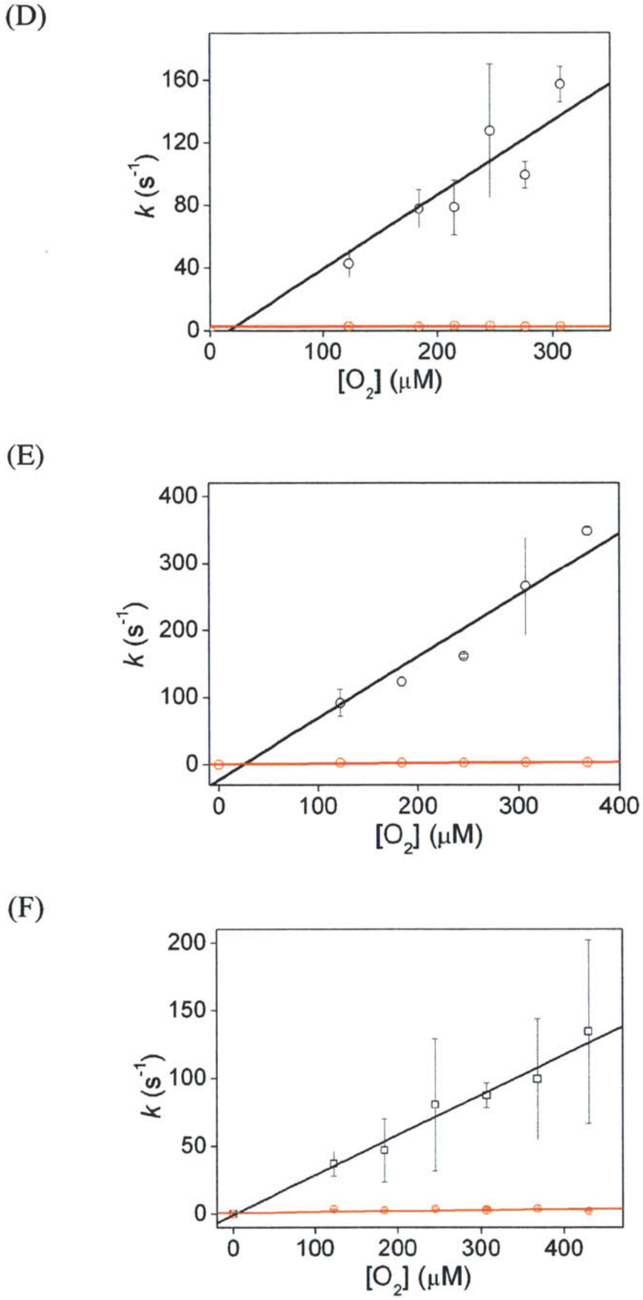

Figure 5.4 Plots of formation rate constants of T201$_{peroxo}$ versus dioxygen concentrations. Formation and decay rates were measured in the reaction of reduced ToMOH variants (~ 60-150 μM in 25 mM MOPS, pH7.0) and 3 equiv of ToMOD to the hydroxylase with various concentrations of dioxygen at 4 °C. (A) T201S, (B) T201S/I100W, (C) T201S/L272E, (D) T201S/V271A, (E) T201S/W167E, and (F) T201S/I276E ToMOH variants. Formation and decay rate constants were represented as black squares and red circles, respectively. Both formation and decay rates were fit to a linear function as

depicted with black and red lines, respectively. Second-order formation rate constants were obtained from a slope of a linear fit. Linear fit of decay rates in all variants, shown in red line, yielded no or very small slope indicating that decay of T201$_{\text{peroxo}}$ were independent of dioxygen concentrations.

F176 is also located in cavity 1 (Figure 5.1). Structural and kinetic alterations as a result of the F176W mutation were therefore expected to be similar to those observed for I100W. The F176W substitution contracts the entrance to cavity 1 (Figure 5.2B). The closest C···C distance between the I100 and F176 is 6.0 Å in the T201S variant is reduced to 4.2 Å by the additional F176W mutation. In addition to the F176W mutation, F205 residue in cavity 1 was substituted to the tryptophan to further probe the putative role of the cavity 1 as part of the dioxygen transfer pathway. Reaction of neither T201S/F176W nor T201S/F205W ToMOH$_{\text{red}}$D with dioxygen, however, produced the optical spectrum of T201$_{\text{peroxo}}$, possibly because both F176W and F205W residues reacted as internal substrates of T201$_{\text{peroxo}}$, as similarly occurred in T201S/I100W mutant and accelerated the decay of T201$_{\text{peroxo}}$. These two variants in cavity 1 failed to accumulate T201$_{\text{peroxo}}$, possibly because the positions where the indole rings are introduced, F176 and F205, are closer to the diiron sites than I100 so that reaction between the oxygenated intermediate and the indole rings occur more rapidly.

The I100A mutation brings about a different structural effect at I100 compared to the I100W, F176W, and F205W variations, enlarging the entrance to cavity 1, as revealed by an X-ray crystal structure analysis of T201S/I100A (Figure 5.2C). In this variant, the shortest C···C distance increases from 5.9 Å to 8.1 Å. As a result, cavity 1 becomes large enough to be fully connected to cavity 2. Although crystal structures of the F176A and F205A variants were not determined, PYMOL[31] simulations (not shown) suggested that the mutations increase the size of cavity 1. The abilities of the T201S/I100A, T201S/F176A, and T201S/F205A variants to activate dioxygen were individually monitored. None showed any evidence of $T201_{peroxo}$ formation, although they were still active enzymes for phenol oxidation under steady-state conditions. One possibility is that adventitious water/proton(s) become accessible through the larger cavity 1 in I100A, F176A, and F205A mutants, which might quench $T201_{peroxo}$, leading to release of H_2O_2. Such autoxidation due to the opening of hydrophobic sites near the active site was previously observed for variants of myohemerythrin.[32]

O_2 Passage through Cavity 2. Residue L272 is located in cavity 2, close to the intersection with cavity 1 and the channel. The closest C···C distances between L272 and cavity 1 (F196) or channel (Q204) residues are 10.6 Å and 6.1 Å, respectively. Structures of T4moH in the absence and presence of T4moD reveal that the orientation of side chain at L272 can vary significantly, suggesting a leucine gate (Figure 5.3B) similar to that identified in sMMOH.[30] Because glutamate is bulkier than leucine, the L272E mutation reduces the size of the protein interior where cavity 1, cavity 2, and the channel merge (Figure 5.2D and Figure 5.3B). As a consequence, the L272E and F196/Q204 residues are 6.1 Å and 5.9 Å apart, respectively. The structural changes suggest that the $T201_{peroxo}$ formation rate will be decelerated if L272 were a part of the dioxygen transfer pathway. Reaction of the T201S/L272E variant of $ToMOH_{red}D$ with dioxygen generated $T201_{peroxo}$ in a yield half the value of the T201S variant (Table 5.4 and Figure 5.4C). This result reveals that cavity 2 is a part of the dioxygen transfer pathway, in conjunction with cavity 1.

A T201S/L272A variant was prepared in an attempt to gauge the effect of an enlarged cavity 2, because removal of the side chain at L272 makes cavity 2 significantly wider than the native and T201S enzymes. Dioxygen activation of the T201S/L272A, however, revealed no detectible formation of $T201_{peroxo}$, probably because of autoxidation as encountered in the T201S/I100A, T201S/F176A, and T201S/F205A mutants described above.

V271 is located in cavity 2. The side chain resides at the interface between cavity 2 and cavity 3 and possibly gates movement between the two cavities during catalysis. The V271A mutation enlarges cavity 2 and creates a direct path from cavity 1 to cavity 3 (Figure 5.2E). During dioxygen activation in the T201S/V271A variant, formation of $T201_{peroxo}$ was observed, yielding a second-order formation rate constant of $T201_{peroxo}$, approximately twice that in T201S (Table 5.4 and Figure 5.4D). This result, in addition to the L272E mutation, therefore, indicates that cavity 2 is utilized in dioxygen transfer.

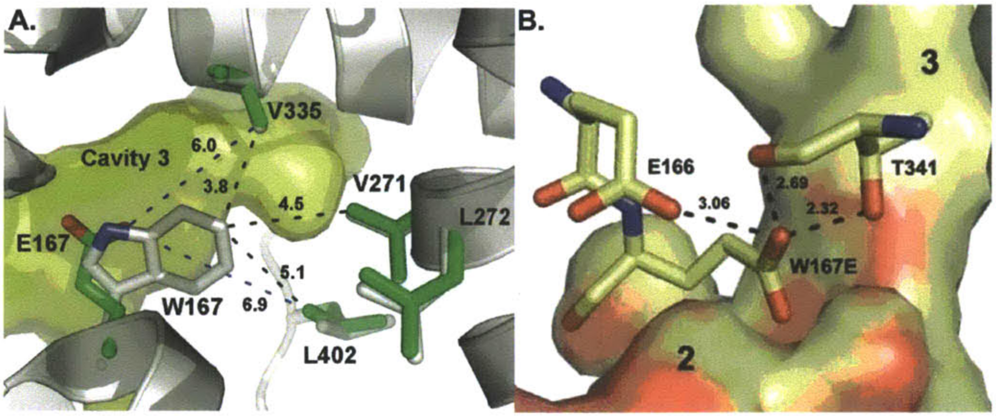

Figure 5.5 Structural changes in T201S/W167E ToMOH variant. (A) Changes in the distance of W167E with adjacent residues between cavity 2 and 3. Wild-type and W167E ToMOH gating residues were depicted as gray and green sticks, respectively. The distance between the W167E $\delta 1$ oxygen and V271 γ carbon atoms was 7.8 Å (not shown). (B) Newly formed hydrogen bondings of W167E with adjacent residues, E166 and T341. Oxygen and nitrogen atoms in W167E, E166, and T341 residues were depicted by red and blue sticks, respectively.

Cavity 3 also Helps to Convey O_2 to the Active Site. The indole ring of residue W167, located in cavity 3, bisects the two hydrophobic 2 and 3 (Figure 5.1 and Figure 5.5A). In the W167E variant, however, hydrogen-bonding interactions with T341 and E166 draw the glutamate side chain out of the interstitial space between cavities 2 and 3 (Figure 5.2F and Figure 5.5B). As a result, cavities 2 and 3 merge to form a single chamber, large enough for dioxygen to traverse. When dioxygen was allowed to react with reduced T201S/W167E ToMOH, the second-order formation rate constant was computed to be ~3-fold greater than that of the T201S variant (Table 5.4 and Figure 5.4E). The acceleration of dioxygen transfer to the diiron center arising from this single mutation at W167 reveals that cavity 3 is also on the path of dioxygen transfer, allowing it to pass on to cavities 2 and 1 to the active site diiron center.

The Channel is NOT a Primary Route of O_2 to the Active Site. Residues I276 and L208 are located in the narrowest part of the channel and lie opposite one another. The closet distance between two carbon atoms involving these residues is 5.8 Å. Replacement of I276 with glutamate (I276E) lengthens the side chain and diminishes the size of the channel (Figure 5.2G), the shortest distance between I276E and L208 atoms being 4.6 Å. Such a mutation should retard the access of dioxygen if the channel were involved in O_2 transfer to the active site. Reaction of the T201S/I276E variant with dioxygen returned a second-order formation rate constant for $T201_{peroxo}$ that was unaltered from the value in the T201S variant (Table 5.4 and Figure 5.4F). This result demonstrates that the channel is not a primary pathway for dioxygen delivery.

To highlight the kinetic effects on dioxygen transfer for the five mutants just discussed, we generated relative second-order $T201_{peroxo}$ formation rate constants ($k_{2,\text{T201S/X}}/k_{2,\text{T201S}}$) by dividing the individual rate constant in the double variants ($k_{2,\text{T201S/X}}$) by that for the T201S enzyme ($k_{2,\,\mathrm{T201S}}$) (Table 5.4 and Figure 5.6). Decreasing the size of the cavities in the I100W and L272E variants retards the dioxygen transfer rate constants, with $k_{2,\,\mathrm{T201S/X}}/k_{2,\,\mathrm{T201S}} <1$. The opposite effect was encountered for V271A and W167E in the cavities, $k_{2,\,\mathrm{T201S/X}}/k_{2,\,\mathrm{T201S}}$ being >1. In contrast, decreasing the channel volume by forming the I276E variant yielded $k_{2,\,\mathrm{T201S/X}}/k_{2,\,\mathrm{T201S}} \sim 1$. This combination of kinetic and structural information establishes that the three cavities, but not the channel, supply dioxygen to the active site of the enzyme.

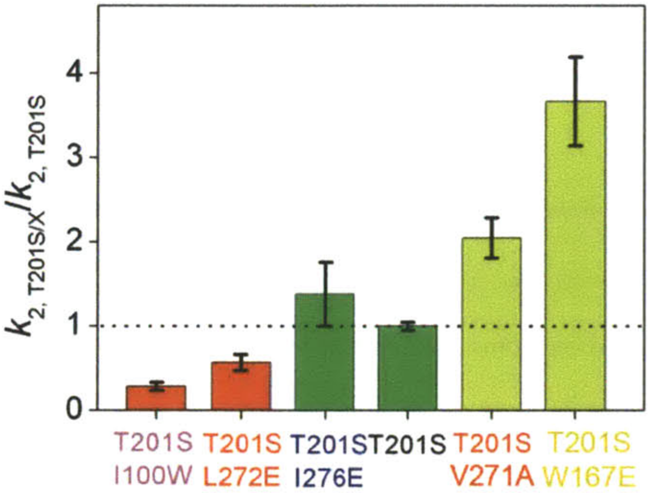

Figure 5.6 Relative formation rate constants of T201$_{\mathrm{peroxo}}$ ($k_{2,\,\mathrm{T201S/X}}/k_{2,\,\mathrm{T201S}}$) in ToMOH variants. Location of the second mutations, I100W, L272E, I276E, V271A, and W167E, were represented by different text colors, pink for cavity 1, red for cavity 2, yellow for cavity 3, and blue for channel. Depending on their relative second-order formation rates, columns were filled in different colors, red, green, and yellow for the values < 1, ≈ 1, > 1, respectively.

The Need for Conformational Changes during Dioxygen Activation. The foregoing structural and kinetic studies demonstrate that cavities 1-3 are utilized for dioxygen transfer. In the resting state structure of ToMOH, however, these cavities are not connected to one another. We therefore speculate that rapid conformational changes must occur during catalysis to form a connected trajectory for dioxygen access to the diiron active site. Simultaneously, the channel must close off to ensure selective delivery of O_2 through the cavities. The postulated protein fluctuations will probably occur on the microsecond time scale, based on the $T201_{peroxo}$ formation rates. Temporary opening/closing of hydrophobic sites is probably gated by the I100, L272, V271, and W167 residues as discussed above. Different orientations of these residues were in part observed in the T4moHD complex structure, where cavities 1 and 2 are connected, and the channel is sealed upon regulatory protein binding (Figure 5.1B).[22] Therefore, component interactions between the hydroxylase and regulatory protein are critical for triggering breathing motions in the *a*-subunit of the hydroxylase and gate substrate access to the active site diiron center. This conclusion thus explains a previous report that introduction of the cognate regulatory protein, MMOB, to the sMMOH accelerates the rate of dioxygen consumption, by ~1000 fold.[18] Although cavities 1 and 2 are connected as a consequence of the binding of the regulatory protein, further conformational changes are required to form a trajectory to the active site that includes cavity 3. Such a change might be induced by the presence of molecular oxygen itself, as proposed previously for carbon monoxide.[33] Given that cavities appear to be a conserved feature of BMMs, they are most likely not simple packing defects but rather programmed units for O_2 transfer in all the proteins.

Because BMM hydroxylases react with dioxygen even in the absence of hydrocarbon substrates, conformationally gated dioxygen transfer is presumably a conserved strategy designed to control the choreographed consumption of multiple substrates in a timely manner. These simple but elegant protein motions physically increase and decrease the dimensions of the transport pathway, similar to the inhale/exhale motions of breathing. We speculate that the channel structure evolved for aromatic substrate access and/or product egress because it is found only in arene-oxidizing ToMOH and T4moH enzymes. We also conjecture that PHH, which catalyzes phenol oxidation, might have a channel for the same purpose. The absence of a well-defined aromatic substrate pathway in the only available X-ray structure of PHH[27] is now explicable because of the presence of the bound cognate regulatory protein, which we now know can close the channel, as observed in the T4moHD structure,[22] which contains the bound regulatory protein.

5.4 CONCLUSION

Structural and kinetic studies of ToMOH variants have revealed that alterations in the size of a series of three cavities leading from the protein exterior to the active site significantly accelerate or decelerate dioxygen transfer rate constants, as measured by the formation of a diiron(III) peroxo intermediate upon reaction of the diiron(II) protein with dioxygen. Structural alterations of the channel by which aromatic substrates access the active site had no effect on the rate constant. These results are consistent with the hypothesis that dioxygen access to the diiron center involves migration through the cavities. A previously reported structure of the related toluene monooxygenase, T4moH, support the hypothesis that, in complex with its regulatory protein, the orientation of a few key residues can rearrange to form a specific pathway via the cavities for dioxygen transfer. Given that these cavities are conserved in all BMMs, the dioxygen transfer path delineated here is likely to be universal in this family. Temporary protein breathing motions that open and close the cavities may regulate the dioxygen consumption in a variety of enzymes where the presence of all substrates is not required for dioxygen reactivity.

ACKNOWLEDGEMENTS

I thank Grant Gucinski and Prof. Matthew H. Sazinsky (Pomona College, Claremont, CA) for the X-ray crystallographic studies.

REFERENCE

1. Poulos, T. L.; Finzel, B. C.; Gunsalus, I. C.; C., W. G.; Joseph, K. (1985) *J. Biol. Chem. 260*, 16122-16130.
2. Stubbe, J.; Nocera, D. G.; Yee, C. S.; Chang, M. C. Y. (2003) *Chem. Rev. 103*, 2167-2202.
3. Reece, S. Y.; Hodgkiss, J. M.; Stubbe, J.; Nocera, D. G. (2006) *Phil. Trans. R. Soc. B 361*, 1351-1364.
4. Shih, C.; Museth, A. K.; Abrahamsson, M.; Blanco-Rodriguez, A. M.; Di Bilio, A. J.; Sudhamsu, J.; Crane, B. R.; Ronayne, K. L.; Towrie, M.; Vlcek Jr., A.; Richards, J. H.; Winkler, J. R.; Gray, H. B. (2008) *Science 320*, 1760-1762.
5. Schoenborn, B. P.; Watson, H. C.; Kendrew, J. C. (1965) *Nature 207*, 28-30.
6. Cohen, J.; Kim, K.; King, P.; Seibert, M.; Schulten, K. (2005) *Structure 13*, 1321-1329.
7. Montet, Y.; Amara, P.; Volbeda, A.; Vernede, X.; Hatchikian, E. C.; Field, M. J.; Frey, M.; Fontecilla-Camps, J. C. (1997) *Nature 4*, 523-526.
8. Doukov, T. I.; Iverson, T. M.; Seravalli, J.; Ragsdale, S. W.; Drennan, C. L. (2002) *Science 298*, 567-572.
9. Leahy, J. G.; Batchelor, P. J.; Morcomb, S. M. (2003) *FEMS Microbiology Reviews 27*, 449-479.
10. Notomista, E.; Lahm, A.; Di Donato, A.; Tramontano, A. (2003) *J. Mol. Evol. 56*, 435-445.
11. Merkx, M.; Kopp, D. A.; Sazinsky, M. H.; Blazyk, J. L.; Müller, J.; Lippard, S. J. (2001) *Angew. Chem. Int. Ed. 40*, 2782-2807.
12. Wallar, B. J.; Lipscomb, J. D. (1996) *Chem. Rev. 96*, 2625-2657.
13. Rosenzweig, A. C.; Frederick, C. A.; Lippard, S. J.; Nordlund, P. (1993) *Nature 366*, 537-543.
14. Whittington, D. A.; Rosenzweig, A. C.; Frederick, C. A.; Lippard, S. J. (2001) *Biochemistry 40*, 3476-3482.
15. McCormick, M. S.; Lippard, S. J. (2011) *Manuscript In Preparation*
16. Sazinsky, M. H.; Bard, J.; Di Donato, A.; Lippard, S. J. (2004) *J. Biol. Chem. 279*, 30600-30610.
17. Song, W. J. (2011) Understanding Orchestrated Chemical Reactions in Toluene/*o*-Xylene Monooxygenase from *Pseudomonas Sporium* OX1, Ph.D. Thesis (Massachusetts Institute of Technology, Cambridge, MA).
18. Liu, Y.; Nesheim, J. C.; Lee, S.-K.; Lipscomb, J. D. (1995) *J. Biol. Chem. 270*, 24662-24665.
19. Stahl, S. S.; Francisco, W. A.; Merkx, M.; Klinman, J. P.; Lippard, S. J. (2001) *J. Biol. Chem. 276*, 4549-4553.
20. Cafaro, V.; Scognamiglio, R.; Viggiani, A.; Izzo, V.; Passaro, I.; Notomista, E.; Dal Piaz, F.; Amoresano, A.; Casbarra, A.; Pucci, P.; Di Donato, A. (2002) *Eur. J. Biochem. 269*, 5689-5699.
21. Pikus, J. D.; Studts, J. M.; Achim, C.; Kauffmann, K. E.; Münck, E.; Steffan, R. J.; McClay, K.; Fox, B. G. (1996) *Biochemistry 35*, 9106-9119.
22. Bailey, L. J.; McCoy, J. G.; Phillips, J., George N.; Fox, B. G. (2008) *Proc. Natl. Acad. Sci 105*, 19194-19198.

23. Goto, Y.; Klinman, J. P. (2002) *Biochemistry 41*, 13637-13643.
24. Murray, L. J.; Naik, S. G.; Ortillo, D. O.; García-Serres, R.; Lee, J. K.; Huynh, B. H.; Lippard, S. J. (2007) *J. Am. Chem. Soc. 129*, 14500-14510.
25. Gill, S. C.; von Hippel, P. H. (1989) *Analytical Biochemistry 182*, 319-326.
26. Murray, L. J.; Garcia-Serres, R.; McCormick, M. S.; Davydov, R.; Naik, S. G.; Kim, S.-H.; Hoffman, B. M.; Huynh, B. H.; Lippard, S. J. (2007) *Biochemistry 46*, 14795-14809.
27. Sazinsky, M. H.; Dunten, P. W.; McCormick, M. S.; Di Donato, A.; Lippard, S. J. (2006) *Biochemistry 45*, 15392-15404.
28. McCormick, M. S.; Sazinsky, M. H.; Condon, K. L.; Lippard, S. J. (2006) *J. Am. Chem. Soc. 128*, 15108-15110.
29. Murray, L. J.; García-Serres, R.; Naik, S.; Huynh, B. H.; Lippard, S. J. (2006) *J. Am. Chem. Soc. 128*, 7458-7459.
30. Rosenzweig, A. C.; Brandstetter, H.; Whittington, D. A.; Nordlund, P.; Lippard, S. J.; Frederick, C. A. (1997) *Proteins 29*, 141-152.
31. DeLano, W. L. (2002) *The PyMOL Molecular Graphics System* (DeLano Scientific, Palo Alto, CA).
32. Xiong, J.; Phillips, R. S.; Kurtz, J., Donald M.; Jin, S.; Ai, J.; Sanders-Loehr, J. (2000) *Biochemistry 39*, 8526-8536.
33. Tomita, A.; Sato, T.; Ichiyanagi, K.; Nozawa, S.; Ichikawa, H.; Chollet, M.; Kawai, F.; Park, S.-Y.; Tsuduki, T.; Yamato, T.; Koshihara, S.-y.; Adachi, S.-i. (2009) *Proc. Natl. Acad. Sci. USA 106*, 2612-2616.

Appendix A.

Insights into the Different Dioxygen Activation Pathways of Methane and Toluene Monooxygenase Hydroxylases

* Author contribution

The author was involved in the design of the experiments and discussion of the computational calculation results in combination with the experimental results reported in Chapter 2. Computational calculation studies were performed by Dr. Arteum D. Bochevarov, Jianing Li, and Prof. Richard A. Friesner (Columbia University, New York, NY).

** Reprinted with permission from a following publication,

Arteum D. Bochevarov, Jianing Li, Woon Ju Song, Richard A. Friesner, Stephen J. Lippard "Insights into the Different Dioxygen Activation Pathways of Methane and Toluene Monooxygenase Hydroxylases" *J. Am. Chem. Soc.* **2011**, *133*, 7384-7397.

JACS
JOURNAL OF THE AMERICAN CHEMICAL SOCIETY

ARTICLE

pubs.acs.org/JACS

Insights into the Different Dioxygen Activation Pathways of Methane and Toluene Monooxygenase Hydroxylases

Arteum D. Bochevarov,[†] Jianing Li,[†] Woon Ju Song,[‡] Richard A. Friesner,[*,†] and Stephen J. Lippard[*,‡]

[†]Department of Chemistry, Columbia University, New York, New York 10027, United States

[‡]Department of Chemistry, Massachusetts Institute of Technology, Cambridge, Massachusetts 02139, United States

S *Supporting Information*

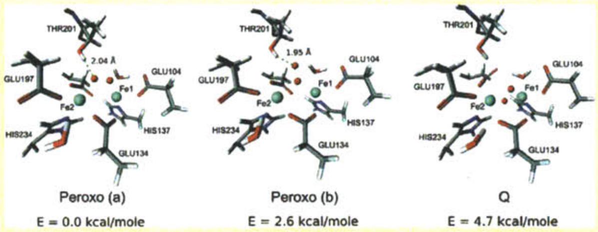

ABSTRACT: The methane and toluene monooxygenase hydroxylases (MMOH and TMOH, respectively) have almost identical active sites, yet the physical and chemical properties of their oxygenated intermediates, designated P*, H_{peroxo}, Q, and Q* in MMOH and $ToMOH_{peroxo}$ in a subclass of TMOH, ToMOH, are substantially different. We review and compare the structural differences in the vicinity of the active sites of these enzymes and discuss which changes could give rise to the different behavior of H_{peroxo} and Q. In particular, analysis of multiple crystal structures reveals that T213 in MMOH and the analogous T201 in TMOH, located in the immediate vicinity of the active site, have different rotatory configurations. We study the rotational energy profiles of these threonine residues with the use of molecular mechanics (MM) and quantum mechanics/molecular mechanics (QM/MM) computational methods and put forward a hypothesis according to which T213 and T201 play an important role in the formation of different types of peroxodiiron(III) species in MMOH and ToMOH. The hypothesis is indirectly supported by the QM/MM calculations of the peroxodiiron(III) models of ToMOH and the theoretically computed Mössbauer spectra. It also helps explain the formation of two distinct peroxodiiron(III) species in the T201S mutant of ToMOH. Additionally, a role for the ToMOD regulatory protein, which is essential for intermediate formation and protein functioning in the ToMO system, is advanced. We find that the low quadrupole splitting parameter in the Mössbauer spectrum observed for a $ToMOH_{peroxo}$ intermediate can be explained by protonation of the peroxo moiety, possibly stabilized by the T201 residue. Finally, similarities between the oxygen activation mechanisms of the monooxygenases and cytochrome P450 are discussed.

■ INTRODUCTION

Soluble methane monooxygenase and toluene *o*-xylene monooxygenase belong to the family of bacterial multicomponent monooxygenases (BMMs) that specialize in the transformation of C−H chemical bonds into the C−OH groups for a variety of hydrocarbons.[1−4] Methane monooxygenase hydroxylase (MMOH) has been extensively studied,[5−12] and the toluene monooxygenase hydroxylase (TMOH) has also generated considerable interest[13−16] after its three-dimensional structures became available.[15,17−21] Soluble MMOH enzymes are found in two phylogenetically related proteins, MMOH-Mc and MMOH-Mt, purified from two related organisms, *Methylococcus capsulatus* (Bath) and *Methylococcus trichosporium* OB3b, respectively. A TMOH enzyme similarly occurs in a variety of organisms, two of which will be discussed in this work: toluene/*o*-xylene monooxygenase hydroxylase (ToMOH) and toluene 4-monooxygenase hydroxylase (T4moH), expressed in *Pseudomonas stutzeri* OX1 and *Pseudomonas mendocina* KR1, respectively. These particular variants of MMOH and TMOH have been characterized crystallographically and are most accessible for theoretical analysis. The active sites in each pair are almost identical.

Despite having very similar active sites, the MMOH and TMOH enzymes differ in chemical behavior, something that has puzzled researchers. Not only do they have reactivity specific for distinct types of hydrocarbons, but the properties and the structures of their oxygenated intermediates also differ.[4,13,14] Some light has been shed on the problem after the identification of an extended channel connecting the surface of ToMOH with its active site, a channel that is absent in MMOH.[18] Another advance was the preparation and spectroscopic study of ToMOH mutant forms in which the residue threonine-201, located near the active site, was substituted by other amino acids, serine in particular.[14] Important implications for the kinetics of the reaction and for the catalytic cycle emerged as a result of the substitution.

In the present study we reprise the structural differences between MMOH and TMOH active sites and investigate the energetic consequences of rotation about the threonine $C_\alpha-C_\beta$ bond (T213 in MMOH and T201 in TMOH) by molecular mechanics (MM) and quantum mechanics/molecular mechanics (QM/MM) computational methods. Studying threonine-201 in TMOH and its analog in MMOH is important because understanding their respective abilities to influence the

Received: November 16, 2010
Published: April 25, 2011

dx.doi.org/10.1021/ja110287y | *J. Am. Chem. Soc.* 2011, 133, 7384–7397

chemistry of the diiron sites may be key to the explanation of differences in the intermediates formed by the two proteins. There are several reasons to ascribe a principal role to this threonine residue: (i) It is strictly conserved in the BMM family and located at the active site; (ii) its mutations have a measurable effect on the catalytic mechanism; (iii) its rotational configurations are markedly different in the available crystal structures of MMOH and TMOH forms; (iv) it is involved in an extended hydrogen-bonding network that stretches from the active site to the surface of the protein and may provide a mechanism for proton delivery during the catalytic cycle; and (v) as we demonstrate here, the threonine potential energy profiles correlate strongly with experimentally observed trends in the formation of the hydroxylase intermediates. Based on our theoretical analysis, we formulate a hypothesis that can explain the differences in the behavior of the intermediates and provide further insight into the role that the threonine plays in tuning the chemistry of the BMM enzyme active sites.

The implications of our findings stretch beyond the field of BMM enzymes. The intermediary role of the threonine residue, the proton delivery network fashioned at the diiron site that includes the threonine residue and the neighboring asparagine, and the demonstrated protonation of the peroxo-intermediates in ToMOH reveal strong similarities between the oxidative mechanisms of ToMOH and cytochrome P450.[22,23] We discuss these similarities in more detail in the Relation to Cytochrome P450 Section immediately preceding the conclusion.

It is also important to point out the use of computational methodology in the present paper, as mandated by the objectives of our study. There are many protein pairs in nature that are significantly homologous in structure and similar if not identical in function, as is the case for MMOH and ToMOH. Typically such pairs are analyzed by sequence comparisons, structural superpositions, and other bioinformatics tools, and differences in chemistry are then inferred from data generated in this fashion, leaving much to be understood at an atomic level. Here, we begin with an analysis of this type but proceed to a detailed study of hypotheses emerging from the sequence and X-ray data comparison by using state of the art MM and QM/MM simulations. More generally, the problem we pose from a computational perspective is how to take two extremely complex systems which have a high degree of structural homology and identify precisely what structural elements are responsible for differences in their chemistries. While QM/MM studies focusing on a single protein are common, comparative analyses using high-level computations and successfully making multiple semiquantitative points of contact with experiment are relatively rare. Thus, in addition to being of interest to researchers directly involved in work on MMOH, ToMOH, and related metalloenzymes, such as P450, the description of a successful strategy for using a combination of sequence, structure, high-level energetics, and spectroscopic computations to explicate the differences in related but chemically distinct, protein pairs should be valuable for both theoretical and experimental chemists who wish to understand protein-catalyzed reactions at an atomic level of detail.

■ COMPUTATION DETAILS

Three computational methods were used in this project to compute energies: MM, QM/MM, and Monte Carlo (MC).

The MM method was applied to generate rotational profiles of serine and threonine in several protein structures. Except when the QM/MM-optimized geometries were available (for the ToMOH protein only), all the crystal structures were obtained from the Protein Data Bank (PDB) and subsequently treated by the independent cluster decomposition algorithm (ICDA) method[24] to assign the positions of the hydrogen atoms and resolve certain misassignments that could be present in the crystal structure. The correct charges of atoms and protonation states of the ligands around the active site were specified manually. As an energy function, the OPLS-AA[25] molecular mechanics force field was used.

The QM/MM method realized in the program QSite[26] and based upon the frozen orbital approach[27−29] for the quantum/classical interface was used to compute high-quality energies of the oxygenated intermediates as well as to minimize their structures. Prior to the QM/MM calculations, the geometry of the MM part of the protein system was optimized with tight convergence criteria. The protonation states of amino acid residues in the protein matrix were assigned based on the distances to neighboring groups which are likely to form a salt bridge. Typically, the cutoff distance for a salt bridge was 3 Å. Multiple residues competing for a salt bridge were resolved manually, with the preference given to the residues located at the shortest distance. The residues on the surface not forming salt bridges were neutralized, and the total charge of all systems studied with QM/MM was kept zero.

The QM part was treated with the B3LYP DFT functional (unrestricted orbitals), while the MM part was handled with the OPLS-AA force field. All QM/MM computations were conducted without cutoffs for electrostatic interactions. For the geometry optimizations, we utilized a smaller basis set (LACVP**[30−32] on iron atoms, and 6-31G* on all other atoms in the QM region) than that with which the single point energy was subsequently computed (LACV3P** on iron atoms, aug-cc-pVTZ without the *f*-functions on the active site waters and the dioxygen, and cc-pVTZ without the *f*-functions on all remaining QM atoms). The antiferromagnetic coupling between the two Fe atoms was treated by the broken symmetry wave function formalism, in the same manner as in our earlier QM/MM study.[10] All the QM/MM energies given in this work correspond to the single point energies obtained with the larger basis set.

In MC sampling of model structures, we used the combination of MC torsion sampling (MCMM) and large-scale low-mode sampling (*l*-LMOD).[33,34] During exploration of the configurational space of the models, the distance between two Fe atoms and the O−O distance in the dioxygen-derived ligand were constrained.

The density functional theory (DFT) optimization of protonated model structures utilized the B3LYP functional, Wachters basis set on Fe atoms, and cc-pVDZ basis set on all the other atoms.

In computing the Mössbauer parameters of the model structures we followed the methodology of isomer shift parametrization and functional/basis set selection from our recent work.[35] The B3LYP functional was used to compute the isomer shift, whereas O3LYP was the functional of choice for the quadrupole splitting parameter. The completely uncontracted Partridge-1 basis set was placed on the iron atoms, and the conventional cc-pVDZ basis resided on the rest of atoms of the model. Our Mössbauer benchmarking study[35] indicates that these are currently the best functional/basis set combinations for the prediction of the isomer shift and the quadrupole splitting parameters. The molecular model systems for Mössbauer calculations were produced from the corresponding active sites by truncation and hydrogen capping.

■ COMPARISON OF MMOH AND TMOH ACTIVE SITES

To date, almost 30 MMOH and over 10 TMOH crystal structures have been deposited in the PDB. The active sites of all the crystallized MMOH and TMOH forms share a considerable degree of similarity. The identical elements of the immediate coordination environment (the so-called first shell), regardless of

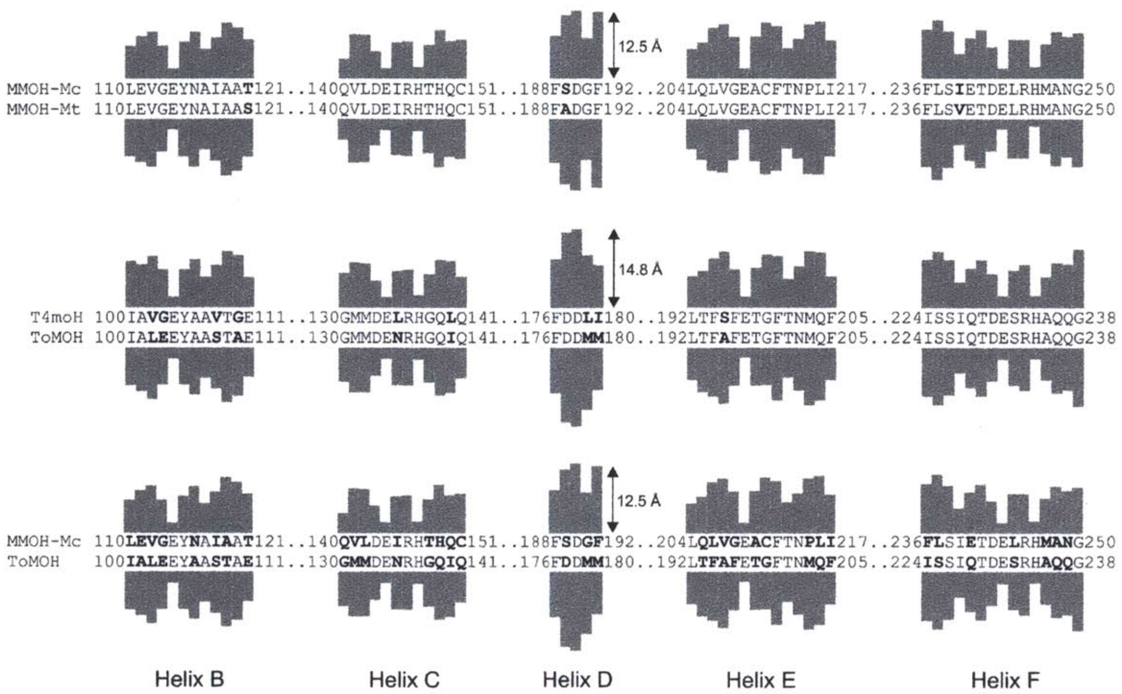

Figure 1. Comparison of the residues around the diiron core in MMOH-Mc (PDB 1MTY), MMOH-Mt (PDB 1MHY), T4moH (PDB 3DHG), and ToMOH (PDB 2INC) crystal structures. The height of the bars above and below the residue codes signifies the approximate distance between the closest atoms belonging to the residue and the diiron core. The substitutions are highlighted in bold.

the oxidation state of the iron atoms, comprise two histidine and four glutamine side chains, with the histidine residues in MMOH and TMOH using different nitrogen atoms to coordinate to the iron atoms.[18] The amino acid residues are fixed elements of the structures, whereas the water molecules, hydroxide ions, and molecules from the crystallization solution that are located in immediate proximity to the iron atoms are variable elements. Their presence fluctuates from structure to structure and depends on the oxidation state of the iron atoms, crystallization conditions, and complex formation with the regulatory protein. The positions of all groups coordinated to iron, including side chains, are subject to translational or rotational modifications. Many amino acids surrounding the coordinating ligands (the second shell) are conserved between MMOH and TMOH, which makes the architecture of their active sites nearly identical.

In any study of the differences in chemistry between MMOH and TMOH intermediates, it is the fixed elements of their active site structures (amino acids) that we have to focus on. As a starting point, it is important to investigate deviations within the MMOH and TMOH structure groups, in order to understand whether we can use one structure as representative of the entire group. MMOH-Mc and MMOH-Mt show almost no variation in the surroundings of the diiron center. Out of the 58 residues located in the active site-forming helices, MMOH-Mc and MMOH-Mt differ only by three (see Figure 1). Only one of these three differences ($V \leftrightarrow I$) is close to the diiron center; however, it involves an inessential residue. A more detailed overall comparison of the two MMOH proteins has been undertaken earlier.[36,37] The mutations differentiating ToMOH from T4moH are more numerous and include 9 out of the analogous 58 residues, but all of them are located relatively far from the diiron center and most of them are inessential for our study (see Figure 1). The number of mutations around the active site agrees with the phylogenetic placement of these proteins[38] based on the entire α-subunit: MMOH-Mc is closer to MMOH-Mt than ToMOH is to T4moH. Notwithstanding these differences, we may conclude that, as far as the chemistry of the active site is concerned, any of the two members of each group may be considered as representative of the group as a whole.

Next, we turn to the differences between the MMOH and TMOH active site environments. Figure 1 reveals a great number of differences: 35 residues out of the 58 do not match when MMOH-Mc and ToMOH sequences are aligned. It is clear that the majority of the changes occur in residues relatively distant from the active site. All residues coordinated to the iron atoms are conserved, but there are several key changes in the 'second' and the 'third' shells. Ones of particular interest, being closest to the active site, are listed in Table 1. Residues not directly coordinated to the diiron center but with side chains that are not obstructed from the diiron center by other residues are considered second shell. This shell may play a direct role by interacting with the variable elements of the active site, such as the dioxygen or water molecules. Residues having some other amino acid chains between them and the diiron center are considered third shell. This shell is considered to be of relatively low importance, although in the catalytic cycle, it could still play a role in stabilizing second-shell conformations.

From Table 1, we can identify important differences in the active sites of MMOH and ToMOH. Substitutions 1, 4, 7, and 8 are not very interesting. The first is not even conserved across both variants of the TMOH family. The side chains of mutations 4 and 7 are relatively distant (about 7 Å) from the diiron center. Substitution 8 deserves somewhat more attention because A235

Table 1. Mutated Residues Closest to the Diiron Center of MMOH-Mc (1MTY) and ToMOH (2INC) [a]

substitution no.	MMOH-Mc	comment	ToMOH	location	conserved?
1	G113	2nd shell	E103	3rd shell, points away from diiron	No[b]
2	T121	3rd shell	E111	2nd shell, H-bond through water with E134	No[c]
3	Q140	2nd shell, H-bond with E144	G130	3rd shell	Yes
4	T148	2nd shell, points away from diiron	G138	3rd shell	Yes
5	Q205	3rd shell	T193	2nd shell	Yes
6	I217	2nd shell	F205	2nd shell	Yes
7	E240	3rd shell, points away from diiron	Q228	3rd shell, points away from diiron	Yes
8	M247	3rd shell, points away from diiron	A235	2nd shell	Yes

[a] The column 'conserved?' indicates whether the shown mutation is shared by all the members of the groups MMOH and TMOH. [b] E103 in ToMOH and G103 in T4moH. [c] T121 in MMOH-Mc and S121 in MMOH-Mt.

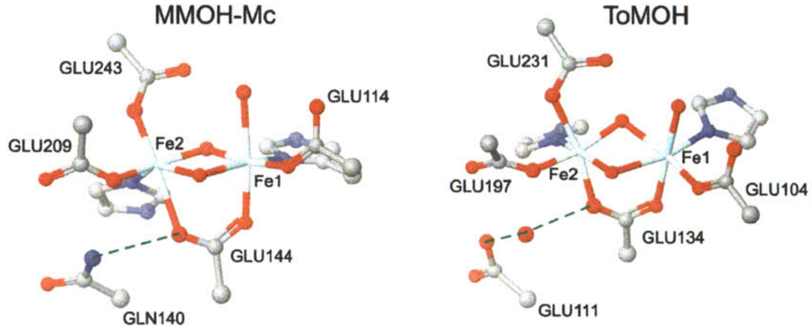

Figure 2. The hydrogen bonds (traced with the dashed green lines) formed by the bridging carboxylate and preserved in MMOH-Mc and ToMOH crystal structures despite the mutations in the second shell residues. The color-coding is as follows: carbons are gray, oxygens are red, nitrogens are blue, and irons are cyan. Hydrogen atoms are omitted for clarity.

of the ToMOH family is located in the second shell. However, its importance is not clear. The other four mutations are more significant. Substitution 2 is not conserved in both variants of the MMOH family, but the residues associated with this substitution in MMOH-Mc and MMOH-Mt have a functionally similar side chain: threonine and serine, respectively, so that we may consider it to be effectively conserved. Alteration T121 (MMOH) → E111 (ToMOH) is unusual. The side chain of E111 is apparently hydrogen bonded to a water molecule, which is in turn hydrogen bonded to the critical residue E134 serving as a ligand for the diiron center (see Figure 2). T121 of MMOH does not form hydrogen bonds with E144, and therefore substitution T121 (MMOH) must play a role different from → E111 (ToMOH). Interestingly, substitution T121 (MMOH) → E111 (ToMOH) is complementary to substitution number 3 in Table 1: Q140 (MMOH) → G130 (ToMOH). The backbone of Q140 (MMOH) is aligned with the backbone of G130 (ToMOH). But G130 (ToMOH) has only a hydrogen atom for a side chain and cannot carry out the apparently important function similar to that of Q140 in MMOH. This function in ToMOH is accomplished by the side chain of E111, even though its backbone is not aligned with that of MMOH Q140. Backbones of MMOH Q140 and ToMOH E111 are not aligned, but their side chains have the same function in the stabilization of the active site. The role and the significance of this hydrogen bond are currently not understood. Substitution 6 changes the aliphatic hydrophobic group of isoleucine into the aromatic hydrophobic group of phenylalanine in the second shell of both protein subfamilies. Whether the presence of the phenyl ring in the second shell of ToMOH might lead to a $\pi-\pi$ interaction with the aromatic substrate is unknown but should not be discounted. The analogous residue in aromatic-oxidizing phenol monooxygenase is also phenylalanine.[39]

It is unlikely that any single substitution of those just discussed will explain the profoundly dissimilar scenarios by which dioxygen is activated in MMOH and TMOH. It is more probable that the effect of these substitutions is cumulative and that they all contribute to the observed differences. Moreover, studying the changes provides just one window on understanding differences in the MMOH and TMOH catalytic cycles. At least two additional resources remain. The first is the effect of the regulatory protein on the secondary structure of helix E and the presence of an additional ordered water molecule in the vicinity of the diiron core. The ability to observe catalytic intermediates in the MMOH and ToMOH reaction cycles requires the presence of the respective regulatory proteins. The second resource is the rotatory conformation of the conserved threonine T213 in MMOH and T201 in TMOH, vide infra.

We now briefly discuss the effects of the regulatory protein binding on structure before moving to the rotameric forms of of the threonine, which comprise the key subject of this work. Out of the four proteins that we compared, only one was crystallized in complex with its regulatory protein, T4moH,[21] hereafter referred to as T4moHD. There are two noticeable modifications from the structure of the hydroxylase in the absence of the regulatory protein. The first is a distortion of helix E, which affects the secondary structure of two residues, T201 and N202, involved in a hydrogen-bond network leading from the surface of

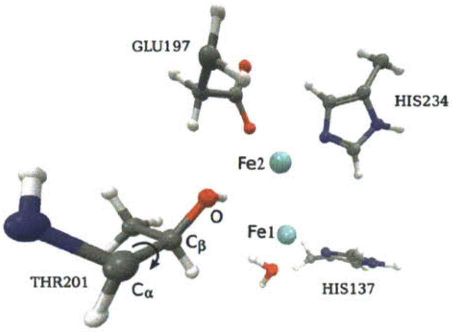

Figure 3. The locations of the two iron atoms and C_β and O atoms of threonine (or serine in the mutant) relative to one another. These atoms form the Fe1−Fe2−C_β−O dihedral angle denoted 2Fe-THR in the text. The arrow shows a rotation around the C_α−C_β bond used to construct plots in Figures 6 and 7.

the protein to the active site and is thought to be important for the proton shuttling.[39] As a result of this distortion, T201 and N202 no longer reside in the α-region of the E helix but belong to a transitional structure between α and π helices. As a further consequence, T201 recedes from the diiron center; the distance from its backbone oxygen atom to Fe_2 increasing from 5.36 Å to 6.26 Å. The regulatory protein thereby creates some extra space between the diiron core and the residues T201, Q228, and F205 located just beside it. The other modification is the presence of a new water molecule apparently hydrogen bonded to the water molecule coordinated with Fe1. It is located in the extra space just mentioned. The presence of this additional water molecule may have important implications for the hydrogen-bond network extending to the surface of the protein and for the role it may play in the formation of a peroxo species; the latter point is discussed below. These changes brought about by the regulatory protein in T4moH are noteworthy, but whether they are mirrored in ToMOH and, most importantly, the MMOH proteins is currently unknown. When a crystal structure for the corresponding MMOH and its cognate regulatory protein MMOB becomes available for one of the MMOH proteins, it will be clear whether the regulatory protein has an identical structural role, or, perhaps, induces a distinct set of changes that might contribute to factors that distinguish the chemical properties of the MMOH and TMOH intermediates.

■ THREONINE CONFORMATIONS IN MMOH AND TOMOH CRYSTALS

In this section we describe the rotatory conformations of the threonine residues observed in MMOH and TMOH crystal structures and discuss the consequences that these conformations might have for stabilizing the catalytic intermediates. The next section will focus on the rotational energy profiles.

In order to quantify the rotational configurations we refer to the dihedral angle Fe1−Fe2−C_β−O illustrated in Figures 3 and 4, hereafter 2Fe-THR. Positive values of the dihedral angle represent the situation when the threonine hydroxyl group turns toward the diiron center and when negative values correspond to the opposite orientation. Because the C_α backbone carbon atom to which the threonine hydroxymethyl group is attached may shift slightly from structure to structure, the value of the dihedral angle does not necessarily define the distance of the oxygen atom to the diiron center, which would correlate with the possibility of threonine participation in dioxygen activation. We therefore require additional geometrical information to describe this structural element. Tables 2 and 3 contain this additional information and include the rotatory geometry of threonine with respect to the diiron center. These tables clearly reveal that positive 2Fe-THR dihedral angles signal a significantly shorter (about 1 Å) distance from the threonine hydroxyl group to the diiron core. An interesting caveat is the set of distances for T4moHD. For this structure, a positive dihedral angle corresponds to d_{Fe1}−O and d_{Fe2}−O distances that are about the same as those in other proteins where the dihedral angle is negative. This result occurs because the regulatory protein distorts the secondary structure of helix E and drives T201 away from the diiron site by about 1 Å. Presumably, the structures of MMOH and/or ToMOH in complex with their respective regulatory proteins would have similarly negative dihedral angles, with distances that are larger than those corresponding to the positive angle.

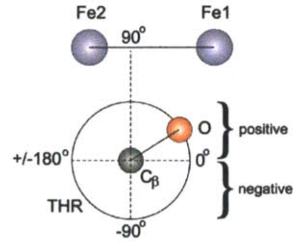

Figure 4. A schematic projection down the C_α−C_β bond of the threonine (or serine) C_β−O bond onto the plane in which two iron atoms lie and which is perpendicular to the C_α−C_β bond. This projection reveals that when dihedral angle Fe1−Fe2−C_β−O changes (due to rotation around C_α−C_β bond of threonine), the distance between the hydroxyl oxygen and the diiron center also changes. The positions and the values of four Fe1−Fe2−C_β−O angles (0°, ±90°, ±180°) in the projected picture are shown. Because threonine is allowed to move parallel to the line connecting the iron atoms, a particular dihedral angle does not necessarily indicate the proximity of the oxygen atom to the diiron center. For this reason, the distances Fe_1−O and Fe2−O are used in addition to the Fe1−Fe2−C_β−O angle in Table 2 to indicate the nearness of the threonine hydroxyl group to the diiron center.

Another observation that follows from the tables is the striking difference in dihedral angles for the MMOH and TMOH structures. If we disregard soaked structures, which are likely to have distorted and unnatural geometries, then we can conclude that in MMOH the threonine hydroxyl is rotated in a direction away from the diiron center, whereas in ToMOH it always faces the iron atoms. As discussed below, we believe that the difference has far-reaching implications for the stability of the peroxo intermediates with respect to conversion to the hydroxylating intermediate Q in MMOH. The distance between the threonine hydroxyl oxygen atom and the diiron core, even in the case of a positive dihedral angle, is too large to allow a direct interaction between the two. But when we consider that a peroxo ion O_2^{2-} can be positioned between the threonine and the iron atoms, the distance appears just right. Our QM/MM optimizations on ToMOH predict that a strong hydrogen bond will form between the threonine OH group and the coordinated peroxo ion. Such an interaction helps make the peroxo structure 4.7 kcal/mol more stable than a Q-type intermediate, a putative di(μ-oxo)diiron(IV) unit in which the O atoms are too far away from the threonine to form a hydrogen bond.

Table 2. Rotational Conformations of T213 in MMOH with Respect to the Diiron Center in a Variety of Crystal Structures[a]

structure	protein	oxidation state	2Fe-THR, deg	$d_{Fe1}-O$, Å	$d_{Fe2}-O$, Å	χ, deg	comment
1XU3	MMOH-Mc	+3, +3	109.0	6.02	5.61	113.8	soaked in bromophenol
			163.1	6.66	5.42	75.2	
1XU5	MMOH-Mc	+3, +3	−89.4	7.13	6.65	−48.2	soaked in phenol
			164.7	6.56	5.54	72.3	
1XVB	MMOH-Mc	+3, +3	−153.8	7.82	6.55	−68.9	soaked in 6-bromohexanol
			−155.6	7.86	6.53	−67.1	
1XVC	MMOH-Mc	+3, +3	−78.0	7.08	6.63	−58.8	soaked in 8-bromooctanol
			−77.5	6.91	6.37	−61.0	
1XVD	MMOH-Mc	+3, +3	−76.8	6.76	6.45	−59.4	soaked in 4-fluorophenol
			160.6	6.53	5.45	77.5	
1XVE	MMOH-Mc	+3, +3	−77.9	7.29	7.10	−61.1	soaked in 3-bromo-3-butenol
			−100.9	7.71	7.23	−42.3	
1XVF	MMOH-Mc	+3, +3	−81.1	7.16	6.80	−56.6	soaked in chloropropanol
			−109.8	7.38	6.81	−26.3	
1XVG	MMOH-Mc	+3, +3	155.6	6.36	5.22	78.8	soaked in bromoethanol
			168.8	6.55	5.63	69.4	
1XMF	MMOH-Mc	+3, +3	−75.3	6.80	7.09	−70.7	Mn replaces Fe; soaked
			−89.6	7.09	7.07	−60.0	
1XMH	MMOH-Mc	+2, +2	−87.0	7.28	6.95	−59.4	Co replaces Fe
			−92.4	7.27	6.82	−50.9	
1FZ0	MMOH-Mc	+2, +2	−74.7	7.32	6.76	−46.7	
			−80.7	7.37	6.62	−53.9	
1FZ1	MMOH-Mc	+3, +3	−89.2	7.19	6.80	−48.4	
			162.1	6.65	5.60	73.5	
1FZ2	MMOH-Mc	+2, +3	−69.8	7.21	6.61	−56.2	soaked
			−71.7	7.28	6.64	−54.3	
1FZ3	MMOH-Mc	+3, +3	169.0	6.62	5.66	68.3	soaked at pH 6.2 (0.1 M PIPES)
			−84.9	6.96	6.29	−55.9	
1FZ4	MMOH-Mc	+3, +3	−82.7	6.94	6.45	−53.4	soaked at pH 8.5 (0.1 M TRIS)
			−82.7	7.10	6.42	−54.6	
1FZ6	MMOH-Mc	+3, +3	−77.8	7.09	6.81	−16.7	soaked in 1 M methanol
			−112.9	7.22	6.60	−59.0	
1FZ7	MMOH-Mc	+3, +3	−68.8	6.69	6.53	−70.3	soaked in 0.9 M ethanol
			161.9	6.56	5.58	70.6	
1FZ8	MMOH-Mc	+3, +3	21.7	6.00	6.13	−171.1	soaked in bromoethane
			176.6	6.72	5.72	65.5	
1FZ9	MMOH-Mc	+3, +3	−85.2	7.31	6.61	−53.1	soaked in iodoethane
			100.1	6.59	7.20	−54.2	
1FZH	MMOH-Mc	+3, +3	−70.6	6.58	6.24	−66.4	pressurized with xenon
			−178.9	6.36	5.50	54.8	
1FZI	MMOH-Mc	+3, +3	−68.1	6.85	6.97	−62.0	pressurized with xenon
			−58.9	7.00	6.91	−75.7	
1MHY	MMOH-Mt	+3, +3	−87.6	6.77	6.23	−46.0	
1MHZ	MMOH-Mt	+3, +3	−97.5	6.75	6.03	−43.6	
1MTY	MMOH-Mc	+3, +3	−72.5	7.10	6.80	−61.9	
			−58.2	6.91	6.80	−75.7	
1MMO	MMOH-Mc	+3, +3	−90.1	6.99	6.41	−48.5	
			−90.5	7.03	6.45	−48.0	

[a] The distances $d_{Fe1}-O$ and $d_{Fe2}-O$ are measured between the corresponding iron atom and the oxygen of the threonine hydroxyl group; the dihedral angle 2Fe-THR (Fe1−Fe2−C_β−O) is illustrated by Figures 3 and 4. The dihedral angle N−C−C_α−O characterizing the internal rotation of the threonine is also given and denoted χ. The two values given for each entry correspond to the two different protomers of MMOH-Mc. The crystal structure notation corresponds to that of the PDB.

Figure 5 shows the active site geometries of the two lowest-energy peroxo intermediates and a Q-type intermediate predicted by the QM/MM optimization starting from the ToMOH 2INC crystal structure. The relative energies of these

Table 3. Rotational Conformations T201 in TMOH with Respect to the Diiron Center in a Variety of Crystal Structures[a]

structure	protein	oxidation state	2Fe-THR, deg	$d_{Fe1}-O$, Å	$d_{Fe2}-O$, Å	χ, deg	comment
3I5J	T4moHD	+3, +3	141.2	7.37	6.24	58.9	
3I63	T4moHD	+3, +3	139.4	7.32	6.19	56.2	H_2O_2 is loosely bound to Fe atoms
3DHG	T4moH	+3, +3	156.0	6.45	5.36	66.5	
			135.3	6.48	5.27	78.5	
3DHH	T4moHD	+3, +3	136.6	7.37	6.26	57.9	
3DHI	T4moHD	+2, +2	137.6	7.33	6.64	58.9	
2RDB	ToMOH	+3, +3	157.4	7.03	5.67	64.6	I100W mutant
2IND	ToMOH	+2, +2	164.9	7.13	5.98	64.9	Mn replaces Fe
2INC	ToMOH	+3, +3	161.8	6.71	5.62	64.0	
1T0Q	ToMOH	+3, +3	164.4	6.88	5.74	66.0	
1T0R	ToMOH	+3, +3	147.8	6.67	5.45	78.5	with azide bound
1T0S	ToMOH	+3, +3	179.7	6.84	5.65	57.6	soaked in 4-bromophenol

[a] The distances $d_{Fe1}-O$ and $d_{Fe2}-O$ are measured between the corresponding iron atom and the oxygen of the threonine's hydroxyl group; the dihedral angle 2Fe-THR ($Fe1-Fe2-C_\beta-O$) is illustrated in Figures 3 and 4. The dihedral angle $N-C-C_\alpha-O$ characterizing the internal rotation of the threonine is also given and denoted χ. The crystal structure notation corresponds to that of the PDB.

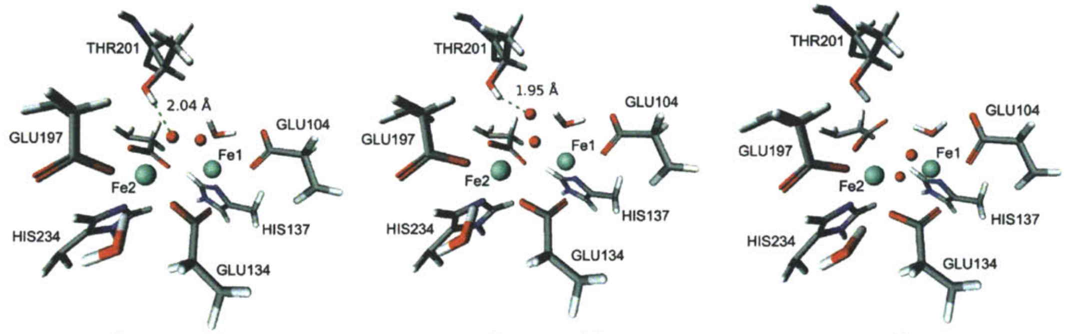

Peroxo (a)
E = 0.0 kcal/mole

Peroxo (b)
E = 2.6 kcal/mole

Q
E = 4.7 kcal/mole

Figure 5. The two lowest-energy ToMOH peroxo structures (left, *cis*-μ-1,2, and center, μ-1,1) and the Q structure (η^2,η^2) optimized with the QM/MM method (B3LYP/OPLS2001); the only unlabeled residue is GLU231. Their relative energies computed in the larger basis set are given below. The dashed green lines indicate the hydrogen bonds formed between the T201 residue and the peroxide ion. The color-coding is as follows: hydrogens are white, carbons are gray, oxygens are red, nitrogens are blue, and irons are cyan.

structures are also shown. One other peroxo intermediate found in the course of optimization did not form a hydrogen bond with T201 and was several kcal/mol higher in energy than the Q structure. We therefore ascribe to this hydrogen bond the stabilization effect that helps make the peroxo more favorable than Q. In contrast, our previous QM/MM study of MMOH predicted almost identical energies for the peroxo and Q structures.[10] The peroxo structure in that study had no possibility to form a hydrogen bond with T213, which was pointed away from the active site and therefore could not be stabilized by such an interaction. The present findings agree well with experimental observations. In MMOH, the peroxo intermediate transforms spontaneously into Q, which serves as the principal substrate oxidizing agent.[6] In ToMOH, intermediate Q is not observed, and oxidation is performed by a peroxo species.[13] Our conclusion is further supported by the fact that the peroxo intermediates of MMOH and ToMOH have very different quadrupole splittings in their Mössbauer spectra, 1.51 mm/s in both MMOH-Mc and MMOH-Mt and 0.67 mm/s in ToMOH. Such different quadrupole splittings indicate a different geometry of the active site or a different protonation state. The observation that the threonine may stabilize the peroxo intermediate in TMOH but not in MMOH is thus in accord with the thermodynamics and compatible with the Mössbauer measurements.

During the course of our QM/MM studies of the ToMOH protein using the 2INC crystal structure as the starting geometry, the crystal structure of T4moH in complex with its regulatory protein (PDB 3DHH) became available. The latter structure is valuable for theoretical modeling of the TMOH catalytic cycle because the regulatory protein is essential for the efficiency of the oxidation and because it is also complexed to either T4moH or ToMOH in most experiments. As we have already mentioned, and as evident from the data in Table 3, the regulatory protein increases the distance between the threonine side chain and the diiron center by about 1 Å. This change makes it much more difficult for a strong hydrogen bond OH···O−O, such as that observed in the peroxo structures based on the 2INC geometry, to occur. However, formation of the complex between T4moH and its regulatory protein brings an additional water molecule to the active site cavity that is situated between the diiron center and

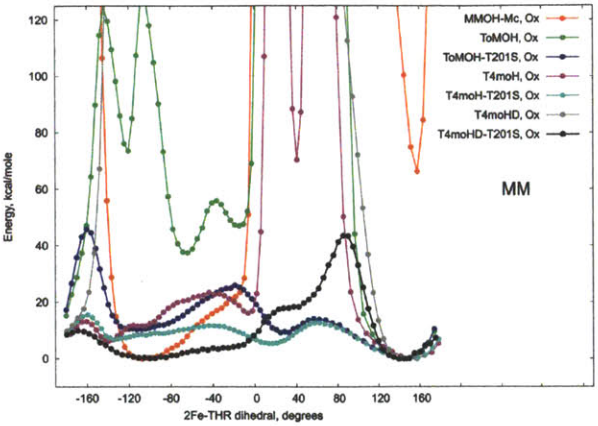

Figure 6. Rotation profiles of threonine in various MMOH and TMOH proteins computed with the MM method. In MMOH, threonine corresponds to T213, and in TMOH, it stands for T201. The T201S mutant curves were produced by replacing the methyl group in the corresponding threonine crystal structures with a hydrogen atom.

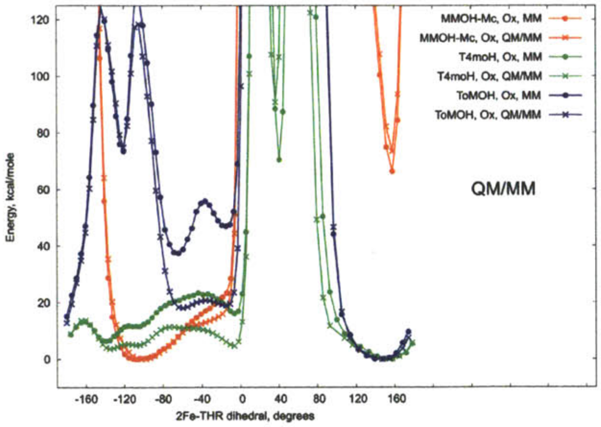

Figure 7. Rotational profiles of threonine in various MMOH and TMOH proteins computed with the QM/MM method. In MMOH, threonine corresponds to T213, and in TMOH it stands for T201.

the threonine hydroxyl. It is conceivable, therefore, that stabilization of the peroxo intermediate in the presence of the regulatory protein occurs through this water filling in the extra 1 Å of space between the threonine OH group and the peroxo ion. Currently we are investigating this hypothesis by studying the intermediates by the QM/MM method starting from the T4moHD crystal structure. In addition, the peroxo ion may be protonated,[14,17,40] which permits other patterns for the hydrogen-bond network between the peroxo ion and the threonine hydroxyl group, as is discussed next Section.

■ THREONINE ROTATIONAL ENERGY PROFILES

The mutation of ToMOH T201 into a very similar residue, serine, leads to significant changes in the oxidation chemistry of the reduced hydroxylase.[14] Judging from the Mössbauer and optical spectra, when in complex with the regulatory protein (ToMOD), the mutant produces two types of peroxo structures upon reaction with O_2: the ToMOH$_{\text{peroxo}}$ and T201$_{\text{peroxo}}$ species. The ratio of the concentrations of the two types of the diiron intermediates is approximately 1:1.[17]

The hypothesis set forth in the previous section proposes that an MMOH-like peroxo, T201$_{\text{peroxo}}$, can be formed when the threonine points its hydroxyl group away from the diiron center. According to this hypothesis, the Thr→Ser mutation must facilitate the rotation around the $C_\alpha-C_\beta$ bond. As an evaluation of this suggestion and possibly to provide a verification of our hypothesis, we carried out a straightforward computational study in which a series of single-point energies were generated for different dihedral angles 2Fe-THR and in which all other atoms not participating in the rotation were frozen. We also considered whether the regulatory protein would have any effect on the barrier to rotation, because in T4moHD it notably affects the position of the threonine compared to wild-type T4moH.

Threonine rotation was studied by two computational methods: MM and QM/MM. The first is more suitable for faster but less accurate work, whereas the second is good for more accurate, quantitative analysis albeit computationally much more expensive. We applied the MM method to probe the problem and to formulate initial conclusions and then repeated the most interesting rotational profiles by using the QM/MM method, to ascertain the quality of the MM results.

Figure 6 superimposes threonine or serine rotational profiles for the oxidized states of six different proteins: MMOH-Mc, ToMOH, ToMOH-T201S, T4moH, T4moH-T201S, and T4moHD-T201S. The energy is plotted as a function of the dihedral angle 2Fe-THR rather than the χ (N−C−C−O) angle around which the rotation was actually performed. The functional transformation of χ into Fe1−Fe2−C_β−O is important because the value of χ does not necessarily relate to the distance of the threonine hydroxyl with respect to the diiron center, and this position is key in our discussion. Moreover, the backbone deformation effected by the regulatory protein in T4moHD makes the same values of the χ angle (in, say T4moH vs T4moHD) correspond to substantially different positions of the hydroxyl with respect to the diiron core, so that comparing χ angles in different proteins for the sake of evaluating our idea about the threonine rotation becomes problematic. Note, for example, the different regions to which the experimental χ angles belong in the nondeformed TMOH and TMOHD crystal structures.

As indicated in the diagram of Figure 4, positive values of the 2Fe-THR angle in Figure 6 reflect the situation when the OH group is directed toward the iron atoms, whereas negative angles are for the OH group pointing *away* from the iron atoms. In MMOH and ToMOH the rotation energy minima are located approximately at −102.9 and 139.2 corresponding to χ angles of −40 and 85.0. The change of the minima compared to the 2Fe-THR angles observed in the corresponding crystal structures is most likely due to the crystal structure relaxation during the theoretical modeling plus the inherent limited accuracy of the MM method, although the latter is expected to have a small contribution to the error. The change in shift is less pronounced in terms of the χ angle, which suggests that the relaxation affects the diiron core more than it does the side chain of the threonine.

Figure 6 clearly demonstrates several important points about the structural properties of the threonine in the MMOH and TMOH proteins. First, it confirms the pattern observed earlier for the crystal structures of the wild-type MMOH and TMOH. The hydroxyl group in MMOH strongly prefers negative angles, whereas in TMOH it assumes a different configuration, with positive angles. Even though ToMOH (green curve) has high-energy rotational minima corresponding to the negative angle, the very high barriers separating negative angles from positive angle minima do not leave the $C_\alpha-C_\beta$ bond much kinetic possibility to rotate. The rotation in the T4moH (magenta curve) is much less restricted. One of the barriers gets significantly smaller, and the energy of the MMOH-type threonine rotational configuration is higher than the absolute minimum by over 6 kcal/mol (compare with roughly 38 kcal/mol in the case of ToMOH). Nevertheless, the TMOH-type configuration should be highly predominant, even in T4moH.

Second, the association of the regulatory protein with T4moH changes the rotational energy landscape dramatically (compare the magenta and gray curves). The regulatory protein totally prohibits rotation of the hydroxyl by imposing an enormously high barrier, which essentially freezes the rotation to adopt the configuration where the OH group faces the active site. Possibly, in this manner it imposes a certain specificity for the formation of only one type of peroxo intermediate, compared with the case of the ToMOHD-T201S mutant discussed below. Because the crystal structure of ToMOHD is unavailable, we were not able to check what effect the regulatory protein has on ToMOH or its mutants, but we expect it to be very similar to the effect observed in T4moHD.

Third, the mutation of the threonine into serine in the TMOH proteins produces another dramatic change in the rotational energy curves. While preserving the absolute minima at the positive angles, the energies of the local minima at the negative angles are drastically reduced. Additionally, the barriers to rotation fall sharply in magnitude so that rotation around the $C_\alpha-C_\beta$ bond and the population of both configurations (MMOH-like and TMOH-like) become possible. The effect is most pronounced when the regulatory protein associates with T4moH (black curve). The MMOH configuration in this case is separated from TMOH by only 9.9 kcal/mol of a barrier and lies higher only by 0.2 kcal/mol. This energy profile qualitatively agrees with the experimental observation that the ToMOHD-T201S mutant generates two peroxo forms in comparable proportion. The energy difference of 0.2 kcal/mol closely corresponds to the ratio of 1:1 that would be predicted using the $\exp(-\Delta H/kT)$ formula, if we assume that $\Delta E \approx \Delta H$ and use the temperature of 277 K at which the experiment was performed. However, beside the $\Delta E \approx \Delta H$ approximation, we have to remember that the two forms with comparable concentrations were observed on ToMOHD-T201S, and not T4moHD-T201S, the energy profile of which we are currently discussing. Additionally, we do not currently know the structure of peroxo TMOH, and so it would be difficult to model its threonine rotation profile. Our preliminary calculations based on the ToMOH (a) peroxo model from Figure 5 indicate that the presence of O_2^{2-} in the active site, and even the formation of the hydrogen bond between O_2^{2-} and T201 does not significantly alter the general shape of the ToMOH (Ox) curve. These several approximations allow us to conclude that the energy separation of 0.2 kcal/mol obtained from the T4moHD-T201S curve and the ratio of the comparable peroxo populations in the experiment are in an excellent qualitative agreement. Overall, the rotational energy profiles in Figure 6 reveal the major influence of the regulatory protein and also explain how the threonine mutation into serine can lead to a formation of both peroxo structure types.

Figure 7 compares several MM rotational energy curves with QM/MM curves for the same structures. The QM/MM method, based on the B3LYP DFT functional, should be considered significantly more accurate than MM. We must remember, however, that B3LYP itself is not without defects, especially when metal atoms are present, and so its predictions should be viewed with caution. Because the QM/MM method is much more computationally expensive than MM, it would be wasteful to apply QM/MM if the accuracy of MM is sufficient. Therefore, the goal of the comparison in Figure 7 is to ascertain whether the MM energy profiles can be trusted without the recourse to the QM/MM method. From Figure 7 we note that MM and QM/MM agree almost quantitatively in the regions of the 2Fe-THR from −180 to −140 and from 100 to 180 of the 2Fe-THR angle. The agreement in the region from −140 to −100 is only qualitative, with the differences in energy bewteen QM/MM and QM in some cases over 30 kcal/mol, but the shapes of the corresponding QM/MM and MM curves are similar throughout. This region of qualitative agreement contains the MMOH-like minima and is thus a potentially important span of angles. These or other QM/MM curves that we computed (not shown) did not alter our qualitative conclusions regarding the role of the regulatory protein and the effect of the mutation, but should more quantitative calculations be made in the future (especially with the goal of computing ΔG, and not only ΔE), the QM/MM method should be chosen.

A recent experimental study[17] describing crystal structures and dioxygen activation characteristics of several ToMOH mutants (T201S, T201G, T201C, and T201V) confirms our rotational profiling. T201S is crystallized with the hydroxyl group of serine-201 pointing toward the diiron center with the corresponding 2Fe-THR angle equal to 141°, in agreement with the ToMOH-T201S curve in Figure 6. It is interesting that T201G displays a small amount of catalytic activity, even though it cannot form a hydrogen bond with the peroxo group. A plausible explanation for this result is that glycine, being small and nonhydrophobic, lets an extra water take the place of an otherwise bulky residue. This water might assist in stabilizing the corresponding peroxo species and in proton delivery during the catalytic cycle. The T201 V mutant, having a bulky and hydrophobic residue is, not surprisingly, the least active.

■ MÖSSBAUER SPECTRA AND PROPOSED STRUCTURES OF THE PEROXO INTERMEDIATES

The remaining issue of interest is the nature of the geometrical structures of the peroxo intermediates for MMOH and TMOH proteins. In the previous section we showed that the appearance of one or another peroxo intermediate, or both, as in the case of the T201S mutant, in the experiment correlates well with the position of the energetic minima on the threonine rotation energy profile. In an earlier section, we showed that the QM/MM optimization predicted two $\text{ToMOH}_{\text{peroxo}}$ structures stabilized by a hydrogen bond formed between T201 and the peroxo ion, a geometry that would be impossible for MMOH. There has been disagreement in the past over the structure of the peroxo intermediate in MMOH, in particular, whether it has the η^2,η^2 or *cis*-μ-1,2 geometry.[10,41−43] In any case, neither of these geometries can form a hydrogen bond with T213 because the distance is too long, and therefore the structure may differ from the types illustrated in Figure 5.

The geometrical differences between the ToMOH structures and their lower energy with respect to a Q-type structure are consistent with the experimental failure to detect the latter in this enzyme. However, the peroxo structures shown in Figure 5 cannot be *exactly* correct for at least two reasons. First, they were

Table 4. Computed Mössbauer Characteristics of Some Geometrical Models of the ToMOH Intermediates Whose Structures Are Shown in Figure 5

form	Fe	oxidation state	spin	δ_{exp}, mm/s	$\lvert\Delta E\rvert_{exp}$, mm/s	δ, mm/s	$\lvert\Delta E\rvert$, mm/s
peroxo (a)	Fe1	+3	+5	0.54	0.67	1.02	3.02
	Fe2	+3	−5	0.54	0.67	0.65	0.44
peroxo (b)	Fe1	+3	+5	0.54	0.67	1.00	2.71
	Fe2	+3	−5	0.54	0.67	0.59	0.34

optimized starting from a ToMOH structure not associated with ToMOD. The crystal structure of T4moHD, an excellent model for ToMOHD, revealed that there is additional space occupied by an extra water molecule separating T201 and the diiron center, by comparison with T4moH, so that the hydrogen-bond formation *directly* between T201 and the peroxo ion coordinated to the iron atoms would be unlikely. Second, the Mössbauer characteristics that we computed for these structures deviate widely from the experimentally observed values (see Table 4). At the same time, the theoretically predicted Mössbauer spectra of MMOH peroxo candidates agree well with the experiment.[41,35] Nevertheless, we still present and discuss these peroxo structures because for the first time they illustrate the kinds of structural elements that might explain the different chemical behavior of the MMOH and TMOH intermediates and serve as a first approximation for forthcoming modeling. Importantly, through certain modifications in the geometries it is possible to eliminate both obstacles mentioned above and reconcile theory with experiment. The rest of this section explains how.

As the rotational energy profiles of T201 suggest and as proposed in the literature[14,40] based on experimental studies, T201 must participate in the stabilization of the TMOH peroxo intermediate. The water molecule that accompanies binding of the regulatory protein can serve as a hydrogen-bonding bridge between the peroxo ion and the threonine side chain. Possible hydrogen-bond networks between O_2^{2-} and T201 through the water molecule are shown in Figure 8. Such networks may involve protonation, as, for example, models (a) and (b), and this proton can be carried by the extra water molecule as H_3O^+. In Figure 8 we placed the proton on the peroxide anion, the most basic species. However, when the oxygen-containing species is bound to the two Fe(III) ions, its basicity will change. Other modes of coordination of O_2^{2-} with the diiron center are possible, and the choice of the μ-1,1 coordination in Figure 8 is purely for illustrative purposes. Both the μ-1,1 and μ-1,2 binding modes, for example, provide just enough space for the protonated peroxo ion and the water molecule hydrogen bound to it to fit between the diiron center and the threonine residue. A detailed study of the relative stabilities of such structures will be the subject of a separate study. Here we are only concerned with proposing how peroxo structures, such as those in Figure 5, could be modified in the presence of the regulatory protein so that T201 can be involved in the stabilization of the peroxo structure despite the increased distance between the O_2^{2-} and the hydroxyl group.

The next task is to explain why the Mössbauer spectra of the MMOH- and TMOH-type peroxo species are different from one another. The MMOH peroxo intermediate displays only one signal with an isomer shift δ and a quadrupole splitting ΔE_Q equal to 0.66 and 1.51 mm/s, respectively.[6] The Mössbauer parameters of the TMOH-type peroxo are: $\delta = 0.55$ and $\Delta E = 0.67$ mm/s, also comprising only one signal.[13] Although there is a noticeable difference in the isomer shift, it is the change in the quadrupole splitting parameter that is the most striking. The transition from $\Delta E = 1.51$ mm/s in MMOH to $\Delta E = 0.67$ mm/s in ToMOH may mean a significant alteration in the structure of the active site, most probably involving charged atoms or altered electron effects of the bound ligands, because such effects typically have a marked influence on the quadrupole splitting.[44−46]

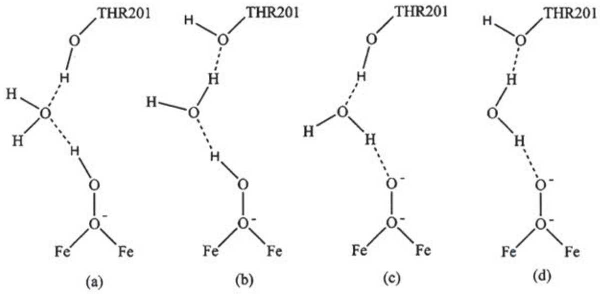

Figure 8. Possible hydrogen-bond networks stabilizing the peroxo structure of μ-1,1 coordination in the TMOHD complex. Models (a) and (b) are protonated.

As we noted before and as Table 4 reports, the computed Mössbauer characteristics of the peroxo structures shown in Figure 5 are totally incompatible with the experimental values. There may be several explanations for this discrepancy. Peroxo structures (a) and (b) in Figure 5 may be artifacts of TMOH because the TMOHD active site, involving an additional water molecule, might be essential for a proper modeling of peroxo intermediates and, consequently, reproduction of their Mössbauer spectra. However, this explanation appears improbable, because the substitution of the $O_2^{2-}\cdots HO{-}Thr$ hydrogen bond by the $O_2^{2-}\cdots H_2O\cdots HO{-}Thr$ hydrogen bond as a result of the complexation with the regulatory protein should not cause a significant change in the quadrupole splitting. Another, more plausible, explanation is that we did not sufficiently explore the configurational space in the course of the QM/MM optimization. Although we started with eight different peroxo models that converged to four distinct coordinations, many other geometries corresponding to local energy minima might exist, which either lie far from the starting geometries or which simply have not been found by the optimization algorithm. This problem is a common one of theoretical optimizations that involve several essential degrees of freedom and where the targeted geometry is not known for certain from experiment. Finally, the peroxo structure may be protonated, which may result in a significant change of the quadrupole splitting. From some studies[47,48] it can be inferred that certain protonated oxo-bridged diferric structures have much lower quadrupole splittings than their unprotonated analogs. This observation has a direct relevance to our predicament of matching the low quadrupole splitting of a peroxo species.

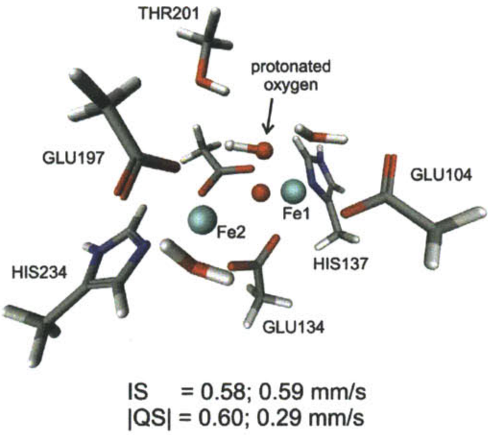

Figure 9. The geometry and the Mössbauer characteristics of one of the protonated model peroxo structures optimized with B3LYP (the μ-1,1 type coordination of the dioxygen molecule). The structure is shown in perspective in order to avoid atoms blotting one another; the only unlabeled residue is GLU231. The protonated distal oxygen atom is indicated. The color-coding is as follows: hydrogens are white, carbons are gray, oxygens are red, nitrogens are blue, and irons are cyan.

In order to address the two latter possibilities, we generated over 60 possible model peroxo diiron(III) structures within the ToMOH active site with the help of MC sampling. We presumed that sampling the T4moHD active site at this stage of the investigation would be undesirable because it would involve several extra degrees of freedom due to the additional water molecule, the presence of which would probably not contribute to significant changes in the quadrupole splitting parameters. Then, we computed the Mössbauer characteristics of all these structures, and none of the quadrupole splittings was close to the experimental value of ΔE = 0.67 mm/s for both iron atoms. We usually got quadrupole splittings having large values for both iron atoms, 1−3 mm/s, or one iron with a low value (less than 1 mm/s) while the other iron was characterized by a large value (over 2 mm/s), similar to the situation observed for peroxo structures (a) and (b) in Figure 5. It is only when we began to place protons on our model structures that we observed a significant drop in the quadrupole splittings of the resulting protonated species.

Figure 9 presents a DFT-optimized protonated model structure of the TMOH active site along with the corresponding Mössbauer characteristics, which are quite close to the experimental values. The isomer shift is 0.58 and 0.59 mm/s (two signals), and the quadrupole splitting is 0.60 and 0.29 mm/s. Even though this quadrupole splitting does not qualify as providing quantitative agreement with the experimental value (0.67 mm/s), it is qualitatively reasonable. The isomer shift is quite close (the corresponding experimental value is 0.54 mm/s), and both computed characteristics of the protonated structure are in sharp contrast with the computed Mössbauer characteristics of the unprotonated peroxo models from Figure 5 (see Table 4), which clearly contradict the experiment. We stress that the structure shown in Figure 9, with two bridging carboxylate groups and two water molecules, each coordinated to an iron atom, is only an approximate model obtained from a DFT minimization in the absence of the protein environment. We are not suggesting that it is necessarily representative of the true ToMOH peroxo structure.

We do not expect that a water molecule positioned in between the THR-201 residue and the hydroperoxo ion, in a manner sketched in Figure 8a and b, will have a significant effect on the quadrupole splitting because such a change involves uncharged entities that are relatively distant from the diiron core. We constructed a number of approximate protonated peroxo models in the manner of Figure 8a and b, starting from either the 3DHH crystal structure or the converged structures given in Figure 5. We also carried out constrained DFT optimizations of these models. This modeling yielded a cluster of at least 12 structures of varying similarity. Their Mössbauer spectra certainly differed, but one thing remained clear: the presence of an extra water hydrogen bonded with an OH group of T201, on one side, and the protonated peroxo group, on another, did not qualitatively deviate from the experimental Mössbauer spectrum of ToMOH peroxo intermediate. Most of our models had low values (<1.0 mm/s) of quadrupole splitting on both iron atoms, in accordance with our earlier observation for protonated peroxo models without the extra water molecule in the active site. For example, one manually built model protonated peroxo form with an extra water molecule in it gave the isomer shifts (IS) of 0.56 and 0.80 mm/s and the quadrupole splittings (QS) of 0.38 and 0.74 mm/s. Another similar model obtained as a result of a constrained DFT optimization gave IS of 0.63 and 0.70 mm/s and QS of 0.79 and 0.89 mm/s.

Our Mössbauer benchmarking work[35] tested Mössbauer spectra on a set of 31 diverse chemical structures and predicted mean unsigned errors of about 0.02 mm/s for the isomer shift and about 0.1 mm/s for the quadrupole splitting in the region <2.0 mm/s. The computed Mössbauer spectra of the TMOH peroxo models have significantly larger deviation from the reported experimental data. But the above error bounds were obtained on average-sized inorganic molecules with reliable crystal structures. When there is a great structural uncertainty and much more complicated chemical entities (proteins), as in the case of the ToMOH peroxo models, the errors are expected to increase. Therefore, given the approximate nature of our models, we consider our theoretical Mössbauer predictions to be in reasonable agreement with the experiment and the simpler protonated models illustrated by Figure 9.

A proper prediction of the ToMOH peroxo structure should involve a QM/MM modeling starting from the crystal structure with the regulatory protein attached. What the structure in Figure 9 illustrates is that, according to DFT, there exist stationary points of the protonated models which, at the same time, have Mössbauer characteristics that are quite close to the experimental ones. A meticulous study of similar protonated structures (also involving double protonation), both structural and spectroscopic, should be performed in the future following QM/MM optimization. Since the protonation is the only way we found to reconcile the low experimental quadrupole splitting with the theoretical predictions, the generation and the analysis of the protonated structures holds great promise for finding the right structure model for the ToMOH peroxo.

Recently, an X-ray structure of T4moH with H_2O_2 putatively bound to the active site was published (PDB 3I63).[15] Its examination reveals a H_2O_2 molecule loosely bound with the apparently ferric ions. The O−O distance (1.5 Å) in H_2O_2 is very similar to the distance in free H_2O_2, and the shortest distances between the iron atoms and the peroxide oxygen atoms (2.2 and 2.4 Å) are too long to indicate a true peroxo species. Additionally, our Mössbauer calculations based upon the model of this X-ray structure yield the IS equal to 0.83 and 0.85 mm/s and the QS equal to 1.75 and 1.48 mm/s, which is in obvious disagreement with the experimental data (IS = 0.56 mm/s, QS = 0.67 mm/s). All these details make us regard this structure as T4moH cocrystallized with H_2O_2 rather than a protonated peroxo T4moH. As such, it probably has little relevance for the actual geometry of the peroxo species.

■ RELATION TO CYTOCHROME P450

Cytochrome P450 enzymes comprise a family of oxygenases structurally and physiologycally unrelated to BMM.[49] There is little common between the active sites of the two families because the former has a monoiron, thiolate-coordinated heme center and the latter are diiron enzymes that are rich in carboxylate ligands. However, there are striking similarities between the oxygen activation mechanisms of these two families.

The first similarity is the presence of adjacent threonine and asparagine side chains in the vicinity of the active sites of BMM and P450 enzymes. The P450 research community has established an important role that these two residues play in the delivery of protons needed for dioxygen activation.[50–53] Similar function was proposed for these two residues in BMM enzymes.[14,17,21,39,40] More evidence for a similar functional role of the threonine residue in BMM and P450 active sites comes from mutagenesis studies in TMOH and P450 enzymes. Substituting the threonine with residues incapable of forming hydrogen bond with the dioxygen in the active site severely disrupts hydroxylation in either ToMOH,[17] T4moH,[40] or P450.[23,54,55] In contrast, replacing the threonine with serine, thus preserving a hydrogen-bond forming hydroxyl group, alters oxidation mechanism but preserves the oxidative capabilities of either ToMOH[14] or P450.[54]

Another analogy between P450 and BMM families concerns the nature of the peroxo intermediate. There seems to be a consensus regarding the molecular geometry of the so-called Compound 0, a distally protonated peroxo intermediate of P450 enzymes.[56–58] The present work also suggests a distally protonated structure for the TMOH peroxo intermediate based on QM/MM and Mössbauer spectra modeling, providing another link with the P450 oxidative mechanism.

It is unlikely, however, that the parallels between the oxidative mechanisms of BMM and P450 families continue beyond the hydroxyperoxo species. In P450, the oxidation is primarily performed by Compound I, an Fe(IV) radical cation. In MMOH the principal oxidant is an Fe(IV)−Fe(IV) species Q,[10,42,43] whereas in TMOH no oxidative species other than peroxo has been observed.[13] Nevertheless, the similarity between the proton-shuttling hydrogen-bonding network formed with identical residues near the active site as well as an analogous protonation of the peroxo intermediate during the dioxygen activation in two unrelated active sites suggests an intriguing example of convergent mechanistic evolution.

■ CONCLUSION

Nature surpasses human imagination in how it can utilize small modifications in biomolecules in order to fine-tune biochemical processes or produce drastic changes in the phenotype. Countless examples are known where the difference of one hydrogen bond or a single amino acid causes macro-effects. Bacteria with a metabolism that depends upon BMMs seem to exploit small variations in these protein structures for better adaptation to their biological niche. In this work we have examined the structural differences between the two classes of BMM enzymes, MMOH and TMOH, the active sites of which are almost identical, and yet their chemistry is markedly divergent. We focus on the process of dioxygen activation, which produces different types of peroxo species in MMOH and TMOH, according to spectroscopic measurements.

After listing and discussing some notable amino acid differences in the vicinity of the MMOH and TMOH active sites, we cannot find a clear explanation as to how any of these changes can bring about the disparate chemistry of the dioxygen activation of the two enzymes. Then, we narrowed our analysis to the strictly conserved threonine residue in the BMM family (T213 in MMOH and T201 in TMOH) and demonstrated that, in all the nonperturbed crystal structures of MMOH, T213 has a rotational configuration along its $C_\alpha-C_\beta$ bond that is qualitatively distinct from the configuration of T201 in all the crystal structures of TMOH. A series of rotational profiles around the $C_\alpha-C_\beta$ bond of the threonine side chain that we generated using both MM and QM/MM methods are in good agreement with experimental observations and helps explain the formation of two peroxo species in the case of the T201S mutant. According to the rotational energy profiles, the regulatory protein imposes a very tall barrier on rotation of the threonine side chain, perhaps controlling specificity in the formation of the peroxo species of the wild-type proteins. A more detailed study involving other mutants, both theoretically and experimentally, is reserved for the future, to either confirm or refute the hypothesis that the configuration of the threonine is directly related to the formation of one or another type of peroxo species.

Our QM/MM geometry optimizations of the peroxo and Q intermediates of TMOH starting from the 2INC crystal structure (not involving the regulatory protein) demonstrate that the most stable peroxo form, of the μ-1,2 type coordination of the oxygen and stabilized by the hydrogen bond that the peroxo-anion forms with the threonine hydroxyl, is nearly 5 kcal/mol more stable than the Q structure. This result is in contrast to our recent investigation of the MMOH intermediates[10] in which it was shown that the peroxo and Q structures have an almost equal energy. The present computational result is in agreement with experiment, which does not detect a Q form for ToMOH. The computed Mössbauer parameters of the optimized peroxo structures are in disagreement with experiment, and we propose a number of explanations for this fact. In particular, we show that protonation of the peroxo unit can reconcile theoretical and experimental Mössbauer data. Finally, we argue that it will be important to undertake a QM/MM study based on the T4moHD crystal structure, since this structure should be relevant to the intermediates observed in experiment.

More work is required to clarify several remaining issues: the structure of the $ToMOH_{peroxo}$ intermediate and its possible protonation and stabilization through the hydrogen-bonding network involving T201, the relative stability of the peroxo with respect to the Q structure, and the further analysis of the hypothesis (through the studies of the mutant forms) that T201 in TMOH and T213 in MMOH plays a key role in the formation of the peroxo species. However, we believe that the present study, through the insights into the function of the threonine residue, the role of the regulatory protein, and the possibility of protonation at a suitable location in the active site to explain the $ToMOH_{peroxo}$ quadrupole splitting, paves the way toward future progress in understanding the chemistry of the TMOH and MMOH intermediates.

Finally, we wish to highlight the elevated objectives set for the computational methodology in this work. Applying high-level computational tools, such as QM/MM, to single protein systems as well as comparing multiple proteins by bioinformatics-type treatments has become relatively straightforward. But using high-level computations for understanding differences in chemical behavior of large, highly homologous proteins is still a great challenge. This work demonstrates a successful approach to this kind of problem and helps define the aims for the future progress in this area.

■ ASSOCIATED CONTENT

Ⓢ **Supporting Information.** The Supporting Information contains the complete citation of ref 25 and the atomic coordinates of the structures displayed in Figures 5 and 9. This material is available free of charge via the Internet at http://pubs.acs.org/.

■ AUTHOR INFORMATION

Corresponding Author

rich@chem.columbia.edu; lippard@mit.edu

■ ACKNOWLEDGMENT

R.A.F. acknowledges grant no. GM40526 from the National Institute of Health, and S.J.L. acknowledges grant no. GM032134 from the National Institute of General Medical Sciences.

■ REFERENCES

(1) Leahy, J. G.; Batchelor, P. J.; Morcomb, S. M. *FEMS Microbiol. Rev.* **2003**, *27*, 449–479.

(2) Notomista, E.; Lahm, A.; Di Donato, A.; Tramontano, A. *J. Mol. Evol.* **2003**, *56*, 435–445.

(3) Sazinsky, M. H.; Lippard, S. J. *Acc. Chem. Res.* **2006**, *39*, 558–566.

(4) Murray, L. J.; Lippard, S. J. *Acc. Chem. Res.* **2007**, *40*, 466–474.

(5) Wallar, B. J.; Lipscomb, J. D. *Chem. Rev.* **1996**, *96*, 2625–2658.

(6) Merkx, M.; Kopp, D. A.; Sazinsky, M. H.; Blazyk, J. L.; Müller, J.; Lippard, S. J. *Angew. Chem., Int. Ed.* **2001**, *40*, 2782–2807.

(7) Kopp, D. A.; Lippard, S. J. *Curr. Opin. Chem. Biol.* **2002**, *6*, 568–576.

(8) Baik, M.-H.; Newcomb, M.; Friesner, R. A.; Lippard, S. J. *Chem. Rev.* **2003**, *103*, 2385–2420.

(9) Gherman, B. F.; Baik, M.-H.; Lippard, S. J.; Friesner, R. A. *J. Am. Chem. Soc.* **2004**, *126*, 2978–2990.

(10) Rinaldo, D.; Philipp, D. M.; Lippard, S. J.; Friesner, R. A. *J. Am. Chem. Soc.* **2007**, *129*, 3135–3147.

(11) Han, W.-G.; Noodleman, L. *Inorg. Chem. Acta* **2008**, *361*, 973–986.

(12) Tinberg, C. E.; Lippard, S. J. *Biochemistry* **2009**, *48*, 12145–12158.

(13) Murray, L. J.; Naik, S. G.; Ortillo, D. O.; García-Serres, R.; Lee, J. K.; Huynh, B. H.; Lippard, S. J. *J. Am. Chem. Soc.* **2007**, *129*, 14500–14510.

(14) Song, W. J.; Behan, R. K.; Naik, S. G.; Huynh, B. H.; Lippard, S. J. *J. Am. Chem. Soc.* **2009**, *131*, 6074–6075.

(15) Bailey, L. J.; Fox, B. G. *Biochemistry* **2009**, *48*, 8932–8939.

(16) Notomista, E.; Cafaro, V.; Bozza, G.; Di Donato, A. *Appl. Environ. Microbiol.* **2009**, *75*, 823–836.

(17) Song, W. J.; McCormick, M. S.; Behan, R. K.; Sazinsky, M. H.; Jiang, W.; Lin, J.; Krebs, C.; Lippard, S. J. *J. Am. Chem. Soc.* **2010**, *132*, 13582–13585.

(18) Sazinsky, M. H.; Bard, J.; Di Donato, A.; Lippard, S. J. *J. Biol. Chem.* **2004**, *279*, 30600–30610.

(19) McCormick, M. S.; Sazinsky, M. H.; Condon, K. L.; Lippard, S. J. *J. Am. Chem. Soc.* **2006**, *128*, 15108–15110.

(20) Murray, L. J.; García-Serres, R.; McCormick, M. S.; Davydov, R.; Naik, S. G.; Kim, S.-H.; Hoffman, B. M.; Huynh, B. H.; Lippard, S. J. *Biochemistry* **2007**, *46*, 14795–14809.

(21) Bailey, L. J.; McCoy, J. G.; Phillips, G. N., Jr.; Fox, B. G. *Proc. Natl. Acad. Sci. U.S.A.* **2008**, *105*, 19194–19198.

(22) Raag, R.; Martinis, S. A.; Sligar, S. G.; Poulos, T. L. *Biochemistry* **1991**, *30*, 11420–11429.

(23) Altarsha, M.; Benighaus, T.; Kumar, D.; Thiel, W. *J. Am. Chem. Soc.* **2009**, *131*, 4755–4763.

(24) Li, X.; Jacobson, M. P.; Zhu, K.; Zhao, S.; Friesner, R. A. *Proteins: Struct., Funct., Bioinf.* **2007**, *66*, 824–837.

(25) Banks, J. L.; et al. *J. Comput. Chem.* **2005**, *26*, 1752–1780.

(26) *QSite 4.5*; Schrödinger, Inc.: Portland, OR, 2007.

(27) Murphy, R. B.; Philipp, D. M.; Friesner, R. A. *Chem. Phys. Lett.* **2000**, *321*, 113–120.

(28) Murphy, R. B.; Philipp, D. M.; Friesner, R. A. *J. Comput. Chem.* **2000**, *21*, 1442–1457.

(29) Philipp, D. M.; Friesner, R. A. *J. Comput. Chem.* **1999**, *20*, 1468–1494.

(30) Hay, P. J.; Wadt, W. R. *J. Chem. Phys.* **1985**, *82*, 270–283.

(31) Hay, P. J.; Wadt, W. R. *J. Chem. Phys.* **1985**, *82*, 299–310.

(32) Wadt, W. R.; Hay, P. J. *J. Chem. Phys.* **1985**, *82*, 284–298.

(33) Kolossváry, I.; Guida, W. C. *J. Comput. Chem.* **1999**, *20*, 1671–1684.

(34) Keserû, G.; Kolossváry, I. *J. Am. Chem. Soc.* **2001**, *123*, 12708–12709.

(35) Bochevarov, A. D.; Friesner, R. A.; Lippard, S. J. *J. Chem. Theory Comput.* **2010**, *6*, 3735–3749.

(36) Elango, N. A.; Radhakrishnan, R.; Froland, W. A.; Wallar, B. J.; Earhart, C. A.; Lipscomb, J. D.; Ohlendorf, D. H. *Protein Sci.* **1997**, *6*, 556–568.

(37) Coufal, D. E.; Blazyk, J. L.; Whittington, D. A.; Wu, W. W.; Rosenzweig, A. C.; Lippard, S. J. *Eur. J. Biochem.* **2000**, *267*, 2174–2185.

(38) Pikus, J. D.; Mitchell, K. H.; Studts, J. M.; McClay, K.; Steffan, R. J.; Fox, B. G. *Biochemistry* **2000**, *39*, 791–799.

(39) Sazinsky, M. H.; Dunten, P. W.; McCormick, M. S.; Di Donato, A.; Lippard, S. J. *Biochemistry* **2006**, *45*, 15392–15404.

(40) Elsen, N. L.; Bailey, L. J.; Hauser, A. D.; Fox, B. G. *Biochemistry* **2009**, *48*, 3838–3846.

(41) Han, W.-G.; Noodleman, L. *Inorg. Chem.* **2008**, *47*, 2975–2986.

(42) Brunold, T. C.; Tamura, N.; Kitajima, N.; Moro-oka, Y.; Solomon, E. I. *J. Am. Chem. Soc.* **1998**, *120*, 5674–5690.

(43) Yumura, T.; Yoshizawa, K. *Bull. Chem. Soc. Jpn.* **2004**, *77*, 1305–1311.

(44) Ohya, T.; Sato, M. *J. Chem. Soc., Dalton Trans.* **1996**, *8*, 1519–1523.

(45) Cao, C.; Dahal, S.; Shang, M.; Beatty, A. M.; Hibbs, W.; Schulz, C. E.; Scheidt, W. R. *Inorg. Chem.* **2003**, *42*, 5202–5210.

(46) Guerriero, P.; Tamburini, S; Vigato, P. A.; Russo, U.; Benelli, C. *Inorg. Chim. Acta* **1993**, *213*, 279–287.

(47) Wu, F.-J.; Kurtz, D. M., Jr.; Hagen, K. S.; Nyman, P. D.; Debrunner, P. G.; Vankai, V. A. *Inorg. Chem.* **1990**, *29*, 5174–5183.

(48) Tshuva, E. Y.; Lippard, S. J. *Chem. Rev.* **2004**, *104*, 987–1012.

(49) Ortiz de Montellano, P. R. *Cytochrome P450: Structure, Mechanism and Biochemistry*, 3rd ed.; Plenum Press: New York, 2005.

(50) Gerber, N. C.; Sligar, S. G. *J. Biol. Chem.* **1994**, *269*, 4260–4266.

(51) Vidakovic, M.; Sligar, S. G.; Li, H.; Poulos, T. L. *Biochemistry* **1998**, *37*, 9211–9219.

(52) Clark, J. P.; Miles, C. S.; Mowat, C. G.; Walkinshaw, M. D.; Reid, G. A.; Daff, S. N.; Chapman, S. K. *J. Inorg. Biochem.* **2006**, *100*, 1075–1090.

(53) Hlavica, P. *Eur. J. Biochem.* **2004**, *271*, 4335–4360.

(54) Imai, M.; Shimada, H.; Matsushima-Hibaya, Y.; Makino, R.; Koga, H.; Horiuchi, T.; Ishimura, Y. *Proc. Natl. Acad. Sci. U.S.A.* **1989**, *86*, 7823–7827.

(55) Yeom, H.; Sligar, S. G.; Li, H.; Poulos, T. L.; Fulco, A. J. *Biochemistry* **1995**, *34*, 14733–14740.

(56) Davydov, R.; Makris, T. M.; Kofman, V.; Werst, D. E.; Sligar, S. G.; Hoffman, B, M. *J. Am. Chem. Soc.* **2001**, *123*, 1403–1415.

(57) Groenhof, A.; Ehlers, A. W.; Lammertsma, K. *J. Am. Chem. Soc.* **2007**, *129*, 6204–6209.

(58) Altun, A.; Kumar, D.; Neese, F.; Thiel, W. *J. Phys. Chem. A* **2008**, *112*, 12904–12910.

Appendix B.

Multiple Roles of Component Proteins in Bacterial Multicomponent Monooxygenases: Phenol Hydroxylase and Toluene/*o*-Xylene Monooxygenase from *Pseudomonas* sp. OX1

* Author contribution

The author performed the experiments of ToMO system. The parallel studies of PH system were carried out by Dr. Christine E. Tinberg (Lippard Lab, MIT).

* Reprinted with permission from a following publication,

Christine E. Tinberg, Woon Ju Song, Viviana Izzo, Stephen J. Lippard "Multiple Roles of Component Proteins in Bacterial Multicomponent Monooxygenases: Phenol Hydroxylase and Toluene/*o*-Xylene Monooxygenase from *Pseudomonas* sp. OX1"*Biochemistry* **2011**, *50,* 1788-1798

1788 *Biochemistry* **2011,** *50,* 1788–1798
DOI: 10.1021/bi200028z

BIOCHEMISTRY
including biophysical chemistry & molecular biology
Article

Multiple Roles of Component Proteins in Bacterial Multicomponent Monooxygenases: Phenol Hydroxylase and Toluene/*o*-Xylene Monooxygenase from *Pseudomonas* sp. OX1[†]

Christine E. Tinberg, Woon Ju Song, Viviana Izzo, and Stephen J. Lippard*

Department of Chemistry, Massachusetts Institute of Technology, Cambridge, Massachusetts 02139, United States

Received November 11, 2010; Revised Manuscript Received January 23, 2011

ABSTRACT: Phenol hydroxylase (PH) and toluene/*o*-xylene monooxygenase (ToMO) from *Pseudomonas* sp. OX1 require three or four protein components to activate dioxygen for the oxidation of aromatic substrates at a carboxylate-bridged diiron center. In this study, we investigated the influence of the hydroxylases, regulatory proteins, and electron-transfer components of these systems on substrate (phenol; NADH) consumption and product (catechol; H_2O_2) generation. Single-turnover experiments revealed that only complete systems containing all three or four protein components are capable of oxidizing phenol, a major substrate for both enzymes. Under ideal conditions, the hydroxylated product yield was ~50% of the diiron centers for both systems, suggesting that these enzymes operate by half-sites reactivity mechanisms. Single-turnover studies indicated that the PH and ToMO electron-transfer components exert regulatory effects on substrate oxidation processes taking place at the hydroxylase actives sites, most likely through allostery. Steady state NADH consumption assays showed that the regulatory proteins facilitate the electron-transfer step in the hydrocarbon oxidation cycle in the absence of phenol. Under these conditions, electron consumption is coupled to H_2O_2 formation in a hydroxylase-dependent manner. Mechanistic implications of these results are discussed.

Bacterial multicomponent monooxygenases (BMMs)[1] are remarkable enzymes that orchestrate a series of electron-transfer and substrate activation events to prime dioxygen for insertion of a single oxygen atom into a C−H bond or addition across a C=C bond (*1*, *2*). Proteins belonging to this family are subdivided into four classes, soluble methane monooxygenases (sMMOs), phenol hydroxylases (PHs), alkene monooxygenases (AMOs), and four-component alkene/arene monooxygenases (TMOs), based on substrate preference and sequence homology (*3*, *4*). The ability of BMMs to generate potent oxidizing species without damaging their active sites or consuming electrons in a futile manner depends on the dynamic involvement of three or more protein components: a 200−255 kDa dimeric hydroxylase that houses two copies of a carboxylate-bridged diiron catalytic center, a 38−45 kDa reductase that accepts electrons from NADH and shuttles them through its flavin and [2Fe-2S] cluster cofactors into the hydroxylase diiron sites, and a 10−16 kDa regulatory protein that couples electron consumption to hydrocarbon oxidation (*1*, *2*, *5*). For ToMO, an additional 12 kDa Rieske protein acts as an electron conduit between the reductase and the hydroxylase. Timely regulation of interactions between these proteins assures efficient catalysis.

The first step in catalysis by the BMM proteins is the reductive activation of O_2 at the hydroxylase diiron centers for incorporation into substrate. The most extensively studied O_2 activation pathways in BMMs are those of the soluble methane monooxygenases (sMMOs) from *Methylococcus capsulatus* (Bath) and *Methylosinus trichosporium* OB3B. In these systems, reaction of the diiron(II) form of the hydroxylase (MMOH) with O_2 leads to the sequential generation of two peroxodiiron(III) units, P* (*6*, *7*) and H_{peroxo} (*8*−*10*), in the presence of the regulatory protein MMOB. Subsequent transfer of one or two protons (*7*, *11*) leads to rearrangement of the iron−oxygen core and formation of Q, a di(μ-oxo)diiron(IV) species responsible for methane oxidation (*8*, *12*−*14*). In the absence of methane and other substrates, Q decays slowly to H_{ox} via a pathway that is not fully understood (*7*).

The O_2 activation pathway of toluene/*o*-xylene monooxygenase (ToMO) from *Pseudomonas* sp. OX1 was also recently investigated (*15*). Upon reaction of the diiron(II) form of the ToMO hydroxylase (ToMOH) with O_2 in the presence of the regulatory protein ToMOD, a diiron(III) intermediate with no obvious absorption features rapidly formed and subsequently decayed to the diiron(III) protein resting state without progressing through a stable, high-valent Q-like intermediate (*15*, *16*).

[†] This work was funded by Grant GM032134 from the National Institute of General Medical Sciences. C.E.T. thanks the National Institutes of Health for partial support under Interdepartmental Biotechnology Training Grant T32 GM08334. V.I. thanks CEINGE (Biotecnologie Avanzate, Naples, Italy) for partial support.

*To whom correspondence should be addressed. E-mail: lippard@mit.edu. Telephone: (617) 253-1892. Fax: (617) 258-8150.

[1] Abbreviations: AMO, alkene monooxygenase; BMM, bacterial multicomponent monooxygenase; C2,3O, catechol 2,3-dioxygenase; DTT, dithiothreitol; ET, electron transfer; H_{peroxo}, second peroxodiiron intermediate species of MMOH; IPTG, isopropyl β-D-1-thiogalactopyranoside; MMOB, regulatory protein of sMMO; MMOH, hydroxylase component of sMMO; MMOR, reductase protein of sMMO; MOPS, 3-(*N*-morpholino)propanesulfonic acid; NADH, reduced nicotinamide adenine dinucleotide; P*, first peroxodiiron intermediate species of MMOH; PAGE, polyacrylamide gel electrophoresis; PH, three-component phenol hydroxylase; PHH, hydroxylase component of *Pseudomonas* sp. OX1 PH; PHM, regulatory protein component of PH; PHP, reductase component of PH; Q, di(μ-oxo)diiron(IV) intermediate species of MMOH; RFQ, rapid freeze quench; SDS, sodium dodecyl sulfate; sMMO, soluble methane monooxygenase; T2MO, toluene 2-monooxygenase system from *Burkholderia cepacia* G4; T4mo, four-component toluene 4-monooxygenase system from *Pseudomonas mendocina* KR1; TMO, four-component alkene/arene monooxygenase; ToMO, four-component toluene/*o*-xylene monooxygenase protein system from *Pseudomonas* sp. OX1; ToMOC, Rieske [2Fe-2S] protein component of ToMO; ToMOD, regulatory protein component of ToMO; ToMOF, reductase protein component of ToMO; ToMOH, hydroxylase component of ToMO; Tris-HCl, 2-amino-2-(hydroxymethyl)-1,3-propanediol hydrochloride.

The diiron(III) intermediate, with Mössbauer parameters δ = 0.55 ± 0.02 mm/s and ΔE_Q = 0.67 ± 0.03 mm/s, could be a peroxide or hydroperoxide unit (*15*). The spectroscopic characteristics of this species are unusual for a peroxodiiron(III) center, however, which typically exhibits the following values: $\lambda_{max} >$ 650 nm, $\delta >$ 0.6 mm/s, and $\Delta E_Q >$ 1.0 mm/s. These notable differences suggest that the ToMO intermediate must deviate in geometry and/or protonation state from well-characterized diiron(III) peroxide species, but its exact nature remains to be fully elucidated. This species is believed to be the active oxidant in the ToMO system, because rapid freeze quench (RFQ) double-mixing Mössbauer spectroscopic experiments revealed that its rate of decay is accelerated in the presence of the substrate phenol (*15*). Analogous investigations of the O_2 activation pathway of the *Pseudomonas* sp. OX1 phenol hydroxylase hydroxylase component (PHH) revealed a similar intermediate species in this enzyme (*17*).

Although the hydroxylase proteins have been definitively established to house the diiron catalytic reaction centers, the functions of the regulatory proteins of BMMs have been a source of ongoing investigation. These proteins, of which the best-studied is MMOB in sMMO, have been implicated in the O_2 activation, substrate entry, proton-transfer, and electron-transfer phases of the catalytic cycles for hydrocarbon oxidation (*1, 2, 18*). The regulatory proteins increase the rates and electron coupling efficiencies of the steady state hydroxylation reactions (*19–22*), modulate the redox potentials of the hydroxylase diiron site (*23, 24*), accelerate the rates of electron transfer between the reductase and the hydroxylase (*20, 21*), perturb the spectroscopic features of the hydroxylase active site (*19, 25–29*), rearrange the hydroxylase iron ligands (*28, 30, 31*), promote conformational changes in the hydroxylase (*21, 28, 30–33*), gate the access of substrate and solvent to the hydroxylase diiron centers (*30, 34*), alter the substrate specificity and regiospecificity of hydroxylation reactions (*27, 34–36*), promote the binding of an active site water molecule invoked in proton transfer (*30*), modulate the kinetics of the reaction of reduced hydroxylase with O_2 (*37*), and prevent inopportune reduction of the oxygenated iron intermediates of the hydroxylase via untimely electron transfer (*30–32, 38*). At high concentrations, the regulatory proteins inhibit steady state activity in the sMMO, PH, and toluene 4-monooxygenase (T4mo) systems (*19, 20, 39*). The ability of these small, cofactorless proteins to influence so many distinct processes clearly indicates a mechanistic complexity that is not yet fully understood. Further studies of these and other BMM regulatory components are necessary to obtain a complete picture of their functions.

Reductase protein components in the BMM systems provide electrons to the diiron centers in the hydroxylases (*1, 2*). The sMMO reductase MMOR, however, also affects catalysis in a complicated and versatile manner, tuning the redox potentials of the hydroxylase diiron units (*23, 38*), altering the kinetics of the reaction with O_2 (*38*), promoting conformational changes in the hydroxylases (*32, 33*), and influencing how the hydroxylases interact with substrates (*27*). These observations suggest that MMOR regulates catalysis in addition to providing electrons for the reductive activation of dioxygen. Whether this phenomenon is restricted to sMMO or is a general feature of all BMMs is worth establishing and has motivated in part this investigation.

Toluene/*o*-xylene monooxygenase and phenol hydroxylase are the first two enzymes in a pathway that allows *Pseudomonas* sp. OX1 to metabolize aromatics as its sole carbon source (Scheme 1). Enzymes involved in the upstream segment of this pathway, ToMO, PH, and catechol 2,3-dioxygenase (C2,3O), degrade aromatic molecules through oxidation reactions. Downstream "*meta*-cleavage" enzymes then cleave the modified aromatic ring and process the resulting products for entry into major metabolic pathways required for bacterial viability (*39, 40*). Both ToMO and PH have a broad substrate specificity and oxidize a variety of aromatic hydrocarbons in addition to their native substrates, including *o*-, *m*-, and *p*-cresol, several dimethylphenols, and benzene (*39, 41*). By comparison to the sMMO systems, little is known about how the protein components of the *Pseudomonas* sp. OX1 BMMs act together to achieve hydrocarbon oxidation. In the studies undertaken here, we explored the influences of the *Pseudomonas* sp. OX1 PH and ToMO auxiliary proteins on substrate (phenol; NADH) consumption and product (catechol; H_2O_2) formation. The results and their interpretation constitute this report.

MATERIALS AND METHODS

General Considerations. Distilled water was deionized with a Milli-Q filtering system. Tris-HCl gradient gels (4 to 20%) were purchased from Bio-Rad Laboratories. Phenol and catechol were purified by vacuum sublimation prior to use. Other reagents were purchased from Sigma Aldrich and used as received unless otherwise noted.

Protein Purification. PHH was expressed in *E. coli* from a vector containing the *phk*, *phl*, *phn*, and *pho* genes [pGEM3Z/PHΔMΔP]. Construction of this plasmid, as well as expression and purification of the hydroxylase protein from this construct, will be described elsewhere (*17*). Plasmids containing the genes for the PH regulatory protein, PHM [pET22b(+)/PHM], and reductase, PHP [pET22b(+)/PHP], were supplied by A. Di Donato (Università di Napoli Federico II, Naples, Italy). PHP was expressed as described previously, except that $Fe(NH_4)_2(SO_4)_2 \cdot 6H_2O$ and IPTG were added to final concentrations of 200 and 75 μM, respectively, at induction (*39*). The resulting cell paste (~20 g) was sonicated on ice using a Branson sonifier in 30 s pulses for 12 min at 40% output in ~100 mL of 20 mM sodium phosphate (pH 7.0), 1 mM DTT, and 10% glycerol (buffer A) containing 100 units of DNaseI (New England Biolabs). Insoluble material was removed by ultracentrifugation at 18300*g* for 60 min, and the supernatant was filtered through a 0.45 μm membrane and loaded onto a Q Sepharose FF column (100 mL) equilibrated in buffer A. The column was washed with 200 mL of buffer A, after which bound proteins were eluted in 1 L by running a linear gradient from 0.08 to 1.0 M NaCl at a rate of 1.5 mL/min. Fractions containing PHP eluted at ~350 mM NaCl and were identified by SDS–PAGE and by absorbance at 271, 340, and 459 nm. These fractions were pooled and concentrated to ~7 mL using a 30K molecular weight cutoff Amicon centrifugal concentrator (Millipore). The resulting protein was loaded onto a Superdex S75 column equilibrated with buffer A containing 0.2 M NaCl (buffer B). Proteins were eluted by running buffer B over the column at a flow rate of 1 mL/min. Fractions displaying an A_{271}:A_{459} ratio of 2.5–3 and an A_{340}:A_{459} ratio of slightly < 1 and appearing pure by SDS–PAGE were pooled, concentrated, flash-frozen in liquid nitrogen, and stored at −80 °C until further use.

PHM was expressed as described previously (*39*). The resulting cell paste was sonicated on ice using a Branson sonifier in 30 s pulses for 12 min at 40% output in ~100 mL of 25 mM MOPS

Scheme 1: Metabolism of Benzene by *Pseudomonas* sp. OX1

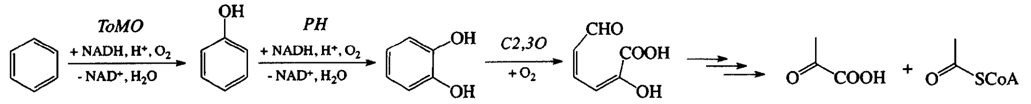

(pH 7.0) and 10% glycerol (buffer C) containing 100 units of DNaseI (New England Biolabs). Insoluble material was removed by ultracentrifugation at 18300*g* for 60 min, and the supernatant was filtered through a 0.45 μm membrane and loaded onto a Q Sepharose FF column (100 mL) equilibrated in buffer C. The column was washed with 200 mL of buffer C, after which bound proteins were eluted in 1 L by running a linear gradient from 0 to 0.5 M NaCl at a rate of 1.5 mL/min. PHM eluted in two peaks centered at ~340 and ~400 mM NaCl that were identified by monitoring the absorbance at 280 nm and by SDS−PAGE and native gel electrophoresis. The contents of fractions corresponding to the first peak, the second peak, or both peaks were pooled and concentrated to ~7 mL using a 3K molecular weight cutoff Amicon centrifugal concentrator (Millipore). The resulting protein was loaded onto a Superdex S75 column equilibrated with buffer C containing 0.2 M NaCl (buffer D). Proteins were eluted by running buffer D over the column at a flow rate of 1 mL/min. PHM eluted in one broad peak with a shoulder. Fractions appearing pure by SDS−PAGE were pooled and concentrated. Properly folded PHM was obtained by thermally denaturing the protein and then letting it refold by slowly cooling the solution to room temperature. For this process, PHM was diluted to 75 μM in 25 mM MOPS (pH 7.0) containing 10% glycerol. The protein was heated to 70 °C over 30 min in a water bath, and then the bath was removed from the heating block and the protein allowed to cool until it reached room temperature. The resulting protein was analyzed by native gel electrophoresis, flash-frozen in liquid nitrogen, and stored at −80 °C until further use.

The hydroxylase, ToMOH (*42*), regulatory, ToMOD (*43*, *44*), Rieske, ToMOC (*42*), and reductase, ToMOF (*45*), components of ToMO and the ToMOH I100W variant (*16*, *46*) were expressed in *E. coli* and purified as described previously. Specific activities of both PH and ToMO were measured using a coupled assay employing catechol 2,3-dioxygenase and phenol as a substrate (*42*). Hydroxylase iron content was determined by the ferrozine colorimetric assay (*47*). Using these procedures, we typically obtained protein activity in the range of 1200−1400 milliunits/mg for PHH and 1100−1300 milliunits/mg for ToMOH, and the iron contents ranged from 3.6 to 4.1 Fe atoms per dimer for PHH and from 3.9 to 4.1 Fe atoms per dimer for ToMOH. Approximate extinction coefficients used to quantify the PH hydroxylase, regulatory, and reductase proteins were calculated from primary amino acid sequences as 600000, 12000, and 21000 M^{-1} cm^{-1}, respectively, at 280 nm. Approximate extinction coefficients used to quantify the ToMO hydroxylase and regulatory proteins, calculated from primary amino acid sequences, were 600000 and 2860 M^{-1} cm^{-1}, respectively, at 280 nm. Extinction coefficients used to quantify the ToMO reductase and Rieske protein were previously reported (*42*).

Single-Turnover Assays. To quantify the amount of catechol formed during a single enzyme turnover, we first reduced the appropriate hydroxylase protein in the presence of phenol and the cognate component proteins to generate the O_2-reactive diiron(II) cofactor. We then exposed the reduced solution to O_2 to initiate the oxygenation reaction. After a 20 min incubation, reaction mixtures were assayed for aromatic product content using high-performance liquid chromatography (HPLC).

PHH or ToMOH, prepared in 400 μL of 0.1 M Tris-HCl (pH 7.5), was reduced in an anaerobic chamber by addition of stoichiometric $Na_2S_2O_4$ or on the benchtop by the addition of stoichiometric NADH in the presence of its cognate auxiliary proteins and phenol. The former procedure allowed us to quantify product in the absence of the electron-transfer proteins PHP or ToMOF and ToMOC because $Na_2S_2O_4$ can reduce the diiron centers of PHH and ToMOH directly. For studies probing PH, reaction solutions contained 100 μM PHH, 0 or 600 μM PHM, 10 or 200 μM PHP, 5 mM phenol, and 200 μM NADH or $Na_2S_2O_4$. For experiments monitoring ToMO, reaction solutions contained 50 μM ToMOH, 0 or 100 μM ToMOD, 100 μM ToMOC, 5 μM ToMOF, 500 μM phenol, and 50 μM NADH or $Na_2S_2O_4$. Accurate $Na_2S_2O_4$ concentrations were determined by anaerobic titration into $K_3[Fe(CN)_6]$ (*48*).

Reduced protein mixtures were allowed to react with 100 μL of O_2-saturated buffer for 20 min at 25 °C and then reactions were quenched by addition of 100 μL of 0.4 M TCA to precipitate the protein. The precipitated protein was removed by centrifugation at 17110*g* for 10 min, and the supernatant was assayed for catechol content by HPLC. HPLC experiments were performed at a flow rate of 1 mL/min on a Vydac C_{18} reversed-phase protein and peptide column at 25 °C. The separation program utilized a two-solvent system step gradient consisting of 0.1% HCOOH in ddH_2O (solvent A) and 0.1% HCOOH in methanol (solvent B). Following injection of 100 μL of sample onto the column, unbound material was removed by washing with 98% A for 10 min. The aromatic compounds were then eluted using a linear gradient from 2 to 98% B over 10 min. Absorbance of the eluent was monitored continuously at 280 and 274 nm. Under these conditions, phenol and catechol eluted at 18.5 and 10.1 min, respectively. Peaks corresponding to phenol or catechol were integrated, and their concentrations were determined by comparison to a standard curve prepared in the same manner as the test solutions. All experiments were conducted in triplicate using enzymes prepared from different batches of cell paste.

Single-turnover studies probing the allosteric effect of *oxidized* electron-transfer protein on the amount of catechol formed by the hydroxylase diiron centers were performed in a similar manner, except that diiron centers of PHH or ToMOH were reduced for 20 min with $Na_2S_2O_4$ prior to addition of the cognate electron-transfer protein (PHP for PH and ToMOC for ToMO) and exposure to O_2-saturated buffer.

H_2O_2 Assays. A colorimetric assay was employed to determine the conditions under which PH and ToMO generate H_2O_2 by uncoupled oxidase activity. For studies monitoring PH, reaction solutions contained 1 μM PHH, 0 or 6 μM PHM, 0.1 or 2 μM PHP, and 200 μM NADH in 500 μL of 0.1 M Tris-HCl (pH 7.5). For reactions probing ToMO, reaction solutions contained 1 μM ToMOH, 0 or 2 μM ToMOD, 2 μM ToMOC, 0.1 μM ToMOF, and 200 μM NADH in 500 μL of 0.1 M Tris-HCl (pH 7.5). All reaction mixtures also contained 10 μM NH_2OH to inhibit the activity of *Escherichia coli* catalase, which can be present as an impurity and affect the interpretation of

BMM H_2O_2 assays (49). For reactions employing substrate, the concentration of phenol was 5 mM. All reactions were performed at 25.0 ± 0.1 or 4.0 ± 0.5 °C. Reactions were initiated by addition of NADH and quenched after a specified reaction time by addition of 100 μL of 0.4 M TCA to precipitate the protein.

H_2O_2 was quantitated colorimetrically with KSCN and $Fe(NH_4)_2(SO_4)_2 \cdot 6H_2O$ (51). However, because unconsumed NADH interferes with the reported procedure, a step was added to inactivate the reducing agent prior to removing the precipitated protein and assaying the supernatants for H_2O_2. Following addition of TCA, reaction mixtures were heated at 90 °C for 15 min and then allowed to cool slowly to room temperature over 45 min. Precipitated protein was then removed by centrifugation at 17110g for 5 min, and 500 μL of supernatant was transferred to a fresh Eppendorf tube. A 200 μL portion of 10 mM $Fe(NH_4)_2(SO_4)_2 \cdot 6H_2O$ in ddH_2O and 100 μL of 2.5 M KSCN in ddH_2O were added to each Eppendorf tube. The reaction mixtures were stirred and allowed to stand for 5 min before their absorption at 480 nm was monitored. Solutions of H_2O_2 in buffer were treated in the same manner as the enzyme reaction mixtures to generate a standard curve. For the standards, the concentration of a freshly prepared H_2O_2 stock solution was determined by measuring the absorbance at 240 nm (ε_{240} = 43.6 M^{-1} cm^{-1}) (52). Data displaying hyperbolic H_2O_2 generation kinetics were fit to the exponential growth model $y = A\ \exp(-kt) + B$ to obtain the first-order rate constant for H_2O_2 production.

Consumption of H_2O_2 by PH was monitored in the absence of NADH. Reaction mixtures contained 0 or 1 μM PHH, 0 or 6 μM PHM, 2 μM PHP, 10 μM NH_2OH, and 1 mM phenol in 500 μL of 0.1 M Tris-HCl (pH 7.5). Reactions were initiated by addition of 10 or 50 μM H_2O_2 and were quenched after specified reaction times with 100 μL of 0.4 M TCA to precipitate the protein. Precipitated protein was removed by centrifugation at 17110g for 5 min, and 500 μL of supernatant was assayed for H_2O_2 content as described for the H_2O_2 generation assays.

H_2O_2 and NH_2OH Inactivation Assays. Two methods were used to assay for inactivation of PH by H_2O_2. In the first, reaction solutions containing 0.5 μM PHH, 3 μM PHM, and 1 μM PHP in 500 μL of 0.1 M Tris-HCl (pH 7.5) were incubated with 0 or 50 μM H_2O_2 and 1 mM phenol for 20 min. Subsequently, 1 mM NADH was added to initiate the hydrocarbon oxidation reaction. These reactions were quenched after a specified time by addition of 100 μL of 0.4 M TCA to precipitate the protein, and the supernatant was assayed for catechol content by HPLC. Plots of catechol formed versus time incubated with H_2O_2 were fit to the linear equation $y = kx + b$ to obtain the protein activity.

For the second method, reaction solutions containing 1 μM PHH, 6 μM PHM, and 2 μM PHP in 500 μL of 0.1 M Tris-HCl (pH 7.5) were incubated with 5 mM NADH for a specified time period, after which phenol was added to a final concentration of 5 mM. Reactions were allowed to proceed for 20 min and then were quenched by the addition of 100 μL of 0.4 M TCA to precipitate the protein, and the supernatant was assayed for catechol content by HPLC. Data were plotted as the percentage of the amount of catechol formed in experiments in which NADH and phenol were added simultaneously (t = 0 min) versus the time that the reaction mixture was incubated with NADH before addition of phenol.

To determine whether addition of the *E. coli* catalase inhibitor NH_2OH affects the activity of PH and ToMO, activity assays were performed in its presence and absence. For PH, reaction solutions contained 2 μM PHH, 12 μM PHM, 4 μM PHP, 1 mM phenol, and 0 or 20 μM NH_2OH in 250 μL of 0.1 M Tris-HCl (pH 7.5). Aliquots of 350 μM NADH were added to initiate hydrocarbon oxidation. Reactions were quenched after 2 or 10 min by addition of 100 μL of 0.4 M TCA to precipitate the protein, and the supernatants were assayed for catechol by HPLC. For ToMO, reaction solutions contained 1 μM ToMOH, 4 μM ToMOD, 2 μM ToMOC, 0.1 μM ToMOF, 2 mM phenol, and 0 or 10 μM NH_2OH in 500 μL of 0.1 M Tris-HCl (pH 7.5). Aliquots of 500 μM NADH were added to initiate hydrocarbon oxidation. Reactions were quenched 1, 5, or 15 min after reaction initiation by addition of 100 μL of 0.4 M TCA to precipitate the protein, and the supernatants were assayed for catechol by HPLC.

NADH Consumption Assays. NADH consumption by PH and ToMO was measured colorimetrically. For studies probing PH, reaction mixtures contained 0 or 1 μM PHH, 0 or 6 μM PHM, 0.1 or 2 μM PHP, and 200 μM NADH in 600 μL of 0.1 M Tris-HCl (pH 7.5). For experiments monitoring ToMO, reaction solutions contained 0 or 1 μM ToMOH, 0 or 2 μM ToMOD, 2 μM ToMOC, 0.1 μM ToMOF, and 200 μM NADH in 500 μL of 0.1 M Tris-HCl (pH 7.5). For reaction mixtures containing substrate, the concentration of phenol was 5 mM. All reactions were initiated by addition of PHP for PH and NADH for ToMO. NADH consumption was monitored continuously by absorbance at 340 nm (ε_{340} = 6220 M^{-1} cm^{-1}). Reaction mixtures were thermostated at 25.0 ± 0.1 °C using a circulating water bath. Data were analyzed by fitting the initial time points to the linear function $y = kx + b$.

RESULTS

Toluene/*o*-xylene monooxygenase (ToMO) and phenol hydroxylase (PH) from *Pseudomonas* sp. OX1 are BMMs responsible for catalyzing the first two steps in the metabolism of benzene, phenol, and other aromatics that can serve as the sole source of carbon and energy for the organism. These enzyme systems must orchestrate the delivery of four substrates, an aromatic hydrocarbon, dioxygen, protons, and electrons, to their carboxylate-bridged diiron centers in the hydroxylase components, where conversion to an aryl alcohol and water occurs. This process requires two or three components in addition to the hydroxylase. In this study, we conducted a series of experiments aimed at investigating the possibility that these components might affect more than one step in the catalytic cycle, thereby playing multiple roles in these systems.

We maintained the ratios of protein components employed in all assays reported here so that they would be those reported to yield the best rates of conversion of phenol to catechol in steady state experiments. For ToMO, maximal product formation rates occur with 2 equiv of regulatory protein ToMOD, 2 equiv of Rieske protein ToMOC, and 0.1 equiv of reductase ToMOF per hydroxylase dimer (42). For most studies, 2 equiv of ToMOD per ToMOH was used; however, because ToMOD does not inhibit steady state activity as noted for other BMM regulatory proteins (42), experiments employing higher ratios of ToMOD were also conducted and are directly comparable to those employing 2 equiv of ToMOD. For PH expressed from the pGEM3Z/PHΔMΔP vector and used throughout these studies, maximal product formation occurred with ~6 equiv of PHM (Figure S1a of the Supporting Information) and 2 equiv of PHP (data not shown) per hydroxylase dimer.

Table 1: Single-Turnover Yields[a]

phenol hydroxylase (PH)			toluene/*o*-xylene monooxygenase (ToMO)		
reaction conditions	reducing agent	% catechol formed per active site	reaction conditions	reducing agent	% catechol formed per active site
PHH	$Na_2S_2O_4$	nd[b]	ToMOH	$Na_2S_2O_4$	6.9 ± 0.2
PHH:6PHM:2PHP	NADH	54 ± 2	ToMOH:2ToMOD:2ToMOC:0.1ToMOF	NADH	50 ± 7
PHH:6PHM:2PHP	$Na_2S_2O_4$	54 ± 1	ToMOH:2ToMOD:2ToMOC	$Na_2S_2O_4$	46 ± 3
PHH_{red}:6PHM:2PHP_{ox}[c]	$Na_2S_2O_4$	24 ± 6	$\text{ToMOH}_{\text{red}}$:2ToMOD:$\text{2ToMOC}_{\text{ox}}$[d]	$Na_2S_2O_4$	29 ± 1
PHH:6PHM	$Na_2S_2O_4$	nd[b]	ToMOH:2ToMOD	$Na_2S_2O_4$	10.0 ± 0.9
PHH:2PHP	$Na_2S_2O_4$	8 ± 3	ToMOH:2ToMOC	$Na_2S_2O_4$	11 ± 2

[a] All experiments were performed at 25 °C. [b] None detected. [c] PHH:6M was prereduced with stoichiometric $Na_2S_2O_4$ prior to the addition of PHP_{ox}. After subsequent addition of O_2-saturated buffer, the solution was assayed for catechol content. [d] ToMOH:2D was prereduced with stoichiometric $Na_2S_2O_4$ prior to the addition of ToMOC_{ox}. After subsequent addition of O_2-saturated buffer, the solution was assayed for catechol content.

Table 2: NADH Consumption Rates[a]

phenol hydroxylase (PH)		toluene/*o*-xylene monooxygenase (ToMO)	
reaction conditions	NADH consumption rate (μM/min)	reaction conditions	NADH consumption rate (μM/min)
PHH	nd[b]	ToMOH	nd[b]
PHH:6PHM:2PHP	67.2 ± 0.7	ToMOH:4ToMOD:2ToMOC:0.1ToMOF	14 ± 2
PHH:2PHP	17.6 ± 0.2	ToMOH:4ToMOD	6.4 ± 0.6
PHH:6PHM:2PHP:phenol	180 ± 7	ToMOH:4ToMOD:2ToMOC:0.1ToMOF:phenol	86 ± 5
2PHP	4.0 ± 0.3	0.1ToMOF:2ToMOC	1.9 ± 0.2

[a] All experiments were performed at 25 °C. [b] No NADH consumption detected.

Single-Turnover Assays. In these experiments, we wished to determine whether the enzyme systems operate by a half- or full-sites mechanism. Both ToMOH and PHH are dimers, and we were interested in learning whether the two protomers would act in concert with (half-sites) or independently of one another (full-sites). We also were interested in defining the minimal number of components necessary to achieve this reaction during a single turnover. For example, although the reductases are not required, does their presence affect the outcome of the reactions?

We first quantified the amount of catechol product formed by various component mixtures during a single-enzyme single turnover using phenol as the substrate (Table 1). A negligible amount of catechol was generated by the hydroxylase proteins PHH or ToMOH when they were reduced with $Na_2S_2O_4$ in the absence of their respective auxiliary proteins (< 10% per diiron sites). Addition of the regulatory protein, PHM or ToMOD, to the cognate hydroxylase prior to reduction of the diiron centers did not significantly enhance product yield (Table 1). For PH, addition of the reductase (PHP) to PHH before reduction with $Na_2S_2O_4$ improved the product yield, although the amount of catechol formed, 8 ± 3% per diiron sites, is too low to be physiologically relevant. In similar experiments, the ToMO Rieske protein, ToMOC, did not substantially affect the amount of catechol formed by ToMOH.

Only the fully reconstituted systems containing the hydroxylase, regulatory protein, reductase, and Rieske protein for ToMO generated a significant amount of catechol. Both PH and ToMO formed only ~50% of catechol with respect to protein active site clusters even though the phenolic substrate was present in great excess, indicating a half-sites reactivity (Table 1). Formation of an active protein ternary complex prior to reduction of the hydroxylase diiron centers presumably mediates efficient product formation.

The results were independent of the electron-transfer mechanism employed, because addition of either NADH, which reduces the hydroxylase active sites via the electron-transfer proteins, or $Na_2S_2O_4$, which directly reduces the diiron centers, generated the same amount of catechol (Table 1). Therefore, low product yields achieved using $Na_2S_2O_4$ with incomplete systems (vide supra) are a consequence of the protein complexation state rather than the use of a nonphysiological reduction procedure.

Because complete (~50%) product yields are achieved when the diiron centers are reduced directly with $Na_2S_2O_4$ in the presence of the electron-transfer proteins, but not in their absence, we surmise that these components influence the active hydroxylase conformation through allosteric effects. To investigate this phenomenon more fully, single-turnover experiments were conducted in which the diiron centers of a hydroxylase/regulatory protein mixture were reduced with stoichiometric $Na_2S_2O_4$ prior to addition of oxidized electron-transfer protein (PHP for PH or ToMOC for ToMO) to the reaction mixture and subsequent exposure to O_2. Inclusion of the appropriate electron-transfer protein in these experiments significantly enhanced product yield. For PH, the yield of catechol increased from undetectable levels in the absence of PHP to 24 ± 6% of the diiron centers in its presence. For ToMO, a 3-fold increase in product yield was promoted by inclusion of ToMOC. Although these results clearly demonstrate that the oxidized electron-transfer protein plays a role in the phenol oxidation process happening at the hydroxylase diiron centers, it is important to note that maximal (~50%) product accumulation did not occur with either enzyme system.

Steady State NADH Consumption by PH and ToMO. We also examined the effects of the auxiliary proteins on steady state catalysis. Table 2 shows the rates of NADH consumption during steady state turnover in the PH and ToMO systems at 25 °C under a variety of conditions. PHH and ToMOH do not consume NADH in the absence of their cognate electron-transfer proteins. Consumption of NADH by the electron-transfer proteins PHP or ToMOC and ToMOF occurs at very modest rates, presumably by uncoupled oxidase activity and generation of H_2O_2 (vide infra). Consumption of NADH by the PH and ToMO electron-transfer protein/hydroxylase complexes is more rapid than for the electron-transfer protein(s) alone, probably because transfer of electrons from the electron-transfer protein to the hydroxylase leads to more rapid regeneration of the oxidized electron-transfer protein, which is then ready to acquire more electrons from NADH. Alternatively, the electron-transfer proteins could assume a conformation that accepts electrons more readily when complexed with their cognate hydroxylases.

Of consequence is the finding that the rates of consumption of NADH by the electron-transfer protein/hydroxylase mixture are accelerated by 2−3-fold with the inclusion of the cognate regulatory protein, a phenomenon also observed in sMMO (*20*). This result suggests that the regulatory proteins play a role in the electron-transfer process, at least when hydrocarbon substrate is not present. As expected, the rates of NADH consumption are significantly enhanced by the presence of the substrate phenol because aromatic hydrocarbon oxidation leads to rapid regeneration of the oxidized protein components.

Steady State H_2O_2 Production by PH and ToMO. NADH consumption experiments clearly demonstrated that PH and ToMO consume electrons in the absence of hydrocarbon substrate (vide supra), and we wished to determine the fate of these reducing equivalents. If these electrons are used to catalyze the two-electron reduction of O_2 to H_2O_2 or the four-electron reduction of O_2 to H_2O, an important insight into the catalytic mechanisms of these protein systems would be provided. We therefore performed steady state experiments to quantify the amount of H_2O_2 produced by PH and ToMO under a variety of conditions. Although we cannot compare quantitatively the results of these experiments to the results of the NADH consumption studies because of differences in the experimental protocols, the results afford a qualitative assessment of the reaction chemistry accessible to the systems.

It is already known that some BMMs generate H_2O_2 catalytically in the absence of hydrocarbon substrate (*15*, *20*, *50*); however, the mechanism of formation of H_2O_2 by these systems is largely unexplored. Production of H_2O_2 might arise from two sources: (i) oxidase activity of the electron transfer protein(s) or (ii) protonation and liberation from peroxodiiron(III) intermediates generated at the hydroxylase diiron active sites during the activation of O_2 (*15*, *17*). To distinguish between mechanisms (i) and (ii), we measured the ability of various protein mixtures to produce H_2O_2. The *E. coli* catalase inhibitor NH_2OH was included in all assays to prevent complications of H_2O_2 generation or consumption by trace *E. coli* catalase impurities (*50*). Importantly, NH_2OH does not interfere with the enzymatic activity of PH or ToMO (data not shown).

Initial attempts to quantify H_2O_2 produced by PH and ToMO utilized a colorimetric method employing KSCN and an Fe(II) source (*51*). However, this procedure had to be modified because unconsumed NADH present in the reaction mixtures interfered with formation of the colored isothiocyanatoiron(III) complex in a complex manner (Figure S2a of the Supporting Information). A method was therefore developed to inactivate the reducing agent prior to H_2O_2 quantitation. Although H_2O_2 is reasonably stable to heat for short time periods (~1 h) under acidic conditions, NADH can be inactivated when exposed to low pH and elevated temperatures (*53*). Accordingly, the quenched reaction mixtures were acidified and heated as described in Materials and Methods before the precipitated protein was removed by centrifugation and the supernatant was assayed for H_2O_2 content. Using this method, a hydrogen peroxide standard curve was found to be independent of NADH concentration (Figure S2b of the Supporting Information).

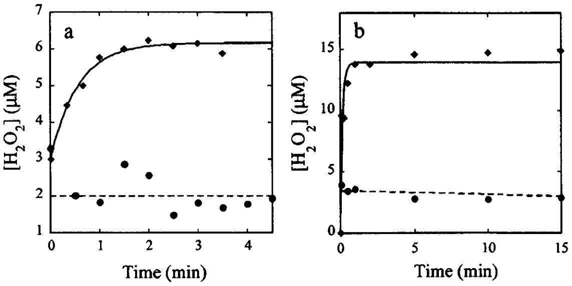

FIGURE 1: Representative profiles of H_2O_2 generated by PH (a) and ToMO (b). (a) H_2O_2 generation profile upon addition of 200 μM NADH to a solution of 1 μM PHH, 6 μM PHM, 2 μM PHP, and 10 μM NH_2OH at pH 7.5 and 4 °C in the presence (◆ and —) or absence (● and ---) of 5 mM phenol. (b) H_2O_2 generation profile upon addition of 200 μM NADH to a solution of 1 μM ToMOH, 2 μM ToMOD, 2 μM ToMOC, 0.1 μM ToMOF, and 10 μM NH_2OH at pH 7.5 and 25 °C in the presence (◆ and —) or absence (● and ---) of 5 mM phenol. Data obtained in the absence of phenol were fit (—) to the single-exponential formation process $y = A\exp(-kt) + B$. Reaction solutions were assayed for H_2O_2 content as noted in the text.

With this revised method, we verified that H_2O_2 is generated by the complete PH and ToMO systems in the absence of phenol (Figure 1, diamonds, solid lines). In the presence of phenol, H_2O_2 is not generated by either system (Figure 1, circles, dashed lines), probably because electron consumption is fully coupled to hydrocarbon oxidation. The H_2O_2 evolution profiles of PH and ToMO in the absence of phenol displayed hyperbolic behavior with non-zero *y*-intercepts. The small amount of apparent H_2O_2 present in the assay mixtures at time zero probably results from protein-bound iron(III) that dissociates upon acid precipitation and then binds to thiocyanate in the reaction mixture to form isothiocyanatoiron(III) and produce the red color detected. Accordingly, the values on the *y*-intercept approximate the iron content of the proteins being assayed. Fits of the H_2O_2 profiles to single-exponential processes returned first-order rate constants of 1.8 min^{-1} for PH at 4 °C and 6.8 min^{-1} for ToMO at 4 °C.

It is important to note for these studies that PH does not consume H_2O_2 in the absence of phenol. Assays employing a 10- or 50-fold excess of H_2O_2 indicated no consumption of H_2O_2 by the enzyme system over 8 min in the absence or presence of PHM and in the presence of NH_2OH (Figure S3 of the Supporting Information). Given these findings, reports that both ToMOH (*15*) and toluene 2-monooxygenase (T2MO) from *Burkholderia cepacia* G4 (*54*) can consume H_2O_2 by means of catalase activity are likely to reflect small amounts of catalase protein contaminants rather than hydroxylase activity as a catalase (*22*, *50*).

The observed hyperbolic behavior of the PH and ToMO H_2O_2 evolution profiles is most likely due to enzyme inactivation by the hydrogen peroxide that is generated, as previously reported for phenol hydroxylase from *Pseudomonas* sp. CF600 (*55*). To examine whether PH is indeed inactivated over the course of the reaction, we treated the enzyme system with NADH for up to 8 min before adding phenol, incubated the mixture for 20 min, and then assayed for catechol content. Catechol yield decreased as a function of NADH−enzyme incubation time, indicating that

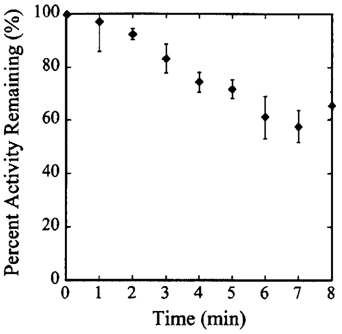

FIGURE 2: Percent PH activity remaining as a function of time following incubation with NADH. Reaction solutions containing 1 μM PHH, 6 μM PHM, and 2 μM PHP in 500 μL of 0.1 M Tris-HCl (pH 7.5) were incubated with 5 mM NADH for a specified time period between 0 and 8 min, after which 5 mM phenol was added. Reactions were allowed to proceed for 20 min and then were quenched by addition of 100 μL of TCA. Catechol content was monitored by HPLC. Data are plotted as the percentage of the amount of catechol formed in experiments in which NADH and phenol were added simultaneously (*t* = 0 min) vs the time that the reaction mixture was incubated with NADH before addition of phenol. Data points represent the average of two trials performed with different batches of protein.

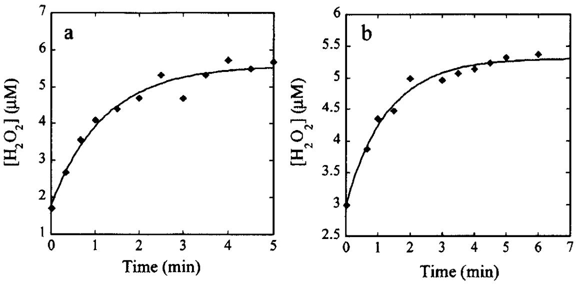

FIGURE 3: (a) Representative profile of H_2O_2 generation (◆) upon addition of 200 μM NADH to 2 μM PHP at pH 7.5 and 4 °C. Similar reaction profiles were obtained in the presence of NH_2OH. (b) Representative profile of H_2O_2 generation (◆) upon addition of 200 μM NADH to a solution of 1 μM PHH, 6 μM PHM, 0.1 μM PHP, and 10 μM NH_2OH at pH 7.5 and 4 °C. Data were fit (—) to the single-exponential formation process $y = A\exp(-kt) + B$. Reaction solutions were assayed for H_2O_2 content as noted in the text. See the text for a comment on the non-zero ordinate intercepts.

time-dependent protein inactivation does indeed occur under the conditions employed in the steady state H_2O_2 assays (Figure 2). To determine whether the observed enzyme inactivation could be mediated by formation of H_2O_2, the enzyme system was incubated with a 100-fold excess of H_2O_2 for 20 min prior to assaying for catechol content. HPLC quantification revealed that the H_2O_2-exposed system generated only 63% of the catechol observed for the untreated enzyme. Together, these results indicate that the hyperbolic nature of the H_2O_2 generation curve probably results from enzyme inactivation by H_2O_2. We note that the enzyme inactivation process observed in these studies seems to occur more slowly than the H_2O_2 generation curve plateaus but argue that the results of the two experiments can be compared only qualitatively because of inherent differences in experimental conditions, most notably the type of product monitored. The mechanism of enzyme inactivation probably stems from H_2O_2-mediated free radical damage to the PH proteins. Similar behavior is expected for ToMO (*15*).

To delineate the mechanism of production of H_2O_2 by PH, we examined the abilities of the reductase and hydroxylase to independently generate it. PHP produces H_2O_2 in the presence of O_2 and NADH (Figure 3a). The reaction is also characterized by hyperbolic H_2O_2 evolution, and a fit of the data to an exponential growth model revealed a first-order rate constant *k* of 0.82 min^{-1} at 4 °C. Under similar conditions, PHP does not consume H_2O_2 in the absence of NADH (Figure S4 of the Supporting Information). The measured rate of formation of H_2O_2 by 2 equiv of PHP is insufficient to account for the H_2O_2 formed by the complete enzyme system, however. It is therefore likely that H_2O_2 arises instead from PHH or from PHH and PHP. To distinguish between these two possibilities, we performed H_2O_2 assays with PHH, 6 equiv of PHM, and 0.1 equiv of PHP. At this substoichiometric ratio of PHP to PHH, electron consumption and product formation are fully coupled (*39*) and the oxidase activity of the reductase protein should be negligible. These conditions led to the release of H_2O_2 from the hydroxylase in a hyperbolic fashion with a first-order rate constant *k* of 0.77 min^{-1} at 4 °C (Figure 3b). However, the rate of H_2O_2 production under these conditions is also insufficient to account for the H_2O_2 generation profile observed in the presence of the complete, stoichiometric enzyme system. We therefore conclude that H_2O_2 arises from both PHP oxidase activity and generation at the hydroxylase diiron centers with the fully reconstituted system.

In contrast to that from PH, evolution of H_2O_2 from ToMO occurs only from the hydroxylase diiron center. Because the fully coupled experiments employed substoichiometric amounts of reductase (ToMOF) and because ET from ToMOC to ToMOH is rapid (*56*), it is unlikely that substantial amounts of H_2O_2 result from the oxidase activity of these proteins. To verify this hypothesis, we measured the generation of H_2O_2 by the complete system in which ToMOH was replaced by its I100W variant, which has a tryptophan residue installed near the enzyme active site and undergoes a different O_2 activation pathway than wild-type hydroxylase. Although both ToMOH and its I100W variant form a peroxodiiron(III/III) intermediate upon reaction of the reduced protein with O_2, that generated by ToMOH I100W decays via a one electron-transfer pathway to form a W$^\bullet$ and a mixed-valent diiron(III/IV) species (*46*) rather than directly proceeding to the diiron(III) resting enzyme state as observed for wild-type species (*15*). The W$^\bullet$ is then quenched via recombination with a hydroxyl radical originating from the diiron center. As a result, ToMOH I100W is not catalytic and displays a negligible specific activity.

H_2O_2 assays employing ToMOH I100W exhibited a significantly diminished rate of H_2O_2 formation compared to those using wild-type ToMOH, with a *k* of 0.84 min^{-1} at 25 °C, and a marked decrease in the total amount of H_2O_2 generated relative to that of the wild-type protein (Figure 4). These observations suggest that the hydroxylase is the component of the system responsible for generating H_2O_2. The decreased rate of H_2O_2 produced by ToMOH I100W is attributed to the competing process of intermediate decay, which will not produce H_2O_2. Similarly, the diminished amount of H_2O_2 produced by ToMOH I100W is attributed to its inability to engage in catalytic reaction behavior.

DISCUSSION

The remarkable ability of BMM systems to perform challenging hydrocarbon oxidation reactions in a regioselective manner depends on the coordinated efforts of three or more protein components. Regulation of the dynamic interplay between these proteins is crucial to maintaining effective and sustainable

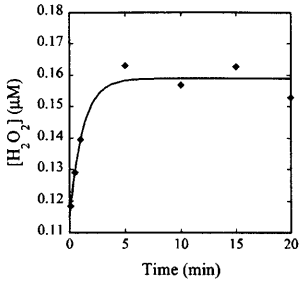

FIGURE 4: Representative H_2O_2 generation profile upon addition of 200 μM NADH to a solution of 1 μM ToMOH I100W, 2 μM ToMOD, 2 μM ToMOC, 0.1 μM ToMOF, and 10 μM NH_2OH at pH 7.5 and 25 °C in the absence of phenol. Data were fit (—) to the single-exponential formation process $y = A\exp(-kt) + B$. Reaction solutions were assayed for H_2O_2 content as noted in the text.

enzyme systems. However, these protein interactions are complicated, and the functions of the individual protein components are still not fully understood.

Evidence of Half-Sites Reactivity in PH and ToMO. The observations that the complete PH or ToMO systems generate ~50% of the product per active site in single-turnover assays (Table 1) and that fewer than 50% of the diiron sites proceed though the common peroxodiiron(III) intermediate thought to be responsible for arene oxidation during O_2 activation (*15*, *17*) indicate that these proteins react by a half-sites reactivity mechanism. In this model, negative cooperativity between the two active site protomers assures a mechanism in which only one subunit of the dimer activates O_2 at a time. Such allosteric communication ensures that the other active site is simultaneously engaged in the reductive phase of the catalytic cycle. In support of this mechanism, the crystal structure of the PHH–PHM complex revealed a regulatory protein bound at only one side of the hydroxylase dimer (*31*), suggesting that one active site in the dimer proceeds through the catalytic cycle at a time.[2] In contrast, MMOH does not proceed by a half-sites type of mechanism, because 90–100% of the product forms per diiron sites in single-turnover assays (*38*).

Electron-Transfer Proteins Regulate Hydroxylase Chemistry. Single-turnover experiments reveal that BMM electron-transfer proteins affect the O_2 activation and/or substrate oxidation steps of catalysis as well as reducing the hydroxylase diiron sites, because the product yield is greatly enhanced by the presence of these proteins even when physiological electron transfer is not operative (Table 1). This conclusion is based on single-turnover assays in which addition of oxidized electron-transfer protein to a prereduced hydroxylase/regulatory protein mixture generated more product than that obtained from a reduced hydroxylase/regulatory protein mixture (Table 1). Although maximal (~50%, vide infra) catechol accumulation does not occur under these conditions, the amount of product formed is significantly greater than that generated in the absence of the appropriate ET protein. Because ET from the reductase to the hydroxylase should not occur under these conditions, the enhancement of product yield must arise solely from allosteric effects. The mechanism(s) by which the electron-transfer protein regulates phenol oxidation is unknown; however, studies with sMMO suggest that the binding of MMOR induces a long-lived conformational change in MMOH (*27*, *32*, *33*) and that MMOR modulates product regiospecificity, presumably by altering hydroxylase–substrate interactions (*27*). The PH and ToMO ET proteins might therefore affect hydroxylase activity by opening a conformationally responsive substrate gate. In the presence of the appropriate electron-transfer protein, the hydroxylase would assume a conformational setting in which hydrocarbon substrates can more readily access the active site. Recent structural studies of the T4mo hydroxylase/regulatory protein complex (*30*) indicate that the hydrocarbon substrate must enter the active site prior to binding of the regulatory protein, before or during reduction of the hydroxylase, adding further support to this argument.

The regulatory roles of the ET proteins have a more marked effect in PH and ToMO than in sMMO, because single-turnover product yields are more significantly affected by the presence of the regulatory protein than in sMMO. PHH or ToMOH alone cannot catalytically generate a significant amount of product; however, reduced sMMO hydroxylase, MMOH, produces ~40% propylene oxide per diiron site in single-turnover reactions using propylene as substrate and ~80% in the presence of the regulatory protein, MMOB (*38*). MMOR also slightly enhances the product yield in these experiments. Addition of 0.5 equiv of MMOR to a mixture of MMOH and MMOB prior to reduction of the protein by $Na_2S_2O_4$ increases the product yield only from ~80 to ~88% (*38*), a smaller and less significant effect than in PH or ToMO. The reasons for the differences between PH/ToMOH and sMMO are unknown, but because it is likely that the mechanisms of hydrocarbon substrate ingress differ between these systems (*57*), conformational changes in the hydroxylase induced by binding of the electron-transfer protein could regulate hydrocarbon substrate entry.

Regulatory Proteins Regulate ET. These experiments revealed that consumption of NADH by PH and ToMO is retarded in the absence of the regulatory protein when hydrocarbon substrate is not present (Table 2). Similar studies have been reported for sMMO (*20*). These results implicate the regulatory protein in the ET process, although the molecular details of this process are not understood. X-ray crystal structures of hydroxylase/regulatory protein complexes from *Pseudomonas* sp. OX1 PH (*31*) and *P. mendocina* KR1 T4mo (*30*) show that the regulatory protein binds to the hydroxylase at the proposed docking site of the cognate electron-transfer protein. It is likely that the regulatory protein promotes a long-lived conformational change in the hydroxylase that persists after its dissociation and facilitates ET protein binding and/or electron transfer to the hydroxylase diiron centers (*30*). A similar role of the sMMO regulatory protein has been proposed (*32*).

Generation of H_2O_2 by BMMs. In the presence of a hydrocarbon substrate, H_2O_2 is not produced by PH or ToMO (Scheme 2) because all reducing equivalents are used productively to form hydroxylated product and H_2O (Scheme 2a). In the absence of a hydrocarbon substrate, however, PH and ToMO generate H_2O_2. Under the conditions employed for our experiments, production of H_2O_2 results from the hydroxylase (Scheme 2b) and, in the case of PH, from the oxidase activity of the reductase protein (Scheme 2c).

Previous studies probing the reactions of chemically reduced PHH (*17*) or ToMOH (*15*) with O_2 in the presence of the appropriate regulatory protein revealed that long-lived peroxodiiron(III)

---

[2] X-ray crystal structures of oxidized and reduced hydroxylase–regulatory protein complexes of *Pseudomonas mendocina* KR1 toluene 4-monooxygenase reveal 1 equiv of regulatory protein bound to each protomer of the hydroxylase, however (*30*). The reason for this difference is unknown.

Scheme 2: Evolution of Products by PH or ToMO in the Presence (i) or Absence (ii) of Phenol and by PHP in the Absence of Phenol (iii)

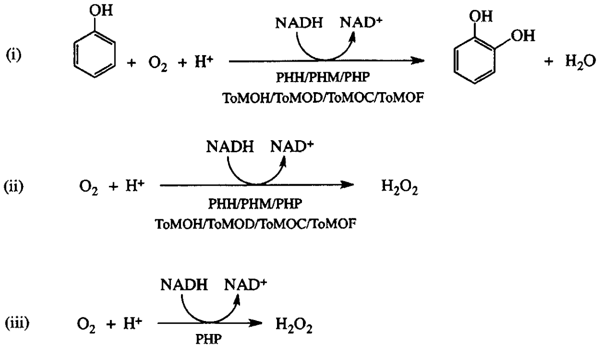

Scheme 3: Proposed Mechanisms of O_2 Activation by ToMO and PH

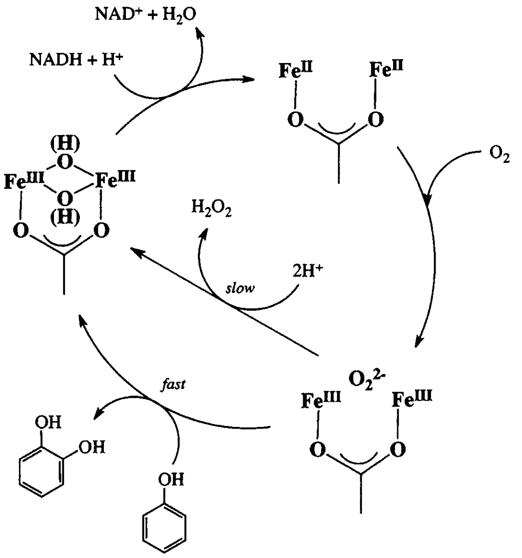

intermediate species with unique spectroscopic and optical characteristics accumulate and decay to a diiron(III) product without forming any high-valent iron species (Scheme 3). This species is thought to be responsible for rapid oxidation of a hydrocarbon substrate (*15*). The studies presented in this work indicate that decay of the peroxodiiron(III) transients will occur by protonation and liberation of the bound peroxide unit as H_2O_2 in the absence of a hydrocarbon substrate. Consistent with this proposal is the observation that sMMO does not produce H_2O_2 under steady state conditions (*20*). In this system, the second peroxodiiron(III) intermediate that accumulates, H_{peroxo}, rapidly converts to the di(μ-oxo)diiron(IV) species Q, which can decay by acquiring two electrons and two protons to release H_2O and form the diiron(III) resting state (*20*, *58*).

In the context of the cell, the choice of whether the reducing equivalents are used to generate hydroxylated product and H_2O or H_2O_2 is under kinetic control for PH and ToMO: much slower kinetics of formation of H_2O_2 (Figure 1) relative to that of formation of catechol (*39*, *42*) (Figure S1 of the Supporting Information) ensures that electrons are not used unproductively to generate H_2O_2 when the hydrocarbon substrate is present (Scheme 3). This kinetic effect might reflect a thermodynamic preference of the system for an un- or monoprotonated peroxodiiron(III) species rather than its diprotonated form, enforced by the electrostatic environment of the enzyme active sites. In this manner, the enzymes have evolved to control the product outcome such that only productive hydroxylated product is formed in the presence of a hydrocarbon substrate.

CONCLUDING REMARKS

In conclusion, these experiments reveal that the auxiliary proteins of PH and ToMO affect catalysis in a well-controlled manner. The regulatory proteins PHM and ToMOD accelerate ET, and the ET proteins regulate substrate oxidation. Unraveling the details of the molecular mechanisms underlying these dynamic protein interactions is crucially important for understanding these remarkable systems in future studies.

ACKNOWLEDGMENT

We thank Dr. Rachel K. Behan for helpful discussions.

SUPPORTING INFORMATION AVAILABLE

Figures S1–S4 as described in the text. This material is available free of charge via the Internet at http://pubs.acs.org.

REFERENCES

1. Murray, L. J., and Lippard, S. J. (2007) Substrate Trafficking and Dioxygen Activation in Bacterial Multicomponent Monooxygenases. *Acc. Chem. Res. 40*, 466–474.
2. Sazinsky, M. H., and Lippard, S. J. (2006) Correlating Structure with Function in Bacterial Multicomponent Monooxygenases and Related Diiron Proteins. *Acc. Chem. Res. 39*, 558–566.
3. Leahy, J. G., Batchelor, P. J., and Morcomb, S. M. (2003) Evolution of the Soluble Diiron Monooxygenases. *FEMS Microbiol. Rev. 27*, 449–479.
4. Notomista, E., Lahm, A., Di Donato, A., and Tramontano, A. (2003) Evolution of Bacterial and Archaeal Multicomponent Monooxygenases. *J. Mol. Evol. 56*, 435–445.
5. Wallar, B. J., and Lipscomb, J. D. (1996) Dioxygen Activation by Enzymes Containing Binuclear Non-Heme Iron Clusters. *Chem. Rev. 96*, 2625–2657.
6. Brazeau, B. J., and Lipscomb, J. D. (2000) Kinetics and Activation Thermodynamics of Methane Monooxygenase Compound Q Formation and Reaction with Substrates. *Biochemistry 39*, 13503–13515.
7. Tinberg, C. E., and Lippard, S. J. (2009) Revisiting the Mechanism of Dioxygen Activation in Soluble Methane Monooxygenase from *M. capsulatus* (Bath): Evidence for a Multi-Step, Proton-Dependent Reaction Pathway. *Biochemistry 48*, 12145–12158.
8. Liu, K. E., Valentine, A. M., Wang, D., Huynh, B. H., Edmondson, D. E., Salifoglou, A., and Lippard, S. J. (1995) Kinetic and Spectroscopic Characterization of Intermediates and Component Interactions in Reactions of Methane Monooxygenase from *Methylococcus capsulatus* (Bath). *J. Am. Chem. Soc. 117*, 10174–10185.
9. Liu, K. E., Wang, D., Huynh, B. H., Edmondson, D. E., Salifoglou, A., and Lippard, S. J. (1994) Spectroscopic Detection of Intermediates in the Reaction of Dioxygen with Reduced Methane Monooxygenase Hydroxylase from *Methylococcus capsulatus* (Bath). *J. Am. Chem. Soc. 116*, 7465–7466.
10. Valentine, A. M., Stahl, S. S., and Lippard, S. J. (1999) Mechanistic Studies of the Reaction of Reduced Methane Monooxygenase Hydroxylase with Dioxygen and Substrates. *J. Am. Chem. Soc. 121*, 3876–3887.
11. Lee, S.-K., and Lipscomb, J. D. (1999) Oxygen Activation Catalyzed by Methane Monooxygenase Hydroxylase Component: Proton Delivery during the O–O Bond Cleavage Steps. *Biochemistry 38*, 4423–4432.
12. Lee, S.-K., Fox, B. G., Froland, W. A., Lipscomb, J. D., and Münck, E. (1993) A Transient Intermediate of the Methane Monooxygenase Catalytic Cycle Containing an $Fe^{IV}Fe^{IV}$ Cluster. *J. Am. Chem. Soc. 115*, 6450–6451.

13. Lee, S.-K., Nesheim, J. C., and Lipscomb, J. D. (1993) Transient Intermediates of the Methane Monooxygenase Catalytic Cycle. *J. Biol. Chem. 268*, 21569–21577.

14. Shu, L., Nesheim, J. C., Kauffmann, K., Münck, E., Lipscomb, J. D., and Que, L., Jr. (1997) An $Fe_2^{IV}O_2$ Diamond Core Structure for the Key Intermediate Q of Methane Monooxygenase. *Science 275*, 515–518.

15. Murray, L. J., Naik, S. G., Ortillo, D. O., García-Serres, R., Lee, J. K., Huynh, B. H., and Lippard, S. J. (2007) Characterization of the Arene-Oxidizing Intermediate in ToMOH as a Diiron(III) Species. *J. Am. Chem. Soc. 129*, 14500–14510.

16. Murray, L. J., García-Serres, R., Naik, S., Huynh, B. H., and Lippard, S. J. (2006) Dioxygen Activation at Non-Heme Diiron Centers: Characterization of Intermediates in a Mutant Form of Toluene/*o*-Xylene Monooxygenase Hydroxylase. *J. Am. Chem. Soc. 128*, 7458–7459.

17. Izzo, V., Tinberg, C. E., García-Serres, R., Naik, S., Huynh, B. H., and Lippard, S. J., manuscript in preparation.

18. Merkx, M., Kopp, D. A., Sazinsky, M. H., Blazyk, J. L., Müller, J., and Lippard, S. J. (2001) Dioxygen Activation and Methane Hydroxylation by Soluble Methane Monooxygenase: A Tale of Two Irons and Three Proteins. *Angew. Chem., Int. Ed. 40*, 2782–2807.

19. Fox, B. G., Liu, Y., Dege, J. E., and Lipscomb, J. D. (1991) Complex Formation between the Protein Components of Methane Monooxygenase from *Methylosinus trichosporium* OB3b: Identification of Sites of Component Interaction. *J. Biol. Chem. 266*, 540–550.

20. Gassner, G. T., and Lippard, S. J. (1999) Component Interactions in the Soluble Methane Monooxygenase System from *Methylococcus capsulatus* (Bath). *Biochemistry 38*, 12768–12785.

21. Green, J., and Dalton, H. (1985) Protein B of Soluble Methane Monooxygenase from *Methylococcus capsulatus* (Bath): A Novel Regulatory Protein of Enzyme Activity. *J. Biol. Chem. 260*, 15795–15801.

22. Pikus, J. D., Studts, J. M., Achim, C., Kauffmann, K. E., Münck, E., Steffan, R. J., McClay, K., and Fox, B. G. (1996) Recombinant Toluene-4-monooxygenase: Catalytic and Mössbauer Studies of the Purified Diiron and Rieske Components of a Four-Protein Complex. *Biochemistry 35*, 9106–9119.

23. Liu, K. E., and Lippard, S. J. (1991) Redox Properties of the Hydroxylase Component of Methane Monooxygenase from *Methylococcus capsulatus* (Bath): Effects of Protein B, Reductase, and Substrate. *J. Biol. Chem. 266*, 12836–12839.

24. Paulsen, K. E., Liu, Y., Fox, B. G., Lipscomb, J. D., Münck, E., and Stankovich, M. T. (1994) Oxidation-Reduction Potentials of the Methane Monooxygenase Hydroxylase Component from *Methylosinus trichosporium* OB3b. *Biochemistry 33*, 713–722.

25. DeWitt, J. G., Rosenzweig, A. C., Salifoglou, A., Hedman, B., Lippard, S. J., and Hodgson, K. O. (1995) X-ray Absorption Spectroscopic Studies of the Diiron Center in Methane Monooxygenase in the Presence of Substrate and the Coupling Protein of the Enzyme System. *Inorg. Chem. 34*, 2505–2515.

26. Fox, B. G., Hendrich, M. P., Surerus, K. K., Andersson, K. K., Froland, W. A., Lipscomb, J. D., and Münck, E. (1993) Mössbauer, EPR, and ENDOR Studies of the Hydroxylase and Reductase Components of Methane Monooxygenase from *Methylosinus trichosporium* OB3b. *J. Am. Chem. Soc. 115*, 3688–3701.

27. Froland, W. A., Andersson, K. K., Lee, S.-K., Liu, Y., and Lipscomb, J. D. (1992) Methane Monooxgenase Component B and Reductase Alter the Regioselectivity of the Hydroxylase Component-catalyzed Reactions: A Novel Role for Protein-Protein Interactions in an Oxygenase Mechanism. *J. Biol. Chem. 267*, 17588–17597.

28. Mitić, N., Schwartz, J. K., Brazeau, B. J., Lipscomb, J. D., and Solomon, E. I. (2008) CD and MCD Studies of the Effects of Component B Variant Binding on the Biferrous Active Site of Methane Monooxygenase. *Biochemistry 47*, 8386–8397.

29. Pulver, S. C., Froland, W. A., Lipscomb, J. D., and Solomon, E. I. (1997) Ligand Field Circular Dichroism and Magnetic Circular Dichroism Studies of Component B and Substrate Binding to the Hydroxylase Component of Methane Monooxygenase. *J. Am. Chem. Soc. 119*, 387–395.

30. Bailey, L. J., McCoy, J. G., Phillips, G. N., Jr., and Fox, B. G. (2008) Structural Consequences of Effector Protein Complex Formation in a Diiron Hydroxylase. *Proc. Natl. Acad. Sci. U.S.A. 105*, 19194–19198.

31. Sazinsky, M. H., Dunten, P. W., McCormick, M. S., Di Donato, A., and Lippard, S. J. (2006) X-ray Structure of a Hydroxylase-Regulatory Protein Complex from a Hydrocarbon-Oxidizing Multicomponent Monooxygenase, *Pseudomonas* sp. OX1 Phenol Hydroxylase. *Biochemistry 45*, 15392–15404.

32. Blazyk, J. L., Gassner, G. T., and Lippard, S. J. (2005) Intermolecular Electron-Transfer Reactions in Soluble Methane Monooxygenase: A Role for Hysteresis in Protein Function. *J. Am. Chem. Soc. 127*, 17364–17376.

33. Gallagher, S. C., Callaghan, A. J., Zhao, J., Dalton, H., and Trewhella, J. (1999) Global Conformational Changes Control the Reactivity of Methane Monooxygenase. *Biochemistry 38*, 6752–6760.

34. Wallar, B. J., and Lipscomb, J. D. (2001) Methane Monooxygenase Component B Mutants Alter the Kinetics of Steps Throughout the Catalytic Cycle. *Biochemistry 40*, 2220–2233.

35. Mitchell, K. H., Studts, J. M., and Fox, B. G. (2002) Combined Participation of Hydroxylase Active Site Residues and Effector Protein Binding in a *Para* to *Ortho* Modulation of Toluene 4-Monooxygenase Regiospecificity. *Biochemistry 41*, 3176–3188.

36. Zheng, H., and Lipscomb, J. D. (2006) Regulation of Methane Monooxygenase Catalysis Based on Size Exclusion and Quantum Tunneling. *Biochemistry 45*, 1685–1692.

37. Liu, Y., Nesheim, J. C., Lee, S.-K., and Lipscomb, J. D. (1995) Gating Effects of Component B on Oxygen Activation by the Methane Monooxygenase Hydroxylase Component. *J. Biol. Chem. 270*, 24662–24665.

38. Liu, Y., Nesheim, J. C., Paulsen, K. E., Stankovich, M. T., and Lipscomb, J. D. (1997) Roles of the Methane Monooxygenase Reductase Component in the Regulation of Catalysis. *Biochemistry 36*, 5223–5233.

39. Cafaro, V., Izzo, V., Scognamiglio, R., Notomista, E., Capasso, P., Casbarra, A., Pucci, P., and Di Donato, A. (2004) Phenol Hydroxylase and Toluene/*o*-Xylene Monooxygenase from *Pseudomonas stutzeri* OX1: Interplay between Two Enzymes. *Appl. Environ. Microbiol. 70*, 2211–2219.

40. Powlowski, J., and Shingler, V. (1994) Genetics and Biochemistry of Phenol Degradation by *Pseudomonas* sp. CF600. *Biodegradation 5*, 219–236.

41. Arenghi, F. L. G., Berlanda, D., Galli, E., Sello, G., and Barbieri, P. (2001) Organization and Regulation of *meta* Cleavage Pathway Genes for Toluene and *o*-Xylene Derivative Degradation in *Pseudomonas stutzeri* OX1. *Appl. Environ. Microbiol. 67*, 3304–3308.

42. Cafaro, V., Scognamiglio, R., Viggiani, A., Izzo, V., Passaro, I., Notomista, E., Dal Piaz, F., Amoresano, A., Casbarra, A., Pucci, P., and Di Donato, A. (2002) Expression and Purification of the Recombinant Subunits of Toluene/*o*-Xylene Monooxygeanse and Reconsitution of the Active Complex. *Eur. J. Biochem. 269*, 5689–5699.

43. Bertoni, G., Martino, M., Galli, E., and Barbieri, P. (1998) Analysis of the Gene Cluster Encoding Toluene/*o*-Xylene Monooxygenase from *Pseudomonas stutzeri* OX1. *Appl. Environ. Microbiol. 64*, 3626–3632.

44. Scognamiglio, R., Notomista, E., Barbieri, P., Pucci, P., Dal Piaz, F., Tramontano, A., and Di Donato, A. (2001) Conformational Analysis of Putative Regulatory Subunit D of the Toluene/*o*-Xylene-Monooxygenase Complex from *Pseudomonas stutzeri* OX1. *Protein Sci. 10*, 482–490.

45. Song, W. J., Behan, R. K., Naik, S. G., Huynh, B. H., and Lippard, S. J. (2009) Characterization of a Peroxodiiron(III) Intermediate in the T201S Variant of Toluene/*o*-Xylene Monooxygenase Hydroxylase from *Pseudomonas* sp. OX1. *J. Am. Chem. Soc. 131*, 6074–6075.

46. Murray, L. J., García-Serres, R., McCormick, M. S., Davydov, R., Naik, S. G., Kim, S.-H., Hoffman, B. M., Huynh, B. H., and Lippard, S. J. (2007) Dioxygen Activation at Non-Heme Diiron Centers: Oxidation of a Proximal Residue in the I100W Variant of Toluene/*o*-Xylene Monooxygenase Hydroxylase. *Biochemistry 46*, 14795–14809.

47. Gibbs, C. R. (1976) Characterization and Application of FerroZine Iron Reagent as a Ferrous Iron Indicator. *Anal. Chem. 48*, 1197–1201.

48. Lambeth, D. O., and Palmer, G. (1973) The Kinetics and Mechanism of Reduction of Electron Transfer Proteins and Other Compounds of Biological Interest by Dithionite. *J. Biol. Chem. 248*, 6095–6103.

49. Switala, J., and Loewen, P. C. (2002) Diversity of Properties Among Catalases. *Arch. Biochem. Biophys. 401*, 145–154.

50. Elsen, N. L., Bailey, L. J., Hauser, A. D., and Fox, B. G. (2009) Role for Threonine 201 in the Catalytic Cycle of the Soluble Diiron Hydroxylase Toluene 4-Monooxygenase. *Biochemistry 48*, 3838–3846.

51. Hildebrandt, A. G., and Roots, I. (1975) Reduced Nicotinamide Adenine Dinucleotide Phosphate (NADPH)-Dependent Formation and Breakdown of Hydrogen Peroxide during Mixed Function Oxidation Reactions in Liver Microsomes. *Arch. Biochem. Biophys. 171*, 385–397.

52. Messner, K. R., and Imlay, J. A. (2002) *In Vitro* Quantitation of Biological Superoxide and Hydrogen Peroxide Generation. *Methods Enzymol. 349*, 354–361.

53. Yang, X., and Ma, K. (2005) Determination of Hydrogen Peroxide Generated by Reduced Nicotinamide Adenine Dinucleotide Oxidase. *Anal. Biochem. 344*, 130–134.

54. Newman, L. M., and Wackett, L. P. (1995) Purification and Characterization of Toluene 2-Monooxygenase from *Burkholderia cepacia* G4. *Biochemistry 34*, 14066–14076.
55. Cadieux, E., Vrajmasu, V., Achim, C., Powlowski, J., and Münck, E. (2002) Biochemical, Mössbauer, and EPR Studies of the Diiron Cluster of Phenol Hydroxylase from *Pseudomonas* sp. Strain CF 600. *Biochemistry 41*, 10680–10691.
56. Song, W. J., and Lippard, S. J. (2011) unpublished results.
57. McCormick, M. S. (2008) Structural Investigations of Hydroxylase Proteins and Complexes in Bacterial Multicomponent Monooxygenase Systems. Ph.D. Thesis, Massachusetts Institute of Technology, Cambridge, MA.
58. Lund, J., Woodland, M. P., and Dalton, H. (1985) Electron Transfer Reactions in the Soluble Methane Monooxygenase of *Methylococcus capsulatus* (Bath). *Eur. J. Biochem. 147*, 297–305.

BIOGRAPHICAL NOTE

The author was born in Ulsan, Republic of Korea on August 27, 1981 to Changgyu Song and Younghee Choi. She was raised along with one sister, Jiyoon Song. She attended Ewha Womans University in Seoul, where she earned dual Bachelor of Science degrees in Science Education and Chemistry Education. The author then pursued post-undergraduate studies in Chemistry department at Ewha Womans University in the laboratory of Prof. Wonwoo Nam. Upon receiving her M.S., she came to MIT in the fall of 2006 to start graduate studies on a diiron-containing enzyme, toluene/*o*-xylene monooxygenase to understand orchestrated chemical reactions in the laboratory of Prof. Stephen J. Lippard. After graduation, the author plans to pursue postdoctoral studies in the laboratory of Prof. Akif Tezcan at University of California at San Diego, CA and to study the design and evolution of metalloenzymes.

Woon Ju Song

EDUCATION

Ph.D. Inorganic Chemistry	Massachusetts Institute of Technology, Cambridge, MA
2006-2011	Advisor: Professor Stephen J. Lippard
M.S. Chemistry	Ewha Womans University, Seoul, Korea
2003-2005	Advisor: Professor Wonwoo Nam
B.A. Chemistry Education	Ewha Womans University, Seoul, Korea
2000-2003	
B.A. Science Education	Ewha Womans University, Seoul, Korea
2000-2003	

HONORS/SCHOLARSHIP

2005-2006, Research Internship from National Research Foundation of Korea
2003-2004, Research Scholarship from Research Institute for Basic Sciences at Ewha Womans University
MAGNA CUM LAUDE
2000-2003, Dean's List

PUBLICATIONS

Woon Ju Song and Stephen J. Lippard "Mechanistic Studies of Reactions of Peroxodiiron(III) Intermediates in T201 Variants of Toluene/*o*-Xylene Monooxygenase Hydroxylase" *Biochemistry,* **2011**, *Accepted*

Arteum D. Bochevarov, Jianing Li, Woon Ju Song, Richard A. Friesner, Stephen J. Lippard "Insights into the Different Dioxygen Activation Pathways of Methane and Toluene Monooxygenase Hydroxylases" *J. Am. Chem. Soc.* **2011**, *133*, 7384-7397.

Christine E. Tinberg, Woon Ju Song, Viviana, Izzo, Stephen, J. Lippard "Multiple Roles of Component Proteins in Bacterial Multicomponent Monooxygenases: Phenol Hydroxylase and Toluene/*o*-Xylene Monooxygenase from *Pseudomonas sp.* OX1" *Biochemistry* **2011**, *50*, 1788-1798.

Woon Ju Song, Michael S. McCormick, Rachel K. Behan, Matthew H. Sazinsky, Wei Jiang, Jeffery Lin, Carsten Krebs, Stephen J. Lippard "Active Site Threonine Facilitates Proton Transfer during Dioxygen Activation at the Diiron Center of Toluene/*o*-Xylene Monooxygenase Hydroxylase" *J. Am. Chem. Soc.* **2010**, *132,* 13582-13585.

Woon Ju Song, Rachel K. Behan, Sunil G. Naik, Boi Hanh Huynh, Stephen J. Lippard "Characterization of a Peroxodiiron(III) Intermediate in the T201S Variant of Toluene/o-

Xylene Monooxygenase Hydroxylase from *Pseudomonas sp.* OX1" *J. Am. Chem. Soc.* **2009**, *131*, 6074-6075

Min-Jung Kang, Woon Ju Song, Ah-Rim Han, Young S. Choi, Ho G. Jang, Wonwoo Nam "Mechanistic Insight into the Aromatic Hydroxylation by High-Valent Iron(IV)-oxo Porphyrin π-Cation Radical Complexes" *J. Org. Chem.*, **2007**, *72,* 6301-6304

Woon Ju Song, Mi Sook Seo, Serena DeBeer George, Takehiro Ohta, Rita Song, Min-Jung Kang, Takehiko Tosha, Teizo Kitagawa, Edward I. Solomon, Wonwoo Nam "Synthesis, Characterization, and Reactivities of Manganese(V)-Oxo Porphyrin Complexes" *J. Am. Chem. Soc.,* **2007**, *129*, 1268-1277

Woon Ju Song, Ying Ji Sun, Sun Kyung Choi, Wonwoo Nam "Mechanistic Insights into the Reversible Formation of Iodosylarene–Iron Porphyrin Complexes in the Reactions of Oxoiron(IV) Porphyrin π -Cation Radicals and Iodoarenes: Equilibrium, Epoxidizing Intermediate, and Oxygen Exchange" *Chem. Eur. J.* **2005**, *12*, 130-137

Woon Ju Song, Yon Ok Ryu, Rita Song, Wonwoo Nam "Oxoiron(IV) Porphyrin π-Cation Radical Complexes with a Chameleon Behavior in Cytochrome P450 Model Reactions" *J. Biol. Inorg. Chem.* **2005**, *10*, 294-304

Se-Eun Park, Woon Ju Song, Yon Ok Ryu, Mi Hee Lim, Rita Song, Kwan Mook Kim, Wonwoo Nam "Parallel Mechanistic Studies on the Counterion Effect of Manganese Salen and Porphyrin Complexes on Olefin Epoxidation by Iodosylarenes" *J. Inorg. Biochem,* **2005**, *99*, 424-431

Wonwoo Nam, Yon Ok Ryu, Woon Ju Song "Oxidizing Intermediates in Cytochrome P450 Model Reactions" *J. Biol. Inorg. Chem,* **2004**, *9*, 654-660

József Kaizer, Eric J. Klinker, Na Young Oh, Jan-Uwe Rohde, Woon Ju Song, Audria Stubna, Jinheung Kim, Eckard Münck,, Wonwoo Nam, Lawrence Que, Jr. "Nonheme $Fe^{IV}O$ Complexes That Can Oxidize the C-H Bonds of Cyclohexane at Room Temperature" *J. Am. Chem. Soc,* **2004**, *126,* 472-473

PRESENTATIONS

240th American Chemical Society National Meeting & Exposition, Boston, MA, Aug. 22-26, 2010, Oral Presentation "Dioxygen Activation in T201 Variants of Toluene/*o*-Xylene Monooxygenase Hydroxylase from *Pseudomonas sp.* OX1"

The Microbial Systems (and beyond) Seminar @ Parsons at MIT, Cambridge, MA, Oct. 12, 2010, Oral Presentation "Proton and Dioxygen Transfer in Toluene/*o*-Xylene Monooxygenase Hydroxylase"

Frontiers in Metallobiochemistry at The Penn State University, University Park, PA, June 2-5, 2010, Poster Presentation “Dioxygen Activation in T201 Variants of Toluene/*o*-Xylene Monooxygenase Hydroxylase from *Pseudomonas sp.* OX1”

Metals in Biology Gordon Research Conference, Ventura, CA, Jan. 31-Feb. 5, 2010, Poster Presentation “Dioxygen Activation in T201 Variants of Toluene/*o*-Xylene Monooxygenase Hydroxylase from *Pseudomonas sp.* OX1”

Bioinorganic Gordon Research Seminar Ventura, CA, Feb. 4-7, 2010, Poster Presentation “Dioxygen Activation in T201 Variants of Toluene/*o*-Xylene Monooxygenase Hydroxylase from *Pseudomonas sp.* OX1”

The 2005 International Chemical Congress of Pacific Basin Societies (Pacifichem), Hawaii, HI, Dec. 15-Dec. 20, 2005 Poster Presentation “Oxoiron(IV) Porphyrin π-Cation Radical Complexes with a Chameleon Behavior in Cytochrome P450 Model Reactions”

The Second Asian Biological Inorganic Chemistry Conference (AsBIC-II) in conjunction with Third Symposium on Advances in Bioinorganic Chemistry, Goa, India, Dec. 5-10, 2004, Poster Presentation “Oxoiron(IV) Porphyrin π-Cation Radical Complexes with a Chameleon Behavior in Cytochrome P450 Model Reactions”